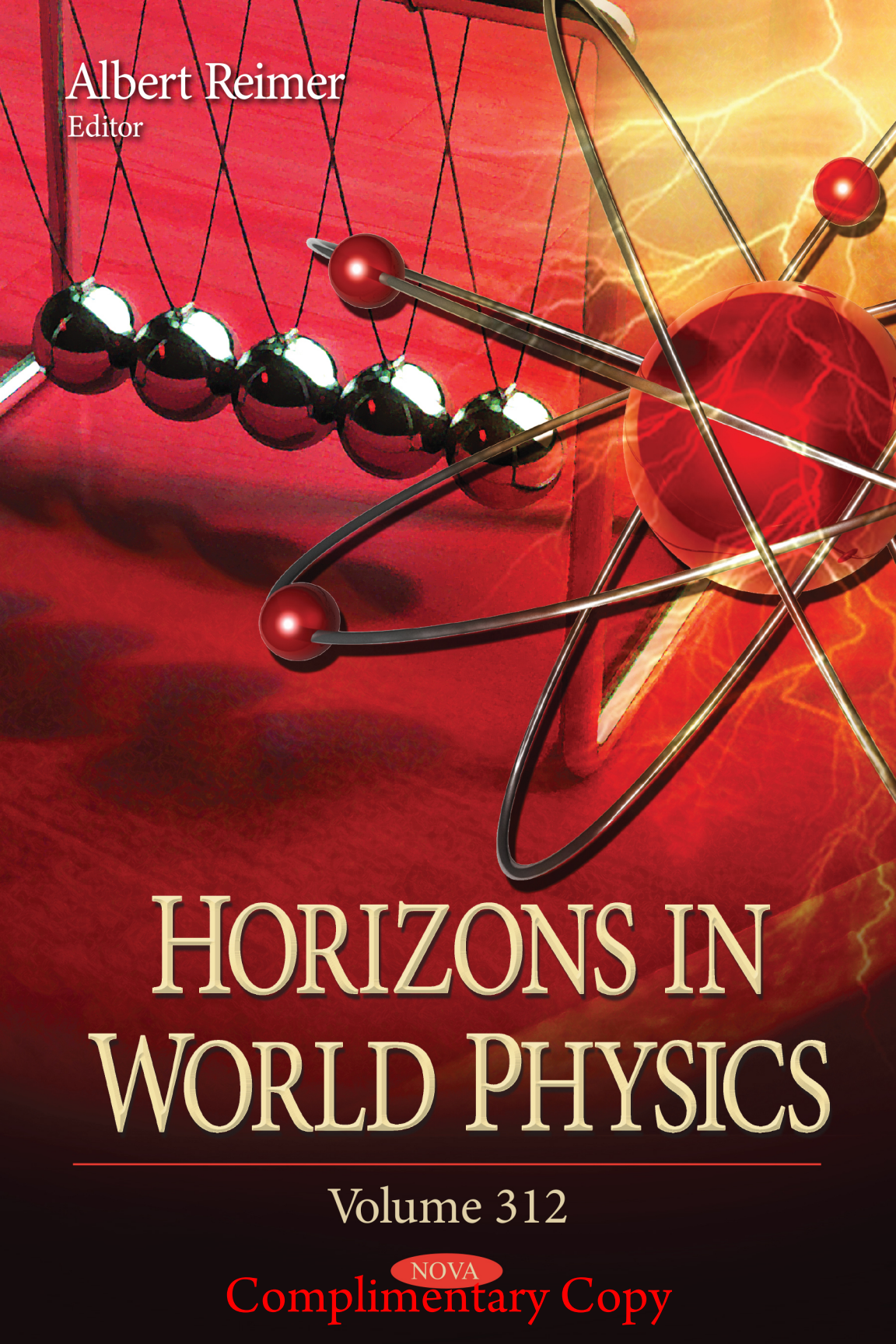
Albert Reimer
Editor
HORIZONS IN
WORLD PHYSICS
Volume 312
NOVA
Complimentary Copy

Horizons in World Physics

Horizons in World Physics

Horizons in World Physics. Volume 311
Albert Reimer (Editor)
2023. ISBN: 979-8-89113-192-7 (Hardcover)
2023. ISBN: 979-8-89113-234-4 (eBook)

Horizons in World Physics. Volume 310
Albert Reimer (Editor)
2023. ISBN: 979-8-89113-006-7 (Hardcover)
2023. ISBN: 979-8-89113-027-2 (eBook)

Horizons in World Physics. Volume 309
Albert Reimer (Editor)
2023. ISBN: 979-8-88697-641-0 (Hardcover)
2023. ISBN: 979-8-88697-762-2 (eBook)

Horizons in World Physics. Volume 308
Albert Reimer (Editor)
2023. ISBN: 979-8-88697-226-9 (Hardcover)
2023. ISBN: 979-8-88697-593-2 (eBook)

Horizons in World Physics. Volume 307
Albert Reimer (Editor)
2022. ISBN: 978-1-68507-549-1 (Hardcover)
2022. ISBN: 978-1-68507-574-3 (eBook)

More information about this series can be found at
https://novapublishers.com/product-category/series/horizons-in-world-physics/

Albert Reimer
Editor

Horizons in World Physics

Volume 312

Library of Congress Cataloging-in-Publication Data

ISBN: 979-8-89113-522-2(eBook)

Published by Nova Science Publishers, Inc. † New York

Contents

Preface

This book is a compilation of fourteen chapters on the most recent discoveries in World Physics. In Chapter One, the author's new interdisciplinary approach, based on nonlocal transport equations with memory obtained in nonequilibrium statistical mechanics, describes structural evolution on the mesoscale using principles developed in adaptive systems control theory. The distinctions and similarities in the evolution of four types of solitary waves propagating in an elastic nonlinear material are studied and commented on in Chapter Two. The atomic nuclei clusters (ANC) - genomes of viruses and bacteria, molecular clusters, domains, coils in the biocenosis of liquid manure were studied in Chapter Three. In Chapter Four, the traditional problem of longitudinal waves in collisionless plasma is solved. Chapter Five is a report of the procedure and results of estimating the temperatures of extrasolar planets discovered by NASA's Kepler-Mission to determine which may be potentially habitable. Chapter Six explores how we might utilize extrasolar planet density data to help develop criterion for distinguishing between the different types of extrasolar planets, such as Earths, Mini-Neptunes, and Neptunes. In Chapter Seven the authors observed the tracks of Earth's axions in the direction of the Sun and M1, which led to the conclusion that the planet had collided with a massive cloud of preons. In Chapter Eight, the International System of Physical Quantities (ISQ) was adapted to the new system (BPSQ) based on the characteristics of the proton's baryon form. The next chapter displays photographs of the Earth's axions tracks that are desorbed in the direction of magnetic storms on the Sun at the beginning of August 2023. A model of the desorption process is presented, and observation results are explained. In Chapter Ten, photographs of the tracks of the Moon's axions are exhibited against the background of the tracks of the Earth's axions during the period of intense magnetic storms on the Sun (December 2023) as a result of falling into the preon cloud. In the following chapter, photographs of the Earth's axion tracks are presented again, this time with the appearance of a new cloud of preons in the constellation Virgo. In Chapter Twelve the

author discusses the classical theory of molecular optical activity. In Chapter Thirteen, the authors investigate the IVPs for n-dimensional Schrödinger and wave equations. The final chapter provides a brief review of the consequences of the hypothesis regarding the existence of a background of superstrong interacting gravitons.

Chapter 1

Closed Loop of Internal Control in High-Rate Transfer Processes

Tatiana Khantuleva*
Department of Physical Mechanics, Saint-Petersburg State University,
Saint-Petersburg, Russia

Abstract

Conventional models of continuum mechanics adequately describe only rather slow transfer processes. Experimental studies of high-rate and short-duration processes found out that the system's response significantly lags behind the impact of force and is accompanied by self-organization of internal structure on the mesoscale. Far from local equilibrium the dynamic structure evolves towards a more stable state of the system, obeying certain internal laws. Unlike usual continuum models, the description of such processes cannot be localized both in space and time. The new interdisciplinary approach developed by the author, based on nonlocal transport equations with memory obtained in nonequilibrium statistical mechanics, describes structural evolution on the mesoscale using principles developed in the theory of control of adaptive systems. According to the Maximum Entropy principle, the goal of system evolution is to maximize the total entropy in the system. Speed Gradient principle determines the fastest way to the goal under constraints imposed and forms closed loops of internal control due to feedback between the structure evolution and macroscopic properties of the system. By transforming its dynamic structure, the system adapts to external influences and minimizes its irreversible losses. So, the inclusion of self-organization and closed loops of internal control is

* Corresponding author's email: t.khantuleva@spbu.ru.

In: Horizons in World Physics. Volume 312
Editor: Albert Reimer
ISBN: 979-8-89113-513-0

necessary for adequate modeling of processes that are far from local equilibrium. The proposed “flexible” modeling makes the description of nonequilibrium processes closed and provides an effective way to solve a wide range of modern practical problems related to the development of new technologies, intelligent systems and forecasting of catastrophic processes.

Keywords: internal control, feedback, nonlocal modeling, mesostructure, self-organization, turbulence, entropy production

1. Introduction

Uniform description of the motions of various media in a wide range of conditions is a problem that has not been solved until now. The main difficulty is that the state of the system, under sufficiently intense external influence, can quickly and radically change. Processes in which the state of a system or the mode of its functioning changes radically are considered transient. These include processes such as laminar-turbulent transition, elastic-plastic transition, transitions with a change in the phase state of the medium or its internal structure. Such transient processes usually occur with an increase in the speed of the process. In this case, a strong change in the state of the system occurs in a very short time, during which the state of the system cannot approach local thermodynamic equilibrium. Therefore, all high-rate and short-duration processes are highly nonequilibrium processes.

Classical continuum mechanics that describes the behavior of macroscopic systems on rather large spatiotemporal scales is valid close to local equilibrium (Khantuleva, 2022, chap. 1). In continuum mechanics there is a concept of the medium model, for example, the models of an ideal gas, Newtonian fluid, or an elastic solid. When the initial and final properties of the system are so different that their descriptions can relate to different disciplines, a linear combination of such models is usually used. Such combined models include, for example, the Voicht model of a viscoelastic medium, Maxwell’s model, which takes into account the relaxation properties of the medium, semi-empirical models of non-Newtonian media, turbulence models of different types, etc.

All such models are required to complete the set of macroscopic equations of mass, momentum and energy transport in real media. However, it turned out that all of them have a very narrow range of applicability and are

completely unsuitable for predictions when changing external conditions. All attempts to generalize them to wider classes of processes, as a rule, lead to very cumbersome constructions that lose the physical visibility inherent in basic models. Latest advances in computer technology have allowed the creation of universal software packages to solve a wide range of practical problems. However, the problem of the choice of the closing relations built into the computer complex package is still remained.

Experimental results, obtained from the study of nonequilibrium processes in various branches of mechanics (hydrodynamics of turbulent flows, multi-phase flows, shock-induced processes in solids, biomechanical processes), show many similar features of the non-classical response of the system to external influences (Khantuleva, 2022, chap. 2). The experiment shows that both liquids and solids in response to short-duration loading behave elastically, while even solids can flow under long-duration loading. In the transition zone, high-rate processes are often accompanied by the self-organization of new elements of the internal structure (Mescheryakov, 2003, 2021) on an intermediate between macro and microscales, such as boundary layers, mass velocity pulsations, vortex structures, various localized inhomogeneities, etc. The observable effects of self-organization are characterized not only by the medium properties (composition, phase state), but also by loading and boundary conditions and depend on the geometry and sizes of the system. The special features of the processes far from local equilibrium are considered in section 2.

Despite completely different initial states, any medium under load tends to approach a more stable state, as far as the imposed constraints allow (Jaynes, 1979; Khantuleva, 2022, chap. 4). It means that there are patterns common to all media, inherent in transition processes not only between qualitatively different states of the system, but also in phase transitions, changes in modes and mechanisms of transfer of mass, momentum and energy. In order to predict when and under what conditions such a transition will occur, it is necessary to develop unified mathematical description that is valid for various media in a wide range of loading conditions, taking into account the effects of self-organization.

New interdisciplinary approach to modeling nonequilibrium processes, developed by the author of the paper (Khantuleva, 2000,2003, 2005, 2022(chap.5)) on the basis of the results obtained in nonequilibrium statistical mechanics (Zubarev, 1972, 1974) and cybernetic physics (Fradkov, 2007, 2008, 2017), contains a physically significant way of structuring the uncertainty that arises when describing nonequilibrium processes, and is

adequately integrated with the modern trend in mathematics towards discretization. Based on rigorous results of nonequilibrium statistical mechanics, it is a fundamentally new, universal and economical way to describe a complex of nonequilibrium transport processes in open systems. The main advantages of the approach are listed in section 3.

Within the framework of the developed approach, the evolution of the system far from local equilibrium proceeds in parallel with the evolution of the turbulent structure of the medium at the mesoscopic scale, between which a feedback is established. In section 4, based on the Speed Gradient (SG) principle (Fradkov, 2008), which is one of the methods of the theory of adaptive control, internal control of a highly nonequilibrium process through feedback is introduced, which will complete the description beyond the applicability of continuum mechanics models.

In section 5, within the framework of Maximum Entropy principle (Jaynes, 1979) the problem of choosing an appropriate goal function is considered in accordance with the results of nonequilibrium thermodynamics (Zubarev, 1974). The algorithm for the fastest path to achieving a goal that controls the evolution of the system is presented in section 6. Section 7 shows that the stationary state of the system cannot exist for a long time away from local equilibrium due to new information emerging as a result of the self-organization of a new dynamic structure of the medium (Klimontovich, 1987).

To demonstrate how internal control works in high-rate processes, two examples are considered in the paper. In section 8, using the example of a test problem in the Rayleigh formulation (Rayleigh, 1911), a high-speed shear fluid flow near a solid boundary is considered (Khantuleva, Shalymov, 2017). In accordance with the results (Klimontovich, 1987), it is shown that the self-organization of turbulent structures leads to a decrease in entropy production in the system, that is, it reduces irreversible energy losses compared to laminar flow at the same speed.

The second example, presented in section 9, based on the developed approach, describes the problem of propagation of a waveform induced by a high-rate impact on a metal target (Mescheryakov, Khantuleva, 2015; Khantuleva, 2022, chap. 7-8). It is shown that, according to the rigorous results of nonequilibrium thermodynamics (Zubarev, 1974), the entropy production far from local equilibrium can become negative due to self-organization and inertial aftereffects accompanying short-duration processes in solids.

2. High-Rate and Short-Duration Transfer Processes

The development of modern science and technology brings to the fore the study of high-rate and short-duration processes that are accompanied by a number of features that fundamentally distinguish them from slow quasi-stationary processes. From the standpoint of traditional continuum mechanics, these features make the behavior of the medium at high strain rates anomalous.

Experimental studies in hydrodynamics of turbulent flows, multi-phase flows, shock-induced wave processes in solids revealed many similar features in response of various media to impulse external influence. Attempts to apply conventional mathematical models of continuum mechanics far from thermodynamic equilibrium led to serious errors. The main problem is that all physical concepts are related to the system states near local equilibrium and a generalization of one concept implies the revision of all fundamentals of thermodynamics. In order to avoid contradictions in mathematical modeling, it is necessary to understand the features (Khantuleva, 2022, chap. 2) that characterize the system's response to an external disturbance that throws the system out of equilibrium.

In order to understand physical nature of the processes far from local equilibrium it is necessary to link the state of the system with the scale on which it is considered. High-rate and large gradient processes are characterized by very small typical spatiotemporal scales. On such a scale, the influence of the medium internal structure cannot be neglected. Just the same situation takes place inside thin layers near inter-phase boundaries and for the processes in media with complicated internal structure (multi-component, multi-phase). Such nonequilibrium processes cannot be described by the equations of continuum mechanics (Khantuleva, 2022, chap. 1).

In contrast to the linear deterministic approach, when the system response is proportional to the external influence, the system response to a high-rate impact must lag behind the impact itself due to the finite speed of propagation of disturbances. The delay is closely related to inertia of the medium and memory of its previous state, which determine the system's response to a short-duration impact. Delayed response to multiple influences can lead to fluctuations, system instability, transients and structural changes. The influence of a single factor among all other effects becomes indistinguishable due to the closed loops formed in the system. The behavior of the system becomes ambiguous, little predictable and poorly reproducible in experiments.

With high-rate deformation of a real medium, as experiments show, the parameters characterizing the properties of a specific medium in generally

accepted models of continuous media cease to be constant and begin to depend on the deformation rate, integral properties of the system, its sizes and geometry (Zubarev, 1974).

The appearance of size effects in the process under study is a sign that these conditions go beyond the scope of continuum mechanics. The dependence of the properties of a system on its size means that traditional similarity criteria used in continuum mechanics become insufficient for predicting the behavior of systems of different sizes.

Turbulent effects are an inherent property of transport processes that go far from equilibrium. Unlike laminar flows of the medium, in which random fluctuations are insignificant and small disturbances that arise quickly decay, maintaining flow stability, in a turbulent flow, small disturbances will grow over time due to the huge number of degrees of freedom. Due to the large gradients of processes occurring far from local equilibrium, their typical scales are small. Over a short time interval, slow diffusion-transport mechanisms of dissipative processes cannot ensure the complete conversion of kinetic energy into heat on a microscopic scale (Ravichandran et al., 2002, Lee, 2003). As a result, part of the energy that tends to dissipate reaches only an intermediate level and remains there in the form of movement of new mesoscopic degrees of freedom.

There is still no theory that satisfactorily predicts the behavior of turbulent processes. The inability to make reliable predictions about the possible development of a turbulent process is a significant obstacle to technical progress. Previous made attempts to create a universal model of turbulence gradually gave way to the understanding that turbulence phenomena should be studied from a more general point of view (Lu, 2014).

In addition to the occurrence of turbulence, high-rate and short-duration processes are accompanied by various inertial and relaxation effects, the spatiotemporal scales of which occupy an intermediate position between macro- and microscale levels. Inertial effects are especially important when moving condensed matter, which has a high density and, accordingly, inertia. Inertia is usually not taken into account in continuum mechanics equations. This is one of the reasons why the equations of continuum mechanics are unsuitable for describing processes that are far from equilibrium.

In contrast to the self-organization of dissipative structures formed due to mechanisms of slow diffusion transport (Nicolis, Prigogine, 1977), the self-organization of turbulent structures is a dynamic process that can develop by changing the degree of its order. The observed effects of self-organization are characterized not only by the properties of the medium (composition, phase

state), but also by the loading mode, boundary conditions, size and shape of the system. Collective effects, turbulent structures and other mesoscale processes accompanying nonequilibrium transport spread the system's response throughout its volume. Collective effects lead to the inadequacy of localized differential mathematical models and require integral approaches to the description of nonequilibrium processes.

The interaction between the forming elements of the mesoscopic structure leads to the evolution of the system. Consequently, the steady state of a system under constraints imposed far from equilibrium cannot be stable. The problem of stability of a nonequilibrium state of a system should be closely related to the evolution of the system over time, taking into account its history.

The problem of a uniform description of the motions of the medium in a wide range of conditions has not been solved. In conditions that go beyond the applicability of commonly used models, the choice of one or another closing equation is a very non-trivial task. The active development of numerical methods and the creation on their basis of universal software systems that use the latest achievements in the field of computer technology is undoubtedly a significant step forward in the development of instrumentation for mechanical researchers to solve practical problems. However, the problem of closing the transport equations in such software packages essentially comes down to the voluntary choice of one or another model built into a given computer complex, without indicating under what conditions one or another model should be used. Therefore, the task of determining the limits of applicability of certain approaches and developing a more general and universal apparatus seems very relevant at present.

The experimental study of the processes far from equilibrium is an extremely complex and time-consuming task, since the nature of nonequilibrium processes in real media and their characteristics are infinitely diverse. Their experimental study requires high-precision measuring instruments that will allow monitoring very rapid changes in process parameters both in time and space. In addition to technical problems, in the experimental study of nonequilibrium processes there are also fundamental difficulties in processing and interpreting the results obtained.

The effects observed under highly nonequilibrium conditions convincingly indicate that continuum mechanics models are completely unsuitable for describing high-rate transport processes. During the processes accompanied by such effects, a radical change in the physical transport mechanisms occurs that require corresponding changes in the system model. To meet these requirements, internal control through feedback must be

included in the system model. Thus, the description of highly nonequilibrium processes in real media represents a new class of problems of mechanics of inhomogeneous media, for which a necessary element of closing mathematical models is the introduction of internal feedback. Mathematical modeling with the closed loops of internal control between changes in the internal structure of the medium and its macroscopic behavior should be based on the principles of control theory.

The next section presents a fundamentally new integral approach to the problem of describing processes occurring far from local thermodynamic equilibrium, based on the results of nonequilibrium statistical mechanics using control theory methods.

3. New Interdisciplinary Approach to Describe Highly Non-Equilibrium Transport Processes

Attempts to include integral effects in the macroscopic description of the behavior of a system outside of equilibrium have been made for a long time. A critical analysis of the current situation with the description of nonequilibrium transfer processes allows us to conclude that in order to describe processes far from local thermodynamic equilibrium, it is necessary to move to a deeper level of description compared to the average, macroscopic level. Such a description based on first principles is given by nonequilibrium statistical mechanics.

Back in the second half of the last century, within the framework of nonequilibrium statistical mechanics, D.N. Zubarev (Zubarev, 1972, 1974) proved from first principles that far from equilibrium, macroscopic transport equations cannot be localized either in space or in time. Using the nonequilibrium statistical operator method, he derived generalized integral-differential macroscopic transport equations, nonlocal in space and time and applicable far from equilibrium, without restrictions on the averaging scale.

From the point of view of nonequilibrium statistical mechanics, in the case of an arbitrary deviation from the equilibrium state of the system, virtually any level of averaged description will be obviously incomplete. The effects of nonlocality and memory are the price to pay for the inevitable incompleteness of the description of the process in an open nonequilibrium system. A characteristic feature of the generalized description is the preservation of integral information about the system in the generalized macroscopic transfer

equations when describing its local properties. According to his results, the response of the medium to high-rate deformation should be nonlinear, nonlocal, and dependent on the prehistory.

However, the generalized description of nonequilibrium processes developed by Zubarev remained incomplete, since the relaxation transport kernels in the nonlocal transport equations with memory were unknown nonlinear functionals of macroscopic gradients. This circumstance became an obstacle to the use of nonlocal models in practical problems for several decades. Attempts to build empirical models of integral kernels led to very crude models and did not allow satisfying the natural boundary conditions imposed on the system. Although the nonlocal transport equations obtained by Zubarev are the only fundamentally new universal mathematical models obtained in science over the past two hundred years, they have not yet received further development.

Therefore, it was necessary, based on generalized nonlocal Zubarev equations, to develop a new approach to the description of nonequilibrium processes beyond the concept of continuum mechanics, which would organically include all the effects accompanying nonequilibrium transport.

Based on the nonlocal thermodynamic relationships with memory obtained in the first principle nonequilibrium statistical theory (Zubarev, 1972, 1974) a principally new interdisciplinary approach is proposed to describe temporal evolution far from local equilibrium (Khantuleva, 2022, chap. 5). Within the framework of the developed approach, the evolution of a system far from local equilibrium is determined by the dynamics of spatiotemporal correlations (DSTC) at the mesolevel, which controls the macroscopic behavior of the system through feedbacks. The unknown integral transport kernels in the nonlocal transport equations derived by Zubarev are replaced at the mesolevel by nonequilibrium correlation functions connecting thermodynamic fluxes $\mathbf{P}(\mathbf{r}, t)$ and gradients of macroscopic fields $\mathbf{X}(\mathbf{r}, t)$. Nonequilibrium space-time correlation functions $\mathbf{R}(\mathbf{r}, \mathbf{r}', t, t')$ contain all the information about the nonequilibrium state of the system. The most complete macroscopic information about the system is the history of macroscopic fields throughout the entire volume of the system. Although in the general case the complete information is not available, the main stages in the temporal evolution of correlation functions can be traced.

Back in the 1940s, N.N. Bogolyubov (Bogolyubov, 1960) laid the foundations of the dynamic theory of kinetic phenomena that allows one to sequentially obtain kinetic equations or directly hydrodynamic equations from the so-called “first-principles”. To do this, he mathematically formulated the

hypothesis of the attenuation of spatiotemporal correlations in the system that is associated with the concept of successive stages of the relaxation process each of which is characterized by its own time scales and types of the reduced description of nonequilibrium systems. According to the hypothesis of Bogolyubov, the spatiotemporal correlations attenuate over time during the system relaxation towards thermodynamic equilibrium.

It means that the correlations fade as the macroscopic gradients smooth out approaching the final stage of relaxation when a state close to local equilibrium is established. To model this process, it is necessary to introduce into nonlocal and retarded dependencies a set of parameters **s** of correlation functions that characterize typical scales of spatiotemporal correlations.

$$\mathbf{P}(\mathbf{r},t) = \int_{\mathbf{0}}^{\mathbf{t}} dt' \int d\mathbf{r}' K(\mathbf{r},\mathbf{r}',t,t',\mathbf{s})\mathbf{X}(\mathbf{r},t) \underset{\mathbf{s}\to\mathbf{0}}{\longrightarrow} k\,\mathbf{X}(\mathbf{r},t). \quad (1)$$

In contrast to the statistical-mechanical description, which includes only two scale levels, micro- and macroscopic, the new approach introduces a mesoscopic scale through correlation function, on which the evolution of the system occurs far from thermodynamic equilibrium. In the limiting case at $\mathbf{s} \underset{t\to\infty}{\longrightarrow} 0$, when spatiotemporal correlations decay, the nonlocal thermodynamic relations are transformed into local relations of linear thermodynamics with transport coefficients k (1). In the framework of the proposed approach, to simplify the description, the correlation function K is a scalar, $K(\mathbf{r},\mathbf{r}',t,t') = Sp\mathbf{R}(\mathbf{r},\mathbf{r}',t,t')$**,** which is a spherical part of the unknown tensor correlation function.

Works (Zubarev, 1974; Khantuleva, 2022, chap. 5) show that generalized relationships (1) for momentum transport in the limiting cases of undamped and completely damped correlations characterize the elastic and hydrodynamic responses of the medium, respectively. Both cases are described by the differential transport equations of continuum mechanics, while in transient modes of finite-size correlations the transport equations remain integral-differential.

Although the type of the nonequilibrium correlation function is unknown, the fact that the dynamics of space-time correlations in generalized equations determines the macroscopic behavior of the system far from equilibrium indicates the possibility of their use for mathematical modeling of the self-organization of dynamic structures at an intermediate, mesoscopic scale.

Within the framework of the proposed approach (Khantuleva, 2022, chap. 5; Khantuleva, Mescheryakov, 2022), it was shown that even without

knowledge of the explicit form of nonequilibrium correlation functions in nonlocal transport equations, it is possible to construct effective models of thermodynamic relationships between forces and fluxes and to complete the description of nonequilibrium processes. The model correlation function constructed within the framework of this approach describes the dynamics of the distribution of spatiotemporal correlations during nonequilibrium transport process. Parameters of the distribution are the moments of nonequilibrium correlation functions, which have a physical meaning.

In particular, during high-rate momentum transport in a real medium, the spatial correlation function $B(\mathbf{r},\mathbf{r}')$ generates, in addition to the generalized transport coefficient, higher-order moments that characterize the properties of momentum carriers on the mesoscale, and form the dynamic structure of the medium.

The moment the 0th order $k_0(\mathbf{r}) = \int d\mathbf{r}' B(\mathbf{r},\mathbf{r}') = \mu(\mathbf{r})$ of the spatial correlation function $B(\mathbf{r},\mathbf{r}')$ generalizes the effective viscosity to nonequilibrium conditions, the 1st order moment $\mathbf{k}_1(\mathbf{r}) = \int d\mathbf{r}' B(\mathbf{r},\mathbf{r}')(\mathbf{r}-\mathbf{r}') = \boldsymbol{\beta}$ determines the shift vector of the center of the spatial distribution of correlations relative to the point $\mathbf{r}$ under nonequilibrium conditions. The 2d moment $k_2(\mathbf{r}) = \int d\mathbf{r}' B(\mathbf{r},\mathbf{r}')(\mathbf{r}-\mathbf{r}')^2 = \varepsilon^2 - 2\,\mathbf{r}\cdot\boldsymbol{\beta}(\mathbf{r})$ determines the dispersion of the distribution of spatial correlations ε^2.

According to the physical meaning of the first moments of the spatial distribution of correlations, in the process of smoothing the gradients of macroscopic fields in the system, dynamic structures in the form of clusters with almost identical values of macroscopic densities will be formed. Finite-size clusters move as almost solid particles at different velocities and interact with other clusters. A particle of a medium with a characteristic radius ε moves almost like a solid body, the center of inertia of which is shifted by the vector $\boldsymbol{\beta}(\mathbf{r})$. In a nonuniform velocity field, a force $\mathbf{F}$ acts on it from other such particles, causing it to rotate $\mathbf{S} = \boldsymbol{\varepsilon} \times \mathbf{F}$. Due to the shear $\boldsymbol{\beta}$, an orbital torque, $\mathbf{M} = (\boldsymbol{\varepsilon} + \boldsymbol{\beta}) \times \mathbf{F}$, arises, which bends the trajectory of such a mesoparticle.

The asymmetric distribution of finite-size spatial correlations at finite time intervals can be interpreted as turbulent structures generated by the interaction of mesoparticles with each other and with inter-phase boundaries near which the gradients are large. The turbulent momentum transport is accompanied by a nonequilibrium exchange of momentum, angular momentum and energy between mesoparticles themselves and mesoparticles with boundaries.

The identification of relationships between spatiotemporal correlations on the mesoscale and the dynamic structure of the system was a big step into the field of highly nonequilibrium processes.

The constructed mathematical model of spatial correlations for high-speed transport processes contains a dependence on parameters that represent the first three statistical moments of the nonequilibrium correlation function, providing a transition to continuum mechanics with a decrease in macroscopic gradients,

$$B(\mathbf{r},\mathbf{r}';\mu,\boldsymbol{\beta},\varepsilon) = \frac{\mu}{\varepsilon}\exp\left\{-\frac{\pi(\mathbf{r}-\mathbf{r}'-\boldsymbol{\beta})^2}{\varepsilon^2}\right\} \underset{\varepsilon\to 0}{\longrightarrow} \mu\delta(\mathbf{r}-\mathbf{r}'). \quad (2)$$

The model function of spatial correlations (2) describes quasi-stationary transport at high speeds and small characteristic spatial scales. The same function can be constructed for temporal correlations. However, memory effects are negligibly small for quasi-stationary processes when approaching the final stage, while at the initial wave stage of relaxation they play a significant role. Modeling short-duration wave processes will be considered in section 8.

The model parameters $\mu, \boldsymbol{\beta}, \varepsilon$, or in general, the set $\mathbf{s}$, being the first moments of the correlation function, are also unknown functionals of the history of macroscopic fields in the system, but in a rougher averaged form. If we conditionally consider them constant for a certain area of the medium, these parameters must be determined by additional information in the constraints imposed on the system from the outside that support a given state of the system.

If this information is sufficient to determine them, then these constraints can be written in the form of some nonlinear functional relationships with respect to these parameters. In particular, such information may be contained in boundary conditions

$$\Phi_i[\mathbf{P}(\mathbf{r}),\mathbf{X}(\mathbf{r}),\mu,\boldsymbol{\beta},\varepsilon,](\mathbf{r}=\boldsymbol{\Gamma}_\mathbf{i}), i = 1,2,3,\dots m. \quad (3)$$

Here Φ_i are nonlinear functionals with respect to the model parameters, obtained from boundary conditions for nonlocal transport equations, m is the number of these conditions. The joint solution of nonlocal transport equations and functional relationships for parameters completely solves the problem of self-organization in the system and determines the spectrum of sizes of turbulent structures for a given external influence on the system.

As when solving inverse problems in quantum mechanics, for a bounded spatial region the size spectrum of the medium structure should be discrete, and far from the boundaries, where continuum mechanics is valid, it should become continuous.

However, the information in the constraints imposed on the system is always insufficient to maintain the stationary state of the system far from local equilibrium. According to the results of Zubarev (Zubarev, 1974), the most complete macroscopic description of a system includes all information about the history of the system. Since, according to Bogolyubov's hypothesis (Bogolyubov, 1960), over time the system forgets this information, then in the general case the description of a nonequilibrium state is always incomplete. Experiments also show that highly nonequilibrium states last only a finite time, after which they lose stability and begin to evolve.

The temporal evolution of the system, which results from the interaction of structural elements of the medium on the mesoscale, is described further by cybernetic methods developed within the framework of the control theory of adaptive systems with feedback (Fradkov, 2007, 2008, 2017).

4. The Methods of the Theory of Adaptive Control to Complete Mathematical Model of the System

Unlike engineering applications of control theory, cybernetic physics (Fradkov, 2007, 2008, 2017) is aimed at obtaining information about the state of the system and its use for control the behavior of the system. The system under study must be open to exchange energy and information with its surroundings. The information (and, therefore, the structure that is the carrier of information) plays a critical role in control processes but it is always incomplete because the information carrier is the evolving internal structure of the system.

The use of partial information about the state of the system in the control algorithm makes it possible to complete mathematical model of the system. Internal feedbacks play an essential role in constructing a model of the system. The most important problem of cybernetic physics is the study of the laws of system closure using control algorithms (feedbacks).

The formal statement of the problem in control theory begins with the choice of the model of the controlled system and the model of the control goal.

In the case of internal control when the loading mode is fixed, the parameters of the system structure play the role of control parameters.

The achievement of the goal depends on the initial conditions for the system. Non-traditional classes of goals do not completely determine the behavior of the system but only partially, setting a wide class of acceptable trajectories of motion. Such problems belong to the field of partial control the study of which has begun only recently. For nonequilibrium transport processes, only a part of the control parameters of the medium internal structure can be determined by the methods of cybernetic physics while the other part of them is directly determined by the mode of external loading of the system. Thus, nonequilibrium transport processes can also be attributed to the area of partial control or even more complex type of control.

According to the terminology of control theory, this means that the synthesis of control should be carried out under conditions of significant uncertainty. Therefore, a special role belongs to the methods of adaptive control. One of such methods is the Speed Gradient (SG) principle (Fradkov, 2007, 2008, 2017).

SG principle claims: of all possible motions, the system implements the ones for which control parameters vary in the direction of speed-gradient of some goal functional. If the constraints are imposed on a movement of the system, then the direction changes to satisfy the constraints imposed.

The method is intended for solving control problems for time-continuous systems in which the control goal is specified using a goal function. For a continuous non-stationary and nonlinear system (Fradkov, 2007, 2008, 2017),

$$\frac{dx}{dt} = F(x, u, t), \tag{4}$$

where x is the system state vector and u is a controlling vector, the control goal is specified by the relation

$$Q(x(t), t) \longrightarrow 0, t \to \infty, \tag{5}$$

where $Q(x, t) \geq 0$ is a smooth goal function. The goal function can have an integral form. In this case it is called the goal functional.

Since the goal function $Q(x(t), t)$, clearly does not depend on the control parameters u, within the framework of the SG algorithm it is necessary to find the rate of change of a quantity $Q(x(t), t)$, which is a scalar function $dQ/dt = w(x, u, t)$ depending on u:

$$w(x,u,t) = \frac{\partial Q(x,t)}{\partial t} + |\nabla_x Q(x,t)|^T F(x,u,t).$$

The gradient of the function $w(x,u,t)$ by the control parameters is:

$$\nabla_u w(x,u,t) = \left[\frac{\partial w}{\partial u}\right]^T = \left[\frac{\partial F}{\partial u}\right]^T \nabla_x Q(x,t).$$

The Speed Gradient (SG) algorithm for the control parameters $u(t)$ is written as the feedback law in two forms:

- in the finite form $u(t) = u(0) - g\nabla_u w(x,u,t)$, (6)

- in the differential form $\frac{du}{dt} = -g\nabla_u w(x,u,t)$, (7)

where $g > 0$ is a symmetric positive definite gain matrix. The resulting algorithm can naturally be called the speed gradient algorithm since the change in $u(t)$ occurs in proportion to the gradient of the rate of change $Q(x,t)$.

For the goal functional in the form

$$Q = \int_0^t R(x(t'),u(t'),t')dt', \quad (8)$$

the SG algorithm is identical in form to the top-down descent algorithm for the function $R(x,u,t)$. The algorithm makes sense if the function $R(x,u,t)$ is explicitly control-dependent.

For the correct and reasonable choice of the control parameters of the SG algorithm, it is necessary to check the conditions for their applicability. Main conditions are the convexity of the function $dQ/dt = w(x,u,t)$ on $u(t)$ and the existence of such a vector $u(t)$ that $w(x,u,t) \leq 0, \forall x$ (attainability condition).

The methods of the theory of adaptive control can serve as a basis for constructing mathematical models of dynamic systems of any physical nature. At the same time, the SG principle allows us to look at such problems from a new, non-traditional point of view. The task of constructing a model of the system can be posed as a search for a law of evolution of the control parameters that provide the required properties of the system.

5. Selecting the Goal Function for System Evolution Based on Nonequilibrium Thermodynamics

The evolution of a physical system must have its own direction determined by thermodynamic principles associated with the relaxation of the system to more equilibrium states with the maximum possible value of entropy. According to Maximum entropy principle (MEP) (Jaynes, 1979), the entropy in the system during the relaxation to thermodynamic equilibrium increases until it reaches its maximal value due to irreversible dissipation of mechanical energy into heat (kinetic energy of chaotic motion on the microscale).

The most general definition of the entropy, valid for nonequilibrium processes, was obtained using the nonequilibrium statistical operator method developed by Zubarev (Zubarev, 1974), which maximizes the entropy for a given history of the system. The method shows that the MEP principle, with adequate use of information about the system, can work far from equilibrium and give new results.

Interesting consequences follow from the Zubarev's results on the behavior of entropy far from local equilibrium. Using the nonequilibrium statistical operator method, Zubarev derived a generalized evolution criterion, which states that in a real nonequilibrium process there is a decrease in part of the entropy production compared to the entropy production in the linear thermodynamics of irreversible processes near local equilibrium.

Yu.L. Klimontovich (Klimontovich, 1987) believed that such a decrease in entropy corresponds to the preservation of some part of the information about the initial impact on the system, and the carrier of this information is the internal structure of the system. At the final stage of relaxation near local equilibrium, dissipative processes gradually compensate for this decrease until entropy finally reaches a maximum at the equilibrium state. Under these conditions, the generalized criterion for the evolution of macroscopic systems coincides with the criterion of Prigogine and Glansdorff (Glansdorff, Prigogin, 1972), and for a close-to-equilibrium stationary state, Prigogine's theorem on the minimum entropy production is obtained. In this case, the local entropy production $\sigma(\mathbf{r}, t) = \mathbf{P}(\mathbf{r}, t) \cdot \mathbf{X}(\mathbf{r}, t) \geq 0$ is always non-negative.

Far from local equilibrium, as shown in (Zubarev, 1974), it cannot be argued that the 2nd law of thermodynamics can be extended not only to the local production of entropy, but also to the integral production of entropy in the entire system until all processes in it are completed

$$S(+\infty) - S(-\infty) = \int_{-\infty}^{+\infty} dt \int d\mathbf{r}\, \sigma(\mathbf{r}, t) \geq 0.$$

This means that at different stages of a nonequilibrium process in some parts of the system, its entropy production can become negative. This does not contradict the 2nd law of thermodynamics, which refers to the system as a whole and not to each of its points separately. It means that in the general case, when the entropy production includes spatial nonlocality and memory effects, the entropy can fluctuate, increasing only on average. Far from thermodynamic equilibrium, the total entropy of the system, experiencing spatial and temporal fluctuations during the system evolution, increases only on average in accordance with the 2nd law of thermodynamics. It follows that the principle of maximum entropy production, which claims to be valid in the region of strong nonequilibrium, is correct only near local equilibrium where the entropy fluctuations can be neglected.

Note that taking into account nonlocality corresponds to taking into account all higher gradients of macroscopic fields. Under these conditions, regions of finite size may arise in the system in which the entropy production will be negative due to spatial correlations. Since entropy characterizes the degree of chaos of the system at the level of its internal structure, the loss of a part of the entropy should mean that the collective effects associated with spatial nonlocality lead to some degree of ordering of the internal structure of the system at a larger scale than microscopic structure. Such a situation, for example, takes place in turbulent fluid flows when at high flow speeds a certain ordered vortex structure of the flow arises. At the same time, it was proved that the entropy of the turbulent flow is less than that of the laminar one at the same speed (Klimontovich, 1987). If we use the concept of information entropy (Jaynes, 1957), then we can assume that new information has appeared in the system, the carrier of which is the new internal structure of the system.

When both spatial nonlocality and memory effects about previous states of the system take place, the local entropy production can become negative due to retardation of the medium response from the impact. Thermodynamic force and the conjugate flux can have opposite signs in a certain part of the system for a certain time interval. It is possible even in the entire system during a certain finite time interval. A high degree of ordering of the system structure can be achieved only far from local equilibrium when the processes are characterized by small space-time typical scales. It should be noted that memory carriers most often represent wave structures that can quickly

propagate without changing their characteristics over significant distances covering the entire system. For example, when a shock-induced wave passes through a solid body, a new mesoscopic structure may be formed in it. The irreversible part of this dynamic structure can remain frozen into the medium behind the traveling wave.

Thus, in contrast to the MEP principle, it is not the information entropy that should be maximized, but the generalized entropy according to Zubarev's results (Zubarev, 1974) under given constraints imposed on the system. It should be assumed that the achievement of its maximum determines the global goal of evolution, during which entropy increases only on average.

Therefore, in order to set the direction of evolution and its goal, it is necessary to introduce slow time Ψ, which makes the goal achievable, neglecting the fluctuation of entropy production away from equilibrium. In this case, it is reasonable to assume that the evolution of the dynamic structure $\mathbf{s}(\Psi)$ proceeds more slowly than the macroscopic gradients are smoothed out. In synergetics, a necessary condition for self-organization of a system is the separation of process variables by scale into fast and slow. If the characteristic times of change of macroscopic fields are of the same order as the time of change of the dynamic structure, then under given initial conditions and imposed constraints, the global goal may become unattainable and the evolution of the system may stop. The section 9 presents a real situation when, due to the negative entropy production in a wave propagating through the medium, the self-organization of a mesoscopic structure in a solid material becomes irreversible and the structure can no longer evolve further.

According to the basic law of thermodynamics (Glansdorff, Prigogin, 1972), the change in entropy dS as a result of the process of deformation of the medium is determined by irreversible losses during the mutual transformation of the work of deformation PdV performed by stress P and specific internal energy E

$$TdS = dE + PdV.$$

It is generally accepted that dE is due to reversible energy exchange whereas dS determines dissipative losses of mechanical energy. However, far from local equilibrium, we cannot separate the reversible and irreversible parts of thermodynamic fluxes and forces in advance because they change during the loading process. Then, the deformation work defines the joint result of all energy transformations. Since the reversible processes do not contribute into the entropy production, the deformation work can be considered as a

generalized entropy production valid far from equilibrium, $PdV = TdS - dE$, which is the product of thermodynamic force $dV = d(1/\rho)$ and flux P.

In the framework of the developed approach, the generalized total entropy production over the process history in the system is chosen as a goal function of free evolution

$$\Delta S(t, \mathbf{s}(\Psi)) = \int_0^t dt \int d\mathbf{r} \int_0^t dt' \int d\mathbf{r}' K(\mathbf{r}, \mathbf{r}', t, t', \mathbf{s}(\Psi)) \mathbf{X}(\mathbf{r}', t') \cdot \mathbf{X}(\mathbf{r}, t). \quad (9)$$

In the framework of the SG principle, the rates of the structure sizes $d\mathbf{s}(\Psi)/\mathrm{d}\Psi$ are chosen as the control parameters.

According to the SG algorithm, the goal function should be differentiated by time. When the total entropy production reaches its maximum, the integral entropy production turns into zero.

$$\mathrm{Q}(t, \mathbf{s}(\Psi)) = \frac{\mathrm{d}}{\mathrm{dt}} \Delta S(t, \mathbf{s}(\Psi)) = \int d\mathbf{r}\, \sigma(\mathbf{r}, t, \mathbf{s}(\Psi)) \to 0. \quad (10)$$

When constraints connected to loading conditions are imposed on the system, the goal functional for the system evolution under constraints imposed, in accordance with MEP [30], is written as follows

$$\mathrm{Q}(t, \mathbf{s}(\Psi)) = \int d\mathbf{r}\, \sigma\big(\mathbf{r}, t, \mathbf{s}(\Psi)\big) + \sum_{\mathbf{m}} \lambda_{\mathrm{m}} \Phi_{\mathrm{m}}[t, \mathbf{s}(\Psi)], \quad (11)$$

where λ_{m} are Lagrangian multipliers and m is a number of constraints imposed on the system in the form of functionals. The constraints do not allow the system to reach equilibrium. It is seen that when $\mathrm{Q}(t, \mathbf{s}(\Psi)) \to 0, \Psi \to \infty$ under the constraints imposed, the integral entropy production $\int d\mathbf{r}\, \sigma(\mathbf{r}, t, \mathbf{s}(\Psi))$ cannot reach 0 but tends to minimize its value. This indicates that Prigogine's theorem on the minimum entropy production in a stationary state, proven within the framework of linear thermodynamics of irreversible processes near local equilibrium, takes place far from local equilibrium.

6. Mathematical Model of System Evolution Far from Local Equilibrium

Since nonequilibrium effects characterizing high-rate and short-duration processes arise on an intermediate scale between macro and micro levels, the

temporal evolution of a system far from equilibrium should also be described on the mesoscale of the internal structure of the system. Modeling the evolution of a system far away from equilibrium using methods of control theory requires the formulation of the goal of the system evolution, the choice of control parameters and a suitable control algorithm. In the previous section the goal function of time evolution is determined in accordance with the MEP principle (Jaynes, 1979) and with the results of nonequilibrium statistical thermodynamics on the behavior of entropy far from equilibrium (Zubarev, 1974). The mesoscale structure parameters are chosen as control parameters.

In real problems, as a rule, the constraints imposed on the system are not sufficient to keep the system in one state for a long time far away from equilibrium. The evolutionary process in the system occurs to some extent spontaneously, obeying some internal laws. Depending on the initial state of the system, the loading mode, and the total transferred amount of energy, the system can either return to its original state if the process is reversible or go into another state with new internal structure that differs from the initial one. The laws governing the internal structure transformation are defined by thermodynamic principles and the energy exchange between different degrees of freedom on the mesoscale. The structure transformation can lead to different instabilities and change macroscopic properties of the system. The energy reaches the mesoscopic level in the form of wave-vortex pulsations or wave packets that compose dynamic structure resulted from the high-rate loading.

To complete the formulation of the problem in scope of the control theory, it is necessary to choose the path to achieve the goal. One of the simplest and most intuitive methods of cybernetic physics (Fradkov, 2007, 2008, 2017) is the SG principle that was developed in the theory of adaptive control and later applied to describe the dynamics of various physical systems. The structure evolution accompanied by self-organization on the mesoscale is more slow process compared to high-rate change of local gradients of macroscopic densities. Therefore, differential SG algorithm can be applied to describe the structure evolution on the mesoscale and the consistent macroscopic temporal evolution of the system far away from local equilibrium.

In accordance with MEP (Jaynes, 1979), the goal functional for the system evolution under constraints imposed is written as follows

$$\mathrm{Q}(t,\mathbf{s}(\Psi)) = \int d\mathbf{r}\,\mathbf{P}\big(\mathbf{r},t,\mathbf{s}(\Psi)\big)\cdot\mathbf{X}(\mathbf{r},t) + \sum_{\mathbf{m}}\lambda_{\mathrm{m}}\Phi_{\mathrm{m}}[t,\mathbf{s}(\Psi)]\,0, \qquad \Psi\to\infty. \tag{12}$$

For the slow mesostructure evolution the SG algorithm is identical in form to the top-down descent algorithm for the function $Q(t, \mathbf{s}(\Psi))$ depending on $\mathbf{s}$ only as on parametrs (Khantuleva, Shalymov, 2017; Khantuleva, 2022, chap. 8)

$$\frac{d\mathbf{s}(\Psi)}{d\Psi} = -\boldsymbol{g}\nabla_{\mathbf{s}}Q(t, \mathbf{s}(\Psi)). \quad (13)$$

Multiplier $\boldsymbol{g} > 0$ is matrix of empiric gain coefficients characterizing inertial properties of the system internal structure. The temporal evolution described by the equations (13) corresponds to the criterion of the system evolution by Glansdorf and Prigogine (Glansdorf, Prigogine, 1972)

$$\frac{\partial}{\partial\Psi\partial t}\Delta S(t, \mathbf{s}(\Psi)) = -\nabla_{\mathbf{s}}Q \cdot \boldsymbol{g}\nabla_{\mathbf{s}}Q \leq 0.$$

The set of nonlinear differential equations (12) with respect to the parameters $\mathbf{s}(\Psi)$ describes the evolution of the structure on the mesoscale. To solve the problem, it is necessary to set the boundary and initial conditions for the macroscopic transport equations and the initial conditions for the evolution of the structure on the mesoscale. Since nonlocal macroscopic equations with memory are valid up to the boundaries of the system, it becomes possible to set real conditions that describe the processes of exchange with the environment across the boundaries of the system. As for the conditions at the mesolevel, for this you need to know the initial structure of the real system. Of course, this is not as simple as it might seem, since our knowledge about the state of a nonequilibrium system is always incomplete. To develop adequate mathematical methods for solving such problems, working under conditions of incomplete information about internal structural processes in real complex systems, comprehensive theoretical and experimental research is necessary.

Nonlocal macroscopic transport equations, including dependence on the correlation parameters, together with equations for the evolution of these parameters in accordance with the algorithm (12), determine the size and lifetime of mesoparticles transferring mass, momentum and energy in high-speed and short-term processes. In the general case, the nonlinear set of equations (12) can have many solutions. For a bounded system, the size spectrum of space-time correlations, as in quantum mechanics, must be discrete. Far from the boundaries of the system, the spectrum of sizes becomes continuous as in continuum mechanics. In accordance with the model of the

evolution of structure on the mesoscale (12), the size spectrum of spatiotemporal correlations evolves over time; some sizes can increase, others disappear and new ones appear.

The graphical interpretation of the SG method (Khantuleva, Shalymov, 2017; Khantuleva, 2022, chap. 8) represents the path of the system evolution as a gradient descent along the hypersurface of the integral entropy production of the system constructed over the phase space of the control parameters under imposed constraints. The model of the system, which includes a closed control loop with feedback between the evolution of the structure at the mesolevel and the macroscopic behavior of the system, makes it possible to predict the change in its dynamic properties by tracing the evolutionary paths of the system's structure.

These regularities (12)-(13) operate the thermodynamic evolution of the system. Far from equilibrium, the number of degrees of freedom involved in the mesoscopic evolution cannot be known in advance and, moreover, it can spontaneously change over time even under the fixed constraints imposed on the system. Therefore, the set of parameters describing nonequilibrium processes will always be incomplete. As discussed earlier, the price to pay for this incompleteness is the inclusion of spatial nonlocality and memory effects.

The set of equations based on SG principle (12) allows a closed formulation of problems on high-gradient and high-rate processes. The mesoscale structure evolution occurs in parallel with the temporal evolution of macroscopic fields of mass, momentum and energy densities in the system. The evolving parameters of the internal structure $\mathbf{s}(\Psi)$ influence the macroscopic fields and the entropy production in the system and, through feedback, even can change the type of macroscopic equations. In turn, the change of the integral entropy production leads to a transformation of the internal structure. Due to this self-consistency, internal control is established in the system through feedback. In this way, within the framework of SG algorithm, closed internal control loops are formed between the evolution of the structure on the mesoscale and the time evolution of the macroscopic system. Such feedback between turbulent structures and macroscopic response of the system to an external influence is an inherent element of the internal control. The control close-loops are known to make systems more stable than "rigid" program control.

The structuring of the system generated by the nonequilibrium transport processes and the subsequent temporal evolution of the system structure are the basis that connects the description of nonequilibrium processes with the theory of adaptive control. It is the structure of the system that is the carrier of

information through which the internal feedback control is established in the system.

So, the inclusion of the self-organization and internal control close-loops are prerequisites for an adequate modeling of the processes far from local equilibrium.

7. The Emergence of New Information during Self-Organization in Open System

In open thermodynamic system the entropy can change both due to the entropy production inside the system on account of dissipation of mechanical energy during transport processes $d_{in}S$ and due to the entropy fluxes across the system boundaries $dS=d_{in}S+d_{ex}S$. In order to maintain the steady state of the system out of equilibrium, the entropy produced in the system must be ejected out of the system into its environment across the boundary $d_{in}S+d_{ex}S=0$.

It is known that there is a relationship between entropy and information. From the law of conservation of information and entropy (Klimontovich, 1987), formulated by Klimontovich,

$$S+I=S_{max}, \tag{14}$$

it follows that $dS+dI=0$. According to Bogolyubov's hypothesis, the system forgets the information about its history when approaches equilibrium $I \underset{t\to\infty}{\longrightarrow} 0, S \underset{t\to\infty}{\longrightarrow} S_{max}, dS \underset{t\to\infty}{\longrightarrow} 0$. It is generally accepted that the stationary state out of equilibrium is maintained by the information in the constraints imposed on the system by its interaction with surroundings.

However, as the process rate increases, the entropy production grows and the information in the constraints can become insufficient to maintain the stationary state out of local equilibrium. The initial structure of the system begins to evolve towards a more stable state. In order to hold its balanced state the system must decrease the entropy production and increase the information. The new information can arise in the system far from local equilibrium only due to self-organization of dynamic structures. The formed structural elements become carriers of information on the mesoscale. The self-organization of new structure and its evolution is described by the set (13) where the information given in the constraints imposed on the system is divided into two parts: $I=I_{ex}+I_{in}(\boldsymbol{s})$:

$$Q = \frac{d}{dt}(S + I_{ex} + I_{in}(\boldsymbol{s}(t)), \quad \frac{d}{dt}(S + I_{in}(\boldsymbol{s}(t)) = 0. \tag{15}$$

Here, I_{ex} is the external information in the constraints and $I_{in}(\boldsymbol{s})$ is the new information due to self-organization. Then, even on stationary conditions $I_{ex}=const$ the internal balance in the system out of local equilibrium cannot be maintained for a long time because slow dissipative processes responsible for the entropy production gain cannot keep up with the self-organization. Therefore, it can be concluded that the farther from equilibrium the state of the system is, the more unstable it is.

For example, with increasing flow speed a laminar-turbulent transition occurs as a result of the self-organization of a turbulent structure. Far from local equilibrium the correlation function originates dynamic formations on the mesoscale capable to rotate and interact like some mesoparticles. Transporting mass, momentum and energy, the formed mesoparticles decrease the entropy production and dissipative effects are replaces by inertial ones. Due to new vectors generated by the system, the mesoparticle trajectories begin to twist and the system itself becomes anisotropic. The new information generated on the mesoscale induces the transition to turbulent motion in the system. As a result, the entropy production decreases making the system state more unstable. This is in accordance with the results obtained by Klimontovich (Klimontovich, 1987) who showed that at the same high speeds the entropy production in turbulent flow was less than in laminar flow.

8. Shear Fluid Flow Near a Solid Boundary in the Rayleigh Formulation

When modeling unsteady hydrodynamic processes, the test problem is considered to be the Rayleigh problem (Rayleigh, 1911). The solution of this problem for the Newtonian model of a liquid medium, which describes the process of relaxation of shear viscous stress and the establishment of a stationary equilibrium state, is obtained in explicit form.

Rayleigh's problem is formulated as follows. The infinite thin plane plate ($L \to \infty, l \to 0$) at the moment of time t=0 is instantly set in motion parallel to itself at a constant velocity U. The movement pattern is shown in Figure 1.

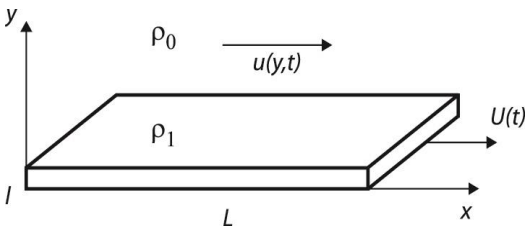

Figure 1. The shear flow scheme in the Rayleigh problem.

In this formulation, the movement of a viscous incompressible Newtonian fluid is described by the parabolic equation for the macroscopic shear velocity u ,

$$\frac{\partial u}{\partial t} = \nu \frac{\partial^2 u}{\partial y^2}, \tag{16}$$

where ν is the kinematic shear viscosity, and the y-axis is directed normal to the plate. For given initial and no-slip boundary conditions,

$$u(y, t = 0) = 0, u(y = 0, t) = U, u(y \to \infty, t) \to 0, \tag{17}$$

Eq. (16) has a solution,

$$u(y, t) = U\left(1 - \mathrm{erf}\frac{y}{2\sqrt{\nu t}}\right). \tag{18}$$

From solution (18), the normal velocity gradient takes the form,

$$\frac{\partial u}{\partial y} = -\frac{U}{\sqrt{\pi \nu t}} exp\left\{-\frac{y^2}{4\nu t}\right\}.$$

In terms of linear thermodynamics, shear stress is proportional to the velocity gradient (18),

$$P(y, t) = \nu \frac{\partial u}{\partial y} = -\frac{\nu U}{\sqrt{\pi \nu t}} exp\left\{-\frac{y^2}{4\nu t}\right\}. \tag{19}$$

The expression (19) has a δ-shaped singularity at $y = 0, t \to 0$ which is a consequence of the parabolicity of equation (16). If the acceleration value at the initial moment of time $\partial u/\partial t(y, t = 0)$ is finite, then there is an initial

flow regime, which equation (16) does not describe correctly, since it does not take into account the finiteness of the speed of propagation of disturbances in the medium.

Rayleigh's solution shows that over time a stationary state is established when all the fluid comes into uniform motion along with the plate. In the inertial coordinate system moving with the plate, the stationary fluid state is in complete thermodynamic equilibrium with the plate. In the process of the stress relaxation arising in the system, the total entropy production tends to its maximum. For the Rayleigh solution, one can easily obtain the time evolution of the system towards equilibrium.

Within the Newtonian model of a viscous fluid, the local entropy production for pure shear tends to zero over time,

$$\sigma(y,t) = \frac{\partial u}{\partial t} P(y,t) = \nu \left(\frac{\partial u}{\partial y}\right)^2 = \frac{\nu U^2}{\pi \nu t} exp\left\{-\frac{y^2}{2\nu t}\right\} \underset{t\to\infty}{\longrightarrow} 0\,. \qquad (20)$$

The total entropy production, entropy generation in the system from the beginning of the process, is

$$\Delta S(t) = \int_0^t dt \int_0^\infty dy\, \sigma(y,t) = \int_0^t dt \int_0^\infty dy \frac{\partial u}{\partial y} P(y,t) = \frac{U^2 2\sqrt{\nu t}}{\sqrt{\pi}}\,. \qquad (21)$$

According to Eq. (21), the generation of entropy due to the infinity of the plane grows infinitely with time, $\Delta S(t \to \infty) \to \infty$.

The rate of entropy generation or the integral entropy production has the form,

$$\frac{d}{dt}\Delta S(t) = \int_0^\infty dy\, \sigma(y,t) = \frac{\nu U^2}{\sqrt{2\pi\nu t}}\,. \qquad (22)$$

The rate of entropy generation during the establishment process decays to zero, $d/dt\ \Delta S(t \to \infty) \to 0$.

At the initial moment, with instantaneous acceleration (with infinite acceleration), the rate of entropy generation is infinite, $\frac{d}{dt}\Delta S(t \to 0) \to \infty$, $\Delta S(t \to 0) \to 0$.

In fact, the final acceleration can be considered instantaneous only on large time scales compared to the acceleration time of the plate. Therefore, the presence of a singularity at $t \to 0$ indicates the unsuitability of the parabolic equation (16) at small times.

It can be shown that equation (16), describing the system evolution to equilibrium at the hydrodynamic stage of relaxation, can be derived based on SG principle. According to MEP, the goal function of the temporal evolution is maximization of the total entropy production (21) corresponding to zero value of its rate (22). Indeed, with the acceleration of the medium, $\frac{\partial u}{\partial t}$, chosen as a control parameter and the goal function (21), SG algorithm in the finite form describes temporal evolution of the system. Since the function (21) does not depend on the control parameter $\partial u/\partial t$, we should take time derivative of the function (21) to construct the control algorithm

$$\frac{d}{dt}\Delta S = 2\nu \int_0^\infty dy \frac{\partial u}{\partial y}\frac{\partial^2 u}{\partial y \partial t}. \tag{23}$$

Taking the integral in (23) by parts gives a function that explicitly depends on the control parameter, $\partial u/\partial t$,

$$\frac{d}{dt}\Delta S = 2\nu \left[\frac{\partial u}{\partial y}\frac{\partial u}{\partial t}\right]_{y=0}^{y\to\infty} - 2\nu \int_0^\infty dy \frac{\partial u}{\partial y}\frac{\partial^2 u}{\partial y^2}. \tag{24}$$

Then, the finite form of the SG algorithm (6) can be written as follows

$$\frac{\partial u}{\partial t} = 2g\nu \frac{\partial^2 u}{\partial y^2}. \tag{25}$$

The resulting Eq. (25) coincides with Eq. (16) up to the constant factor $2g\nu$. With the parameter $g = \frac{1}{2}$ the match becomes complete.

So, the Eq. (16) describes the hydrodynamic relaxation stage of the temporal evolution of the shear flow of viscous fluid in accordance with SG principle. In the general 3D case, for the total entropy production based on the linear thermodynamics of irreversible processes it is possible to show that the Navier–Stokes equations describe the fastest path to equilibrium in accordance with SG principle on the hydrodynamic stage of evolution without any constraints imposed.

However, during a high-speed movement of the plate, energy from the macroscopic scale level does not have time to go down to the microscopic scale. Remaining on intermediate scales (Ravichandran et al., 2002) the energy form the dynamic structure of the system as new energy carriers in response to strong and short external impact. As a result, the energy dissipation

is replaced by inertial effects which decrease the entropy production in the system compared with the hydrodynamic stage of the system evolution.

The process of momentum transport from the plate to the medium occurs in stages. The initial acceleration stage of the process is accompanied by the generation of shear waves, which propagate from the surface of the plate and cannot be described by the parabolic equation (16). Between the initial wave and the final hydrodynamic (described by solution (18)) stages, there is a transition regime in which vortex-wave structures are formed, gradually attenuating due to viscous dissipation. At this stage, a turbulent boundary layer regime can be formed which slowly evolves over time in accordance with the SG principle.

Within the framework of the nonlocal modeling of nonequilibrium processes based on DSTC approach (Khantuleva, 2022, chap. 5) such a regime can be describe by quasi-stationary nonlocal model,

$$P(y,t) = \nu \int_0^\infty \frac{dy'}{\varepsilon} \exp\left\{-\frac{\pi(y'-y-\gamma)^2}{\varepsilon^2}\right\} \frac{\partial u}{\partial y'} \xrightarrow[\varepsilon,\gamma\to 0]{} \nu \frac{\partial u}{\partial y}. \qquad (26)$$

The integral expression for shear stress (26) contains an integral kernel, in which the smoothing scale is determined by the radius of spatial correlations ε, while the shift parameter γ is associated with the influence of the rigid boundary (plate). The nonlocal model describes the shear stress relaxation as the evolution of dynamic structure of the medium through the parameters, ε, γ, which slowly evolve over evolutionary time Ψ. The δ-type integral kernel in (26), thanks to the shift parameter γ>0, provides a uniform limit transition to the Rayleigh solution (18) throughout the entire half-space, including the boundary y =0. In this case, the velocity gradient and viscous stress are no longer proportional to each other.

An approximate solution to the Rayleigh's problem can be obtained by substituting solution (18) under the integral (26),

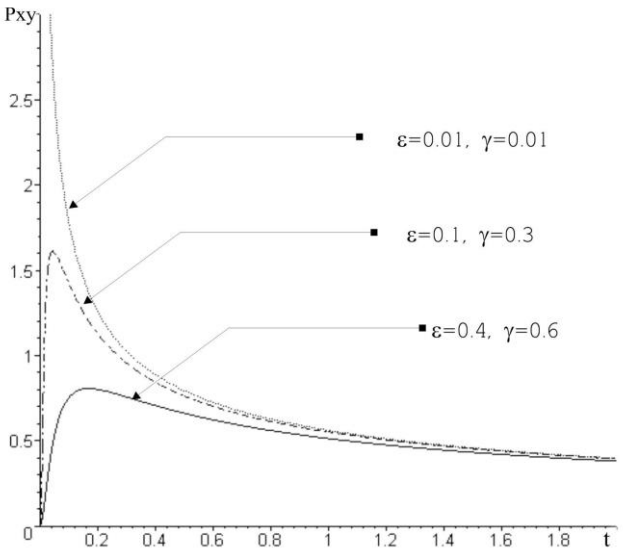

Figure 2. The behavior of the friction on the plate $P(y=0,t)$ for certain values of the model parameters, ε, γ.

$$P(y,t) = -\nu \frac{U}{\sqrt{\pi \nu t}} \int_0^\infty \frac{dy'}{\varepsilon} \exp\left\{-\frac{\pi(y'-y-\gamma)^2}{\varepsilon^2}\right\} \exp\left\{-\frac{y'^2}{4\nu t}\right\}. \quad (27)$$

Figure 2 shows how friction on the surface of the plate $P(y=0,t)$ changes with time for different values of the parameters of the nonlocal model

The parameters of the nonlocal model ε, γ in the expression for the shear stress (26) have a physical meaning associated with the spatial dimensions of the structural vortex-wave elements of the medium formed in the transition regime. Their evolution in accordance with the SG principle determines the evolution of the turbulent flow towards minimizing the function of the integral entropy production,

$$\mathrm{Q}(t) = \frac{d}{dt}\Delta S(t) = \int_0^\infty dy\, \sigma(y,t) = \nu \left(\frac{U}{\sqrt{\pi \nu t}}\right)^2 \int_0^\infty dy\, exp\left\{-\frac{y^2}{4\nu t}\right\} P(y,t), \quad (28)$$

with the approximate expression for the shear stress (27).

The SG algorithm defines the top-down descent along the surface $\mathrm{Q}(t, \varepsilon, \gamma)$ constructed above the plane of the control parameters ε, γ.

$$\frac{d\varepsilon}{dt} = -g\frac{\partial Q}{\partial \epsilon}, \quad \frac{d\gamma}{dt} = -g\frac{\partial Q}{\partial \gamma}. \tag{29}$$

The evolution path begins at a point on the entropy production surface with coordinates that specify the sizes of the surface roughness of the plate ε_0, γ_0. During the flow evolution, when the path goes down, the sizes of the dynamic structure increase, while the surface $Q(t, \varepsilon, \gamma)$ itself descends and flattens, reducing the rate of evolution. The evolution stops when the surface becomes a plane at zero level of the entropy production. The final point of the flow evolution depends on the inertial properties of the fluid and on the initial conditions associated with properties of the plate surface. In the general case, even at long times, equilibrium may not be achieved.

A completely different situation arises if the structure parameters evolve not only over time but also with distance from the plate. To describe it, additional information is required, which can only be provided by special experimental studies.

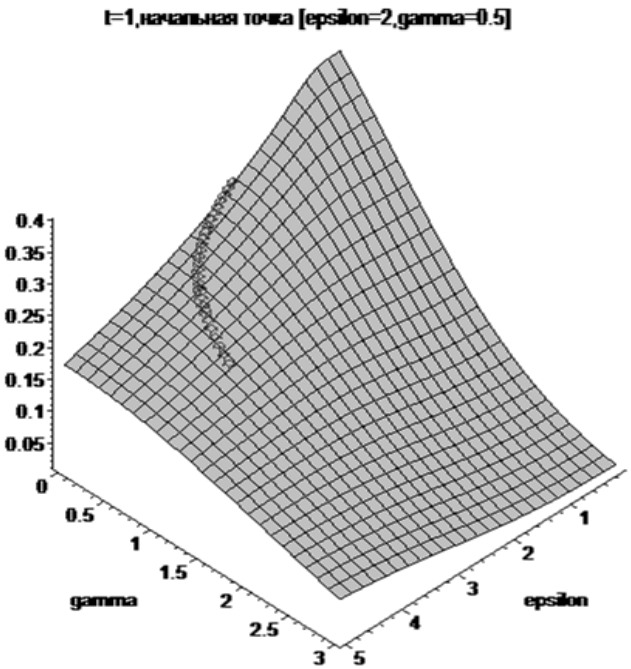

Figure 3. The top-down descent of the evolutionary path along the surface $Q(t, \varepsilon, \gamma)$ with feedback from the surface evolution.

9. Shock-Induced Self-Organization of Mesostructure in Solid Materials

Compared to liquid media, the states of solids induced by a high-speed impact are characterized by the greatest degree of deviation from equilibrium. From the point of view of thermodynamics, these processes proceed far from local equilibrium, which makes inapplicable all generally accepted ideas of thermodynamics, historically tied to thermodynamic equilibrium. Experiments on high-rate deformation of solid materials (Ravichandran et al., 2002; Meshcheryakov, 2021) have confirmed that during short-duration processes, slow diffusion transport mechanism of dissipation of the kinetic energy into heat is replaced by inertial effects, which lead to a delay in the response of the medium to external influences. Long-term aftereffects do not allow localizing the relationship between the force and the reaction it causes and fundamentally distinguish high-rate deformation from slow quasi-stationary processes described by differential equations.

Structural studies of high-rate deformation of solid materials have discovered completely new types of defective structures – rotations that belong to an intermediate, mesoscopic level. These facts indicate that turbulence occurs not only in liquid and gaseous media, but also in solids during high-rate deformation. In order to explain the observed experimental results and to describe the structure formation on the mesoscale, the DSTC approach based on the correlation dynamics was used.

During the shock loading, the correlated initial state of the solid material breaks; the shock-induced wave propagates in dispersive medium as a set of wave packets preserving only a small part of the initial correlation on the mesoscale-1. The wave packets become carriers of mass, momentum and energy during high-rate deformation of condensed matter. After the force of the impact ceases to act, they interact and spread out forming a larger wave packet on the mesoscale-2, in which the initial material state can partially recover. When, during high-rate deformation, the motion on the mesoscale-1 becomes turbulent and the mass velocity dispersion increases, the initial material state does not have time to be restored during the short wave period and the turbulent structures remain frozen into material after the wave leaves.

Within the framework of the developed DSTC approach in order to describe the shock-induced waveform propagation in condensed matter, an integral relationship between the stress and strain-rate with model correlation function is constructed (Khantuleva, 2022, chap.7). Two different

spatiotemporal scales of wave motions separate fast processes within the waveform and its slow evolution as it propagates through the material. The corresponding variables separation in scales is the necessary condition for self-organization effects.

In the framework of the proposed modeling nonequilibrium momentum transport, the stress relaxation is defined by the dynamics of spatiotemporal correlations during the system evolution towards a more stable state. It must be noticed that during high-strain-rate and short-duration processes it is impossible to separate the elastic and plastic parts of stress and deformation in a correct way since the elastic limit begins to depend on the strain-rate. In contrast to the processes described by continuum mechanics models that are valid near local equilibrium, high-rate processes far from equilibrium are accompanied by post-shock effects, which, thanks to the system's memory of the loading history, continue even after the external impact has already ended. The plastic wave front is the effect of post-shock relaxation.

The problem on the planar shock-induced waveform propagation was solved in paper (Meshcheryakov and Khantuleva, 2015; Khantuleva, 20022, chap. 7). In the frame of reference linked to the elastic precursor travelling at the sound speed C along x-axis $\varsigma = (t - x/C)/t_R$, $\xi = \frac{x}{L}(t_R$ is the loading time, and L is a typical length of the wave propagation) the problem was reduced to the integral equation with respect to the mass velocity with the model correlation function

$$v = \int_0^{\omega} d\varsigma' \exp\left\{-\frac{\pi(\varsigma-\varsigma'-\theta)^2}{\tau^2}\right\}\frac{\partial v}{\partial \varsigma'},\ \omega = \begin{cases}\varsigma, \varsigma \le 1\\ 1, \varsigma > 1\end{cases}. \tag{30}$$

The control parameters τ, θ normalized to the loading time t_R ($\tau(\xi)$is the typical temporal scale of the correlation forming the waveform on the mesoscale-2 and $\theta(\xi)$is the retardation of the inertia center of the mesopacket from the elastic precursor) and depending on the slow variable are described by the set (12). The equation (30) has two different solutions during the shock $\omega \le 1$ and for the post-shock effects $\omega > 1$. In Figure 4 the solution with $\omega \le 1$ describes the elastic precursor 0A formed when the shock has broken the initial correlation in the material. The solution with $\omega > 1$ describes the post-shock recovery of the initial state of the material which was erroneously called plastic front AB (Gilman, 2003). It was shown that together the two obtained solutions adequately describe both experimentally observed waveforms and their propagation along the metal target (Meshcheryakov and Khantuleva,

2015). Figure 4 shows how the shock-induced waveforms change as the control parameters τ, θ increase during propagation along the target.

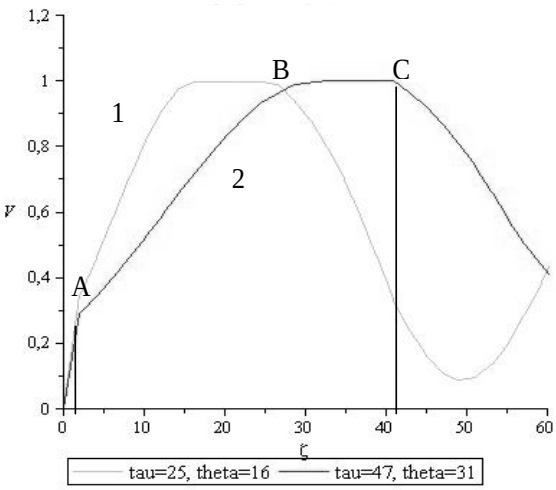

Figure 4. Mass velocity waveforms at two distances from the shocked surface.

The goal function (11) for the shock-induced waveform evolution during its propagation takes the form

$$Q(\tau,\theta) = \int_0^p d\varsigma \, \frac{\partial v}{\partial \varsigma} \int_0^\omega d\varsigma' \exp\left\{-\frac{\pi(\varsigma-\varsigma'-\theta)^2}{\tau^2}\right\} \frac{\partial v}{\partial \varsigma'}. \quad (31)$$

The right-hand part of (31) is the integral entropy production for the wave period p. The generalized entropy production in the propagating waveform (31) is defined by the deformation work done by shock without its separation into reversible and irreversible parts.

The parameter $\tau = t_r/t_R$ determines the process mode depending on whether the relaxation time t_r or the duration of the external action t_R is greater. In elastic wave characterized by undamped memory $\tau \to \infty$ the integral entropy production turns to 0

$$Q \to \int_0^p d\varsigma \, \frac{\partial v}{\partial \varsigma} \int_0^\omega d\varsigma' \frac{\partial v}{\partial \varsigma'} \to \int_0^p d\varsigma \, \frac{\partial v}{\partial \varsigma} \, v(\varsigma) = \frac{v^2}{2}\Big|_0^p = 0. \quad (32)$$

This is reversible process as far as elastic waves do not transport mass.

Vice versa, in plastic flow when the system forgets its initial state $\tau \to 0$, the integral production of entropy will be non-negative due to dissipation according to the laws of linear thermodynamics of irreversible transport processes:

$$Q \to \tau \int_0^\infty d\varsigma \left(\frac{\partial v}{\partial \varsigma}\right)^2 \geq 0 \,. \tag{33}$$

Between these two limiting cases $\tau \sim 1$ (finite-time memory) there is a region of highly non-equilibrium processes where the dissipative effects can be partially replaced by the inertial ones. Decreasing dissipation lowers the integral entropy production. When the motion of wave packets on the mesoscale-1 becomes turbulent, the turbulent transition can lower the entropy production level to negative values $Q < 0$. According to the rigorous results obtained in nonequilibrium thermodynamics, this does not contradict to the 2d law of classical thermodynamics (Zubarev, 1974). It means that the deformation work defining the generalized entropy production (31) corresponds to the difference $TdS - dE$ where $TdS < dE$. If dissipative losses are neglected, then the deformation work is completely converted into the internal energy of the material. Unlike gases, a solid material does not have time to heat up during very short compression (Ravichabdran at al., 2002) and its internal energy is the potential energy of interaction of its structural elements but not kinetic energy (heat).

So, when the potential energy of the material structure is larger than the kinetic energy of the wave packets, their movement ceases and the self-organization of new material structure occurs. As in quantum mechanics, the boundary conditions imposed on the system lead to discretization of the size spectrum of the internal structure (system structuring). This situation is entirely corresponds to the capture of a particle by a potential well in quantum mechanics (Khantuleva and Kats, 2020). Therefore, self-organization on the mesoscale can be considered a quantum effect.

During loading and unloading, the force, acting only for a very short period of time t_R, is proportional to normalized mean accelerations $\partial v/\partial \varsigma = 1$ and $\partial v/\partial \varsigma = -1$ respectively. After the force ceases to act, stress relaxation occurs. Taking into account the wave front and the trailing edge, the expression for the production of entropy inside the impact-induced waveform (31) without separation into reversible and irreversible parts takes the form

$$Q(\tau,\theta)=\int_0^1 d\varsigma\int_0^{\varsigma} d\varsigma'\exp\left\{-\frac{\pi(\varsigma-\varsigma'-\theta)^2}{\tau^2}\right\}-$$
$$\int_b^{b+1} d\varsigma\left[\int_0^1 d\varsigma'\exp\left\{-\frac{\pi(\varsigma-\varsigma'-\theta)^2}{\tau^2}\right\}-\int_b^{\varsigma} d\varsigma'\exp\left\{-\frac{\pi(\varsigma-\varsigma'-\theta)^2}{\tau^2}\right\}\right]. \quad (34)$$

For clarity it is useful to construct a surface $Q(\tau,\theta)$ above the plane of the control parameters τ,θ. Within SG principle the relief of the surface (34) shown in Figure 5 defines the direction and rate of the waveform evolution depending on the initial point on the surface.

On the entropy production surface $Q(\tau,\theta)$ it is seen that the hill with positive entropy production in the region of very short correlations corresponds to the scope of continuum mechanics. On the plane part of the surface elastic waves propagate without structure transformation.

The entropy well happens as a result of the unloading wave that meets the retarded part of the load wave. When a shock wave disrupts correlations in a solid material, wave packets are formed due to dispersion, and the unloading wave induces a counter flow of wave packets, If the wave packets originated by load meet the packets moving towards them, the movement within the waveform can become turbulent. It means that due to self-organization of new information, the entropy production within the waveform decreases. In a solid, the initial state is characterized by the zero entropy production, and its decrease forms a well with negative values of the entropy production. In liquids it is impossible, since the entropy production in the initial state has a large positive value due to strong dissipation. Turbulent transition in liquids decreases the entropy production but retains a positive value.

Beginning from the initial surface point τ_0,θ_0 corresponding to the shock-induced state of the material on the hillside (Figure 5), the evolutionary path descends along the surface gradient. If the evolutionary path leads into the entropy well, the structure evolution stops. This means that the evolutionary process was irreversible. In Figure 5 one can see an entropy hill arising due to dissipation at small structure scales and an entropy well due to rapid unloading of the material.

The waveform propagates along the material at a sound speed and a part of mesostructures (rotations or shears) looses their velocity and may fall behind the waveform. In the case, they remain frozen into material, since their movement is only possible within the waveform due to the energy obtained during shock loading.

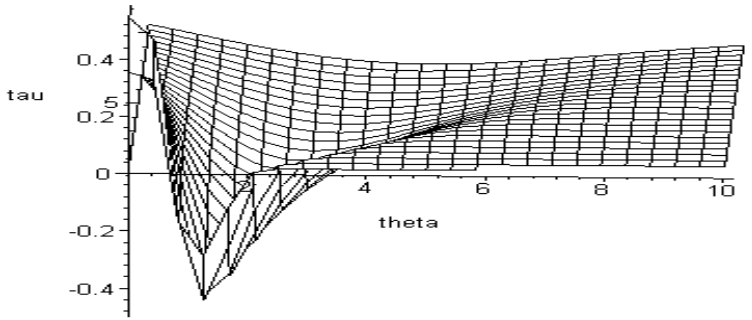

Figure 5. The relief of the integral entropy production $Q(\tau,\theta)$ in the shock-induced waveform.

For the shock loading, the maximum depth of the entropy well is reached when unloading begins from the pulse plateau. It can be shown that the entropy well moves away from the origin as the duration of the pulse plateau increases. This means that the entropy well is a result of the resonance between post-loading effects and unloading wave, which is only possible for short-duration processes in condensed matter (medium with long memory). The sizes and type of the resulting structures should be determined by the depth and shape of the entropy well formed by the unloading wave.

The presence of feedback between macro and mesoevolution through the function $Q(\tau,\theta)$ sets the surface in motion and bends the downward path. Therefore, the speed of descent must play a very important role in the final result. The second, even weak impact in a short period of time also distorts the surface and can significantly change the trajectory of evolution.

Therefore, it becomes possible to control the process of forming the structure of the material due to its special processing. Such a problem belongs to the type with partial control, which requires special solution methods.

Conclusion

1) The transport mechanisms responsible for high-rate processes take place on the mesoscale between macro and microscales and cannot be described by continuum mechanics models.
2) The DSTC approach for adequate description of the transport mechanisms far from local equilibrium developed on the rigorous basis of the methods of nonequilibrium statistical thermodynamics

(Zubarev, 1974) and control theory (Fradkov, 2007, 2008, 2017) proposes new mathematical model that includes self-organization of turbulent structures and their temporal evolution as a closed loop control with feedback.

3) Speed gradient (SG) principle by Fradkov (Fradkov, 2008) determines the fastest path to a more stable state under constraints imposed on the system and plays the role of a driver of system evolution in the internal control mechanism. A system model that includes a closed control loop between the evolution of the mesoscale structure and the macroscopic behavior of the system allows one to predict the dynamic properties of the system by tracing the trajectories of its evolution during a nonequilibrium process.
4) Unlike traditional synergetic models of dissipative processes (Glansdorff, Prigogin,1972), where the type of the mathematical model is predetermined, self-consistent nonlocal models are “soft” models that can change their type depending on external conditions (Arnold, 2005). Open physical system described by such a model far from local equilibrium can adapt to its surroundings by transforming its internal structure and reducing its irreversible losses.
5) According to the results of nonequilibrium statistical thermodynamics (Zubarev, 1974), far from local equilibrium it is impossible to separate processes into reversible and irreversible until they are entirely completed. Since the total entropy production can fluctuate on finite times, a real situation is possible for solids when, after removing the load, turbulent structure stops evolving and irreversibly remains in the material in the form of an experimentally detected new defect structure. The situation occurs when the evolutionary path falls down in the entropy well, which corresponds to the capture of the wave packet by a potential well of the crystal lattice.
6) Comparison of the physical nature of the processes far from local equilibrium with quantum mechanics principles shows that some quantum effects take place on the mesoscalle between macro and microlevels (Khantuleva, Kats, 2020).
7) Partial use of external control of impact on a solid material in combination with an internal control mechanism through feedback can develop a technology for producing materials with specified properties.

Thus, this interdisciplinary DSTC approach at the intersection of mechanics, physics and cybernetics can describe impact and high-rate transport processes in open systems of various natures, including living and intelligent systems. Although the developed self-consistent nonlocal approach to describing highly nonequilibrium processes (Khantuleva, 2022, chap. 5,6) is a fundamentally new, universal and economical way to describe a complex of nonequilibrium phenomena, it is still far from generally accepted. However, it should be kept in mind that as long as theorists use "hard" models (Arnold, 2005) of complex, rapidly changing processes without closed loops of internal control and the evolution of information structures associated with these processes, the gap between the capabilities of fundamental science and practical needs will not be overcome.

Disclaimer

None

References

Arnold VI. *Arnold's problems.* Berlin, Springer; 2005.

Bogoliubov NN. *Problems of dynamic theory in statistical physics.* Oak Ridge TN: Technical Information Service; 1960.

Gilman JJ. Response of condensed matter to impact. In: *High Pressure Shock Compression of Solids VI. Old Paradigms and New Challenges*. (Eds: Y-Y. Horie, L. Davison, N.N. Thadhani) Springer, Berlin; 2003: 279-296.

Fradkov AL. *Cybernetical physics: from control of chaos to quantum control.* Berlin: Springer-Verlag; 2007.

Fradkov AL. Speed-gradient entropy principle for nonstationary processes. *Entropy* (2008) 10: 757-764.

Fradkov AL. Horizons of cybernetical physics. *Philosophical Transactions of the Royal Society A: Mathematical, Physical and Engineering Sciences* (2017) 375 : 20160223.

Glansdorff P, Prigogin I. *Thermodynamic theory of structure, stability and fluctuations.* Wiley Interscience;1972.

Jaynes E. *The maximum entropy formalism.* Canbridge, MA: MIY; 1979.

Jaynes E. *Information theory and statistical mechanics.* 1,2. (1957) 106, 108: 620-630. doi:10.1103/PhysRev.106.620.

Khantuleva TA. Models of Continuum Mechanics and Their Deficiencies. (chap. 1) In: *Mathematical Modeling of Shock-Wave Processes in Condensed Matter. Shock Wave*

and High Pressure Phenomena. Springer, Singapore; 2022. https://doi.org/10.1007/978-981-19-2404-0_1

Khantuleva TA. Specific Features of Processes Far from Equilibrium. (chap. 2) In: *Mathematical Modeling of Shock-Wave Processes in Condensed Matter. Shock Wave and High Pressure Phenomena*. Springer, Singapore; 2022. https://doi.org/10.1007/978-981-19-2404-0_2.

Khantuleva TA. Thermodynamic Concepts Out of Equilibrium. (chap. 4) In: *Mathematical Modeling of Shock-Wave Processes in Condensed Matter. Shock Wave and High Pressure Phenomena*. Springer, Singapore; 2022. https://doi.org/10.1007/978-981-19-2404-0_4.

Khantuleva TA. Non-local theory of high-rate straining followed by structure formations. *J. Phys. 4, France* (2000) 10. EDP Sciences, Les Ulis: 485-490.

Khantuleva TA. The shock wave as a nonequilibrium transport process. In: *High-pressure compression of solids VI: old paradigms and new challenges* (Y.Horie, L.Daison, N.N.Thadhani, Eds.) Springer, Berlin; 2003 : 215-254.

Khantuleva TA. Internal control in nonequilibrium transport. *Proc. the 2nd International Conference "Physics and Control 2005" (PhysCon 2005)* IEEE 05EX1099C ISBN 0-7803-9235-3.05: 41-46.

Khantuleva TA. Self-organization at the mesolevel at high-rate deformation of condensed media. *Chem. Phys.* (2005) 24(11): 36-47.

Khantuleva, TA. New Approach to Modeling Non-equilibrium Processes. (chap. 5) In: *Mathematical Modeling of Shock-Wave Processes in Condensed Matter. Shock Wave and High Pressure Phenomena*. Springer, Singapore; 2022. https://doi.org/10.1007/978-981-19-2404-0_5.

Khantuleva TA, Shalymov DS. Modelling non-equilibrium thermodynamic systems from the speed-gradient principle. *Philosophical Transactions of the Royal Society A. Theme issue: Horizons of cybernetical physics* (2017) 375(2088): 2016220.

Khantuleva TA. The Shock-Induced Planar Wave Propagation in Condensed Matter. (chap. 7) In: *Mathematical Modeling of Shock-Wave Processes in Condensed Matter. Shock Wave and High Pressure Phenomena*. Springer, Singapore; 2022. https://doi.org/10.1007/978-981-19-2404-0_7.

Khantuleva TA. Evolution of Waveforms During Propagation in Solids. (chap. 8) In: *Mathematical Modeling of Shock-Wave Processes in Condensed Matter. Shock Wave and High Pressure Phenomena*. Springer, Singapore; 2022. https://doi.org/10.1007/978-981-19-2404-0_8.

Khantuleva TA, Meshcheryakov YI. Shock-Induced Mesoparticles and Turbulence Occurrence. *Particles* (2022) *5*(3): 407-425. https://doi.org/10.3390/particles5030032.

Khantuleva TA, Kats VM. Quantum Effects on the Mesoscale. *Particles* (2020) *3*: 562-575.

Klimontovich YL. Entropy evolution in self-organization processes. H-theorem and S-theorem. *Physica* (1987) 142A:374. Doi: 10.1016/0378-4371(87)90031-8

Lee J. The Universal Role of Turbulence in the propagation of Strong Shocks and Detonation Waves. *High-pressure compression of solids VI: old paradigms and new challenges (Eds.: Y. Horie, L. Davison, N.N.Thadhani.*). Springer; 2003: 121-144.

LuYonghuaYanPing Physics of turbulence generation and sustenance in a boundary layer. *Computers & Fluids* (2014) 102(10): 353-384.

Mescheryakov YI. Meso-Macro Energy Exchange in Shock Deformed and Fractured Solids. *High-pressure compression of solids VI: old paradigms and new challenges (Eds.: Y. Horie, L. Davison, N.N.Thadhani*.). Springer; 2003: 169-212.

Meshcheryakov YI., Khantuleva TA. Nonequilibrium Processes in Condensed Media. Part 1. Experimental Studies in Light of Nonlocal Transport Theory. *Physical Mesomechanics* (2015) 18(3): 228-243

Meshcheryakov Y. *Multiscale mechanics of shockwave processes.* Springer Nature. Singapore;2021. http://doi.org/10.1007/978-981-16-4530-3.

Nicolis G, Prigogine I. *Self-Organization in Nonequilibrium Systems. From Dissipative Structure to Order Through Fluctuations.* N.Y.: Wiley; 1977.

Ravichandran G, Rosakis AJ, Hodovany J, Rosakis P. On the convention of plastic work into heat during high-strain-rate deformation. *Shock Compression of Condensed Matter-2001". (Eds. M. D. Furnish, N.N. Thadhani, Y-Y. Horie). AIP Conference Proceedings-620. Melville, NY;* 2002: 557-562.

Rayleigh L. On the motion of solid bodies through viscous liquid. *Philos. Mag.* (1911) 21: 697-711. Doi:10.1080/14786440608637084.

Zubarev DN. *Non-equilibrium Statistical Thermodynamics.* Springer; 1974.

Zubarev DN, Tischenko SV. Nonlocal hydrodynamics with memory. *Physics* (1972) 59(2): 285-304.

Chapter 2

The Evolution of Solitary Elastic Waves with Different Initial Profiles

Jeremiah Rushchitsky*
S. P. Timoshenko Institute of Mechanics, Kyiv, Ukraine

Abstract

The distinctions and similarities in the evolution of four types of solitary waves propagating in an elastic nonlinear material are studied and commented on. These types of waves differ by the mathematical description of the initial profile. Type 1 is the symmetric initial profile and hump-shaped Gauss wave, type 2 is the non- symmetric initial profile and hump-shaped Whittaker wave, type 3 – the non- symmetric initial profile, not hump-shaped and using the special Macdonald function in description wave, type 4 - the nonsymmetric initial profile not hump-shaped and using the algebraic Friedlander function wave. The evolution of the Gauss and harmonic waves, the Whittaker and Gauss waves, and the Macdonald and Friedlander waves is compared and this comparison is commented on. The carried out collating showed different kinds of distinctions and similarities.

Keywords: solitary elastic wave, plane longitudinal and cylindrical radial waves, nonlinear wave equations, evolution of wave's initial profile

* Corresponding Author's Email: rushch@inmech.kiev.ua.

In: Horizons in World Physics. Volume 312
Editor: Albert Reimer
ISBN: 979-8-89113-513-0

1. Introduction

An evolution in the general sense is meant as a gradual (slow) transition from one qualitative state to another one. An antonym to evolution is the revolution, which means the sharp jump-wise transition from one qualitative state to another one. In the theory of waves, the evolution of waves is understood as a gradual (slow) change of the wave's initial profile to another (distorted) profile [6, 16].

The elastic waves do not evolute in their description by the linear theory of elasticity. Therefore, the nonlinear theory of elasticity should be necessarily used when the evolution of elastic waves is studied. This theory includes tens of models of nonlinear deformation each of which is proposed for some specific class of materials [16, 18]. Many traditional engineering materials exhibit nonlinear elastic properties and their nonlinear deformation is described well by the classical five-constant Murnaghan model [16, 18]. Just this model is chosen in the following presentation of solitary elastic waves.

The solitary waves are defined by the attribute of the shape of the wave's initial profile. Exclusion is the class of solitons that usually is considered sepa rately. The shape of a solitary wave must be described by the finite function or the function of finite weight. More simply, this function has to be given at the finite interval and be zero strongly or approximately outside of this interval. A classic example of the solitary wave is the wave with the initial profile in the form of the Gauss function (Gaussian, bell-shaped or hump-shaped function) [4, 8, 16].

This chapter is devoted to the theoretical and numerical analysis of the pro pagation of four kinds of solitary waves which are different in some attributes and show some similarities in other attributes. This analysis results in a series of evident and non-evident distinctions and similarities. Therefore, the main attention is paid to these distinctions and similarities. To the point, let us recall here the maxim given in [3] that the peculiarity of human percep- tion is such that we notice distinctions more often and with less difficulty.

Let us characterize the mentioned kinds of waves. First, they all are one-dimensional displacement waves and are similar in this attribute. But their initial profile representations $u(mx)$ (u, x, m are the displacement in the direction of coordinate x, space coordinate (distance), and the arbitrary scale factor, respectively) differ among themselves. 1. Profile in the form of the Gauss function $u(mx) = u_o e^{-(mx)^2/2}$ [4, 8, 16] (u_o is the amplitude factor,

features: one symmetric hump, a special function is used). 2. Profile in the form of the Whittaker function $u(mx) = u_o W_{1/4;3/4}(mx)$ [8, 12] (features: one non-symmetric hump, a special function is used). 3. Profile in the form of the Macdonald function $u_r(mr) = u_{ro} K_0(mr)$ [8, 13], where u_r, r are the radial displacement and coordinate, respectively (features: nonsymmetric and without a hump, a special function is used). 4. Profile in the form of the Friedlander function $u_r(mr) = u_{ro} e^{-bmr/r_{att}}(1 - mr/r_{att})$ [5, 7, 11], where b, r_{att} are the parameters (feature: non-symmetric and without a hump, an algebraic function is used).

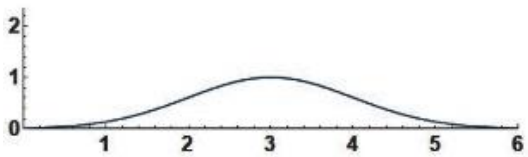

Figure 1. Typical Gauss profile.

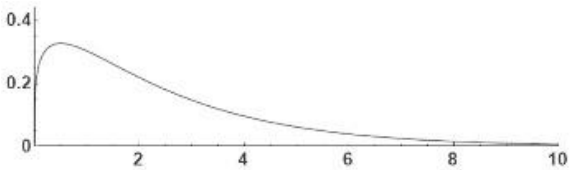

Figure 2. Typical Whittaker profile.

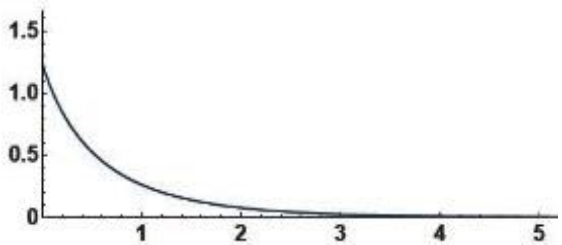

Figure 3. Typical Macdonald profile.

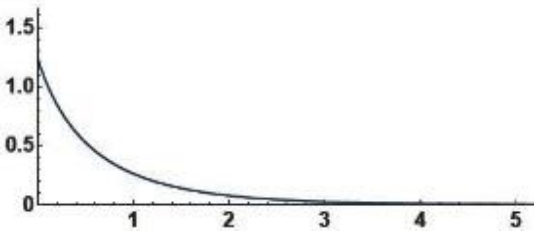

Figure 4. Typical Friedlander profile.

2. Additional Facts Related to Waves, Wave Equations, and Their Approximate Solutions

2.1. Plane Longitudinal and Cylindrical Radial Waves

Both types of waves are the classical ones in the linear theory of elasticity and are called by the attribute of the wavefront [1, 2, 8, 15, 16]. The plane wave has a plane front, whereas the front of the cylindrical wave is curvilinear (circular cylindrical surface). In the considered here one-dimensional case, the plane wave propagates in the direction of the abscissa axis of a cartesian coordinate system and the cylindrical wave propagates in the direction of a radial coordinate of the cylindrical coordinate system. The plane waves divide into three types -longitudinal, transverse vertical and horizontal. In the following, the plane longitudinal and cylindrical radial waves are considered. The difference between them is that a plane wave belongs to the class of free or traveling waves - it is generated “at infinity” and goes “to infinity”- and therefore its amplitude is undefined, while a cylindrical wave has to be generated on a certain cylindrical surface and beyond go “to infinity” and therefore its amplitude is determined exactly according to the boundary condition.

2.2. Nonlinear Five-constant Murnaghan Model

This model can be meant as the classical one in the nonlinear theory of elasticity [18], it describes a large class of industrial materials, is widely used, and is thoroughly commented on in the fundamental books on nonlinear solid mechanics. It is defined by the potential (internal energy of deforma tion)

$$W(\varepsilon_{ik}) = \frac{1}{2}\lambda(\varepsilon_{mm})^2 + \mu(\varepsilon_{ik})^2 + \frac{1}{3}A\varepsilon_{ik}\varepsilon_{im}\varepsilon_{km} + B(\varepsilon_{ik})^2\varepsilon_{mm} + \frac{1}{3}C(\varepsilon_{mm})^3$$ or

$$W = \frac{1}{2}\lambda\left(u_{m,m}\right)^2 + \frac{1}{4}\mu\left(u_{i,k} + u_{k,i}\right)^2 + \left(\mu + \frac{1}{4}A\right)u_{i,k}u_{m,i}u_{m,k} +$$
$$+\frac{1}{2}(\lambda + B)u_{m,m}\left(u_{i,k}\right)^2 + \frac{1}{12}Au_{i,k}u_{k,m}u_{m,i} + \frac{1}{2}Bu_{i,k}u_{k,i}u_{m,m} + \frac{1}{3}C\left(u_{m,m}\right)^3. \quad (1)$$

Here, the nonlinear Cauchy-Green strain tensor is used

$$\varepsilon_{nm}(x_k,t) = (1/2)\left(u_{n,m} + u_{m,n} + u_{n,i}u_{i,m}\right),$$

λ, μ are Lame elastic constants, A, B, C are Murnaghan elastic constants.

The simplest form of potential (1) is used in the following analysis. It is based on the standard assumption that the waves propagate along the abscissa axis, that is $\vec{u} = \{u_k(x_1,t)\}$, and has the form [16]

$$W = (1/2)\left[(\lambda + 2\mu)\left(u_{1,1}\right)^2 + \mu\left[\left(u_{2,1}\right)^2 + \left(u_{3,1}\right)^2\right]\right] +$$
$$+\left[\mu + (1/2)\lambda + (1/3)A + B + (1/3)C\right]\left(u_{1,1}\right)^3 + (1/2)(\lambda + B)u_{1,1}\left[\left(u_{2,1}\right)^2 + \left(u_{3,1}\right)^2\right] \quad (2)$$

The corresponding components of the Kirchhoff stress tensor are as follows

$$t_{11} = (\lambda + 2\mu)u_{1,1} + (3/2)\left[\lambda + 2\mu + 2(A + 3B + C)\right]\left(u_{1,1}\right)^2 +$$
$$+(1/2)\left[\lambda + 2\mu + (1/2)A + B\right]\left[\left(u_{2,1}\right)^2 + \left(u_{3,1}\right)^2\right],$$
$$t_{12} = \mu u_{2,1} + (1/2)\left[\lambda + 2\mu + (1/2)A + B\right]u_{1,1}u_{2,1},$$
$$t_{13} = \mu u_{3,1} + (1/2)\left[\lambda + 2\mu + (1/2)A + B\right]u_{1,1}u_{3,1}. \quad (3)$$

Substitution (3) into the motion equations $\rho u_{i,tt} = t_{ik,k}$ gives the simplest quadratically nonlinear wave equation for the plane longitudinal waves [16]

$$\rho u_{1,tt} - (\lambda + 2\mu) u_{1,11} = N_1 u_{1,11} u_{1,1} \quad N_1 = 3\left[(\lambda + 2\mu) + 2(A + 3B + C)\right]. \quad (4)$$

The corresponding to the cylindrical radial wave nonlinear equation is derived in another way [16]. First, the cylindrical coordinate system (r, ϑ, z) is used. Then an axisymmetric configuration with the symmetry axis Oz is chosen which depends on the radial coordinate only, according to which the components of the nonlinear Cauchy-Green strain tensor can be evaluated through the component u_r of the displacement vector

$$\varepsilon_{rr} = u_{r,r} + (1/2)(u_{r,r})^2, \; r^2 \varepsilon_{\vartheta\vartheta} = u_r r + (1/2)(u_r)^2, \; \varepsilon_{zz} = \varepsilon_{rz} = \varepsilon_{r\vartheta} = \varepsilon_{\vartheta z} = 0 \quad (5)$$

The nonzero components of the Lagrange stress tensor have the form

$$\sigma^{rr} = \lambda\left[u_{r,r} + (u_r/r)\right] + 2\mu u_{r,r} + (2/r)(B + C) u_{r,r} u_r +$$

$$+\left[(1/2)(\lambda + 2\mu) + A + 3B + C\right](u_{r,r})^2 + \left[(1/2)\lambda + B + C\right](u_r)^2 / r^2, \quad (6)$$

$$\sigma^{\vartheta\vartheta} = \lambda\left[u_{r,r} + (u_r/r)\right] + 2\mu(u_r/r) + (2/r)(B + C) u_{r,r} u_r +$$

$$+\left((1/2)\lambda + 3B + C\right)(u_{r,r})^2 + \left[(1/2)(\lambda + 2\mu) + A + B + C\right]\left[\left((u_r)^2 / r^2\right)\right] \quad (7)$$

The two last equations of the three motion equations are satisfied identi cally, the first one is as follows

$$\sigma_{rr,r} + \frac{1}{r}(\sigma_{rr} - \sigma_{\vartheta\vartheta}) - \rho \ddot{u}_r = -\left(u_{r,rr} + \frac{1}{r} u_{r,r}\right)\sigma_{rr} - \frac{1}{r^2} u_r \sigma_{\vartheta\vartheta} - u_{r,r} \sigma_{rr,r}.$$

or the simplest variant in displacement

$$(\lambda+2\mu)\left(u_{r,r}+\frac{u_r}{r}\right)_{,r}-\rho\ddot{u}_r=-N_1u_{r,rr}u_{r,r} \tag{8}$$

Now, two basic nonlinear equations (4) and (8) can be compared. They are very similar in structure. The left parts are the classical linear wave equations written in cartesian and cylindrical coordinates. The right sides are almost identical and include the quadratically nonlinear term.

2.3. Solving the Nonlinear Wave Equations

Write first equations (4) and (8) in the form

$$u_{1,tt}-c_L^2\,u_{1,11}=(N_1/\rho)u_{1,11}u_{1,1}, \tag{9}$$

$c_L=\sqrt{(\lambda+2\mu)/\rho}$ is the velocity of the plane longitudinal elastic wave,

$$u_{r,tt}-(c_L)^2\left[u_{r,rr}+(1/r)u_{r,r}-\left(u_r/r^2\right)\right]=(N_1/\rho)u_{r,rr}u_{r,r}. \tag{10}$$

For the corresponding to (9),(10) linear wave equations, the known theorems are proven [19] that for some conditions the initial wave profile of arbitrary representations $u_1(x)=F(x), u_r(r)=F(r)$ of the solutions in the form $u_1(x,t)=F\left[m(x-c_Lt)\right]$, $u_r(r,t)=F\left[m(r-c_Lt)\right]$ exist (m is the arbi trary scale factor characterizing the wavelength for the harmonic wave and the wave bottom for the solitary wave). Thus, both waves propagate with the same velocity. Note that $\sigma=m(x_1-c_Lt)$ is the standard wave phase variable.

Further, equations (9) and (10) will be analyzed by two approximate app roaches, which are most frequently used in the study of elastic waves in mate rials [16]. It was established that the first three approximations (the first one is the linear) describe quite sufficiently the main wave effects [16, 17].

2.3.1. Method of Successive Approximations (Perturbation Method, The Method of the Small Parameter, Method 1).

Let us describe the method on an example of equation (9). According to the method, the small parameter ε and the function $u_1(x_1,t,\varepsilon)$ in the form of convergent series are introduced

$$u_1(x_1,t,\varepsilon)=u_1^{(1)}(x_1,t)+\varepsilon u_1^{(2)}(x_1,t)+\varepsilon^2 u_1^{(3)}(x_1,t)+\cdots \tag{11}$$

The solution of the nonlinear equation (9) is sought in the form of sequential approximations

$$u_1(x_1,t)=u_1(x_1,t,\varepsilon=1)=u_1^{(1)}(x_1,t)+u_1^{(2)}(x_1,t)+u_1^{(3)}(x_1,t)+\cdots . \tag{12}$$

The first approximation $u_1^{(1)}(x_1,t)$ is the solution of corresponding linear wave equation (9). A feature and characteristic advantage of method 1 is that the arbitrary approximation $u_1^{(n)}(x_1,t)$ is found as the solution of the inhomo geneous linear equation

$$u_{1,tt}^{(n)}-(c_L)^2\,u_{1,11}^{(n)}=(N_1/\rho)u_{1,11}^{(n-1)}u_{1,1}^{(n-1)} . \tag{13}$$

Thus, to find the 2nd approximation, it is necessary to know only the 1st approximation and solve only the inhomogeneous linear wave equation. One only restriction assumes this method – the series (12) must be conver-gent. Usually, this is meant for the first three approximations as the condition $u_1^{(1)}(x_1,t)\square\ u_1^{(2)}(x_1,t)\square\ u_1^{(3)}(x_1,t)$. Note also that this method is applicable to equation (10) by use of the same procedure.

2.3.2. Method of Restrictions on the Gradient of Displacement (Method 2).

An important feature and necessary condition of this method is that the studied nonlinear wave equation must have a special structure: the right-side part of this equation can be carried over to the left-hand-side one and then formally the nonlinear equation can be written as the linear wave equation with the variable wave velocity [17]. Both equations (9) and (10) fulfill this condition.

Case of equation (9). Let us transform equation (9) into the form

$$u_{1,tt}-\left[\left(c_L\right)^2+\left(N_1/\rho\right)u_{1,1}\right]u_{1,11}=0\rightarrow \quad u_{1,tt}-v^2u_{1,11}=0,$$

$$v=c_L\sqrt{1+\alpha u_{1,1}}\ ,\ \alpha=\left[N_1/\left(\lambda+2\mu\right)\right]. \tag{14}$$

Further, two restrictions on the gradient of displacement and other parameters are introduced

$$\left|\alpha u_{1,1}\right|\ll 1\ ,\ \left|\delta=-\left(1/2\right)\alpha m c_L u_{1,1}t\right|\ll 1. \tag{15}$$

The restrictions (15) permit to represent approximately the solution of the nonlinear wave equation (14) within the neighborhood of the classical constant value $\sigma=m\left(x_1-c_Lt\right)$ of the wave phase and with saving only two first approximations in the form

$$u_1\left(x_1,t\right)\approx F\left(\sigma\right)+F_{,1}^{/}\left(\sigma\right)m\delta=F\left(\sigma\right)-\left(1/2\right)\alpha m^2c_Lt\left[F^{/}_{,1}\left(\sigma\right)\right]^2. \tag{16}$$

Taking into account the 3rd approximation introduces some difficulties and complications, which will be commented on in the following.

Case of equation (10). First, this equation should be slightly transformed

$$v_r^2\left[u_{r,rr}+\left(1/r\right)u_{r,r}-\left(u_r/r^2\right)\right]-u_{r,tt}=0\ ,\ v_r=\sqrt{1-\alpha u_{r,r}}\ c_L. \tag{17}$$

Introduce two restrictions

$$\left|\alpha u_{r,r}\right|<1\ ,\ \left|\delta^*=-\left(1/2\right)mc_L\alpha\, u_{r,r}\left[1-\left(1/4\right)\alpha u_{r,r}\ \right]t\right|<1, \tag{18}$$

which admit the allowance for the first three approximations.

The solution of the nonlinear wave equation (17) can be written approxima tely in the neighborhood of the classical phase value $\sigma=m\left(r-c_Lt\right)$ in the form

$$u_r\left(r,t\right)=u_r^oF\left(\sigma\right)+u_r^oF^{/}\left(\sigma\right)\delta^*+\left(1/2\right)u_r^oF^{//}\left(\sigma\right)\delta^{*2}+\cdots \tag{19}$$

where u_r^o is the given constant amplitude coefficient.

After some transformations, the final representations can be obtained: the solution in the form of the first two approximations

$$u_r^{(1+2)}(r,t)=u_r^o F(\sigma)-(1/2)m^2\left(u_r^o\right)^2 c_L\alpha_1 t\left[F'(\sigma)\right]^2, \tag{20}$$

the solution in the form of the first three approximations

$$u_r^{(1+2+3)}{}_r(r,t)=u_r^o F(\sigma)-(1/2)m^2\left(u_r^o\right)^2 c_L\alpha_1 t\left[F'(\sigma)\right]^2+ \\ +(1/8)m^3\left(u_r^o\right)^3(\alpha_1)^2 c_L t\left[F'(\sigma)\right]^3. \tag{21}$$

3. Solitary Wave with the Symmetric Initial Profile in the Form of Gauss Function

3.1. Gauss Profile (Method 1, First Two Approximations)

The 1st approximation $u_1(x_1,t)=u_{1o}e^{-\sigma^2/2}$ should be substituted into the right side of the inhomogeneous linear wave equation (13). Then the 2nd approximation can be found as the solution of the equation

$$u_{1,tt}^{(2)}-(v_L)^2 u_{1,11}^{(2)}=(N_1/\rho)(u_{1o})^2 a^3\sigma\left(1-\sigma^2\right)e^{-\sigma^2}. \tag{22}$$

This solution is searched as $u_1^{(2)}=t\,A(\sigma)e^{-\sigma^2}$ and then the inhomogeneous differential equation relative to function $B(\sigma)=t\,A(\sigma)e^{-\sigma^2}$ $B(\sigma)$ must be considered $\left[B''(\sigma)+3\left(\sigma^2-1\right)B(\sigma)\right]=(u_{1o})^2\alpha a\sigma\left(1-\sigma^2\right)e^{\sigma^2/2}$. The homo geneous equation $B''(\sigma)+3\left(\sigma^2-1\right)B(\sigma)=0$ corresponds to equation (11) from subsection (2.173) of [10] with $a=0,b=3,c=\sqrt{3}$ and can be reduced to the Whittaker equation [9, 16]. So, the solution seems very complicated owing

presence of the factor $\sigma\left(\sigma^2-1\right)$. Thus, the 2nd approximation will ha ve a complicated mathematical form, which should still be found. The analyti cal and numerical analysis of the Gauss wave evolution looks very unpro- mising. In this situation, some advantage has method 2.

3.2. Gauss Profile (Method 2, First Two Approximations)

In this case, the formula (20) can be used what yields the representation

$$u_1^{(1+2)}\left(x_1,t\right)=u_{1o}e^{-\sigma^2/2}-\left(1/2\right)t\alpha c_L m^2\sigma^2\left(u_{1o}\right)^2e^{-\sigma^2}. \tag{23}$$

Two summands can be shortly commented on. The 1st summand is the 1st approximation (linear one, which is characterized by the 1st conditional harmo nic $e^{-\sigma^2/2}$), The 2nd summand includes the 2nd conditional harmonic $e^{-\sigma^2}$ and depends nonlinearly on the bottom factor. Most important is a linear dependence on time which testifies that the Gauss wave evolves and the pro- file is distorted symmetrically due to the appearance of the 2nd conditional harmonic whose amplitude increases with the time (or distance of the wave propagation. Note that the term "harmonic" should be here used sufficiently conditionally. The notion "harmonic" is used nevertheless in the harmonic analysis that is based on the completeness of the functions-harmonics. This completeness is not valid for the Gauss function.

It is the place to compare the scenarios of the evolution of the solitary Gauss wave and classical periodic harmonic wave.

The nonlinear elastic wave with the initial harmonic profile is studied well [RS]. In the case of a plane longitudinal elastic wave of the initial wave amplitude u_{1o}, frequency ω, and wavenumber k

$$u_1\left(x_1,t\right)=u_{1o}\cos\left(k_Lx_1-\omega t\right) \tag{24}$$

the corresponding to (23) solution has the form [RS]

$$u_1^{(1+2)}\left(x_1,t\right)=u_{1o}\cos\left(k_Lx_1-\omega t\right)+\frac{x_1N_1\left(u_{1o}\right)^2k_L^2}{8\left(\lambda+2\mu\right)}\cos 2\left(k_Lx_1-\omega t\right). \tag{25}$$

Here, the wave velocity is equal c_L and the bottom factor m is changed on the wavenumber k_L.

The solution (25) confirms a generation of the 2nd harmonic owing to the self-generation of the 1st harmonic. As a result, the effect of the 2nd harmonic increases, and it becomes the dominant one. Thus, the evolution of the wave consists of a gradual transition from the profile of the 1st harmonic to the profile of the 2nd harmonic.

Consider some demonstrative pictures showing the scenarios of evolution of the plane periodic harmonic wave and solitary Gauss wave and propose some comments on their similarities and distinctions. All shown plots are built for metallic materials and small strains. The 2D picture shows an evolution in coordinates "distance of propagation – displacement" and the 3D picture – in coordinates "time – distance – displacement."

Figure 5 shows one of the stages of transition from the initial periodic harmonic profile from the 1st harmonic to the 2n one.

Figure 6 shows one of the stages of transition of the initial solitary Gauss profile from the conditional 1st harmonic to the conditional 2nd one.

The distinction of profiles should be outlined first of all – one is periodic and the other is solitary. At that, they both are symmetric during the process of evolution. But another type of similarity is more unpredicted – the top part of the profile draws down and forms two humps. Each hump separately is not symmetric.

The next two figures show this stage of evolution in the 3D pictures.

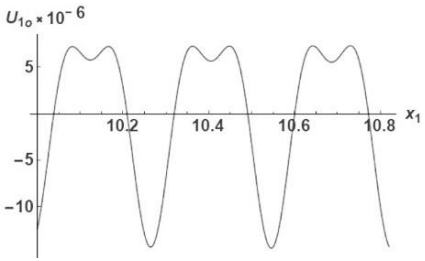

Figure 5. Evolution of the initial harmonic profile.

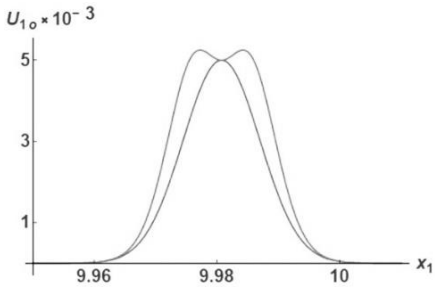

Figure 6. Evolution of the initial Gauss profile.

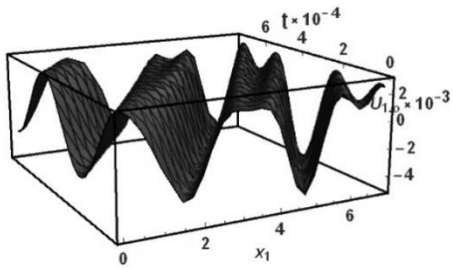

Figure 7. Evolution of the initial harmonic profile.

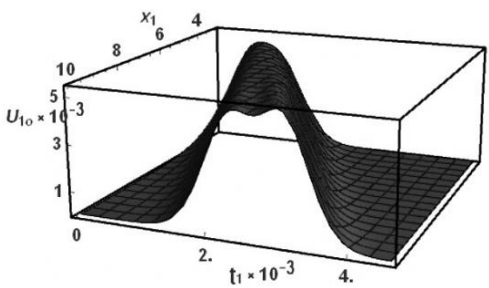

Figure 8. Evolution of the initial Gauss profile.

A comparison shows that the symmetric Gauss wave changes its profile symmetrically in a slightly different way. The conditional 2nd harmonic always gives off a negative additive. So, the slopes of the bell (hump) become stee-per. The upper part of the bell falls and forms two bells.

3.3. Gauss Profile (Method 2, First Three Approximations)

The corresponding to the Gauss profile solution is as follows

$$u_1^{(1+2+3)}(x_1,t)=u_{1o}e^{-\sigma^2/2}-$$

$$-(1/2)\alpha v_L m^2 t\left(u_{1o}\right)^2\sigma^2 e^{-\sigma^2}-(1/8)\alpha^2 v_L m^3 t\left(u_{1o}\right)^3\sigma^3 e^{-3\sigma^2/2}. \qquad (25)$$

Thus, the 3rd approximation introduces new features in the evolution.

Let us show here the solution for the harmonic wave within the framework of the first three approximations. It is formed as the sum of the 1st, 2nd, and 4th harmonics and has the form [16].

$$u_1^{(1+2+3)}(x_1,t)=u_{1o}\cos\sigma+u_{1o}M_L x_1\cos 2\sigma+$$

$$+u_{1o}\left(M_L\right)^3\left(x_1\right)^3\left[-\frac{8}{3}+\frac{5}{2k_L x_1}\sin 4\sigma+\left(-\frac{4}{3}+\frac{11}{8\left(k_L\right)^2\left(x_1\right)^2}\right)\cos 4\sigma\right],$$

$$M=\frac{N_1}{8(\lambda+2\mu)}u_{1o}\left(k_L\right)^2=\frac{1}{8\rho}N_1u_{1o}\frac{k_L^2}{v_L^2}=\frac{1}{8\rho}N_1u_{1o}\frac{\omega^2}{v_L^4}. \qquad (26)$$

First of all, solution (25) shows the asymmetric changes in the wave profile (owing to the presence in the 3rd summand the factor σ^3) in contrary to the case $u_1^{(1+2)}$ which shows the symmetric changes. Besides that, a presence of the cubic nonlinearity in the 3rd approximation, which means the presence of the 3rd conditional harmonic in contrast to the effect of classical harmonic wave case (26), where after the 2nd harmonic the 4th one is generated [16]. Thus, a distinction is essential.

Concentrate now on only the solitary Gauss wave and show some demo nstrative pictures of evolution specificities. Figure 9 corresponds to the initial stage of evolution. The lower graph shows the initial profile $u_1^{(1)}$, and the upper one shows $u_1^{(1+2+3)}$.

The peculiarity of this picture: the initial bell becomes bigger and wider.

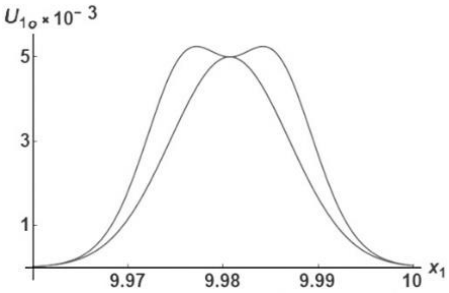

Figure 9. Evolution of the initial Gauss profile.

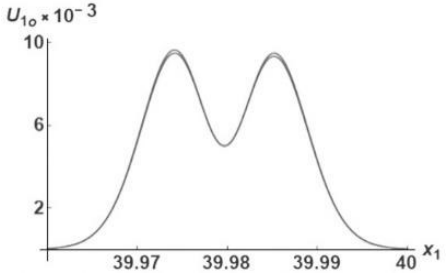

Figure 10. Evolution of the initial Gauss.

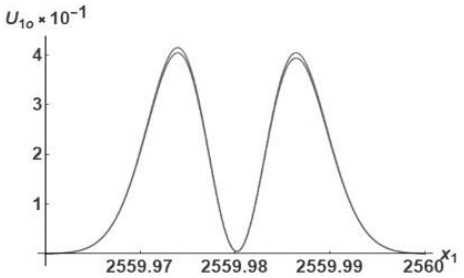

Figure 11. Evolution of the initial Gauss profile (stage 1). profile (stage 2).

Figures 10 and 11 show two profiles ($u_1^{(1+2)}$ and $u_1^{(1+2+3)}$) and present the start of the new wave effect consisting in moving down the left hump and upward of the right one. This effect introduces a new asymmetry in evolution and is unexpected like some other third approximation nonlinear wave effects.

4. Solitary Wave with the Non-symmetric Initial Profile in the Form of Whittaker Function

The Whittaker functions [8, 12] have a common property – their plots have the form of one hump, which is asymmetric relative to the vertical straight line passing through the hump top. These functions depend on two parame ters and fulfill some special ordinary differential equation of the 2nd order. Further, the Whittaker function

$$F\left(x_1\right)=W_{1/4;3/4}\left(mx_1\right) \tag{27}$$

is considered as describing the initial profile of some solitary wave.

4.1. Whittaker Profile (Method 2, First Two and Three Approximations)

The 1st approximation (27) should be substituted into the formulas (20) and (21). Then the approximate representation of the solitary Whittaker wave has the form:

in the case of the first two approximations

$$u_1^{1+2}\left(x_1,t\right)=u_{1o}W_{1/4;3/4}\left(m\sigma\right)-\left(1/2\right)t\alpha c_L m^2\left(u_{1o}\right)^2\left(W'_{1/4;1/4}\left(m\sigma\right)\right)^2 \tag{28}$$

in the case of the first three approximations

$$\begin{aligned} u_1^{1+2+3}\left(x_1,t\right)&=u_{1o}W_{1/4;3/4}\left(m\sigma\right)-\left(1/2\right)t\alpha c_L\left(m\right)^2\left(u_{1o}\right)^2\left(W'_{1/4;1/4}\left(m\sigma\right)\right)^2+\\ &+(1/8)t(\alpha)^2c_L\left(m\right)^3\left(u_{1o}\right)^3\left[W'_{1/4;1/4}\left(m\sigma\right)\right]^3. \end{aligned} \tag{29}$$

Now, the derivative of the function $W_{\kappa,\mu}\left(z\right)$ should be calculated by the general formula

$$\frac{d}{dz}W_{\lambda,\mu}\left(z\right)=\left(\frac{\lambda}{z}-\frac{1}{2}\right)W_{\lambda,\mu}\left(z\right)-\frac{1}{z}\left[\mu^2-\left(\lambda-\frac{1}{2}\right)^2\right]W_{\lambda-1,\mu}\left(z\right),$$

according to which the following formula is valid

$$\left(W_{3/4;1/4}(\sigma)\right)' = \left(\frac{3}{4\sigma} - \frac{1}{2}\right) W_{3/4,1/4}(\sigma) \quad . \tag{30}$$

Then the solutions (28) and (29) have the form:

in the case of the first two approximations

$$u_1^{1+2}(x_1,t) = u_{1o} W_{3/4;1/4}(m\sigma) - \tag{31}$$

$$-(1/2)t\alpha c_L m^2 (u_{1o})^2 \left\{\left[(3/4\sigma) - 1/2\right] W_{3/4,1/4}(m\sigma)\right\}^2 ,$$

in the case of the first three approximations

$$\begin{aligned} u_1^{1+2+3}(x_1,t) &= u_{1o} W_{3/4;1/4}(m\sigma) - \\ &-(1/2)t\alpha c_L m^2 (u_{1o})^2 \left\{\left[(3/4\sigma) - (1/2)\right] W_{3/4,1/4}(m\sigma)\right\}^2 + \\ &+(1/8)t(\alpha)^2 c_L m^3 (u_{1o})^3 \left\{\left[(3/4\sigma) - (1/2)\right] W_{3/4,1/4}(m\sigma)\right\}^3 . \end{aligned} \tag{32}$$

Consider further a few plots built by formulas (31) and (32).

Figure 12 presents the initial stage with two profiles, which correspond to the 1st (linear) approximation and first two approximations They are practi cally identical. Figure 13 presents the next stage with these profiles (1st corre sponds to the upper line and first two -lower line).

Figure 14 presents the stage 3, where the difference between profiles is significant and shows the hump top shift to left side. Figure 11 shows stage 3 in the 3D format (displacement – distance – time).

Thus, some new wave effects can be seen in Figures 12-15: the wave bottom is not changed, the maximal amplitude is increasing, the right slope becomes steeper.

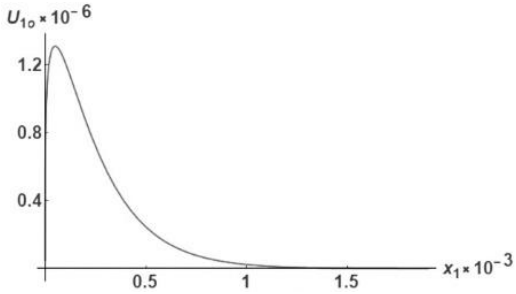

Figure 12. Evolution of the initial Whittaker.

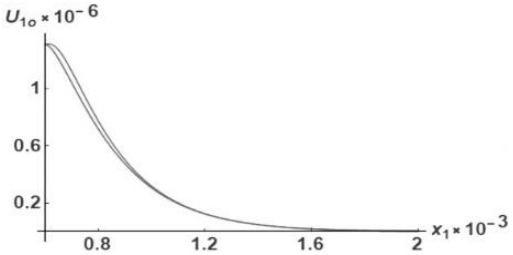

Figure 13. Evolution of the initial Whittaker profile (1 and 1+2 approximations, stage 2) profile (1 and 1+2 approximations, stage 1).

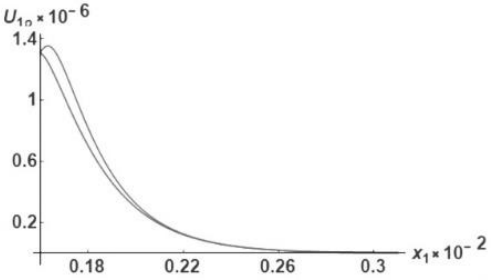

Figure 14. Evolution of the initial Whittaker.

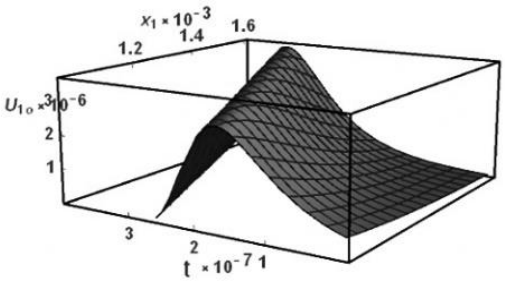

Figure 15. Evolution of the initial Whittaker profile (1 and 1+2 approximations, stage 3) profile (1 and 1+2 approximations, stage 3).

The next four figures show by twos plots which corresponds to the 1+2 and 1+2+3 approximations. Figure 16 corresponds to the stage when the plots are slightly different (here and further, the upper plot corresponds to 1+2 and lower – to 1+2+3 approximations).

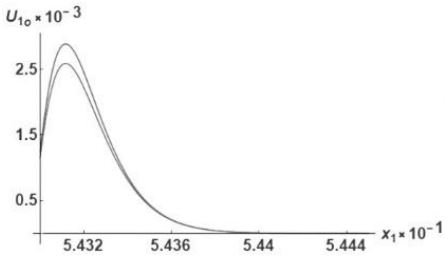

Figure 16. Evolution of the initial Whittaker.

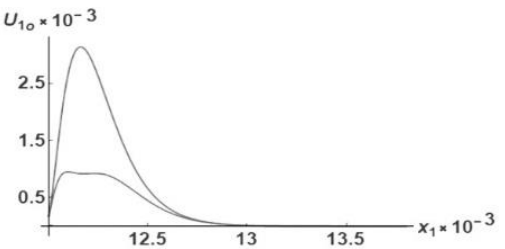

Figure 17. Evolution of the initial Whittaker profile (1+2 and 1+2+3 approximations, profile (1+2 and 1+2+3 approximations, stage 1) stage 2).

Decreasing the hump height only can be seen in Figure 16. Figures 17 and 18 show the next stages of evolution: forming of two humps instead one initial hump.

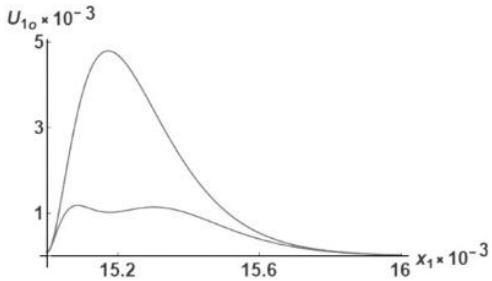

Figure 18. Evolution of the initial Whittaker.

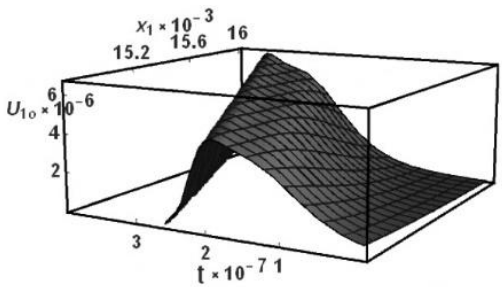

Figure 19. Evolution of the initial Whittaker profile (1+2 and 1+2+3 approximations, profile (1+2 and 1+2+3 approximations, stage 3) stage 3).

Figure 19 presents the stage 3 in the 3D format (displacement - distance - time).

The presented demonstrative Figures 16-19 show an important feature of evolution of the Whittaker wave when the first two and three approxima- tions are compared: the evolution of nonsymmetric profile occurs nonsymmetrically, the wave bottom is not changed, the maximal amplitude is decreasing, the right slope becomes flatter.

Thus, allowance for the 3rd approximation introduces essential changes into the evolution. First of all, the case 1+2+3 approximations demonstrates tendency to forming two nonsymmetric humps. Therefore, this new wave effect can be compared with analogous effects of Gauss and harmonic waves with symmetric profiles. A similarity is obvious: one hump is transformed into

two ones. A main distinction consists in that the symmetric profiles form the symmetric two humps whereas the nonsymmetric profile forms two nonsymmetric humps.

One more observation should be shown here - the harmonic and Gauss waves are quite different as compared with the Whittaker wave, because the first two do not change the maximal value of amplitude whereas the Whittaker wave increases this value.

5. Solitary Wave with the Non-symmetric Initial Profile in the Form of Macdonald Function

The initial profile of Macdonald wave is nonsymmetric, has not a hump and is shown in Figure 3. Besides that, the wave is already not the plane one and is related to the elastic cylindrical radial waves of displacement [5, 7, 9, 11]. It is described by the nonlinear wave equation (8).

The classical linear solution of (8) has a form [1, 2, 9, 15, 16]

$$u_r^{(1)}(r,t) = u_{ro} H_1^{(1)}(k_L r) e^{i\omega t}, \tag{33}$$

where the Hankel function of the first kind and first order is used and u_{ro} is the amplitude factor

$$u_{ro} = -\frac{p_o k_L}{k_L(\lambda+2\mu) H_0^{(1)}(k_L r_o) - \frac{2\mu}{r_o} H_1^{(1)}(k_L r_o)}. \tag{34}$$

This solution shows that the wave is harmonic only asymptotically by the spatial coordinate. The wave intensity decreases over time due to the properties of the Hankel function $H_1^{(1)}$.

Transition from the harmonic wave to the solitary one introduces new mathematical problem caused by the fact that the describing the solitary wave function $F\left[a(r-vt)\right]$ is not harmonic in the time wave. The corresponding to (8) linear wave equation becomes the form when the cylindrical function of the real argument - the Hankel function $H_\lambda(r)$ - does not already the solution

of this equation. This new equation has a solution in the form of the cylindric cal function of the imaginary argument – the Macdonald function $K_\lambda(r)$.

It is necessary further to take the initial profile in the form of the function $F(\sigma)=K_0(\sigma)$. Apply now method 2 and use the formulas (20) and (21).

Then the approximate representation of the Macdonald wave is as follows: for the first two approximations

$$u_r^{1+2}(r,t)=u_{ro}aK_0(\sigma)-(1/2)a^3(u_{ro})^2c_L\alpha_1 t\left[K_0'(\sigma)\right]^2, \tag{35}$$

for the first three approximations

$$\begin{aligned}u_r^{1+2+3}{}_r(r,t)&=u_{ro}aK_0(\sigma)-(1/2)a^3(u_{ro})^2c_L\alpha_1 t\left[K_0'(\sigma)\right]^2+\\&+(1/8)a^5(u_{ro})^3c_L(\alpha_1)^2t\left[K_0'(\sigma)\right]^3.\end{aligned} \tag{36}$$

Further, the derivative should be rewritten using the known formula

$K_0'(\sigma)=-K_1(\sigma)$ to transform the formulas (35, 36) into the new form

$$u_r^{1+2}(r,t)=u_{ro}K_0\left(m(r-c_Lt)\right)-(1/2)m^4(u_{ro})^2\alpha_1c_Lt\left[K_1\left(m(r-c_Lt)\right)\right]^2 \tag{37}$$

$$\begin{aligned}u_r^{1+2+3}(r,t)&=u_{ro}K_0\left(m(r-c_Lt)\right)-(1/2)m^4(u_{ro})^2\alpha_1c_Lt\left[K_1\left(m(r-c_Lt)\right)\right]^2\\&+(1/8)m^5(u_{ro})^3(\alpha_1)^2c_Lt\left[K_1\left(m(r-c_Lt)\right)\right]^3.\end{aligned} \tag{38}$$

The solutions (37, 38) show two evident features: the Macdonald wave evolves due to a direct dependence of the nonlinear summands on time, the Macdonald wave profile has any humps, it is like the hyperbola and is not evolved into the profile with the humps.

The formulas (37, 38) are used for the numerical simulation of wave evolution. The next three plots are built in coordinates "displacement u_r - distance r" for the cases of the 1+2 and 1+2+3 approximations.

Figures 20 and 21 show stages with the negligible and small effect of nonlinearity on the evolution, correspondingly. The left line corresponds to the

1st approximation, and the right line – to the 1+2 approximation. Figure 17 shows that the distorted profile becomes steeper and shifted to the right side from the initial profile.

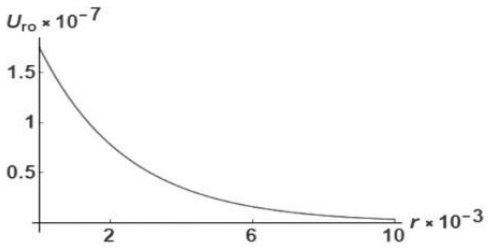

Figure 20. Evolution of Macdonald wave.

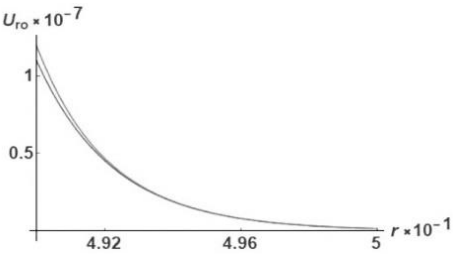

Figure 21. Evolution of Macdonald wave (1+2, stage 1) (1+2, stage 2).

Figure 22 shows the more developed evolution. It saves the displayed in stages 1 and 2 features. The distorted profile becomes still steeper and more shifted to the right side from the initial profile. Figure 23 proposes 3D picture.

So, the shown plots for the Macdonald wave demonstrate that this wave with a profile differing from the previous three wave profiles is distorted in a new way. This way is characterized by some features differing from the basic features: its profile without the hump does not generate humps, a non-symmetry of the profile is saved, the maximal amplitude is increased, and the distorted profile becomes steeper and steeper.

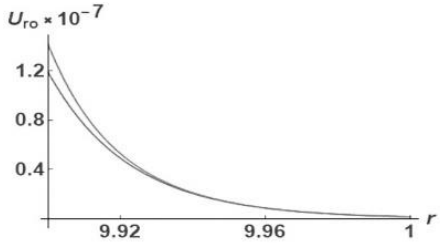

Figure 22. Evolution of Macdonald wave.

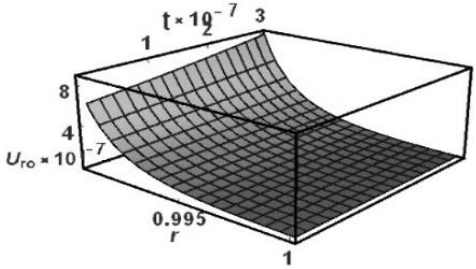

Figure 23. Evolution of Macdonald wave (1+2, stage 3) (1+2, 3D picture).

6. Solitary Wave with the Non-Symmetric Initial Profile in the Form of Friedlander Function

The initial profile of this wave [5, 7, 11] is nonsymmetric, has not a hump and is shown in Figure 4. The linear representation of the Friedlander wave is as follows

$$F(r,t) = u_{ro} e^{-b\left[m\left(r-c_L t\right)\right]/r_{att}} \left(1-\left[m\left(r-c_L t\right)\right]/r_{att}\right), \tag{39}$$

If to understand the representation (39) as the 1st approximation, then the solution in the form of first two approximations follows from the formula (20)

$$u_1(r,t) = u_{ro} e^{-ba\left(r-v_L t\right)/r_{att}} \left[1-a\left(r-v_L t\right)/r_{att}\right] -$$
$$-(1/2)\alpha a^4 v_L t\left(1/r_{att}\right)^2 \left(u_{ro}\right)^2 \left\{1+b\left[1-a\left(r-v_L t\right)/r_{att}\right]\right\}^2 e^{-2ba\left(r-v_L t\right)/r_{att}} \tag{40}$$

This formula describes the change in time (evolution) of the wave profile due to the direct dependence of the nonlinear summand on time. Figures 24-26 show the evolution in the case of the first two approximations and the first three approximations. They show two lines. The left line corresponds to the first two approximations and the right to the first three.

Let us start with some distinction between the Friedlander and four considered in this chapter waves. It consists of mathematical representation of the profiles – the Friedlander wave only is written by the algebraic expression.

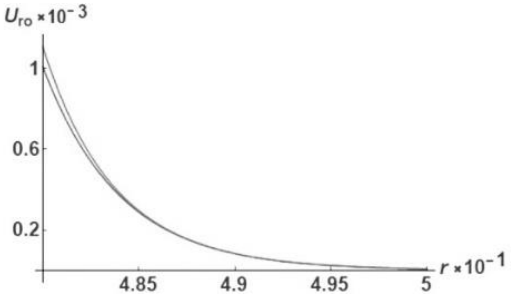

Figure 24. Evolution of Friedlander wave.

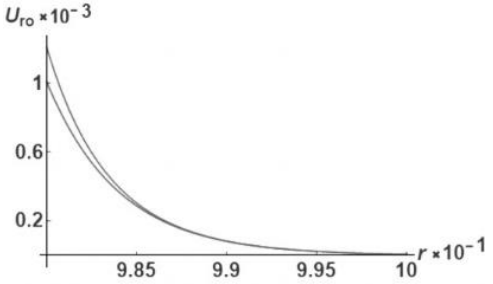

Figure 25. Evolution of Friedlander wave (stage 1) (stage 2).

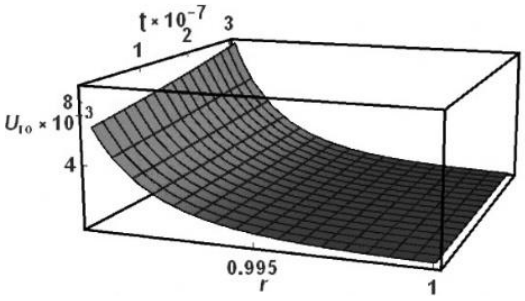

Figure 26. Evolution of Friedlander wave (3D picture).

It seems also to be worth concentrating the attention on the comparison of the evolution of Macdonald and Friedlander waves, which shows that the plots from Figures 20-23 with Figures 23-26 are very similar and the initial profiles of both waves (MacDonald and Friedlander) is that their graphic representation is almost identical.

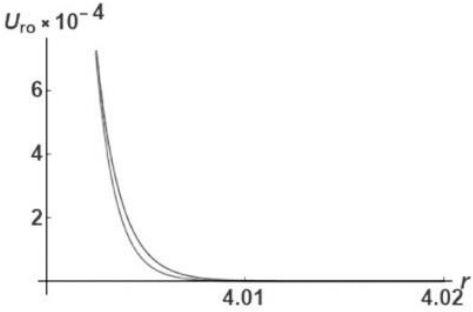

Figure 27. Comparison of evolution of Friedlander and MacDonald waves (stage 1).

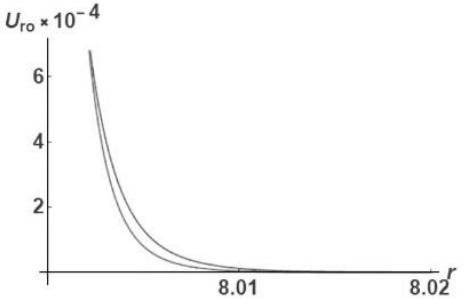

Figure 28. Comparison of evolution of Friedlander and MacDonald waves (stage 2).

Further, the basic formulas (60) (Macdonald wave) and (62) (Friedlander wave) are used in the computer modeling of evolution. The obtained plots show the results of the comparison of the evolution of two waves.

Figures 27 and 28 represent the plots obtained within the framework of the first three approximations (two lines correspond to the studied two waves.

These plots show the nonlinear effect of increasing the convexity, but also they show that the distortion of both profiles is not so significant as for the harmonic, Gauss, and Whittaker profiles.

Conclusions and Comments

This chapter presents an integral fragment of the theory of solitary waves in nonlinearly elastic materials, which considers four types of waves - Gauss, Whittaker, McDonald, and Friedlander waves. The approach used can be extended to other types of solitary waves. The shown scenarios of wave evolu tion in the form of theoretical formulas and computer plots have some obvious and non-obvious distinctions and similarities, which are commented on. Obvious distinctions include the difference in wave types and descrip tions of their initial profiles. Obvious similarities include the fact that all waves are solitary and their profiles are distorted in the process of pro pagation. Non-obvious and unexpected facts consist in the distortion of the symmetric Gauss profile into an asymmetric one, the change in the steepness of the humps in the Gauss and Whittaker waves, the conservation of the size of the bottoms of all types of waves in the process of evolution, the identity of the Macdonald and Friedlander profiles with their very different mathema tical description.

References

[1] Achenbach J. *Wave Propagation in Elastic Solids.* Amsterdam: NorthHolland;1973.

[2] Bedford A., Drumheller D. *Introduction to Elastic Wave Propagation*. Chichester: John Wiley; 1994.

[3] Blekhman I. I., Myshkis A. D., Panovko Y. G. *Applied Mathematics: Subject, Logics, Features of Approaches.* Kiev: Naukova Dumka; 1976. (In Russian).

[4] Cattani C., Rushchitsky J. *Wavelet and Wave Analysis as applied to Materials with Micro and Nanostructure*. Singapore-London: World Scientific; 2007.

[5] Chandra N., Ganpule, S., Kleinschmit, N. N., Feng, R., Holmberg, A. D., Sundaramur thy, A., Selvan, V., Alai, A. 2012. Evolution of blast wave profiles in

simulated air blasts: experiment and computational modeling. *Shock Waves*. 22, P. 403-415.

[6] Engelbrecht J. *Questions about Elastic Waves*. Berlin: Springer; 2015.

[7] Friedlander F. G. 1946. The diffraction of sound pulses. (I. Diffraction by a semi-infinite plate). *Proc. Roy. Soc. Lond. A* 186, P. 322-344.

[8] Gradstein I., Ryzhik I. *Table of Integrals, Series, and Products.* 7th revised ed., eds. Jeffrey A. and Zwillinger D. New York: Academic Press Inc.; 2007.

[9] Harris J. *Linear Elastic Waves*. Cambridge Texts in Applied Mathematics. Cambridge: Cambridge University Press; 2001.

[10] Kamke E. *Differentialgleichungen. Lösungmethoden und Lösungen. (Differential Equations. Methods of Solving and Solutions)*. Wiesbaden: Vieweg+Teubner Verlag. Springer Fachmedien Wiesbaden GmbH; 1977.

[11] Kuriakose M., Skotak, M., Misistia, A., Kahali, S., Sundaramurthy, A., Chandra, N. 2016. Tailoring the Blast Exposure Conditions in the Shock Tube for Generating Pure, Primary Shock Waves: The End Plate Facilitates Elimination of Secondary Loading of the Specimen. *PLoS ONE*, 11(9).

[12] Olde Daalhuis A. B. 2010. *Confluent Hypergeometric Functions.* Chapter 13, P. 383–402. *Whittaker Functions*. 13.14-13.26. In: *Handbook of Mathematical Functions.* Olver, F. W. J., Lozier, D. W., Bousvert, R. F., Clark, C. W. (eds) NIST (National Insti- tute of Standards and Technology) Cambridge: Cambridge University Press.

[13] Press W. H., Flannery, B. P., Teukolsky, S. A., Vetterling, W. T. 1992. *Bessel Functions of Fractional Order, Airy Functions, Spherical Bessel Functions.* (6.7 in *Numerical Recipes in FORTRAN: The Art of Scientific Computing*, 2nd ed. Cambridge: Cambridge University Press, P. 234-245.

[14] Royer D., Dieulesaint E. Elastic Waves in Solids (I,II). *Advanced Texts in Physics.* Berlin: Springer; 2000.

[15] Rushchitsky J. *Theory of Waves in Materials*. Copenhagen: Ventus Publishing ApS; 2012.

[16] Rushchitsky J. Nonlinear Elastic Waves in Materials. Series: *Foundations of Engine ering Mechanics*. Heidelberg: Springer; 2014.

[17] Rushchitsky J. J. *Plane Nonlinear Elastic Waves: Approximate Approaches to Analysis of Evolution*, Chapter in the book "*Understanding Plane Waves*" ed. Cooper W. A. New York: Nova Science Publishers; 2019, 58-80.

[18] Rushchitsky J. *Foundations of Mechanics of Materials.* Copenhagen: Ventus Publish ing ApS; 2021.

[19] Vladimirov V. S. *Equations of the Mathematical Physics*. https://archive.org/details/vladimirov-equations-of-mathematical-physics 2021.

Chapter 3

Systematicity in the Construction of Mass Clumps in Microbiology. Clusters, Domains, Coils, Genes, Genomes, Plasmids, Nucleosomes

Anatoly Zubow[2]
Kristina Zubow[1,*]
and Viktor A. Zubow[1]
[1]Zubow Consulting, NPO, Germany
[2]Group of the Telecommunication Networks Division, TU, Berlin, Germany

Abstract

The atomic nuclei clusters (ANC) - genomes of viruses and bacteria, molecular clusters, domains, coils in the biocenosis of liquid manure were studied. It has been established that the nature of the ANC is the gravitational noise (GN) of the Universe. The activity of genomes depends on their molecular conformations and the nature of their interaction with their surroundings. A characteristic of the masses (m) of genomes is the force constant of their oscillations (**Z**). The phenomenon of a linear dependence of log(**Z**) on log(m) was discovered for hypothetical genome masses without active interaction with their surroundings (via hydrogen bridges, HB). For genomes with small masses, the influence of HB on **Z** is large, but for large masses it is greatly weakened. It was concluded that the masses of genomes in the biocenosis are homologous.

Keywords: systematicity, masses, homologues, biocenosis, gravitational noise

* Corresponding Author's Email: vzubow@googlemail.com.

In: Horizons in World Physics. Volume 312
Editor: Albert Reimer
ISBN: 979-8-89113-513-0

1. Introduction

It is known that atomic nuclei clusters (ANC: molecular clusters, domains, coils, genes, genomes, plasmids, nucleosomes, micelles, chromosomes, etc.) are formed in the gravitational noise (GN) of the Universe [1]. However, we did not find such works for ANC in the community of one biocenosis. GN, according to Chladni's rules (https://ru.wikipedia.org/wiki/Chladni_Figures), allow and prohibit the appearance of certain ANC in them. On the other hand, GN are a superposition of GN of the Universe, local GN typical for a given region of the biosphere on planet Earth, GN arising from a change in the constellation of celestial bodies (planets) closest to us and GN of the community of microorganisms in its biocenosis. Thus, we discovered the influence of the constellation of gas giants (Jupiter and Saturn) on the nature of the interaction of tubulins with their surroundings, Figure 1. It turned out that the GN of the planets affects the quality of hydrogen bridges (HB), through which tubulins communicate informationally with their surroundings [2]. In turn, HBs influence the force constant of oscillations of the ANC (**Z**), and it influences the value of the oscillating mass and the conformation state (dense or loose) of the oscillator itself. All this together changes the biological activity of ANC. Therefore, it was of interest to study these events in the biocenosis, for example, microorganisms.

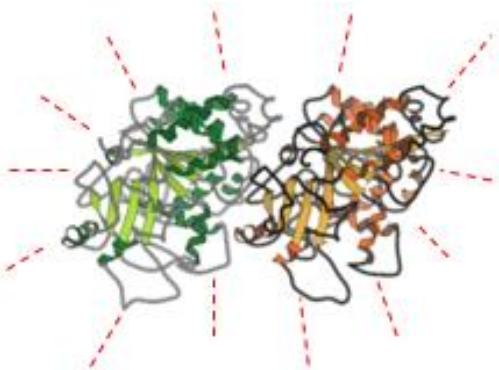

Figure 1. Dimer of α- and β-tubulin (https://ru.wikipedia.org/wiki/Tubulin), molecular mass of 55 kDa and model of its interaction with its surroundings through hydrogen bonds (https://ru.wikipedia. org/wiki/Hydrogen_bond) are shown in dotted lines.

The purpose of this work was to search for the systemic nature of ANC in the biocenosis of microorganisms from the standpoint of their appearance and the influence of the GN of the Universe on them. The main tool for achieving this goal was the analysis of the force constants of ANC oscillations due to the fact that they are indicators of masses and their interaction with the surroundings. Without such interaction with the surroundings, masses are not realized [3].

2. Material and Method

The object of the study was the liquid manure (LM) of cows (free and cowshed regime) of a private farmer in 2023 in the north of Germany (Upper Pomerania). Gravitational mass spectroscopy (GMS) was used as an analysis of ensembles of atomic nuclei clusters (ANC) in the long-range molecular order (LRO) of LM. The GMS sensor was placed in the LM after its homogenization by simple stirring, and the registration of gravitational noise (GN) from ANC oscillations (clusters, domains, coils, genes, genomes, and micellar structures) was performed. GMS spectra were obtained using the first Zubow equation [2]. Positive values of Δf are typical for loose ANC conformations, they reflect the energy fraction of the molecular cluster in the entire ensemble of studied masses, negative $-\Delta f$ values reflect the same, but for dense ANC conformations. Δf is the result of subtracting from the gravitational noise (GN) spectrum of a sample the natural background GN. Samples (in average 10 ml) were maximally protected from external energy physical influences (electromagnetic radiation, mechanical fields and strong sudden pressure drops). Scan time 10 sec. The spectra were calibrated by the masses of water clusters [1…5], nucleosomes with one DNA loop (https://ru.wikipedia.org/wiki/Nucleosome, 233,599 Da), human mitDNA ring (10,653,867 Da, 16.569 bp, https://ru.wikipedia.org/wiki/Mitochondrial_DNA) and mitDNA rings in sugar beet [6] (237,137,757 Da). N is the number of signals in the spectrum (number of ANC kinds), D_c is the part of dense, energy-rich ANCs, M_{GMS} is the average ANC mass. Figure 2 shows the unfolded GMS spectrum of the LN from 08/22/2023 (morning discharge) with indication of the reference ANC used for its calibration.

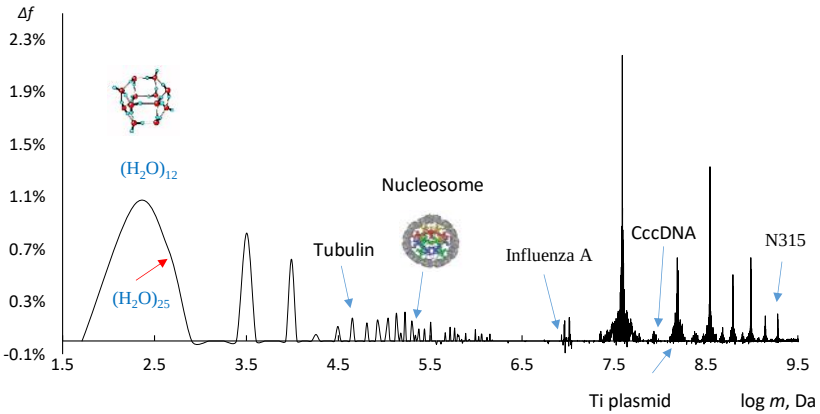

Figure 2. GMS spectrum of the LRO (GN) in the LN on August 22, 2023. Reference masses: base water cluster, 216 Da, [1, 5, 21]; tubulin coils 46.2 kDa [2]; single stranded nucleosome (https://en.wikipedia.org/wiki/Nucleosome), 233,599 Da; *Influenza* virus genome (*influenza A*, https://ru.wikibrief.org/wiki/Influenza_A_virus), 8,737,084 Da; herpes virus genome (cccDNA, https://de.wikipedia.org/wiki/CccDNA), 97,736,000 Da, and the genome of Staphylococcus aureus (N315, https://www.nite.go.jp/en/nbrc/ genome/project/annotation/n315.html), 1,825,778, 567 Da.

3. Analysis and Discussion

Table 1 presents the main characteristics of genomes (literature data) and their experimentally found oscillation force constants using the first Zubow equation [1].

As can be seen from this Table, the deviations of the experimental values of **Z*** from the values of this parameter within the framework of the homologous mass series model are, in general, not significant (log **Z*** = 11.18 ± 0.01). However, for some ANCs, the **Z** values differ markedly from these values for the other genomes. We attribute these differences to the different interactions of ANC with its surroundings. This conformation, in the model of mass homologues, has an unaccounted, pronounced and directed neutrino halo [22], through which the genome interacts with its surroundings and harmonizes its oscillations in the field of biocenosis pendulums. The same can be said for Ti-plasmid, cccDNA, *Influenza* A, NC1 and tubulins. That is, in addition to interacting with their surroundings through hydrogen bonds, ANCs use their neutrino halo for this. From this follows the understanding that in the taxon *E.coli* the ensemble of genomes oscillates like a single pendulum only

because the interaction of the genome with the surroundings, through the HB, is compensated by its other interaction - through the neutrino halo. Thus, the taxon of *E. coli* genomes has its own individual bio field. Let us recall that the neutrino halo around the baryon masses is the second mass of the body, manifested in its inertial properties [22].

Figure 3 shows the curve of the dependence of **Z*** on the masses of ANC in the LM biocenosis.

The series of ANC (Figure 3), within the framework of the large-scale harmony of the Universe, based on the principles of similarity [19], can be considered homological, formed under the influence of common GN. This means that the curve in this Figure hides the homology, distorted by the dynamics of the influence of different fields on the degree of involvement of the ANC in interactions with its surroundings. From the Figure you can also notice that the points for large ANCs 1, 2, 3, 4 and 5 lie on the same straight line, here the influence of HB on their force oscillation constant is small, and for small ANCs, on the contrary, it is very large (points 6...12). It is reasonable to believe that the influence of HB on light masses is stronger than on heavy ones.

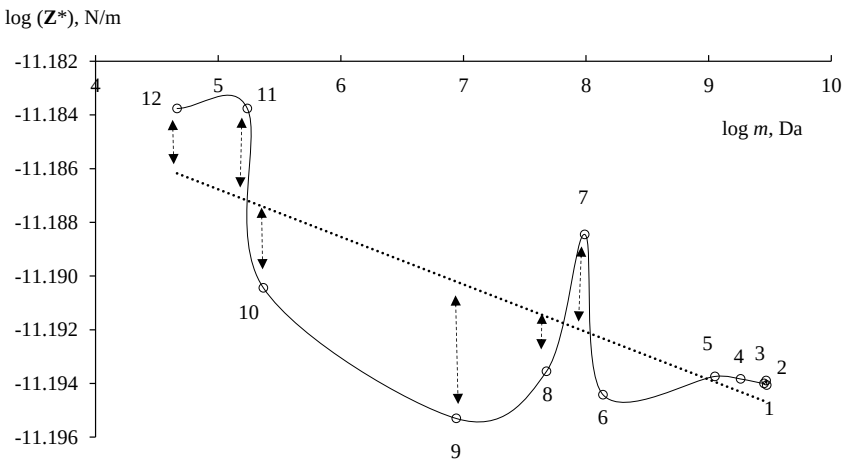

Figure 3. Curve of the current values of force constant oscillations of the ANC **Z*** for some masses of the studied biocenosis (Table 1). 1 – *E.coli* genome, 2 – *Salmonella* genome, 3 – *Mycobacterium tuberculosis* genome, 4 – *Staphylococcus aureus* N315 genome, 5 – *Brucella spp.* genome, 6 – *Agrobacterium tumefaciens* Ti-plasmid, 7 – HSV virus genome (cccDNA), 8 – *Cl. tetani* genome, 9 – *Influenza A* virus genome, 10 – nucleosome, 11 – NC1 domain, 12 – tubulin.

Table 1. Basic characteristics (*m* and Z) of ANC in the LM biocenosis. Z* - experimental values, Z - homology smoothed values

ANC	***m*, Da**	**log *m*, Da**	**Z*, N/m**	**log Z*, N/m**	**logZ, N/m**	**(log Z*-log Z)/log Z**
Tubulin, [7]	46,184	4.664	6.5500E-12	-11.1838	-11.18980	-0.054%
NC1, [8]	172,715	5.237	6.5500E-12	-11.1838	-11.19028	-0.058%
Nucleosome, [9]	233,599	5.356	6.45E-12	-11.1904	-11.19044	0.000%
Influenza, A, [10]	8,737,084	6.941	6.3782E-12	-11.1953	-11.19190	0.030%
Cl. Tetany, [11]	47,634,726	7.678	6.4040E-12	-11.1935	-11.19250	0.009%
cccDNA, [12]	97,736,000	7.990	6.4796E-12	-11.1885	-11.19280	-0.039%
Ti-plasmid, [13]	137,751,824	8.139	6.3911E-12	-11.1944	-11.19290	0.014%
Brucellosis, [14]	1,127,179,000	9.052	6.4012E-12	-11.1937	-11.19374	0.000%
Staph.aur. N315, [15]	1,825,778,567	9.261	6.3998E-12	-11.1938	-11.19383	0.000%
Myc. Tuberculosis, [16]	2,836,613,147	9.453	6.3974E-12	-11.1940	-11.19400	0.000%
Salmonella, [17]	2,941,619,548	9.469	6.3990E-12	-11.1939	-11.19405	-0.001%
E-coli, [18]	2,983,311,025	9.475	6.3965E-12	-11.1941	-11.19407	0.000%

Harmonization of the model (Figure 4), by taking the direction of points 1, 2, 3, 4 and 5 as a basic reference point, allows us to obtain a straight line on which the remaining points lie satisfactorily. In this case, the selection of **Z** values occurs in the second decimal place (Figure 3). Thus, for tubulins, mass values in the literature are given with a large scatter, from 50 to 55 kDa, and as we established in [2], this is the result of differences in GN, leading to changes in the internal and external interactions of macromolecules with their surroundings, through strong HBs. As a result, the chromatograms become wider and it is difficult for the authors to determine the actual masses of tubulins. Different interactions with the surroundings lead to different **Z** values. Figure 4 shows a straight line that is described by the linear equation:

$$\log \mathbf{Z} = -0.0009 \cdot \log m - 11.186.$$

According to this equation, as the mass approaches zero, the **Z** values approach 6.51628E-12 N/m. However, there are no zero masses in the biocenosis. The minimum value belongs to the basic water cluster with the minimum structural energy $(H_2O)_{11}$, i.e., the most stable mass [20]. For the water cluster closest to it (also basic, [21]) of 12 molecules, the **Z** value was already 6.4040E-12 N/m.

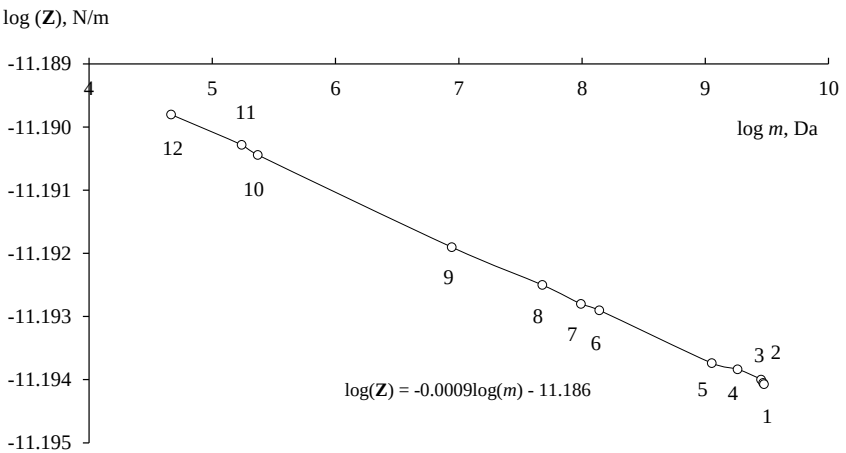

Figure 4. Model. For the force constants of ANC oscillations abridged to a single homological series, see Table 1. Shown here are the values of masses that interact with their surroundings only by fields, i.e., excluding HB.

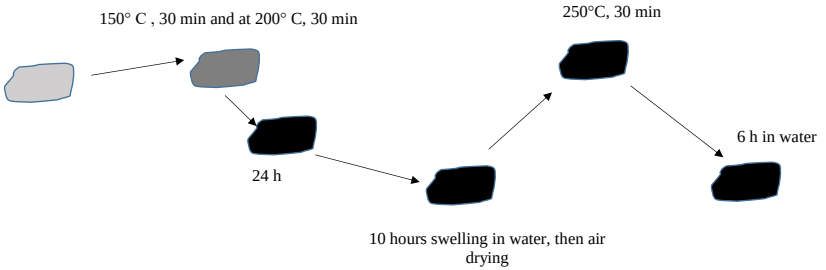

Figure 5. Digraph and routes of procedures with a LM test.

Table 2. The part of dense ANCs (D_c) in the ensemble of oscillators in the range from 200 to 3.6 billion Da, their molecular masses, and their energy parts (Δy) in the ensemble of physical pendulums

		Tubulin	***Influence* A**	**cccDNA**	***Cl. Tetani***
Probe	**D_c**	**46,184[#]**	**8,737,084**	**97,736,000**	**47,634,726**
Start, 12.10.2023, 1 h later	17%	0.10%	0%	0%	0.0478%
After 200°C, 20 min (**A**)	50%	0%	0%	0%	-0.1375%
Probe **A**, again	46%	0%	0%	-0.077%	0.1170%
Probe **A,** 10 h in water	26%	0%	0%	0%	0.0647%
Probe **A,** 250°C, 30 min (**B**), air drying	40%	-0.09%	-0.066%	0%	-0.0749%
B, 6 h in water, air drying	40%	0.15%	0%	0%	0.1202%

So, in a microbiological biocenosis there is a homological series of ANCs that form its bio field, consisting of a field of harmonic pendulums. This bio field should stabilize and protect the biocenosis from external destructive influences, for example, high temperatures.

Figure 5 shows a digraph with routes of operations performed to understand the impact of high temperatures on the biocenosis in LM.

Tables 2...4 present the values of the energy shares of the studied ANCs in the biocenosis when exposed to high temperatures.

As can be seen from Table 2, heating the sample up to 150°C leads to a doubling and even tripling of the proportions of dense energy-rich ANCs. This fact should be understood as the absorption of thermal energy by the ANC ensemble, but in the form of the potential energy of all actors of the ensemble of masses in the range from 200 to 3.6 billion Da. In this case, the average mass of the ANC almost doubles (not indicated in the table). The biocenosis as of October 12, 2023, according to the activity of tubulins in loose conformations, is alive. There are no signals from viral genomes. The genome

of *Cl.tetani* is in a loose active form, the bacterium is dangerous. The situation changes radically when the sample is heated to 200°C for 20 minutes. After this procedure, the signals from oscillating coils of tubulins and viral genomes disappeared. The *Cl.tetani* genome is converted into a dense, inactive form. When re-analyzing the sample (**A**), a day later, a signal from the genome of the HSV virus (cccDNA) appeared in the form of a dense coil of HSV (Δf = -0.077%), and the genome of *Cl.tetani* acquired a loose form (Δf = 0.117%). These events should be understood as the denaturation of the protein coil (tubulin) at 200°C and the disappearance of its signal in the GMS spectrum, like a spherical oscillator. In the *Cl.tetani* genome, its interaction with its surroundings (hydrogen bridges) has been disrupted. Internal genomic interactions began to dominate in it (Δf = -0.1375%). The appearance of the HSV genome signal was unexpected. This dense ball of DNA could only form as a result of the decay of a larger genome in the biocenosis [23], Figure 6.

That is, the biocenosis, even under such harsh conditions, tries to maintain consistency. Further heating and hydration procedures also indicate attempts to return the ensemble of oscillators to their original thermodynamic state. It is carried out by restructuring the energy content of all actors in the ensemble. However, this is a different level of quality. It is not possible to return strands of DNA into rings. Therefore, the new ANC ensemble will be partially represented by masses of genes - phantoms. These are simple strands of DNA.

Tubulin proteins behave somewhat differently. Heating them to 250°C and then saturating them with water does not immediately transform the denatured forms of the protein into dense ones and then into loose, hydrated coils with positive Δf values.

So, the systemic nature of ANC in a biocenosis is an integral characteristic of the thermodynamic stability of the ensemble of oscillator masses as a whole. Consequently, the ensemble of oscillators, as a kind of single creation, strives for a minimum of potential energy. Therefore, this unified formation must have consistency (order) within itself.

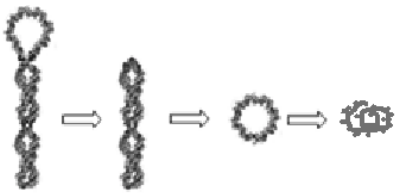

Figure 6. Scheme of the decay of a large ANC (for example, the *Salmonella* genome), [23].

Table 3. Some bacterial genomes, their molecular masses (in Daltons) and energy fractions (Δy) in the ensemble of oscillators in the mass range from 200 to 3.6 billion Daltons

	E-coli	***Salmonella***	**N315**	***Tuberculosis***	**S2, *B. abortus*, I**	**S2, *B. suis*, I**
Date/ANC mass	**2,983,311,025**	**2,941,619,548**	**1,825,778,567**	**2,836,613,147**	**2,053,099,000**	**2,289,723,000**
Start, 12.10.2023, 1 h later	-0.00258%	0.00577%	-0.00908%	0.00727%	-0.0030%	0.0006%
After 200°C, 20 min (**A**)	0.0004%	-0.01402%	0.0442%	-0.00701%	0%	0%
Probe **A**, again	-0.00189%	-0.00229%	0.01640%	0.00176%	0.00244%	0%
Probe **A**, 10 h in water	-0.02240%	-0.00510%	0.00723%	0.00912%	0%	0%
Probe **A**, 250°C, 30 min (**B**), air drying	0.00847%	0.01186%	-0.01987%	0.02221%	0%	0%
B, 6 h in water, air drying	-0.00272%	0.02312%	-0.01739%	0.00833%	0%	0%

Attempts to protect systematicity from thermal destruction of the ANC ensemble can be seen in the genomes of bacteria in the biocenosis, Table 3. This Table presents the signals of large genomes and their responses to thermal effects. Here you can also notice the resistance of the ensemble of oscillators, as a single object, to the destruction of its systematicity by high temperatures. There is a cooperative effect of protecting the ensemble of masses, its internal order (LRO), through resonance from the outside and the systematicity of the LRO from the inside. ANC signals are preserved, but their shape and quality change.

From the data in Tables 2 and 3, the role of water in the formation of the systemic stability of the ensemble of masses in the LM biocenosis is clear. Water here acts as a plasticizer for rigidly chained DNA macromolecules. Let's trace it influence on the behavior of the anhydrides of the Ti-plasmid of *Agrobacterium tumefaciens* R *radiobacter* strain R58, Table 4. In the original sample of LM there are no signals of the Ti-plasmid, but there are signals of its anhydrides with different involvement of water molecules in the genome.

This means that there is no free water in the biocenosis, not even in the original LM; it is all involved in small water cluster forms, and its individual molecules are associated with the components of LM in the form of adsorption, solvate or even inclusion water. The Ti-plasmid itself is a weak water sorbent and is not able to retain it, therefore it is represented by anhydrides. It can be assumed that the systematic nature of the ensemble of masses, in this case, is also not violated. The place of the Ti plasmid in the ensemble is occupied by its anhydrides. Note that heating the biocenosis to 200°C destroys the ring structure of the plasmid and its anhydrides. Subsequent exposure to water for 10 hours reveals coil signals only from the Ti plasmid in loose, hydrated forms in the spectrum. However, heating to 250°C dehydrates this coil only to a coil of anhydride **C**, in a collapsed conformation. Further keeping the sample in water for 6 hours leads to the appearance of signals of all anhydrides in loose forms. But these are no longer the same anhydrides that were in the original biocenosis. These are hydrated coils - analogues of the masses of the original oscillators.

Thus, in this case, too, there is systematicity in the preservation of the ensemble of masses; whether the genome is “alive” or “dead” does not play a role here. What is important is only the preservation of the ensemble of masses as a single unit, as a new form of existence of molecular matter.

Table 4. Ti-plasmid (*Agrobacterium tumefaciens R radiobacter* strain R58) and its anhydrides (**A**, **B**, **C**, **D** and **E**) during heating of the LM, as physical oscillators and their energy parts (Δf) in the ensemble of pendulums with a mass range from 200 to 3.6 billion Daltons

	Ti-plasmid	**Ti-plasmid and its anhydrides**			
Masses (*m*), Da	**137,751,824**	**A, 129,574,300**	**B, 130,378,654**	**C, 130,214,734**	**D, 129,410,887**
Probe		**-2.1(H_2O)/bp**	**-1.9(H_2O)/bp**	**-2(H_2O)/bp**	**-2.16(H_2O)/bp**
Start, 12.10.2023, 1 h later	0%	-0.1186%	0%	-0.0238%	-0.0451%
After 200°C, 20 min (**A**)	0%	0%	0%	0%	0%
Probe **A**, again	0%	0%	0%	0%	0%
Probe **A,** 10 h in water	0.0512%	0%	0%	0%	0%
Probe **A,** 250°C, 30 min (**B**), air drying	0%	0%	0%	-0.0037%	0%
B, 6 h in water, air drying	0%	0.0461%	0.0734%	0.1000%	0.0546%

Conclusion

Microbiocenosis in LM is an element of the ensemble of all biocenoses in the biosphere of planet Earth.

The ANC ensemble in the microbiocenosis of LM is a new form of molecular matter.

The systematicity of the ANC in the microbiocenosis of a LM is a homological series of masses formed by the gravitational noise of the Universe, mainly.

The gravitational noise of the Universe stabilizes the ANC ensemble in a biocenosis from the outside, and the internal systematicity of the ANC in the LRO of the biocenosis from the inside.

The systematic nature of ANC in a microbiocenosis is expressed in the linear dependence of the masses on the force constant of their oscillations.

The main characteristic of the homology of microbiocenosis is the force constant of oscillations equal to log **Z*** = 11.18 ± 0.01, N/m.

The homology of masses in microbiocenosis is stable when genomes are exposed to high temperatures, up to 250°C.

The ensemble of genomes is sensitive to changes in local gravitational noise.

In the ensemble of ANC microbiocenosis, restructuring processes occur to optimize the energy content of each of its homologues.

Sponsoring. To continue work in this direction, we are looking for sponsors. Write to us.

References

[1] Zubow, K., Zubow, A. V., and Zubow, V. A. (2014). The Way to the ETIs. Applied gravitational mass spectroscopy. Nova Sci. Publ. NY, https://www.novapublishers.com/catalog/product_info.php?products_id=42668&osCsid=5bd85d42dc273360fd48126de7be9daf.

[2] Zubow, K., Zubow, A., and Zubow, V. (2023). The mechanism of influence of celestial bodies on activity and Interaction of domains (α- and β-tubulins) with their surroundings. *Advances in Biology*. Ed**.** Charles D. Grant. Nova Publisher Inc. NY., vol. 5, pp…, in print

[3] Zubow, K., Zubow, A., and Zubow, V. (2023). New constant Q = 8.97082E-10, $m^2/s^2 \cdot kg^3$. In $E = Q \cdot m^4$. Vector nature of masses. *Horizons in World Physics*. Ed.

Albert Reimer. NY, vol. 311, pp. 189…198. *Horizons in World Physics*. Volume 311 – Nova Science Publishers (novapublishers.com).

[4] Zubow, K., Zubow, A. V., and Zubow, V. A. (2010). The Phenomenon of Proton Dissolving in Vacuum and of Proton Condensation from Vacuum. Two Forms of Protons, Structure of Nuclei, Electrons and Atoms. *J. of modern physics*, vol. 1, no. 1, pp. 175-184. https://www.researchgate.net/publication/228928173_The_Phenomenon_of_Proton_Dissolving_in_Vacuum_and_of_Proton_Condensation_from_Vacuum_Two_Forms_of_Protons_Structure_of_Nuclei_Electrons_and_Atoms.

[5] Chaplin, M. F. (2013). What is liquid water, *Science in Society*, Iss. 58, 41-45.

[6] Zubow, K., Zubow, A., and Zubow, V. A. (2023). How Nuclear DNA Affects Mitochondrial DNA Horizons in World Physics. Ed. Albert Reimer. Nova Publisher Inc. Ny., volume 308, pp. 185-196 (in Book, 140-156). *Horizons in World Physics*., Volume 308 – Nova Science Publishers (novapublishers.com).

[7] https://ru.wikipedia.org/wiki/Tubulin.

[8] Zubow, K., Zubow, A., and Zubow, V. A. (2016). Phenomenal properties of the domain ensembles in proteins. *Biochemistry & Molecular Biology Journal*. USA., vol. 2, no., 1, pp. 1-10. http://biochem-molbio.imedpub.com/phenomenal-properties-of-the-domain-ensembles-in-proteins.pdf

[9] https://ru.wikipedia.org/wiki/Nucleosome.

[10] https://ru.wikibrief.org/wiki/Influenza_A_virus.

[11] Litusov, N. V. (2013). TETANUS CAUSE Illustrated textbook. State budgetary educational institution of higher professional education “Ural State Medical Academy” of the Ministry of Health of the Russian Federation Department of Microbiology, Virology and Immunology. Ekaterinburg.

[12] https://de.wikipedia.org/wiki/CccDNA.

[13] https://en.wikipedia.org/wiki/Ti_plasmid.

[14] https://ru.wikipedia.org/wiki/Brucella. BRUCELLOSIS. CURRENT STATE OF THE PROBLEM. Edited by Academician of the Russian Academy of Sciences G.G. Onishchenko, corresponding member. RAS A.N. Kulichenko. – Stavropol: Guberniya LLC, 2019. – 336 p.

[15] https://www.nite.go.jp/en/nbrc/genome/project/annotation/n315.html.

[16] https://www.chem.msu.ru/rus/journals/chemlife/genom.html.

[17] https://science-education.ru/ru/article/view?id=16650, https://de.wikipedia.org/wiki/Salmonellen, https://translated.turbopages.org/proxy_u/en-ru.ru.26499e26-64f0e201-d9f35666-74722d776562/https/environmentalmicrobiome.biomedcentral.com/articles/10.1186/s40793-015-0015-z.

[18] Litusov, N. V. (2016). Escherichia Illustrated textbook. State budgetary educational institution of higher professional education “Ural State Medical University” of the Ministry of Health of the Russian Federation Department of Microbiology, Virology and Immunology. Ekaterinburg, pp. 1-36. https://www.wikidoc.org/index.php/Escherichia_coli.

[19] Sukhonos, S. I. (2002). Large-scale harmony of the Universe. M. “New Center”. http://suhonos.ru/rsc/files/masshtabgarmony.pdf.

[20] Satya Bulusu, Soohaeng Yoo, Edo Aprà, Sotiris Xantheas, and Xiao Cheng Zeng Lowest-Energy Structures of Water Clusters $(H_2O)_{11}$ and $(H_2O)_{13}$. J. Phys. Chem., A 2006, 110, 42, 11781–11784. https://doi.org/10.1021/jp0655726.

[21] Bogdanov, E. V. (2000). Manturova G.M. Equimolecular model of water. *Biomedical electronics*., No. 7, pp. 19-28.

[22] Zubow, A., Zubow, K., and Zubow, V. A. (2014). Phenomenon of Axions' and Neutrinos' Clouds around Objects. Nature of inertia. Editor A. Reimer. *Horizons in World Physics*. NY., vol. 282, pp. 53-70. https://www.novapublishers.com/catalog/product_info.php?products_id=50340&osCsid=994455a7afd05deb707594aaf444ed06.
International Journal of Condensed Matter, Advanced Materials, and Superconductivity Research, 2014, volume 13 Issue 1, pp. https://www.novapublishers.com/catalog/product_info.php?products_id=53555&osCsid=9dc3348f7b2274186a8949c752b7f142.

[23] Zubow, K., Zubow, A., and Zubow, V. (2023). Dynamics of aging of liquid manure biocenosis. *Advances in Biology*. Ed. Charles D. Grant. Nova Publisher Inc. NY., in print.

Chapter 4

Complex-Valued Physics: Plasma Waves

V. V. Lyahov*
and V. M. Neshchadim
Institute of Ionosphere of the Republic of Kazakhstan,
Kamenskoye Plateau, Almaty, Kazakhstan

Abstract

Now in physics, the paradigm dominates: real numbers correspond to physical quantities. However, modern physics has accumulated many examples of the opposite kind when complex numbers are used as objects of physical reality. In plasma physics, the frequency $\omega \to \omega + i\delta$ is introduced, while in quantum electrodynamics, in the theory of perturbations, the mass $m \to m + i\varepsilon$ is introduced. Thus, the time has perhaps come to unambiguously consider complex values in physics rather than real numbers exclusively. In this study, the traditional problem of longitudinal waves in collisionless plasma is solved. Our findings show that longitudinal plasma waves, if all world values are complex, have properties that differ from those which we are used to. It is possible that the imaginary part, being unobservable, at the same time must be inherent in a physical quantity, being something of a hidden parameter, and is manifested only indirectly, forcing the system to move along one or another path.

Keywords: field of complex numbers, collisionless plasma, Vlasov equation, current layer, numerical simulation, Earth magnetosphere

* Corresponding Author's Email: v_lyahov@rambler.ru.

In: Horizons in World Physics. Volume 312
Editor: Albert Reimer
ISBN: 979-8-89113-513-0

1. Introduction

Physics is now in the stage of semi-recognition of complex numbers. On the one hand, physics, using a mathematical apparatus, manipulates with complex numbers. On the other hand, "common sense" recommends connecting all observed values exclusively with real numbers. But in two cases, complex quantities have already been introduced into physics as actually existing. In plasma physics, the frequency $\omega \to \omega + i\delta$ is introduced, in quantum electrodynamics, in the theory of perturbations – mass $m \to m - i\varepsilon$ is introduced. Perhaps the time has come to unambiguously put in line with all values complex, not real numbers. In this aspect, the traditional problem of longitudinal waves in collisionless plasma is solved. The tensor of dielectric permeability has been calculated, and the corresponding dispersion equation has been solved.

2. History of the Problem

In 1946, the work of L. D. Landau [1] was published as a reaction to the research begun by A. A. Vlasov [2]. Vlasov, studying plasma oscillations based on the kinetic equation with a self-consistent electromagnetic field introduced by him, faced with the following problem: when studying the dispersion equation for longitudinal waves in a collisionless plasma, an improper integral arose. The velocity integral was determined along the real axis and was twice improper - with infinite limits and a pole feature of the integrand function.

The dispersion equation obtained in [2] has the form:

$$\frac{4\pi \cdot e^2}{k} \int_{-\infty}^{+\infty} \frac{V_x \dfrac{\partial f^o}{\partial \varepsilon}}{(kV_x - \omega)} dV_x dV_y dV_z = 1, \tag{1}$$

the stationary state is described by the Maxwell distribution function.

Vlasov found an approximate solution to the dispersion equation using the decomposition of the submissive function into a series by the powers of a small quantity $\frac{V_x}{u_\phi} = \frac{V_x}{\omega / k}$. This value is small because the selected Maxwell

distribution function quickly decreases with increasing particle velocity, and at the phase velocity $V_x = \omega / k$ is already quite small. The solution thus obtained is limited by the area of small particles velocities and does not consider the contribution of large velocities from the tail of the Maxwell distribution. Vlasov, in essence, ignored the existing divergence of the integral (1) at $\omega = kV_x$.

Landau proposed to take an improper integral (1) by the ultimate bypass of a special point $V_x = \omega / k$. This bypass, of course, is made in a complex plane. The question arises, how to bypass a special point - from above or below? The adiabatic hypothesis comes to the rescue, which requires that the perturbation of the distribution function $\delta f(\bar{P}, \bar{r}, t)$ disappear at $t \to -\infty$. In the accepted time dependency $\delta f \sim \exp(-i\omega \cdot t)$, such a disappearance means the presence of at least a small positive imaginary part of the frequency $\omega \to \omega + i\delta$. In this case, the pole of the submissive function (1) no longer lies on the actual axis along which the integration is carried out but is shifted to the upper half-plane. This gives the rule of bypassing the pole: it must be bypassed from below (the rule of bypassing Landau).

Once again about the main problem of the situation considered: it was necessary to take correctly the improper integral (1). To do this, it was necessary to leave the actual axis and go to the complex plane or, which is also the case, to ascribe a small imaginary part to the frequency. This led to the conclusion that there was a physical possibility of collisionless attenuation of electromagnetic waves in the plasma (Landau attenuation).

3. At the Stage of Semi-Recognition of Complex Numbers

To date, complex numbers have fully entered the use of mathematics. Physics is now in the stage of semi-recognition of complex numbers. On the one hand, physics, using the mathematical apparatus, manipulates with complex numbers. On the other hand, common sense recommends connecting all observed values exclusively with real numbers. Complex calculation is given only an auxiliary, formal-mathematical character. The course of the reasoning of modern physics is this: “We live in the real world, so all quantities should be described by real numbers.” It seems that this statement is completely natural and does not require any additional justification. This statement is an

example of a paradigm and is accepted by natural scientists in fact on faith. They say that the whole development of science confirms this thesis.

But we can give opposite examples. In the theory of relativity, imaginary time is introduced $\tau = i \cdot c \cdot t$. And only in this form, together with three spatial coordinates, does it form a four-dimensional space-time. The fourth axis of space-time is an imaginary quantity. In the theory of relativity, on the one hand, they always emphasize the conditional nature of imaginary time. But, on the other hand, they also always notice that for the first time a deeply essential connection of space and time was discovered.

About the main object of quantum mechanics - a complex-valued wave function, it is said that it itself does not have a physical meaning, but its square has it. This conclusion is already worried. But moreover, it turns out that in the quantum-mechanical principle of superposition it is precisely the wave function that does not have physical meaning, and not its square, possessing this meaning.

In relativistic quantum mechanics, mathematical considerations about the need for the completeness of the wave functions system forced to introduce an idea of the levels of negative energy. But the energy of the resting particle can be negative only if you attribute either the mass - negative or the speed of light - imaginary values. The physical interpretation of this result of the formal mathematical apparatus is given by Dirac. He postulated the fundamental non -observance of states with negative energy because all levels with negative energy are occupied by particles, and therefore no transitions between two levels are impossible (the state of vacuum). But, postulating at first the fundamental unnecessary of such states, physics then indicate the interaction of a hydrogen atom with a vacuum (Lamb shift). So, the background of filled states with negative energy-the vacuum still manifests itself in reality?

When solving a differential equation, one must first solve the so-called characteristic equation. This equation is algebraic, and its solution is sought in the field of complex numbers. In the theory of oscillations, for example, such quantities as frequency and wave vector become complex-valued, and hence the inverse values of them - the period of oscillations and the wavelength become complex.

And finally, a long-known one. The physicist, solving an algebraic equation with real coefficients, often receives complex roots. How to interpret them? Solutions are selected according to the so -called physical meaning. By virtue of some a priori knowledge, a strict mathematical solution is subjected to violence. Paths of physics and mathematics diverge. But should they diverge?

In the absence of general rules, manipulation with complex values of physical quantities resembles art more than science; When necessary - they are introduced into consideration, when it is not necessary - they are taken out of the game. Perhaps for physics it is time to unequivocally put in line with all values complex, not real numbers? Some aspects of this problem are discussed to work [3, 4].

The development of natural science indicates that the objects that existed earlier only as mathematical, "ideal" concepts were filled over time with real content and accepted into the family of physical objects. Examples are negative and irrational numbers. Now a description of the physical quantities is allowed both negative and irrational numbers.

Historically, there was a sequential expansion of the fields of numbers. The field of natural numbers was expanded to the field of integers, then to the field of rational numbers, then to the field of real numbers and, finally, to the field of complex numbers. At the same time, the complex field has a fundamental feature that distinguishes it: it is algebraically closed. The restriction of the physical values of only the field of real numbers seems logically unsatisfactory, since often mathematical operations lead them out of the field of initial definition.

Here, a radical question arises of the correlation of the concepts of quantity and number. It seems natural to accept the following definition, expressed, for example, by A. N. Kolmogorov [5]: "The number is the ratio of two quantities." With this definition, the very fact of the existence of complex numbers immediately entails the conclusion on the existence of complex quantities.

4. Output of the Dielectric Constant Tensor on the Field of Complex Numbers

Let's solve the problem of longitudinal waves in a collisionless plasma, considering all quantities to be complex-valued. Remember that the imaginary addition to the frequency $\omega \to \omega + i\delta$ has already been introduced in plasma physics, as discussed above. And in quantum electrodynamics, in the theory of perturbations, complex mass $m \to m - i\varepsilon$ is introduced.

The tensor of the dielectric permeability of a collisionless homogeneous isotropic plasma, calculated based on the solution of the Vlasov equation, is well known, see, for example, [6], p. 74:

$$\varepsilon^{l}(\omega,k)=1+\sum_{\alpha}\frac{e_{\alpha}^{2}}{\omega k^{2}\varepsilon_{0}}\int d\vec{p}\,\frac{(\vec{k}\vec{v})^{2}}{\omega-\vec{k}\vec{v}}\frac{\partial f_{0\alpha}}{\partial\zeta_{\alpha}}, \tag{2}$$

$$\varepsilon^{tr}(\omega,k)=1+\sum_{\alpha}\frac{e_{\alpha}^{2}}{2\omega k^{2}\varepsilon_{0}}\int d\vec{p}\,\frac{[\vec{k}\vec{v}]^{2}}{\omega-\vec{k}\vec{v}}\frac{\partial f_{0\alpha}}{\partial\zeta_{\alpha}}. \tag{3}$$

here $\varepsilon^{l}(\omega,k)$ and $\varepsilon^{tr}(\omega,k)$ - respectively longitudinal and transverse dielectric permeability, $\zeta_{\alpha}(p)$ - the energy of the particle of the variety α. Note that the integrals (2) and (3) coincide with the integral (1) obtained for the first time by Vlasov.

The motion of massive ions, which have a large inertia, can be neglected to a first approximation, and consider plasma only as an electron plasma. Electrons obey Maxwell's distribution

$$f_{0e}(\vec{p})=\frac{N_{e}}{(2\pi m\kappa T_{e})^{3/2}}\exp(-\frac{p^{2}}{2m\kappa T_{e}}),$$

here κ is the Boltzmann constant, T_{e} and m is the temperature and mass of the electrons.

Let us dwell on the consideration of longitudinal waves. After integration with the components of the momentum perpendicular to the wave vector $\vec{k}$, equation (2) takes the form [7], p.87:

$$\varepsilon^{l}(\omega,k)=1+\frac{\omega_{Le}^{2}}{\omega^{2}}\frac{\beta}{\sqrt{2\pi}}\int_{-\infty}^{+\infty}\frac{x^{2}e^{-x^{2}/2}dx}{x-\beta}, \tag{4}$$

where

$$\omega_{Le}=\sqrt{\frac{N_{e}e^{2}}{\varepsilon_{0}m}},\ x=\frac{p_{x}}{\sqrt{m\kappa T_{e}}},\beta=\frac{\omega}{k}\sqrt{\frac{m}{\kappa T_{e}}}. \tag{5}$$

here ω_{Le} is the electron Langmuir frequency.

We believe that all quantities are complex. To do this, in integral (4) we explicitly enter the real and imaginary parts of all quantities, except for the frequency ω and wave number *k*, which can take real or complex values depending on which problem we are solving - the boundary or the initial one.

$$N_e = \mathrm{Re}(N_e) + i\gamma\,\mathrm{Re}(N_e) = \rho_1 e^{i\varphi_1}, \text{где} \rho_1 = \sqrt{[\mathrm{Re}(N_e)]^2 + [\gamma\,\mathrm{Re}(N_e)]^2}; \varphi_1 = arctg(\gamma) \tag{6}$$

Similarly

$$e = \rho_2 e^{i\varphi_2}, \text{где} \rho_2 = \sqrt{[\mathrm{Re}(e)]^2 + [\gamma\,\mathrm{Re}(e)]^2}; \varphi_2 = arctg(\gamma);$$

$$\varepsilon_0 = \rho_3 e^{i\varphi_3}, \text{где} \rho_3 = \sqrt{[\mathrm{Re}(\varepsilon_0)]^2 + [\gamma\,\mathrm{Re}(\varepsilon_0)]^2}; \varphi_3 = arctg(\gamma);$$

$$m = \rho_4 e^{i\varphi_4}, \text{где} \rho_4 = \sqrt{[\mathrm{Re}(m)]^2 + [\gamma\,\mathrm{Re}(m)]^2}; \varphi_4 = arctg(\gamma);$$

$$\kappa = \rho_5 e^{i\varphi_5}, \text{где} \rho_5 = \sqrt{[\mathrm{Re}(\kappa)]^2 + [\gamma\,\mathrm{Re}(\kappa)]^2}; \varphi_5 = arctg(\gamma);$$

$$T_e = \rho_6 e^{i\varphi_6}, \text{где} \rho_6 = \sqrt{[\mathrm{Re}(T_e)]^2 + [\gamma\,\mathrm{Re}(T_e)]^2}; \varphi_6 = arctg(\gamma).$$

From formulas (5) we get

$$\omega_{Le}^2 = R_1 e^{iF_1}, \text{где} R_1 = \frac{\rho_1 \rho_2^2}{\rho_3 \rho_4}; F_1 = \varphi_1 + 2\varphi_2 - \varphi_3 - \varphi_4 \quad ; \tag{7}$$

$$\beta = \frac{\omega}{k} R_2 e^{iF_2}, \text{где} R_2 = \sqrt{\frac{\rho_4}{\rho_5 \rho_6}}; F_2 = \frac{\varphi_4}{2} - \frac{\varphi_5}{2} - \frac{\varphi_6}{2} \quad ; \tag{8}$$

$$x = \xi e^{iF_3}, \text{где} \xi = \frac{P_x}{\sqrt{\rho_4 \rho_5 \rho_6}}; F_3 = -\frac{\varphi_4}{2} - \frac{\varphi_5}{2} - \frac{\varphi_6}{2}; \tag{9}$$

here ξ is a new integration variable.

Substituting the relations (7) – (9) into formula (4), we get the following expression for the longitudinal tensor of the dielectric permeability:

$$\varepsilon^l(\omega,k) = 1 + \frac{1}{\sqrt{2\pi}} \frac{1}{\omega k} (A_1 + iB_1) \int_{-\infty}^{+\infty} d\xi \frac{\xi^2 \exp\{-\frac{\xi^2}{2}[\cos(2F_3) + i\sin(2F_3)]\}}{\xi - z_1} \tag{10}$$

here

$$A = R_2 \cos(F_2 - F_3); B = R_2 \sin(F_2 - F_3), \tag{11}$$

$$A_1 = R_1 R_2 \cos(F_1 + F_2 + 2F_3); B_1 = R_1 R_2 \sin(F_1 + F_2 + 2F_3), \tag{12}$$

$$z_1 = \frac{\omega}{k}(A + iB). \tag{13}$$

The resulting integral (10) has no special points on the actual axis of integration and is easily calculated using deductions:

$$\varepsilon^l(\omega,k) = 1 + i\sqrt{2\pi}\frac{\omega}{k^3}(A_1 + iB_1)(A + iB)^2 \exp[-\frac{\omega^2}{k^2}\frac{A^2 - B^2}{2}\cos(2F_3)] \cdot$$
$$\{\cos[-\frac{\omega^2}{k^2}AB\cos(2F_3)] + i\sin[-\frac{\omega^2}{k^2}AB\cos(2F_3)]\} \cdot$$
$$\exp[\frac{\omega^2}{k^2}AB\sin(2F_3)]\{\cos[-\frac{\omega^2}{k^2}\frac{A^2 - B^2}{2}\sin(2F_3) + i\sin[-\frac{\omega^2}{k^2}\frac{A^2 - B^2}{2}\sin(2F_3)]\} \tag{14}$$

5. About the Electron Branch of Longitudinal Oscillations

After integration according to the method first proposed by L. D. Landau, equation (2) takes the form [6], p. 76:

$$\varepsilon^l(\omega,k)=1+\sum_\alpha \frac{\omega_{L\alpha}^2}{k^2 v_{T\alpha}^2}[1-J_+(\frac{\omega}{kv_{T\alpha}})], \tag{15}$$

here

$$J_+(x)=-i\sqrt{\frac{\pi}{2}}xW(\frac{x}{\sqrt{2}}),$$

and the function *W(x)* is tabulated [8]. The dispersion equation for longitudinal waves is:

$$\varepsilon^l(\omega,k)=0.$$

Using the decomposition of tensor (15) in the asymptotic case of fast waves whose phase velocity is much greater than the thermal velocities of the particles

$$\frac{\omega}{kv_{T\alpha}} \gg 1, \tag{16}$$

and neglecting the contribution of ion terms, you can get the following expression for the dispersion equation:

$$\varepsilon^l(\omega,k)\approx 1-\frac{\omega_{Le}^2}{\omega^2}(1+3\frac{k^2v_{Te}^2}{\omega^2})+i\sqrt{\frac{\pi}{2}}\frac{\omega\omega_{Le}^2}{k^3v_{Te}^3}\exp(-\frac{\omega^2}{2k^2v_{Te}^2})=0. \tag{17}$$

By virtue of condition (16), the imaginary term in this equation is neglected and, by introducing a priori condition $\omega\approx\omega_{Le}$, its simplified solution is obtained (see, for example, [9]):

$$\omega^2 = \omega_{Le}^2(1+3k^2r_{De}^2), \tag{18}$$

here $r_{De} = \sqrt{\frac{\varepsilon_0 T_e}{e^2 N_e}}$ - electron Debye radius. Oscillations with spectrum (18) are an electron branch of longitudinal oscillations.

6. Zero of a Complex Number. Three Methods for Solving the Dispersion Equation

An approximate analytical solution (18) was obtained in the "pre-computer" era. We find a direct solution of equation (17), calculating it numerically in the "MAPLE" package, and then compare it with the numerical solution of equation (14). As parameters, we take the characteristic values of the plasma of interplanetary space:

$$\begin{aligned}
&e = 1.6\cdot 10^{-19}\,Кл;\\
&m = 9.1\cdot 10^{-31}\,кг;\\
&\varepsilon_0 = 8.85\cdot 10^{-12}\,Ф/м;\\
&\kappa = 1.38\cdot 10^{-23}\,Дж/К;\\
&N_e = 10^6\,м^{-3};\\
&T_e = 10^4\,К;
\end{aligned} \tag{19}$$

Calculations are carried out in the system "SI," the dimension of the frequency everywhere is $[\omega] = c^{-1}$, for the wave number $[k] = м^{-1}$. At these values, the electron Langmuir frequency $\omega_{Le} = 5.54\cdot 10^4\,c^{-1}$, the electron Debae radius $r_{De} = 6.91м$.

Equation (17) contains real and imaginary parts. There are three logically equivalent possibilities to zero a complex number $a+ib = \sqrt{a^2+b^2}\,\exp[i\cdot arctg(\frac{b}{a})]$ - to demand, respectively:

$$1)\ a + i\ b=0,\ 2)\ \sqrt{a^2+b^2}=0,\ 3)\ \begin{cases} a=0, \\ b=0. \end{cases} \tag{20}$$

The results of the numerical solution of equation (17) by the first method (20) are presented in Figure 1. The initial problem is investigated: for the real values of the wave number *k* there are corresponding roots $\omega(k)$ find out.

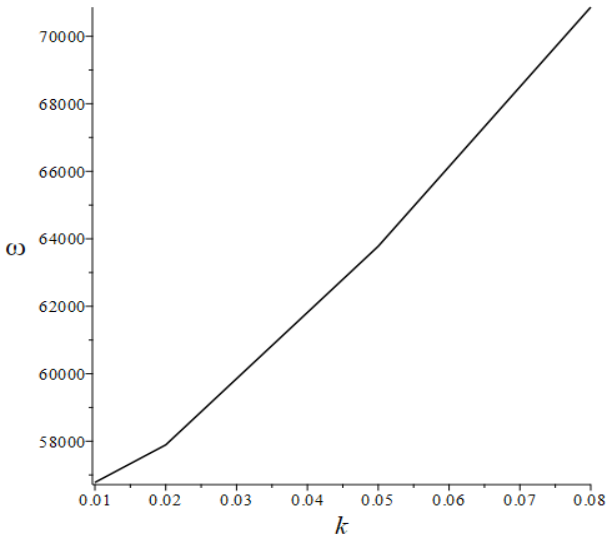

Figure 1. Dispersion curve determined by equation (17).

This curve qualitatively corresponds to the approximate analytical solution (18), begins with the value of the Lengmuir frequency $\omega = \omega_{Le} = 5.54 \cdot 10^4 c^{-1}$, but then grows faster than predicted by the formula (18), and does not form a plateau at the beginning of the pronounced region. It should be noted that this solution had to be sought by equating the zero of the entire expression (17), while the well-known solution (18) was sought by equating zero only its real part. The initial values of the found frequencies do not have imaginary parts, which means that the oscillations in this region of the wavelengths are undamped. At shorter wavelengths, when k > 0.08m-1, the oscillations become fading, with the decrement of attenuation being very small.

The second method (20) does not give solutions.

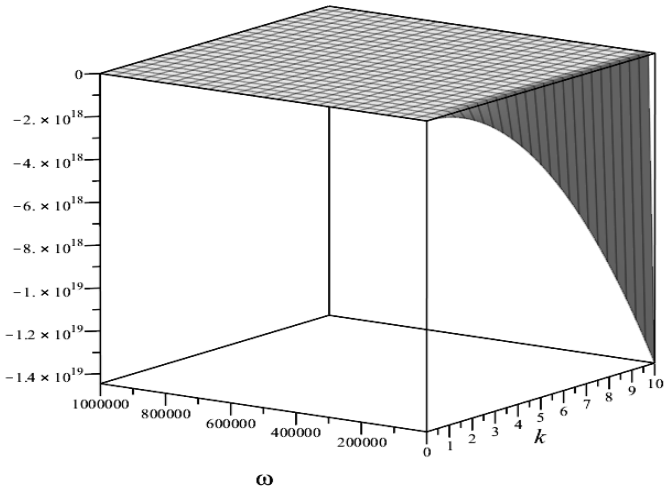

Figure 2. Area of existence of the real part of the tensor (17).

Within the framework of the third method (20), solutions are also absent, since the regions of the real (see Figure 2) and imaginary (see Figure 3) parts of the tensor (17) do not intersect, namely lie in different semi-spaces.

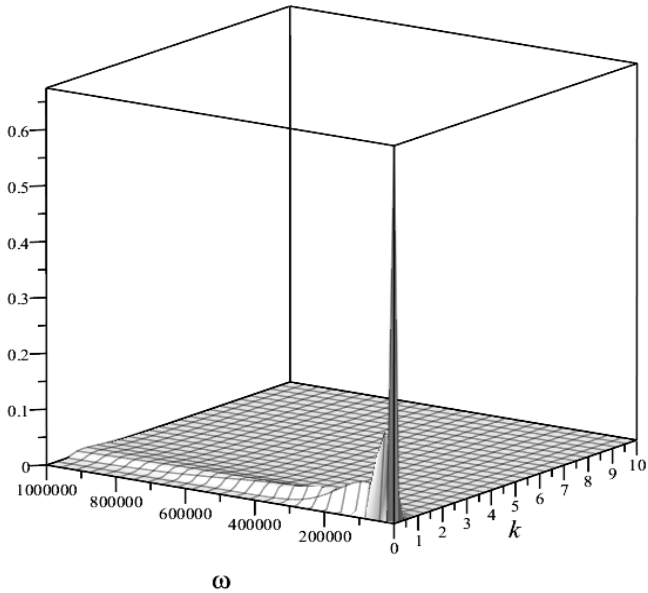

Figure 3. Area of existence of the imaginary part of the tensor (17).

7. Three Methods of Numerical Solution of the Problem

The results of the numeric calculation of the initial problem for the dispersion equation (14) by the first method (20) are presented in Table 1.

As you can see, the found roots have both positive and negative imaginary parts. This indicates that for each wave number there is both a swing mode and a vibration attenuation mode. In general, the medium is unstable, and the increments of the increase are large (comparable to the real parts of the frequencies).

The dispersion curve is as follows:

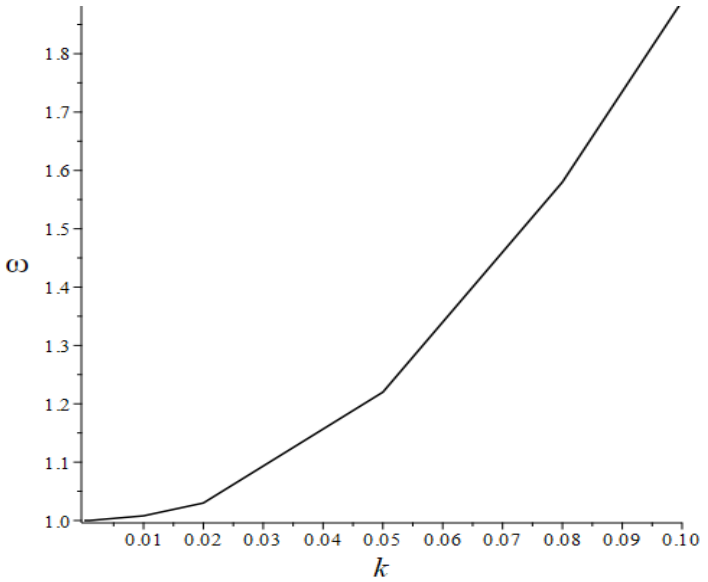

Figure 4. Dispersion curve determined by equation (14).

This curve qualitatively coincides with the dispersion curve in Figure 1 but lies in the region of lower frequencies and begins with the frequency value $\omega = 1.00c^{-1}$.

Table 1. Results of solving the initial problem (14)

k(м$^{-1}$)	0.001	0.01	0.02	0.05	0.08	.0.1
$\omega(c^{-1})$	1.00 ± 0.99i	1.00 ± 0.99i	1.03 ± 0.96i	1.22 ± 0.82i	1.58 ± 0.62i	1.89 ± 052i

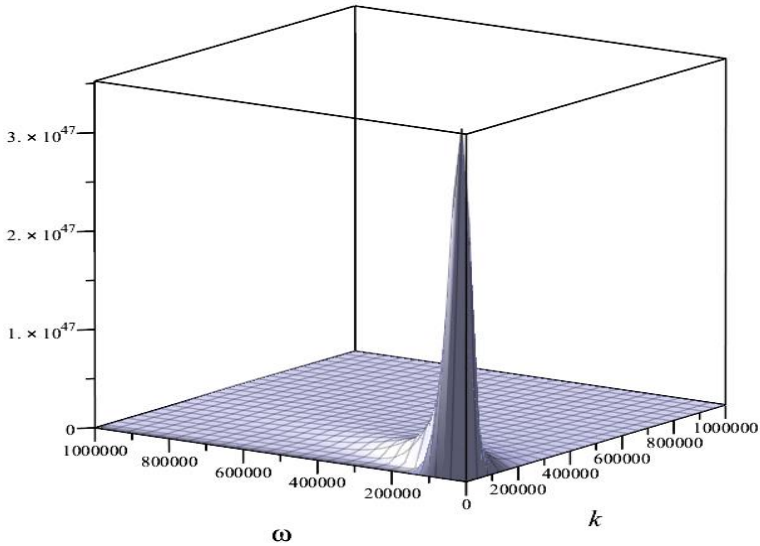

Figure 5. The region of existence of the real part of the tensor (14).

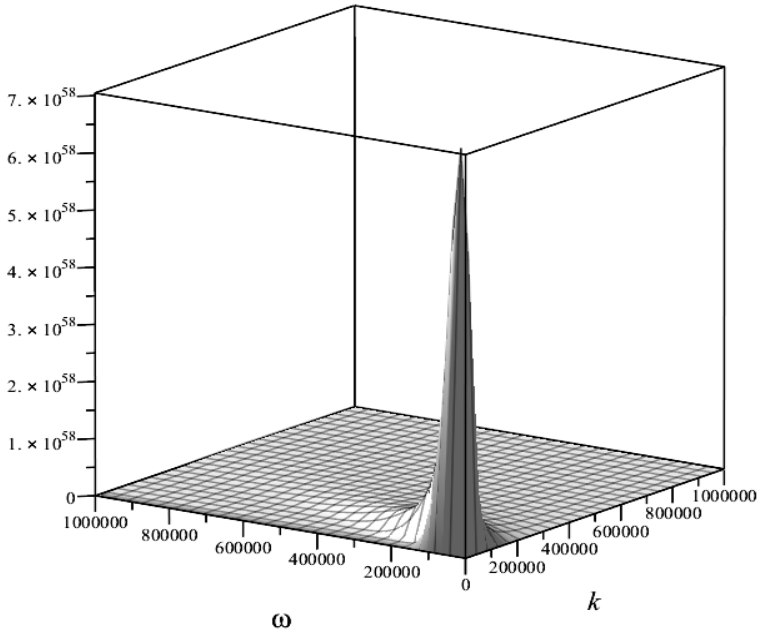

Figure 6. The region of existence of the imaginary part of the tensor (14).

The second method (20) does not give solutions.

Within the framework of the third method (20), solutions are also absent, since the regions of the real (see Figure 5) and imaginary (see Figure 6) parts of the tensor (14) do not intersect, their values differ by 10 orders of magnitude.

Conclusion

It turns out that only the first condition for the conversion of a complex number to zero (20) makes it possible to find a solution to the dispersion equations of the newly obtained (14) and previously known (17).

The resulting tensor of dielectric permeability (14), as well as the Landau tensor introduced into plasma physics (15), has both Hermitian and anti-Hermitian parts. The latter is responsible for absorbing electromagnetic waves in the plasma or buildup them under certain conditions.

Dispersion curves in Figure 1 Figure 4 qualitatively coincide. This may be evidence that the divergence of the integral in the tensor of dielectric permeability (4) is removed in both cases in the same way - by the introduction of imaginary quantities, only in the first case one value is complex - the frequency, in the second, considered by us, all the quantities included in the consideration are considered complex. Note that the results of the solution of the dispersion equation (14) practically do not depend on the magnitude of the imaginary additives; with the parameter $\gamma = 10^{-1}$ they are the same as with $\gamma = 10^{-36}$. This parameter for all quantities was supposed to be the same, which does not exhaust, of course, all possibilities.

It can be assumed that in a complex-valued world the situation we have considered is always realized (equation (14). This is also the case if in the infinitely distant past the system was not in equilibrium. Thus, there was no need to introduce a small imaginary additive to the frequency $\omega \to \omega + i\delta$. If the system has passed into a non-equilibrium state from the equilibrium (there is a transitional state in the system), then it is necessary to introduce a small imaginary positive additive into the frequency. In this case, both scenarios seem to be realized in the system: in the region of Langmuir frequencies there are non-attenuating longitudinal plasma waves, and in the region of low frequencies, longitudinal waves are pendulated, leading to instability of the medium.

Using an example of solving a private problem of plasma waves, the possibility of finding the intended complexity of all physical quantities is investigated. The imaginary parts of physical quantities, if they exist, are probably small, so it is difficult to detect them in ordinary situations. For example, in $\gamma = 10^{-36}$, the imaginary parts can be neglected if the system in question is stable, i.e., a small perturbation of the parameter (in our case it is the imaginary part of the quantity) corresponds to a small perturbation of the solution. But in the case of a singular integral (4) with a pole feature in the denominator of the integrand function, even a small imaginary part can lead to a solution significantly different from a purely real solution. Which is shown in the derivation and solution of the dispersion equations (14). Longitudinal plasma waves in the case of complex-valued physics have properties different from those to which we are accustomed until now.

It is possible that the imaginary part, being unobservable, at the same time must be inherent in a physical quantity, being something of a hidden parameter, and is manifested only indirectly, forcing the system to move along one or another path. An experimental study of this difference would be interesting.

References

[1] Landau L. D., On the oscillations of electron plasma, *JETF* 16, iss. 7, 574 (1946).

[2] Vlasov A. A., On the vibrational properties of electron gas, *JETF* 8, iss. 3, 291 (1938).

[3] Lyahov V. V., Neshchadim V. M., *The role of complex magnitudes in plasma electrodynamics*, Advances in Plasma Physics Research, vol. 5, Nova Science Publishers, Inc., NY., (2006).

[4] Lyahov V. V., Neshchadim V. M., *Models of Plasma Kinetics and Problems with Their Interpretation in the Current Paradigm*, Nova Science Publishers, Inc., NY, (2018).

[5] Kolmogorov A. I., *On the concepts of quantity and number*," collection "Historical and Mathematical Research, Volume 32-33, Moscow, Nauka, (1990).

[6] Alexandrov A. F., Bogdankevich L. S., Rukhadze A. A., *Fundamentals of plasma electrodynamic*, Moscow, Vysshaya shkola, (1988).

[7] Silin V. P., Rukhadze A. A., *Electromagnetic properties of plasma and plasma-like media*, Moscow, Book House "LIBROCOM," (2013).

[8] Faddeeva V. N., Terentyev N. M., *Tables of values of the probability integral*, Moscow, Gostechizdat, (1954).

[9] Bohm D., Gross E. P., Theory of Plasma Oscillations. A. Origin of Medium-Like Behavior, *Phys. Rev*. 75, 1851 (1949).

Chapter 5

Potentially Habitable Extrasolar Planets Discovered by the Kepler-Mission

Michael C. LoPresto*

[1]Department of Astronomy, University of Michigan, Ann Arbor, Michigan, USA

Abstract

The habitable zone of a star is the range of distances from the star at which water can exist as a liquid. Radiation Laws can be used to estimate the distances from different types of stars at which a planet could potentially have temperatures between the freezing and boiling points of water. This can be further verified by estimation of the temperatures of the planets, based not only on their distances from and temperatures of their stars, but also through estimates of the effects of their albedo and greenhouse-effects on their temperatures. What follows is a report of the procedure and results of such estimations made for Earth and Super-Earth type extrasolar planets discovered by NASA's Kepler-Mission to determine which may be potentially habitable.

Keywords: *Kepler* Mission, Transit Method, exoplanet, habitable zone, Earth-like planet, Super-Earth, temperature

Introduction - The Kepler Mission

NASA's *Kepler* Mission began using the transit method of extrasolar planet detection in 2009 with a primary goal of determining whether or not

* Corresponding Author's Email: lopresto@umich.edu.

In: Horizons in World Physics. Volume 312
Editor: Albert Reimer
ISBN: 979-8-89113-513-0

potentially habitable planets, planets similar in size to Earth and orbiting in the habitable zones of their stars, are common in our galaxy. An answer to this question could be the first step in answering one of the most fundamental questions ever asked by the human species, whether or not life and possibly intelligence, exists elsewhere in our galaxy. After taking data on nearly 200,000 stars in a specific target region of the Milky Way, the *Kepler* Mission had discovered over 2000 planets orbiting F, G, K, and M spectral type stars.

Background-Habitable Zones

The *habitable zone* of a star is the range of distances from it where temperatures allow the existence of water in its liquid state on the surface of a planet with sufficient atmospheric pressure. The expected temperature, T_p, of a planet of radius, R_p, based on the fraction of the radiation emitted by a star of Temperature, T_s, and radius, R_s, that the planet absorbs and reemits at an average orbital radius or distance, d, from the star can be estimated with the Stephan-Boltzmann Law, $P = \sigma T^4$, where $\sigma = 5.67 \times 10^{-8}$ W/m^2*K^4 is the Stefan-Boltzmann constant. Assuming that the fraction of the power emitted by the star that a planet absorbs can be set equal to the power emitted by the planet gives

$$\sigma 4\pi R_s d^2 * T_s^4 * (\pi R_p^2/4\pi d^2) = \sigma 4\pi R_p d^2 T_p^4. \quad (1)$$

The quantity in parenthesis $(\pi R_p^2/4\pi d^2)$ is the fraction of the power radiated by the star over a spherical area, $4\pi d^2$, that is absorbed by the cross-sectional area, πR_p^2, of the planet at the planet's orbital distance, d. After many cancellations, (1) is rearranged to give

$$T = T_S * (R_S/2d)^{0.5}. \quad (2)$$

Solving (2) for d and using the range of temperatures at which water can exists as a liquid, T = 373 K to T = 273 K, a necessity for life, gives a habitable zone for our Sun of about 0.56 AU to 1.04 AU. This includes Venus, 0.72 AU, but not Mars, 1.52 AU (and barely includes Earth).

A planet's temperature does *not* depend only on radiation from its star. It is also dependent on the reflectivity or *albedo* of its surfaces and the *greenhouse effect*. Albedo is the percentage of incident radiation that a planet's

surfaces reflect. This can lower a planet temperature and possibly allow it to be closer to a star than expected from calculations considering radiation alone and still maintain a habitable temperature. For instance, Earth's average albedo is about a = 0.31, meaning that its surfaces on average reflects about 31% of the radiation incident upon it from the Sun. Due to radiation alone, Earth's average temperature calculated with (1) would be about T_r = 279 K, but considering the albedo, using the expression $T_a = T_r*(1-a)^{0.25}$ drops the temperature by over 10% to about T_a = 249 K (LoPresto, 2013).

Greenhouse warming occurs when gases in a planet's atmosphere such as water vapor, carbon dioxide and others absorb a portion of the incident radiation from a star after the planet reemits it. This could allow a planet to still be habitable at a further distance from a star than expected only due to radiation and albedo. Using the expression $T_g = T*(1 + \tau)^{0.25}$, where $\tau = 1$, the "thickness" of Earth's atmosphere, to calculate the greenhouse warming in Earth's atmosphere, raises the average temperature from that expected from radiation and its albedo by almost 20% to about 296 K (LoPresto, 2013).

Due to the possible cooling of a planet due to albedo and warming due the greenhouse effect, the habitable zone for a star could be wider than a range calculated with (1) alone, based *only* on radiation and the temperatures for liquid water. Considering this, the habitable zone for our Sun could be from 0.6 AU to 2 AU. The inner estimate is just outside the 0.56 AU, calculated above with (1), limit for liquid water. A combination of albedo and less greenhouse warming than occurred on Venus could possibly allow a planet at this distance to be habitable. The outer estimate includes Mars and considers the possibility that a more massive planet than Mars, retaining a thicker atmosphere, could experience more greenhouse warming, resulting in more habitable temperatures.

Using (2) at 0.6 AU and 2 AU gives inner and outer (radiation) temperatures of our Sun's habitable zone of 360 K and 197 K. These temperatures can now each be used as T in equation (3) below, which is (2) solved for d with meters converted to AU and the units of R_S to solar radii, to estimate limits for the habitable zone of any star based on its Kelvin temperature and radius;

$$d = 0.00232 \text{ AU} * (R_S/R_{Sun}) *(T_S/T)^2. \quad (3)$$

Once these limits are calculated for a star, they can be compared to the orbital radius of any planet in orbit to determine whether or not it lies within a habitable zone.

Table 1. Numbers of each planet type discovered by the Kepler Mission

Planet Type	Radius (Earths)	Number	% of N = 2276
Larger	>15	15	0.7
Jupiter (Gas Giant)	6 to 15	127	5.6
Neptune (Ice Giant)	2 to 6	1075	47.2
Super Earth	1.25 to 2	725	31.9
Earth Like	<1.25	333	14.6

Obtaining and Analyzing the Data

Data on the planets discovered by the *Kepler* Mission was downloaded from the *NASA Exoplanet Archive*, Figure 1 shows spreadsheet data for the first few of over 2000 planets. The orbital periods (column D) were given in units of days, the orbital semi-major axes (E) in AU, the planet masses. and radii (F and G) in "Jupiters," the stellar distances and temperatures in parsecs and Kelvins and the stellar masses and radii in solar units (the values for the Sun = 1). The planet masses and radii were converted from "Jupiters" to "Earths" by multiplying column F by Jupiter's mass of 318 Earths and column G by Jupiter's radius of 11.2 Earths.

The spreadsheet data was then sorted on the planet radius column (G) in increasing order and the number of each planet type was recorded (planets for which there was no radius data were deleted bring the total number of planets down from 2293 to 2276) the results are shown Table 1 and Figure 2.

To search for potentially habitable planets, data for all planets other than Earth-like and Super Earths were deleted which reduced the number of planets to 1308. Planets any larger than Super Earths are expected to be of a mostly gas and liquid composition as are the Jupiter-like, Jovian planets of our solar system while it is considered possible that Super Earths are composed of rock and metal as are our solar system's Earth-like, terrestrial planets. To leave a margin for error, planets of a radius of up to 2.3 Earths, 15% above the Super-Earth cut-off were retained. The inner and outer limits of the habitable zone of every star remaining were then calculated with (3). Next, the data was sorted by increasing star temperature (column 1 in Figure 1). Figure 3 is a comparison of the numbers of each spectral- type of star found by *Kepler* to have Earth-like planets or Super-Earths in orbit. Table 2 shows this data, the temperature and mass range for each star type and the innermost and outermost limits of the habitable zones calculated with (3), that are similar to those that are generally accepted (Hall, 2017; Livio & Silk, 2017).

A data set for each spectral type of star in Table 2 was extracted then sorted in order of increasing distance of the planets from their stars (column E in Figure 1). Planets for which there was no orbital distance given in the data had to be deleted, leaving the total number of planets left at a very manageable 493. Seventeen (17) planets, about 0.04% of the 2293 discovered by the Kepler Mission were found lie within the habitable zones of the M, K and G-type stars surveyed and recorded in Table 3. Note that no planets were found in the habitable zones of F-type stars. Initially it was believed that due to higher level of ultraviolet radiation, F-type stars were not good candidates for planets, even within their habitable zones, with the potential to support life, but more recent studies have suggested that this be rethought since F-type stars have very wide habitable zones (Sato et al., 2014). The range of the habitable zones of F-type stars calculated with (2), recorded in Table 2, is indeed wider than those of the cooler types of stars.

	A	B	C	D	E	F	G	H	I	J	K	L
1	pl_hostname	pl_letter	pl_pnum	pl_orbper	pl_orbsmax	pl_bmassj	pl_radj	st_dist	st_teff	st_mass	st_rad	rowupdate
2	Kepler-10	b	2	0.837491	0.0172	0.0145	0.132	173	5627	0.91	1.06	10/15/15
3	Kepler-10	c	2	45.2943		0.054	0.21	173	5627	0.91	1.06	6/2/14
4	Kepler-100	b	3	6.88705		0.023	0.118		5825	1.08	1.49	5/14/14
5	Kepler-100	c	3	12.8159		0.003	0.196		5825	1.08	1.49	5/14/14
6	Kepler-100	d	3	35.3331		0.009	0.144		5825	1.08	1.49	5/14/14
7	Kepler-1000	b	1	120.0181			0.425	925	6453	1.4	1.51	5/10/16
8	Kepler-1001	b	1	14.30512			0.281	1009	5491	0.9	0.88	5/10/16
9	Kepler-1002	b	1	4.336429			0.153	425	6144	1.22	1.57	5/10/16
10	Kepler-1003	b	1	3.554857			0.159	873	6109	1.11	1.17	5/10/16

Figure 1. Downloaded data from *Kepler* Mission transferred to an Excel spreadsheet.

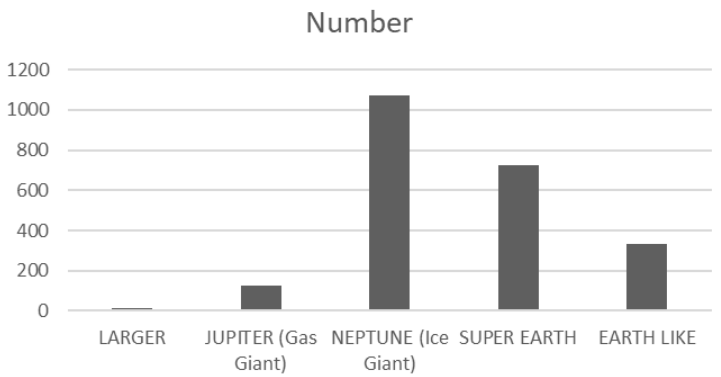

Figure 2. Plot of the number of each planet type discovered by the *Kepler* Mission.

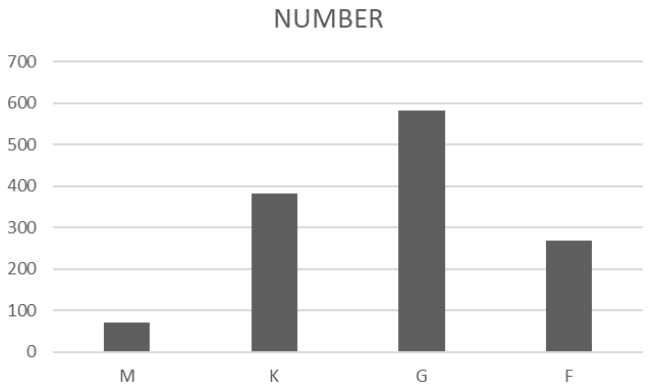

Figure 3. Plot of the numbers of M, K, G and F-type stars surveyed by the *Kepler* Mission.

Figure 4 and Figure 5 are plots of the orbital radii of the planets listed in Table 3 compared to the inner and outer habitable zones of their stars. The planets in Table 3 are all listed in the *Habitable Exoplanets Catalog* maintained by the *Planetary Habitability Laboratory* at the University of Puerto Rico at Arecibo and are considered to be the most promising potentially habitable planets discovered by the *Kepler* Mission.

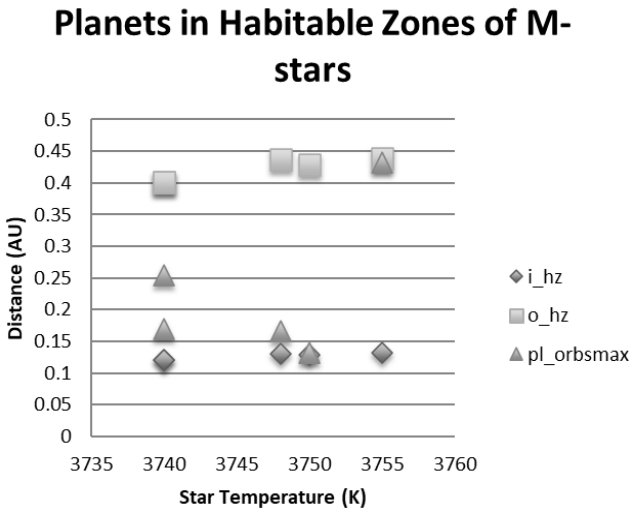

Figure 4. Planets discovered by the *Kepler* Mission with orbital distances within the limits of the habitable zones of M- stars.

Table 2. The temperatures, masses, and range of habitable zone limits of M, K, G and F-type stars surveyed by the Kepler Mission

Star Type	Temperature Range	Mass Range	Inner Hz	Outer Hz	Number of Stars	Percentage of Stars
M-(red) dwarfs	<4000 K	<.5 Sun	0.03 AU	0.5 AU	70	5.4%
K-dwarfs	3900-5200 K	0.45-0.8 Sun	0.2 AU	1.4 AU	382	29.3%
G-Sun-like	5300-6000 K	0.8-1.2 Sun	0.45 AU	2.5 AU	583	44.7%
F-hotter	>6000 K	1-1.4 Sun	0.75 AU	5.2 AU	269	20.6%

The habitability of planets orbiting M-type stars or red dwarfs, as they are called, could be hindered by several factors. The potential habitable zones are so close to the star (see Table 2) that the planets could be subject to both tidal locking and heating. Tidal locking causes a planet's rotation and revolution periods to be the same, this synchronous rotation results in one side of the planet always facing the star and one side always facing away, resulting in an extreme difference in temperatures between one side that is in perpetual daytime and the other in perpetual night. Too much tidal heating could cause the interior of a planet to remain molten resulting in constant violent volcanic eruptions like Jupiter's Moon Io. The brightness of red dwarfs can also be extremely variable. Large numbers of *starspots* (like sunspots) can greatly dim the light the stars emit, and gigantic flares can greatly increase their brightness (Crockett, 2017; ASTRO NEWS, 2016).

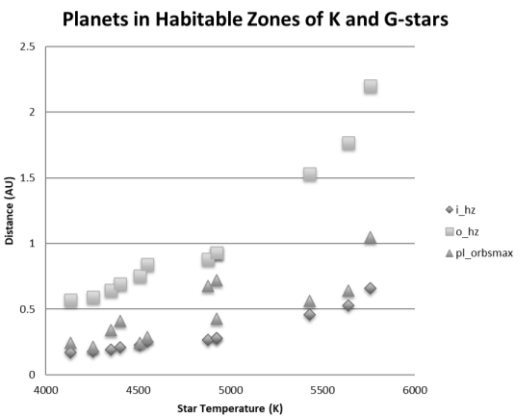

Figure 5. Planets discovered by the *Kepler* Mission with orbital distances within the limits of the habitable zones of K (<5200 K) and G (>5200 K) stars.

Table 3. The 17 planets discovered by the Kepler mission that orbit within their star's estimated habitable zones

pl_hostname	pl_letter	pl_pnum	pl_orbper	pl_orbsmax	pl_radE	st_teff	st_mass	st_rad	i_hz	o_hz	st_type
Kepler-236	c	2	24.0	0.132	1.9936	3750	0.56	0.51	0.128	0.429	M
Kepler-438	b	1	35.2	0.166	1.12	3748	0.54	0.52	0.131	0.437	M
Kepler-296	e	5	34.1	0.169	1.5232	3740	0.5	0.48	0.120	0.401	M
Kepler-296	f	5	63.3	0.255	1.8032	3740	0.5	0.48	0.120	0.401	M
Kepler-186	f	5	129.9	0.432	1.1648	3755	0.54	0.52	0.131	0.438	K
Kepler-235	e	4	46.2	0.213	2.2176	4255	0.59	0.55	0.178	0.595	K
Kepler-440	b	1	101.1	0.242	1.904	4134	0.57	0.56	0.171	0.572	K
Kepler-155	c	2	52.7	0.242	2.24	4508	0.58	0.62	0.226	0.753	K
Kepler-437	b	1	66.7	0.288	2.128	4551	0.71	0.68	0.252	0.842	K
Kepler-283	c	2	92.7	0.341	1.8144	4351		0.57	0.193	0.645	K
Kepler-442	b	1	112.3	0.409	1.344	4402	0.61	0.6	0.208	0.695	K
Kepler-62	e	5	122.4	0.427	1.6128	4925	0.69	0.64	0.278	0.928	K
Kepler-174	d	3	247.4	0.677	2.184	4880		0.62	0.264	0.883	K
Kepler-62	f	5	267.3	0.718	1.4112	4925	0.69	0.64	0.278	0.928	K
Kepler-439	b	1	178.1	0.563	2.24	5431	0.88	0.87	0.459	1.534	G
Kepler-69	c	2	242.5	0.64	1.7136	5638	0.81	0.93	0.529	1.767	G
Kepler-452	b	1	384.8	1.046	1.624	5757	1.04	1.11	0.659	2.199	G

Kepler-452b, the bottom entry in Table 3, when discovered in 2015 was dubbed Earth 2.0. With a radius of 1.6 that of Earth's and being in an orbit around a G-type star very similar to our Sun of just over 1 AU, Kepler-452b may be the extrasolar planet most similar to Earth yet discovered (Chou & Johnson, 2015).

Calculating Planet Temperatures

An alternative approach to determining planetary habitability is to estimate planetary temperatures from the data. Equation (3) can be rearranged to give an actual estimate of a planet's temperature due to the radiation from its star that it absorbs.

$$T_r = 0.0482^* [(R_s/R_{Sun})/d]^{0.5} * T_s, \quad (4)$$

Table 4. Temperatures of Extra Solar Planets discovered by the Kepler-mission calculated considering only radiation from their star, T_r, and then modified, T_m, for possible effects of albedo and the greenhouse effect.

pl_hostname	pl_letter	pl_orbsmax	pl_radE	st_teff	st_rad	i_hz	o_hz	T r	Tm
Kepler-296	F	0.255	1.8032	3740	0.48	0.140	0.401	247	269
Kepler-442	B	0.409	1.344	4402	0.6	0.243	0.695	257	**279**
Kepler-283	C	0.341	1.8144	4351	0.57	0.226	0.645	271	**295**
Kepler-452	B	1.046	1.624	5757	1.11	0.770	2.199	**286**	**311**
Kepler-62	E	0.427	1.6128	4925	0.64	0.325	0.928	**290**	**316**
Kepler-440	B	0.242	1.904	4134	0.56	0.200	0.572	**303**	**329**
Kepler-296	E	0.169	1.5232	3740	0.48	0.140	0.401	**304**	**330**
Kepler-438	B	0.166	1.12	3748	0.52	0.153	0.437	**320**	**348**
Kepler-439	B	0.563	2.24	5431	0.87	0.537	1.534	**325**	**354**
Kepler-69	C	0.64	1.7136	5638	0.93	0.618	1.767	**327**	**356**
Kepler-235	E	0.213	2.2176	4255	0.55	0.208	0.595	**329**	**358**
Kepler-437	B	0.288	2.128	4551	0.68	0.295	0.842	**337**	**366**
Kepler-155	C	0.242	2.24	4508	0.62	0.264	0.753	**348**	378
Kepler-236	C	0.132	1.9936	3750	0.51	0.150	0.429	**355**	386
Kepler-52	D	0.182	1.9488	4263	0.56	0.213	0.608	**360**	392
Kepler-296	D	0.118	2.0832	3740	0.48	0.140	0.401	**363**	395
Kepler-395	C	0.177	1.3216	4262	0.56	0.213	0.608	**365**	397
Kepler-331	D	0.159	1.6352	4347	0.49	0.194	0.554	**368**	400
Kepler-225	C	0.111	1.8368	3682	0.48	0.136	0.389	**369**	401
Kepler-367	C	0.253	1.1984	4710	0.69	0.320	0.915	375	408

The second to last column of Table 4 shows the "radiation temperatures," T_r, for planets calculated with (4) with temperatures between 273 K and 373 K in bold type.

The last column of Table 4 shows the "radiation temperatures" modified for the possible effects of both the above-mentioned *albedo* of the planets' surfaces and *greenhouse effect* in the planet's atmosphere. An "albedo temperature," T_a, for a planet of radiation temperature, T_r, can be calculated in terms of the albedo of its surfaces, a, with the expression (given above)

$$T_a = T_r * (1 - a)^{0.25}, \quad (5)$$

while an expression (also given above) for calculating a "greenhouse temperature" for a planet T_g where τ is the thickness of greenhouse gases in its atmosphere compared to those in Earth's atmosphere, $\tau = 1$.

$$T_g = T_r * (1 + \tau)^{0.25}, \quad (6)$$

As mentioned above, current exoplanet missions may provide data on spectroscopic signatures and thus the compositions of extra solar planet atmospheres and possibly surfaces (Redd, 2016: Crockett, 2016; Wenz, 2017), but at present the only basis for estimates of albedo and atmospheric greenhouse thickness would be to consider Earth-sized *Kepler*-mission planets identified as in their habitable zones as "Earth-like," and therefore assume a similar, $a \sim 0.3$, albedo and $\tau \sim 1$, atmospheric greenhouse thickness.

Using these values in (5) and (6) would multiply the radiation temperature of a planet by a factor of $0.7^{0.25} \sim 0.915$, a decrease in temperature of almost 10%, and a factor of $2^{0.25} \sim 1.189$, an almost 20% increase in temperature. The application of both (5) and (6) results in temperatures modified for albedo and greenhouse warming, T_m, the final column of Table 4, that are a factor of about $0.915*1.189 \sim 1.088$, almost 9% higher than the radiation temperatures.

The "modified temperatures," T_m, in bold type in the last column of Table 4 are those of the planets that would be considered possibly habitable by the standard of an estimated temperature between 273 K and 373 K including the estimated effects of albedo and greenhouse warming. This is a list of only 11 planets rather than the 16 in bold type in the second to last column of Table 4, identified with (4) by radiation temperature alone.

Conclusion

Next steps include space telescope missions such as the *Transiting Exoplanet Survey Satellite* (*TESS*) and the *James Webb Space Telescope* examining exoplanet atmospheres and looking for spectroscopic signatures of chemicals that could be conducive to the presence of life such as carbon dioxide, water, oxygen, and others (Redd, 2016: Crockett, 2016; Wenz, 2017).

References

Astro News, "Tiny, stormy stars are bad news for habitability," *Astronomy*, 44 (3), 13 (March 2016).

Chou F., Johnson M. NASA's Kepler Mission Discovers Bigger, Older Cousin to Earth, NASA, *News and Events July* 23, 2015.

Crockett C., "Putting Eyes on Exoplanets," *Science News*, 32-34, (April 30, 2016).

Crockett C., "The Opportunity Zone," *Science News*, 18-21 (June 24, 2017).

Hall S., "The Secrets of Super Earths," *Sky and Telescope*, 133 (9) 22-29 (March 2017).

Livio M. and J. Silk J., "Where Are They ?" *Physics Today*, 70 (3) 50-57 (March 2017).

LoPresto M. "Adding Albedo and Atmospheres," *Phys. Teach.* 51 (3), 161–162 (Mar. 2013).

Redd N "Why We Haven't Found Another Earth," *Astronomy*, 44 (2), 25-29 (February 2016).

Sato S., Cuntz M., Guerra Olvera, C. M., Jack D., Schroder K. P. Habitability around F-type stars *International Journal of Astrobiology* 13 244-58.

Wenz J, "Get Ready for the Next Generation Planet Hunter" *Astronomy*, 45 (7), 44 (July 2017).

Chapter 6

The Densities of Extrasolar Planets

Michael C. LoPresto*
Department of Astronomy, University of Michigan, Ann Arbor, Michigan, USA

Abstract

Over 200 of the extrasolar planets discovered by NASA's *Kepler*-Mission now have mass data available in addition to the original radius data available when they were discovered. This allows for the calculation of their densities. Plots of these extrasolar planet's densities as a function of their radii allows for comparison to their expected densities based on their size-classifications and the densities of the planets in our own solar system. A comparison of the densities of those considered *Super-Earths*, *Mini-Neptunes* and *Neptunes* can help develop criterion with which to distinguish between these types of extrasolar planets.

Keywords: extrasolar planet, radius, mass, density, Super-Earth, Mini-Neptune

Introduction-Background

The planets of our solar system fit into two major groups; the smaller, lower mass, and higher density, rock and metal, Earth-like or *terrestrial* planets and; the larger, higher mass, and lower density, gas and liquid, Jupiter-like or *Jovian* planets.. **Table 1** compares the mass, radii, and densities of our solar systems planets in terms of the E=1values for Earth.

* Corresponding Author's Email: lopresto@umich.edu.

In: Horizons in World Physics. Volume 312
Editor: Albert Reimer
ISBN: 979-8-89113-513-0

The NASA- *Kepler* Mission originally defined the different extrasolar planet types show in **Table 2** by size. Extrasolar planets of 1.25 Earth radii or less are terrestrial or "*Earths*"; those between 1.25 and 2 Earth radii "*Super-Earths*". This is a new type of planet discovered by the *Kepler*-mission, there are no "*Super-Earths*" in our solar system; 2-6 Earth radii are "*Neptunes,"* distinguishing them from the gas-giant "*Jupiters*," 6-15 Earth Radii; and "*Larger*," > 15 Earth radii (Yaqoob, 2011). There is also an "overlap" category between larger *Super-Earths* and smaller *Neptunes* of up to 3 or 4 Earth radii called "*Mini-Neptunes*." (Goldsmith, 2018; Tasker, 2017). There are also no *"Mini-Neptunes"* in our solar system.

Table 1. The masses, radii, and, densities of the planets of our solar system (Earth mass = Earth Radius = Earth density = 1)

Planet	Mass (Earth = 1)	Radius (Earth = 1)	Density (Earth = 1)
Mercury	0.06	0.38	0.98
Venus	0.82	0.95	0.95
Earth	1.00	1.00	1.00
Mars	0.11	0.53	0.71
Jupiter	318.26	11.21	0.24
Saturn	95.14	9.45	0.13
Uranus	14.54	4.01	0.23
Neptune	17.09	3.88	0.30

Table 2. The number and percentage of each extrasolar planet type as defined by the *Kepler*-mission in the 234 plotted in Figure 2

Planet Type	Radius Range (Earth = 1)	Number	Percentage%
Earths	<1.25	22	9.4
Super Earths	1.25-2	41	17.5
Neptunes	2-6	109	46.6
Jupiters	6-15	52	22.2
Larger	>15	10	4.3
TOTAL		234	100

The *Confirmed Planets* section of the *NASA Exoplanet Archive* includes over 2000 (2311) extrasolar planets discovered by the *Kepler*-mission of

which 234 have both a reported radius, determined by the *transit* method (Johnson, 2016), and mass, determined by the *radial velocity* or *Doppler-detection* method (Johnson, 2016). This allows the density ($\rho = m/v$; v = volume = $4/3*\pi r^3$) of these 234 extrasolar planets to be calculated. Knowledge of the density can be especially useful for determining whether these "overlapping" extrasolar are *Super-Earths* or *Mini-Neptunes*. *Super-Earths* should have a more rock-metal composition and therefore higher densities. *Mini*-Neptunes, being composed of more gases and liquids. should have lower densities. Density could also help determine whether the extrasolar planets of the other categories are similar in composition to those in our solar system of the same classifications. It should be noted that an extrasolar planets could be composed of many different combinations of materials, so it should *not* be assumed that density alone can be used to determine their exact composition. However, knowing the density of an exoplanet can allow for an estimate of whether an exoplanet is more likely a solid, rock, and metal planet, similar to our solar system's *terrestrial* planets or a gas and liquid or icy planet like our *Jovian* planets.

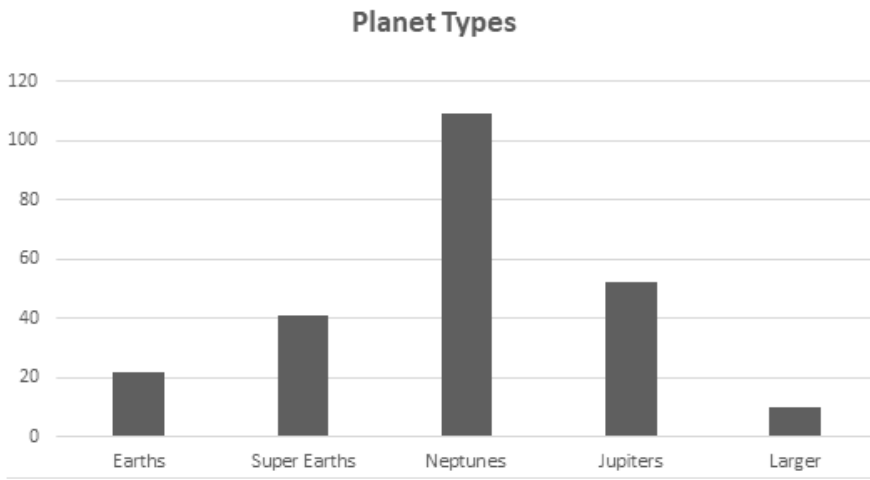

Figure 1. Histogram comparing the number of each extrasolar planet type, as defined by the *Kepler*-mission of the 234 plotted in **Figure 2.**

Data and Analysis

The data for the 234 extrasolar planet for which both the masses and radii were available was converted from Jupiter to Earth masses and radii before the densities were calculated. The data was then sorted with spreadsheets, first by increasing radius so the number of each type of extrasolar planet by size-category (**Table 2** and **Figure 1**) could be determined. Then density vs. radius was plotted for the entire data set to generate **Figure 2**. In turn, the data for extrasolar planets of each separate size-category were individually selected out and sorted according to increasing mass so extrasolar planets that were too massive (Howell, 2017) for the individual size categories could be eliminated. The plots in **Figures 3-8** were then be generated.

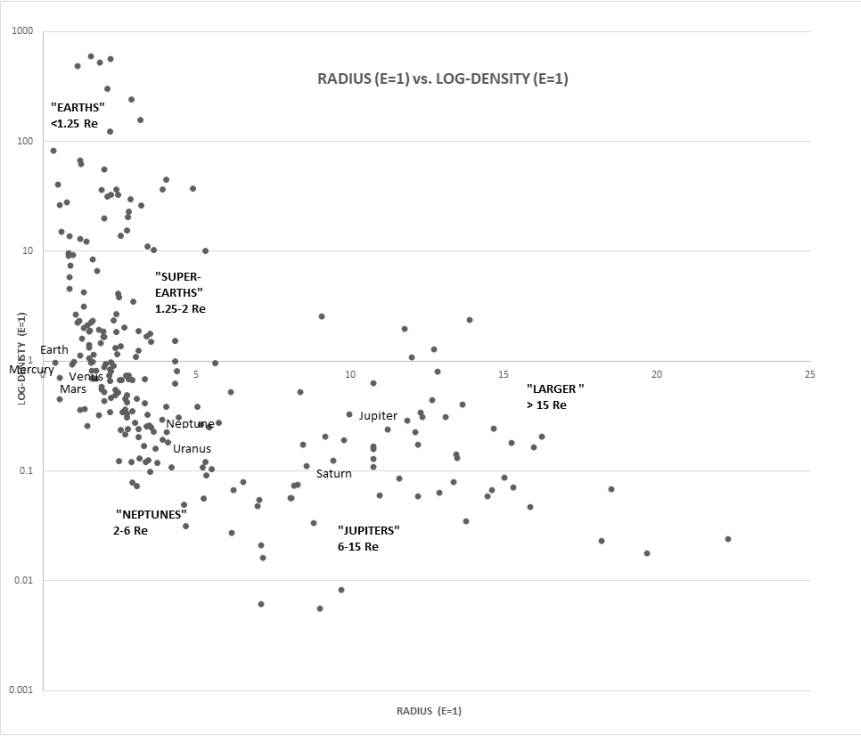

Figure 2. Log-plot of the density (Earth density, E = 1) as a function of the radii (Earth radius, E = 1) of the 234 *Kepler* extrasolar planets (and the planets of our solar system) for which both mass and radius are known.

Figure 2 is a log-plot of densities (Earth density, E = 1) of all 234 extrasolar planets from the *Kepler*-mission data set for which mass and radius are both known and for the planets of our own solar system as a function of their radii. Based on the densities of planets in our own solar system (**Table 1**), the general trend in **Figure 2** of larger planets being less dense is what would be expected. Jupiter and Saturn of our solar system can be seen to appear near the middle of the density range for "*Jupiters*" (6-15 Re). Uranus and Neptune are lower in the density range for the "*Neptunes*" (2-6 Re). The plot also shows the above-mentioned overlap of the *Neptunes* with "*Super-Earths*" (1.25-2 Re). The rock-metal terrestrial planets of our solar system also lie in the lower part of the density range for their extrasolar planet type, "*Earths*" (<1.25 Re).

Results

Earths and Super-Earths

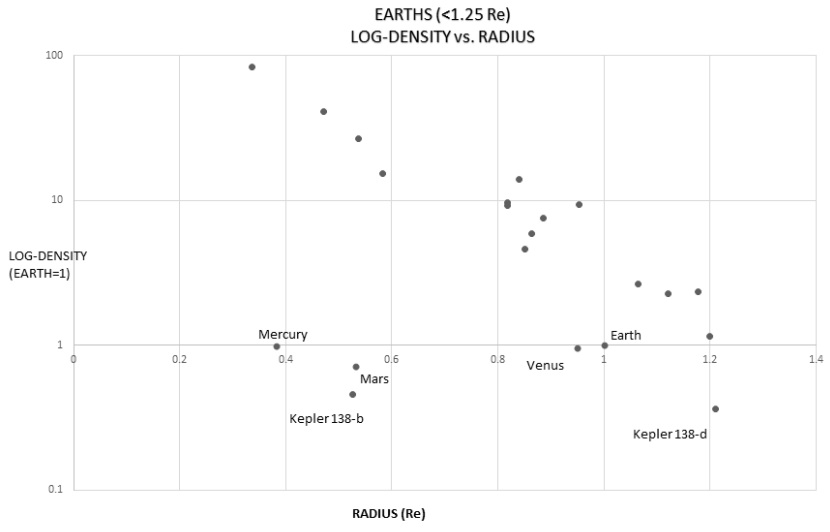

Figure 3. Log-plot of the density (Earth density, E = 1) as a function of the radii (Earth radius, E = 1) for the 17 "*Earths*" (<1.25*Re, <10*Me) in the dataset and those of our solar system.

The upper mass limits for *Earths* is considered 10 times the mass of Earth, above which a planet is considered a "*Mega-Earth*," (Howell, 2017). Of the extrasolar planets in the *Earth* radius range (<1.25 Re) 5 of 22 are more massive than this and not plotted in **Figure 3.** Most of the *Earths* plotted can be seen to have a density higher than those of our solar system suggesting a solid composition. **Figure 3** also shows 5 *Earths* that are a factor of 10 or more times the density of our Earth, the highest being over 80 times as dense. Two of the planets, however, Kepler 138-d and 138-b, are less dense than Mars (density ~ 0.7*Earth density). **Figure 4** is a plot of the planets in the *Super-Earth* radius range (1.25-2 Re) with the exception of 12 planets in with *Mega-Earth* masses. (Howell, 2017) This plot shows most *Super-Earths* to be of higher density than Earth, and therefor also likely of a solid composition, however there are also 2 in this group less dense than Mars.

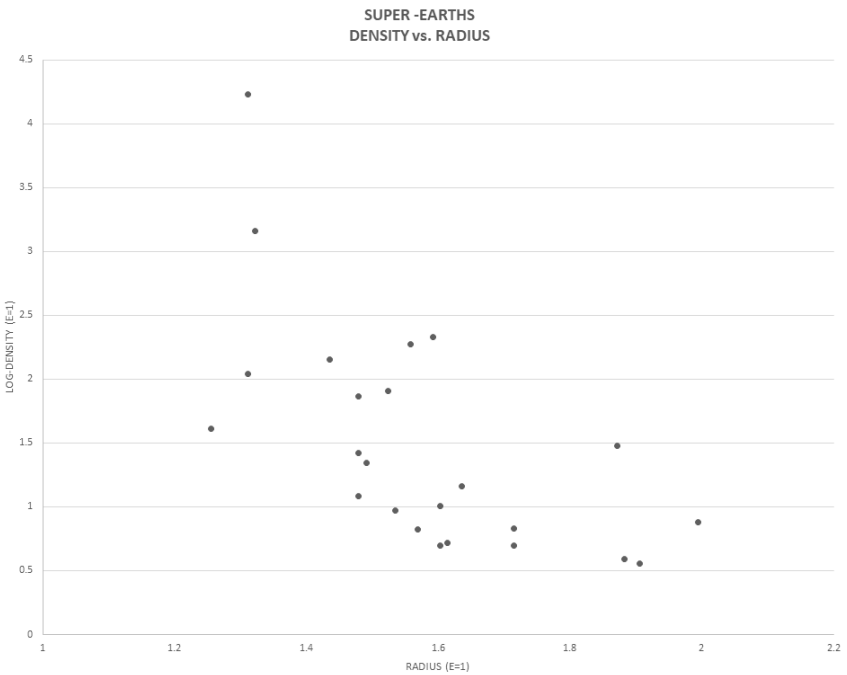

Figure 4. Log-plot of the density (Earth density, E = 1) as a function of the radii (Earth radius, E = 1) for the 29 "*Super-Earths*" (1.25-2 *Re, <10*Me). in the dataset.

Neptunes and Jupiters

Of the 109 extrasolar planets in the *Neptune* (2-6 Re) radius range, 33 are more than 50 times the mass of Earth, considered a limit for *Neptunes* (Howell, 2017), leaving 78 plotted in in **Figure 5** along with our solar system's Uranus and Neptune. The plot shows, as would be expected, that most are less dense than Earth. Our solar system's Uranus and Neptune are in the middle of the range. There are a few with a higher density including 17 that are more dense than Mars. Most of these exoplanets are of radius of about 3 times that of Earth or less. This suggests that they could actually be *Super-Earths.* The lower density extrasolar planets within this radius limit could be classified as *Mini-Neptunes* (Howell, 2017).

Of the 62 planets of *Jupiter* (6-15 Re) and *Larger* (>15e) size, only 1 is too massive (>5000 Earth-masses) for the radius classification (Howell, 2017). As seen in **Figure 6** most have similar density to the gas and ice-giants of our solar system. Of those that are denser, only 4 are of higher density than Earth with one less dense than Earth, but more dense than Mars.

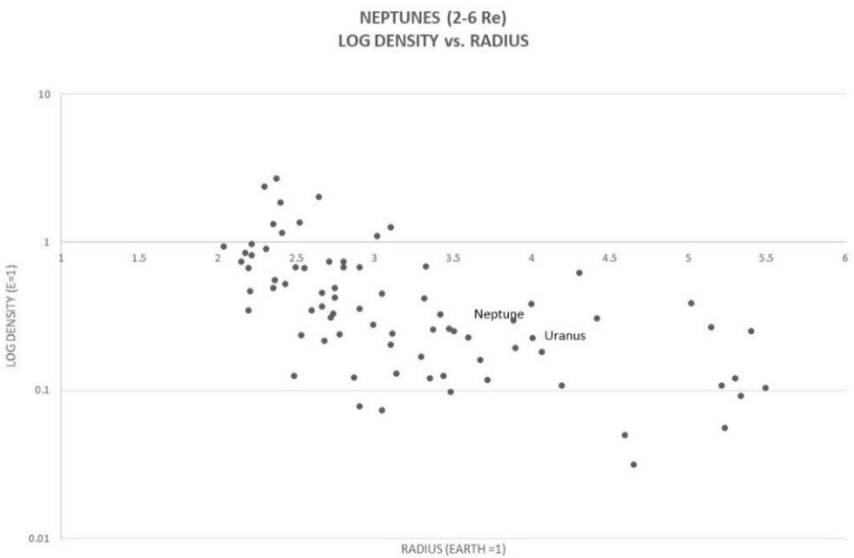

Figure 5. Log-plot of the density (Earth density, E = 1) as a function of the radii (Earth radius, E = 1) for the 78 "*Neptunes*" (2-6 Re, M<50 Me) in the dataset.

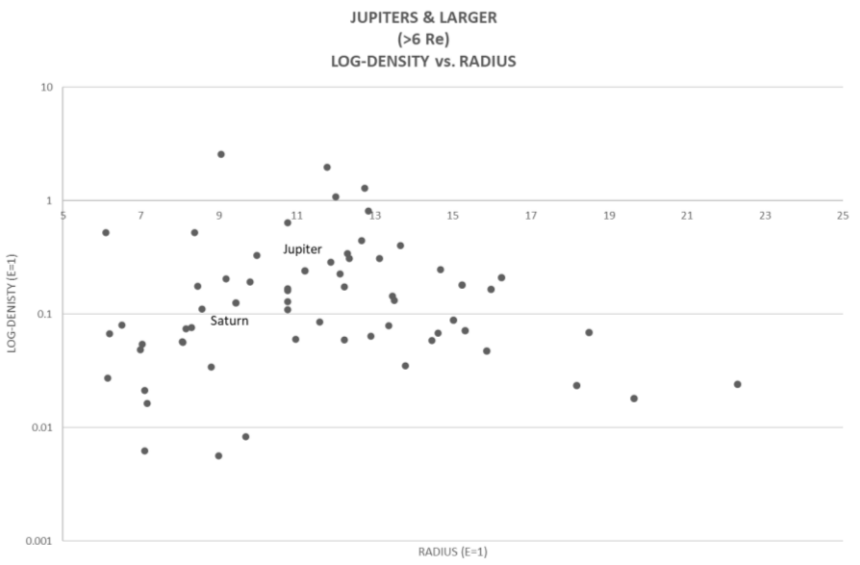

Figure 6. Log-plot of the density (Earth density, E = 1) as a function of the radii (Earth radius, E = 1) for the 61 "*Jupiter*" & "*Larger*" (> 6 Re), < 5000 M_e) in the data set.

Super-Earths or Mini-Neptunes?

Figure 7 is a radius vs. density plot of possible *Mini-Neptunes*, also known as "*Sub-Neptunes*" or "*Gas Dwarfs*." (Goldsmith, 2018) They are defined as having a radius from 2 or 3 (Goldsmith, 2018) or as much as (Tasker, 2017) 4 Earth radii and mass less than 20 Earth masses (Tasker, 2017). Up to 4 Earth radii can also be considered the size limit for *Super Earths* with no clear dividing line between them and *Mini-Neptunes* other than that the latter being a more gaseous version of the former (Goldsmith, 2018). This suggests that, of the 15 higher density extrasolar planets plotted in **Figure 7**, those greater than 0.6 times that of Earth (the least dense being very close to the 0.7*Earth, density of Mars) may actually be *Super Earths.* It has been suggested that density may be a better way to separate *Mini-Neptunes* from *Super -Earths* (Luque & Palle, 2022). There are 29 extrasolar planets of density, < 0.4*Earth, likely *Mini-Neptunes* with 9 that have densities that are < 0. 6 and >0.4*Earth. The plot does seem to show a gap at about a density 0.6*Earth, so this density could perhaps be considered a dividing line between *Super Earths* and *Mini-Neptunes*.

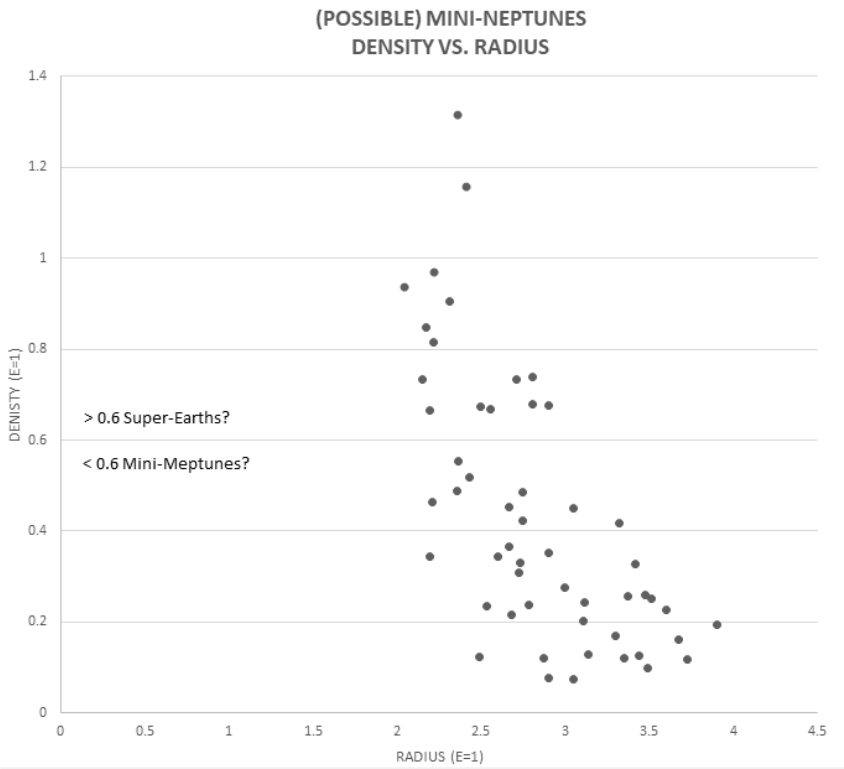

Figure 7. Plot of the density (Earth density, E = 1) as a function of the radii (Earth radius, E = 1) for the 53 "*Neptunes*," from the dataset in the "*Mini-Neptune*" (2-4*Re, < 20*Me) range.

Figure 8 is a plot, of all the possible *Super-Earths* and *Mini-Neptunes* from the 234 *Kepler*-mission dataset. The plot shows the above mentioned "gap" from **Figure 7** at 0.6*Earth's density that is a possible dividing line between *Super-Earths* and *Mini-Neptunes* and a "Radius Cliff" of 3 Earth radii above which all the exoplanets have lower densities and could be considered *Neptunes* rather than *Mini-Neptunes*. It has been suggested that the composition of *Mini-Neptunes* may include more water than the more gaseous *Neptunes*, and less than the rocky *Super Earths*, so that their density could indeed fall in between that of the other two exoplanet types (Luque & Palle, 2022). Kepler 11-b, 128- b and 128-c are the only anomalies with much lower *Neptune* -like densities but smaller *Super-Earth* sizes.

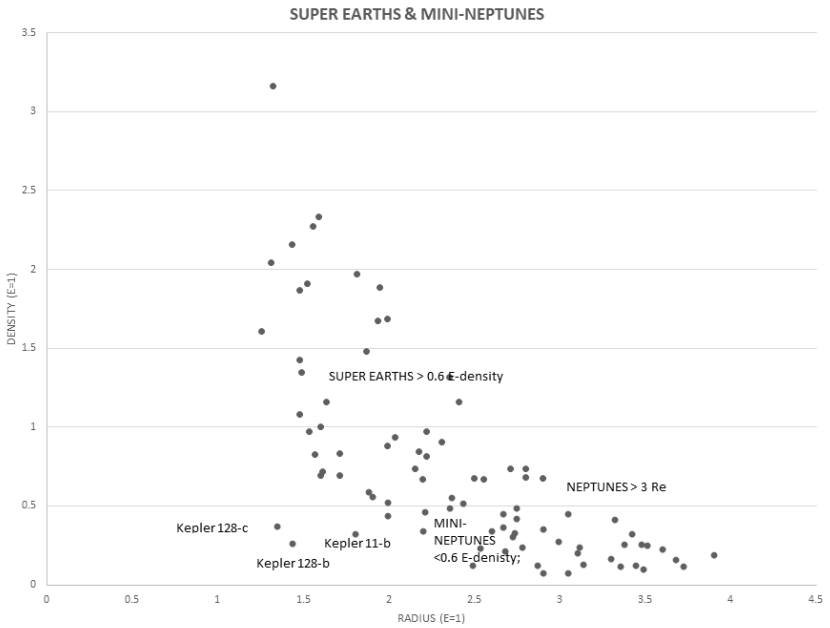

Figure 8. Plot of the density (Earth density, E = 1) as a function of the radii (Earth radius, E = 1) for the 86 extrasolar planets from the dataset in the "*Super-Earth*" (1.25-2*Re, < 10 Me) and "*Mini-Neptune*" (2-4*Re, <20*Me) ranges.

Conclusion

Of the 22 extrasolar planets with "*Earth*" radii, 5 were of "*Mega-Earth*" masses (Howell, 2017) and 2, *Kepler* 138-b and 138-d were very small and of lower density than Mars. Although their orbital distance from their star was not reported, this could suggest that they, like many of the exoplanets in the data set for which the orbital distance is known, are very close to their star and therefore at a high enough temperature to possibly be "*lava worlds*," composed largely of more molten material (Woodall, 2023). Of extrasolar planets with "*Super-Earth*" radii 12 of the 41 had "*Mega-Earth"* masses (Howell, 2017). Of the "*Neptune*" sized extrasolar planets, 33 of 109 were above the maximum mass limit of the category (Howell, 2017) and 17 were of higher density than Mars suggesting that they could be "*Super-Earths."* Of the 62 exoplanets with "*Jupiter*" and "*Larger*" radii only 1 was too massive (Howell, 2017) for the category and only 5 were more dense than Mars, 4 of them being denser than Earth. In all, a total of 51 of the 234 extrasolar planets,

almost 22% were too massive (Howell, 2017) for their size category while, as mentioned above, only a small number of *Earths* and *Jupiters & Larger* extrasolar planets were found to have densities not typical of their category.

When comparing potential "*Super-Earths*" and "*Mini-Neptunes*," the plot in **Figure 7** showed a gap at about 0.6*Earth, suggesting this density as a possible dividing line between "*Super-Earths*" and "*Mini-Neptunes.*" **Figure 8** shows this density-gap at 0.6 *Earth's density as well and a "Radius-Cliff "at about 3 Earth-radii. Above this radius, all the extrasolar planets are of lower densities and are more likely "*Neptune*s." The anomalies, *Kepler* 128-b and 128-c and *Kepler* 11-b of smaller "*Super-Earth*" size and lower "*Neptune*" density could also possibly be so called "lava worlds," (Woodall, 2023) as explained above.

References

Goldsmith, D. (2018). *Exoplanets-Hidden Worlds and the Quest for Extraterrestrial Life.* Cambridge, MA: Harvard University Press, 129-131.

Howell, E. (2017). *Planet Classification: How to Group Exoplanets*. Space.com.

Johnson, J. (2016). *How Do You Find an Exoplanet?* Princeton, NJ : Princeton Univeristy Press, 23-89.

Luque, R., and Palle, E. (2022). Density, not radius, separates water-rich small planets orbiting M dwarf stars. *Science*, 377(6611), 1211-1214.

Tasker, E. (2017). *The Planet Factory-Exoplanets and the Search for a Second Earth*. New York, NY: Bloomsbury Publishing, 97-102.

Woodall, T. (2023). *Study Sheds New Light on Strange Lava Worlds*. Physics .org.

Yaqoob, T. (2011). *Exoplanets and Alien Solar Syst*ems. Baltimore, MD: New Earth Labs-Education and Outreach, 78-79.

Chapter 7

A Giant Cloud of Preons (Voids) in Our Universe: Monitoring Earth's Axions

Anatoly Zubow[1]
Kristina Zubow[2,*]
and Viktor Zubow[2]
[1]Group of the Telecommunication Networks Division, TU, Berlin, Germany
[2]Zubow Consulting, NPO, Germany

Abstract

Observing the tracks of Earth's axions in the direction of the Sun and M1, led us to the understanding that the planet fell into a giant cloud of preons in 2023. The cloud caused the desorption of neutrinos from stars and the subsequent disruption of magnetic fields and further the occurrence of magnetic storms. An idea is given of the size, dynamics and direction of movement of the cloud, like a "hole" consisting of preons responsible for the expansion of the Universe.

Keywords: axions, photographs, tracks, Sun, M1, magnetic storms, preon cloud

1. Introduction

In 2023, a series of solar flares (https://tesis.xras.ru/sun_flares.html?m=9&d=21&y=2023) was accompanied by strong magnetic storms over the past 8

* Corresponding Author's Email: heide-lore@zubow.de.

In: Horizons in World Physics. Volume 312
Editor: Albert Reimer
ISBN: 979-8-89113-513-0

years (https://www.zamg.ac.at/cms/de/geophysik/news/staerkster-geomagnetischer-sturm-seit-fast-acht-jahren#:~:text=In%20der%20Nacht%20von%2023,sogar%20s%C3%BCdw%C3%A4rts%20bis%20nach%20Arizona). Particularly powerful magnetic storms occurred in the summer and autumn of 2023 (https://www.news.de/panorama/857018312/sonnensturm-warnung-heute-am-14-07-2023-aktuell-experte-befuerchten-moeglichen-doppelten-geomagnetischem-sturm/1/#:~:text=%22In%20jedem%20Fall%20k%C3%B6nnte%20eine,Plasma%20ins%20Weltall%20geschleudert%20wurde and https://dzen.ru/a/ZQti60dLLhDv6SWl?utm_referer=yandex.com.

https://meteoagent.com/de/vorhergesagt-warnungen-sonnensturme.

The purpose of this work was to investigate the reasons for this phenomenon.

2. Material and Method

The optical sensor of a surveillance video camera in the city of Simferopol (Russia), Figures 1...3 (30 frames per second) was used as an axion flow sensor. With the help of this camera, we previously established that its sensor is able to record tracks of Earth axions [1].

3. Analysis and Discussion

Figures 1...3 show photographs of the Earth's axion tracks in the direction of M1 (the crab nebula). The tracks in all photographs are directed towards M1, where a supernova explosion previously occurred (https://en.wikipedia.org/wiki/Crab_Nebula), and its young pulsar PSR B0531+21 (https://ru.wikipedia.org/wiki/ PSR_B0531%2B21) should turn into a neutron star and then, with some probability, even into a magnetar. Therefore, our attention was drawn to the direction of the Earth's axion tracks towards this neutron star. The reason for the occurrence of axion flows in this direction are disturbances of magnetic fields and the occurrence of local high temperatures with a high content of freely oscillating protons (FOP), scheme in Figure 4. According to this scheme, axions and neutrinos are absorbed by FOP, and the speed of movement of these elementary particles significantly exceeds the speed of light. Therefore, events on M1 and the appearance of axion tracks could be considered as events in real time.

As can be seen from Figure 1, tracks 1...3, against the background of the "morning star," are almost strictly vertical. An analysis of their direction using the ZET 9 program (www.astrozet.net) pointed to M1. No tracks in other directions were found.

Figure 1. Photographs of axion tracks in the direction of the Crab Nebula (M1) 09.20.2023 at 04:34 CET. Tracks are indicated by numbers. Place of photography: Simferopol, Russia. Magnetic storms on the Sun, Kp + > 3, https://www.Space weatherlive.com/en.html,%20Kiruna,%20Sweden.html.

In Figure 2, the same tracks 1 and 2 are clearly visible, but tracks 0 and 3 are significantly weakened. Note that at this time the planet was in opposition to M1 and the center of our galaxy (> 177°). The expected axion tracks from city lighting lamps are absent.

Figure 3 shows a photograph of axion tracks in the direction of M1, in the early morning hours, to understand the reproducibility of the phenomenon. The tracks of axions 1, 2 and 3 are also clearly visible here, and track 0 can only be seen upon very careful examination; its signal is very weak.

Figure 4 shows a schema of the equilibrium of a proton with axions and neutrinos during its oscillations between the baryon state and the dissolved state in the physical vacuum [2, 3]. According to this scheme, the nature of energy [7] is the content of FOP in the absorber of axions and neutrinos (high-temperature areas on the Sun and M1) and the desorption of these elementary particles from the camera sensor in the direction of the absorber.

Figure 2. Photographs of axion tracks in the direction of the Crab Nebula on September 21, 2023, at 02:12 CET. Tracks are indicated by numbers. Place of photography: Simferopol, Russia.

Figure 3. Photographs of axion tracks in the direction of the Crab Nebula on 09/21/2023 at 04:24 CET. Tracks are indicated by numbers. Place of photography: Simferopol, Russia.

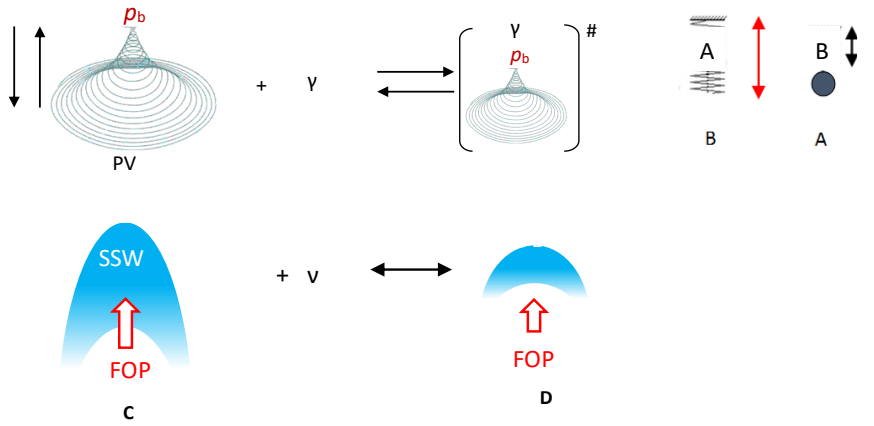

Figure 4. Model of proton oscillations between the physical vacuum and its baryon state (p_b), and the absorption-desorption equilibrium of the interaction of a proton with a neutrino (ν)/axion. For understanding, the oscillation loading models are given on the right and below. **A** – unloaded and **B** – oscillations loaded with adsorbed neutrinos. The so-called "pancakes" (**C** and **D**, https://www.youtube.com/watch? v=lyIEBm5u7-Q) have a vector (broad arrow - gravitational compass) in the direction of a larger bunch of baryonic masses or regions of the surrounding space with a higher FOP content. SSW is a standing shock wave from a neutrino (halo) around a proton. PV - designation of physical vacuum.

Magnetic storms on the Sun (https://tesis.xras.ru/sun_flares.html?m=9&d=21&y=2023), as well as in M1 (https://ru.wikipedia.org/wiki/PSR_B0531%2B21) can be initiated by this cloud and become the beginning of the transformation of the neutron star in M1 into a magnetar (https://en.wikipedia.org/wiki/Magnetar) with magnetic fields more than 10^{11} times higher than those on Earth. In this case, the transformation process will be accompanied by the emergence of local areas in M1 with a very high concentration of freely oscillating protons, which absorb neutrinos and axions from their surroundings. For this reason, the observation results presented in Figures 1....3 become clear. Therefore, the desorption of axions from planet Earth has a real explanation, Figure 5. Here, the desorption vector is directed into the magnetar inside M1.

Figure 5. Constellation of planet Earth in September 2023 relative to the center of our galaxy and M1 (opposition > 177°). The photo of the Crab Nebula is taken from: https://de.wikipedia.org/wiki/Krebsnebel, and the photo of the Black Hole is from: https://de.wikipedia.org/wiki/Sagittarius_A*. The arrows show the direction of the axion tracks, according to the photographs in Figures 1...3.

Figure 6 shows a photograph of axion tracks from street lighting lamps. It can notice that the tracks are in different directions. For better identification, the tracks are marked with numbers. The multi directionality of the tracks indicates the state in which the FOPs are located around the sensors. That is, the camera sensor entered a cloud with a higher FOP content than in the

material of the camera sensor itself or with a very low neutrino content in the cloud (diagram in Figure 4).

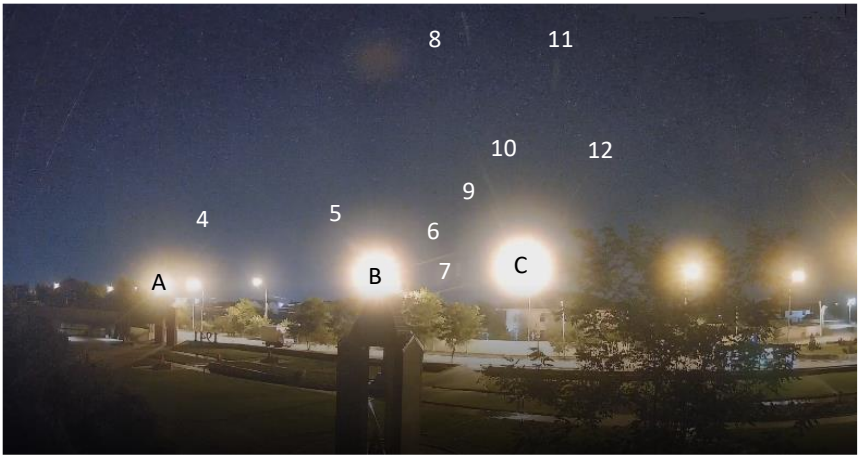

Figure 6. Photographs of axion tracks from street lighting lamps on September 21, 2023 at 19:26 CET. Tracks are indicated by numbers. Place of photography: Simferopol, Russia.

Figure 7. Photo 09/22/2023 at 19:26 CET. Complete absence of axion tracks. Place of photography: Simferopol, Russia.

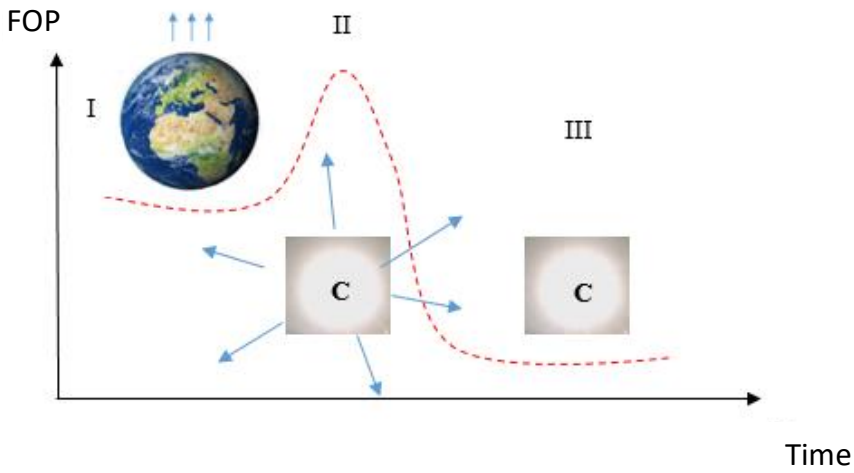

Figure 8. Model of heterogeneity (cloud) in space in which the planet fell. I – axion tracks are directed towards M1 (average FOP density, Figures 1..3), II – high FOP concentration or low concentration of neutrinos/axions in the cloud, multidirectional tracks (Figure 6) and III – low FOP density or high neutrino concentration/ axions (Figure 7). **C** – state of the axion tracks from lamp C in Figures 6 and 7.

In Figure 7, against the background of the morning star, a photograph is given without axion tracks in any direction, to understand the logic of events. It indicates that the cloud has passed our sector of our galaxy.

So, the photographic evidence indicates the passage of a "hole" in the form of a cloud with a low neutrino content from our sector in the galaxy. The potential of this "hole," in the form of a curve of the relative content of FOP (energy) in the cloud, is presented in Figure 8.

Thus, the properties of a cloud with a low content of neutrinos and axions can be attributed to "holes" or void. Such giant clouds are present in the dynamics of elementary particles in the universe. They visit us from time to time, causing disturbances in the equilibrium of these elementary particles with their own clumps/clusters [4] in the form of FOPs on stars.

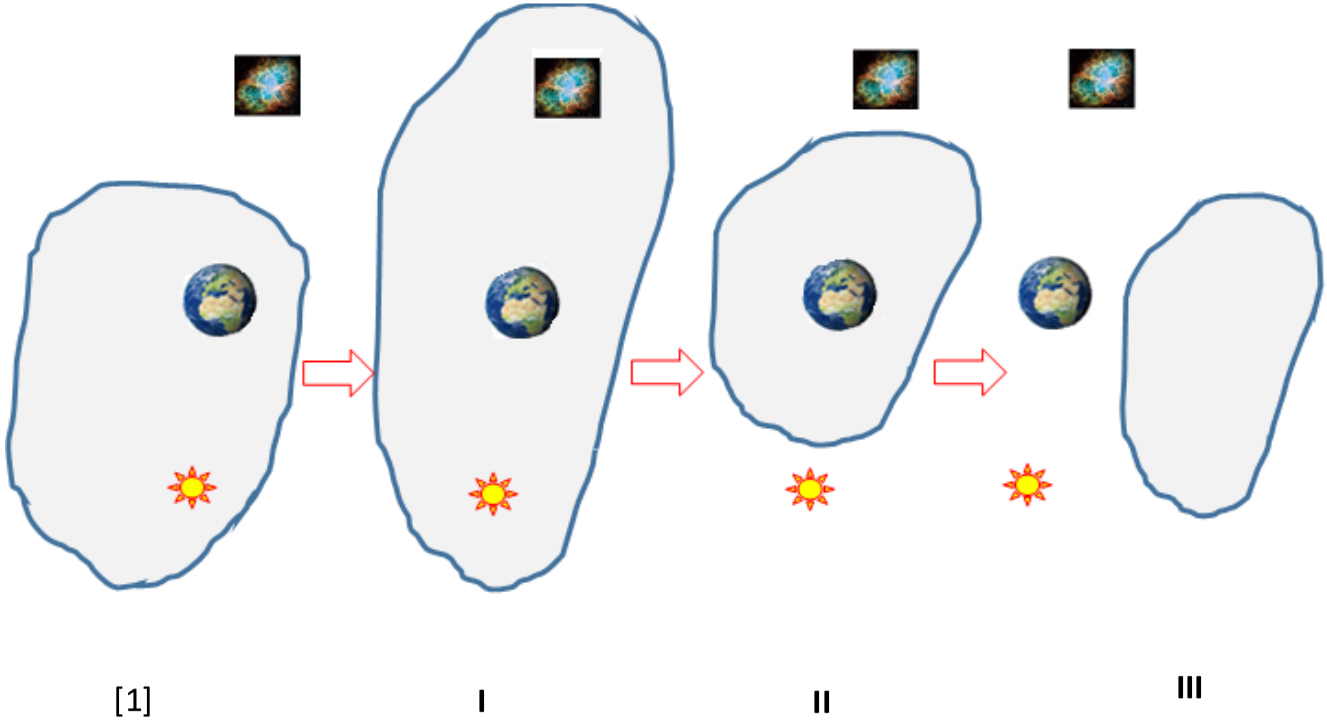

Figure 9. Cloud dynamics models. [1] – axions of the planet Earth in the direction of the Sun, **I** – axions of the Earth in the direction M1 (Figures 1...3), **II** – axions of lighting lamps are directed in different directions, planets inside the cloud (Figure 6) and **III** – the cloud has left the solar system, there are no signals from axions (Figure 7).

Further, it can be assumed that this cloud was the cause of magnetic storms on the Sun and other stars as a result of a violation of the thermodynamic equilibrium of the FOP with the fluxes of neutrinos and axions absorbed by the stars from their surroundings. Since the speed of such neutrino clouds is 10E9 greater than the speed of light [5], it is possible to estimate its size during the events from September 19 to 22, 2023 (4 days, 1E11 km, or 690 AU). Let it be a small cloud. If we take into account that magnetic disturbances have been registered since March 2023, then the size of the large cloud will be 36288 AU or ~ 0.5 lj. That is, the large cloud itself is not homogeneous. On the other hand, the shapes of clouds can be different. For example, one can imagine that only a fragment of a "hole" passed through our solar system. If we imagine that other parts of the cloud caused magnetic storms and even outbursts of super novae in other galaxies, then the size of the "hole" (voids) becomes gigantic, reaching the horizon of the Universe. A hole with a high concentration of FOP or with a low concentration of neutrinos and axions is "filled," with a high probability, filled with preons, which, according to work [6], have the lowest values of oscillation force constants and the lowest interactions with their surroundings, that is, they accelerate the baryon part of the universe, expanding it. For this reason, the cloud can be called a preon cloud. Let us recall that all elementary particles are built from preons [6]. Models of such a cloud can be represented in Figure 9.

Conclusion

In the universe there is a balance between baryonic matter and matter built on preons. In this case, preons are responsible for the expansion, and neutrinos/axions are responsible for its collapse into clumps of baryonic matter.

The Universe is not homogeneous; in addition to baryonic matter, it is represented by clouds of neutrinos, similar in properties to axions and clouds (voids) of preons.

Preon clouds are not homogeneous; they have their own concentration gradients of these elementary particles.

Preon clouds are strong absorbers of neutrinos and axions.

The dynamics of preon clouds are not fully known (direction).

Axion tracks should be used to understand the dynamics of preon clouds and predict magnetic storms on stars.

It is necessary to create a laboratory for monitoring axions.

References

[1] Zubow A., Zubow K., Zubow V. A. Photos of Earth's axion tracks. Horizons in World Physics. Ed. Albert Reimer. NY, 2023, vol. 312, pp.., in print.

[2] Zubow K., Zubow A. V., Zubow V. A. *The Way to the ETIs*. Applied gravitational mass spectroscopy. Nova Sci. Publ. NY, 2014. https://www.novapublishers.com/catalog/product_info.php?products_id=42668&osCsid=5bd85d42dc273360fd48126de7be9daf.

[3] Zubow K., Zubow A. V., Zubow V. A. The Phenomenon of Proton Dissolving in Vacuum and of Proton Condensation from Vacuum. Two Forms of Protons, Structure of Nuclei, Electrons and Atoms. *J. of modern physics*, vol.1, no.1, 2010 pp.175-184. https://www.researchgate.net/publication/228928173_The_Phenomenon_of_Proton_Dissolving_in_Vacuum_and_of_Proton_Condensation_from_Vacuum_Two_Forms_of_Protons_Structure_of_Nuclei_Electrons_and_Atoms.

[4] Zubow A., Zubow K., Zubow V. A. *Cluster construction of elementary particles. Horizons in World Physics*. Ed. Albert Reimer. 2022, vol. 309, pp. 69-80. NY, Nova Publish. Inc. Horizons in World Physics. Nova Science Publishers (novapublishers.com).

[5] Zubow A., Zubow K., Zubow V. A. Blazar TXS 0506+056 and the GN background influences on the LRO of Proteins. *Horizons in World Physics*. Ed. Albert Reimer. NY, NovaPublish. Inc. 2019, vol. 297, pp. 183-200. https://novapublishers.com/shop/horizons-in-world-physics-volume-297/.

[6] Zubow A., Zubow K., Zubow V. A. Preon. Mass and force constant of oscillations in the series of its homologues - elementary particles. *Horizons in World Physics.* Ed. Albert Reimer. NY, 2023, vol. 311, pp... In print.

[7] Zubow A., Zubow K., Zubow V. A. Nature of Energy. Phenomenon of Electric Neutral Particles' Emission in Chemical and Mechano-Chemical Reactions. *Horizons in World Physics.* Nova Sci. Publish. NY, 2014, vol. 22, pp. 37-52. https://www.novapublishers.com/catalog/product_info.php?products_id=50340&osCsid=994455a7afd05deb707594aaf444ed06. International Journal of Condensed Matter, Advanced Materials, and Superconductivity Research, 2014, volume 13 Issue 1. https://www.novapublishers.com/catalog/product_info.php?products_id=53555&osCsid=9dc3348f7b2274186a8949c752b7f142. https://search.proquest.com/openview/7c94c1b2dd200409780d7691af1dd5aa/1?pq-origsite=gscholar&cbl=2034855.

Chapter 8

International System of Quantities (ISQ) Reexamination

Anatoly Zubow[2]
Kristina Zubow[1]
and Viktor A. Zubow[1]
[1]Zubow Consulting, Germany
[2]Group of the Telecommunication Networks Division, TU, Berlin, Germany

Abstract

An adaptation of the International System of Physical Quantities (ISQ) to the new system (BPSQ) was carried out based on the characteristics of the baryon form of the proton.

Keywords: ISQ system, mass, length, time, proton, BPSQ system

1. Introduction

The modern ISQ system is based on subjectively chosen standards, such as the meter, kilogram, and second, which conflicts with the new understanding of the world order and should not have a place in the new physics. There is an urgent need to revise these standards and link them to real, objective standards of baryonic matter, although its share in the Universe is not large (about 4%, [1, 2, 3]). Let's call it the system of standards based on the baryon state of the proton (BPSQ).

In: Horizons in World Physics. Volume 312
Editor: Albert Reimer
ISBN: 979-8-89113-513-0

The aim of this work is to attempt to revise the standards of the International ISQ System and adapt them to new standards based on the baryon state of the proton - BPSQ.

2. Analysis and Discussion

Previously, we found a linear equation to describe masses as a homological series, from elementary particles to planets, stars and galaxies [4]. In this case, masses were considered as vector quantities, the sign of which was their interaction with the surroundings. There is no interaction with the surroundings, then there are no masses as physical objects.

In the new understanding of the masses of physical objects, we will talk about masses as a superposition of dark and baryonic matter. The universal physical object here is the proton in its baryon state. The mass, size and frequency of oscillations between the baryon state and the dissolved state of the proton in a physical vacuum [5, 6] should be taken as the basic reference frames. It is reasonable to believe that all highly developed civilizations in the Universe [5, 7, 8, 9] use these basic reference systems as physical quantities, and our civilization should not lag behind them.

In the equation for the dependence of energy on mass found in [4], on the right side the mass (m) is deliberately given in Daltons, and on the left side, in the coefficient Q, the dimension is given in the ISQ system

$$E=Q\cdot m^{3.94236}, \quad (1)$$

where Q=8.97082E-10, $m^2/s^2\cdot kg^3$, or

$$E=Q\cdot m^4$$

This equation will become correct if we replace the subjective dimensions (m, s and kg, https://ru.wikipedia.org/wiki/Force) with objective ones - the basic characteristics of the proton, its sizes (**д**), oscillation frequency (**в**) and mass (**Da**).

So, in BPSQ should be taken as:

Mass – 1 Dalton (1 **Da**) or 1 kg 5.97872E+26 **Da**
(mass, M according to ISQ, https://ru.wikipedia.org/wiki/Mass),
diameter – 1 *l* (0.8414 ± 0.0019 fm) or in 1 m 1.19E+15 **д**
(length, L according to ISQ, https://ru.wikipedia.org/wiki/Length),

and the time of one oscillation is 1 *t* (2.22E-23 sec) or in 1 sec 2.27E+23 **в** (time, T according to ISQ, https://ru.wikipedia.org/wiki/Time),

then Q in equation (1) will look like this (2):

$$Q = 1.1519E\text{-}106,\ д^2/в^2 \cdot Да^3, \quad (2)$$

and equation (1) is:

$$Э = 1.1519E\text{-}106 \cdot m^{3.94236}, \quad (3)$$

where Э (energy according to BPSQ) has the dimension [$д^2 \cdot Da/в^2$] or in subjective dimensions [$m \cdot l^2/t^2$], or [$m \cdot v^2$]. That is, the energy in the BPSQ is a vector quantity that has the sign of momentum (https://ru.wikipedia.org/wiki/Impulse):

$$Э \rightarrow \vec{m} \cdot \vec{v}^2 = \vec{p} \cdot \vec{v}$$

The physical meaning of this equation can be seen in the example of Brownian motion (https://ru.wikipedia.org/wiki/Brownian_motion). Here, the energy of the mass depends on the impulse, as an integral over the entire volume of the mass (internal and external impulse influences) and the rate of change of their directions, during the inertial reaction of the mass to all impulses, as well as the integral over the entire volume of this mass.

Let's return to the basic values of dimensions in BPSQ. Table 1 presents the coefficients for converting masses from the ISQ system to the BPSQ system.

Table 1. Mass conversion coefficient from ISQ to BPSQ and vice versa

ISQ	BPSQ, Da	BPSQ, Da	ISQ
1 mg	5.97864E+20	1	1.67262E-21, mg
1 g	5.97864E+23	1	1.67262E-24, g
1 kg	5.97864E+26	1	1.67262E-27, kg
1000 kg	5.97864E+29	1	1.67262E-30, T*
Planet mass, 5.9737E24, kg	3.57E+51	1	2.79998E-52, kg
Mass of the Sun, 1.989E30, kg	1.19E+57	1	8.40936E-58, kg
Mass of the Milky Way, 2.98E39, kg	1.78E+66	1	5.60624E-67, kg

*one Ton - non-system technical unit of mass.

Table 2. Presents the coefficients for converting lengths from the ISQ system to the BPSQ system.

Table 2. Length conversion factors from ISQ to BPSQ and vice versa

ISQ	BPSQ, д	BPSQ, д	ISQ
1, Å	1.19E+26	1	8.41E-27, Å
1, nm	1.19E+27	1	8.41E-28, nm
1 μm	1.19E+30	1	8.41E-31, μm
1 mm	1.19E+33	1	8.41E-34, mm
1 m	1.19E+36	1	8.41E-37, m
1 km	1.19E+39	1	8.41E-40, km
Planet diameter, 12,742 km	1.52E+40	1	6.60E-41, km
Diameter of the Sun, 1,400,000 km	1.66E+42	1	6.01E-43, km
Distance Sun-Earth, 150E6 km	1.78E+44	1	5.61E-45, km
Diameter Milky Way, 87,000 lj	9.79E+53	1	1.02E-54, km

Table 3 presents the coefficients for converting times from the ISQ system to the BPSQ system.

Table 3. Coefficient for converting times from ISQ to BPSQ and *vice versa*

ISQ	BPSQ, в	BPSQ	ISQ
1 s	4.5E+22	1, в	2.22222E-23, s
60 s, min	2.7E+24	1, в	3.7037E-25, min
60 min, h	1.62E+26	1, в	6.17284E-27, h
Time of one rotation of the Earth (24 h)	3.888E+27	1, в	2.57202E-28, h
Time of one year (365 days)	1.41912E+30	1, в	7.04662E-31, year
Proton half-life (>10E34 years)	1.41912E+65	1, в	7.04662E-66, years

The hypothetical rest energy of a proton in ISQ is equal to 938.2720881(29) MeV should be taken as the base unit in the new BPSQ and used to recalculate energies, as it is not a real mass without interaction with the surroundings.

To recalculate the dimensions of forces from ISQ (Newton, https://ru.wikipedia.org/wiki/Force) to BPSQ (**С**, force), you should use the following Table 4.

Table 4 presents the coefficients for converting the dimensions of forces from the ISQ system (N, kg·m/s^2) to the BPSQ system (**С**, **Да·д/в**^{2}) and vice versa.

Table 4.

Forces	ISQ, N	BPSQ, C	BPSQ, C	ISQ, N
1 Newton	1	3.51085E+17	1	2.84831E-18
The force of attraction between the Sun and Earth	3.50E+22	1.23E+40	1	8.13804E-41
The force of attraction between the Earth and the Moon	2.00E+20	7.02E+37	1	1.42416E-38
Push force of the engines of the first and second stages of the Soyuz launch vehicle	4.00E+06	1.40E+24	1	7.12078E-25
Pull force of diesel locomotive 2TE70	6.00E+05	2.11E+23	1	4.74719E-24
Sound pressure strength in the human ear at the threshold of hearing	2.00E-09	7.02E+08	1	1.42416E-09

For trigonometric calculations in BPSQ, only the radian measure of angles is used, 1 rad = 180°/π ≈ 57.3° in ISQ.

Conclusion

The transition to a new system of BPSV standards, based on the known characteristics of the baryon form of the proton, is possible and necessary.

Sponsoring

To continue work in this direction, we are looking for sponsors. Write to us.

References

[1] Blennow, M. Basudeb Dasgupta, Enrique Fernandez-Martinez, Nuria Rius. Aidnogenesis via Leptogenesis and Dark Sphalerons. MPP-2010-125, IFIC/10-32, FTUV-10-0909. *arXiv*:1009.3159v1 [hep-ph]. 2010. 16Sep.

[2] Cueva, F., Nucamendi, U. Reconstructing the interaction term between dark matter and dark energy. *arXiv*:1007.2459v1 [gr-qc]. 2010. 15 Jul.

[3] Frampton, P. H. Black Holes as Dark Matter. *AIP Conference Proceedings* (Quantum Theory). 2010, vol. 232**,** pp. 53-57.

[4] Zubow K., Zubow A., Zubow V. New constant Q=8.97082E-10, $m^2/s^2 \cdot kg^3$. In $E=Q \cdot m^4$. Vector nature of masses. *Horizons in World Physics.* Ed. Albert Reimer. NY, 2023, vol. 311, pp. 189…198.
Horizons in World Physics. Volume 311 – Nova Science Publishers (novapublishers.com).

[5] Zubow K., Zubow A.V., Zubow V.A. The Way to the ETIs. *Applied gravitational mass spectroscopy*. Nova Sci. Publ. NY, 2014.
https://www.novapublishers.com/catalog/product_info.php?products_id=42668&osCsid=5bd85d42dc273360fd48126de7be9daf .

[6] Zubow K., Zubow A.V., Zubow V.A. The Phenomenon of Proton Dissolving in Vacuum and of Proton Condensation from Vacuum. Two Forms of Protons, Structure of Nuclei, Electrons and Atoms. *J. of modern physics*, vol.1, no.1, 2010 pp.175-184.
https://www.researchgate.net/publication/228928173_The_Phenomenon_of_Proton_Dissolving_in_Vacuum_and_of_Proton_Condensation_from_Vacuum_Two_Forms_of_Protons_Structure_of_Nuclei_Electrons_and_Atoms.

[7] Zubow K., Zubow A.V., Zubow V.A. Signals from Extraterrestrial Intelligences. *Horizons in World Physics*, editor, Albert Reimer. Nova Science Publishers, Inc. NY. 2013, vol. 280, pp.191-210.
https://www.novapublishers.com/catalog/product_info.php?products_id=38323.

[8] Zubow K., Zubow A.V., Zubow V.A. Super Speed Communication with Uranus Inhabitants. Horizons in World Physics. In *Horizons in World Physics*. Editor Albert Reimer 2013, vol. 281, pp.67-92.
https://www.novapublishers.com/catalog/product_info.php?products_id=43069&osCsid=5bd85d42dc273360fd48126de7be9daf.

[9] Zubow A., Zubow K., Zubow V.A. Dialogue with Extraterrestrial Intelligence (ETI) from Gliese 581 in Real Time. Ed. Albert Reimer. *Horizons in World Physics.* NY, 2013, vol. 281, pp.93-104.
https://www.novapublishers.com/catalog/product_info.php?products_id=43069&osCsid=5bd85d42dc273360fd48126de7be9daf.

[10] Zubow A., Zubow K., Zubow V.A. Dialogue with Extraterrestrial Inhabitants of Kepler-30 in Real Time. Two Super Speed Communication Channels. Ed. Albert Reimer. *Horizons in World Physics.* 2013, vol. 281, pp. 25-30. NY.
https://www.novapublishers.com/catalog/product_info.php?products_id=43069&osCsid=5bd85d42dc273360fd48126de7be9daf.

Chapter 9

Photos of Earth's Axion Tracks

Anatoly Zubow[2]
Kristina Zubow[1]
and Viktor Zubow[1]
[1]Zubow Consulting, Germany
[2]Group of the Telecommunication Networks Division, TU, Berlin, Germany

Abstract

The paper presents photographs of tracks of the Earth's axions that are desorbed in the direction of magnetic storms on the Sun at the beginning of August 2023. A model of the desorption process is given. Observation results are discussed.

Keywords: axions, photographs, tracks, magnetic storms, Sun

1. Introduction

There are a number of works devoted to axions (https://de.wikipedia.org/wiki/Axion, [1, 2, 3], whose role in cosmology and nuclear physics, for example, in resolving the strong CP problem in quantum chromodynamics (QCD) and understanding of the nature of dark matter is key, but the methods of registration and direction of motion of axions are very debatable and ambiguous. The purpose of this work was to detect and register traces of axions.

In: Horizons in World Physics. Volume 312
Editor: Albert Reimer
ISBN: 979-8-89113-513-0

2. Analysis and Discussion

Usually, the decay of an axion into photons ($A^0 \rightarrow \gamma + \gamma$) is used for their detection. These photons with low energies (~1 eV) fall into the infrared region of the electromagnetic spectrum and can in principle be detected by conventional digital cameras, such as the SONY superHAD CCD matrix, [4].

The dissolution of protons in PV [1, 5] has a multistage character. First, protons dissolve to neutrinos/axions and then they dissolve to preons [3], and the lower the gravitational field strength, the greater the dominance of the baryonic proton over its form dissolved in the PV. It follows from this that when opposed to Sun giant; the proton dissolves completely to neutrinos/axion and preons, Figure 1.

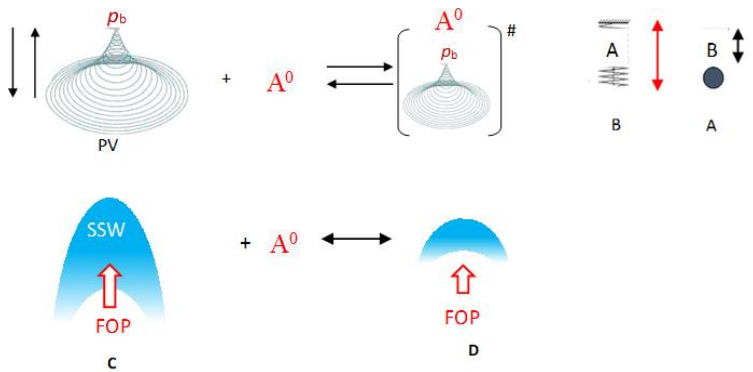

Figure 1. Model of proton oscillations between the physical vacuum (PV) and its baryon state (p_b), and the absorption-desorption equilibrium of the interaction of a proton with an axion (A^0). For understanding, the oscillation loading models are given on the right and below. **A** – unloaded and **B** – oscillations loaded with adsorbed axions. The so-called "pancakes" (**C** and **D**, https://www.youtube.com/ watch?v=lyIEBm5u7-Q) have a vector (broad arrow - gravitational compass) in the direction of a larger bunch of baryonic masses or regions of the surrounding space with a higher free oscillation protons (FOP) content. SSW is a standing shock wave from an axion (halo) around a proton. PV - designation of physical vacuum.

On August 6, 2023, we managed to photograph the quanta of solar axions, which decayed into photons in the atmosphere. On the photo (Figure 2) shows the tracks of these elementary particles (EP), made by a digital camera in the Russian Crimea immediately after sunrise at 06:55 Moscow time (MT). Since these EP are not visible to the eye ($\lambda > 760$ nm), and the digital camera allows to register this events in the range from 760 to 1000 nm, the registration was

successful. As can be seen from this Figure, the star generates bright tracks (16) in the direction of the camera, which are the result of the decay of axions with energies of ~1 eV (EP, ~ 900 nm, or approx. 1 eV or 300 THz) into photons (https://de.wikipedia.org/wiki/CAST-Experiment, ~1 eV). These tracks have the same length, that is, the same nature.

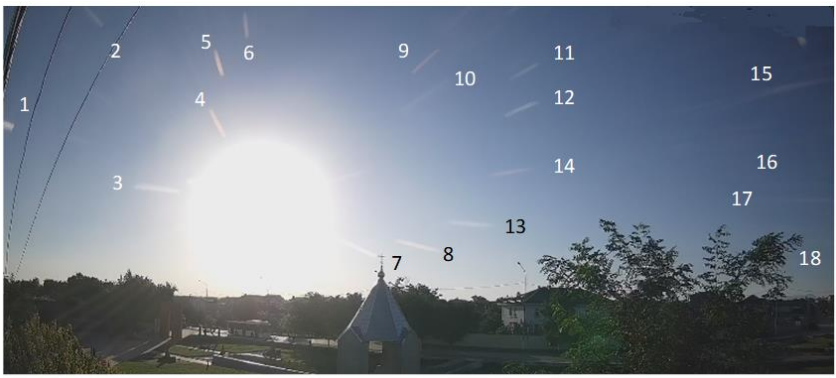

Figure 2. Photos of solar axion tracks over Simferopol on 08/06/2023 at 06:55 MT. 30 fps. The numbers indicate the tracks of axions emanating from the camera sensor in the direction of the star. Auroral activity index Kp=1, https://www.Spaceweather live.com/en.html, Kiruna, Sweden.

For comparison, a photograph was taken under the same conditions, but 2 hours later (Figure 3). In this photograph, a few tracks of axions are found due to the heating of the atmosphere and the increase in brightness.

The question remains: do these photographs show perspective or retrospective? If there are higher temperatures in magnetic storms, and therefore higher FOP [6] concentrations, then these are the Earth's axions and we see a perspective in the photographs. Otherwise, the flux of solar axions in the direction of the Earth. As will be shown below (Figures 3...7), the tracks are repeated, and one would think that these are simple sun glare. But it's not. Their repeatability is the result of desorption of axions from the same places of the camera sensor, from the same nuclei of atoms, reacting selectively to FOP in solar flares (coronal mass ejection - CME). With an increase in the CME intensity (an increase in the Kp4 index from 1 on August 6, 2023, to 4 on August 8, 2023, Figures 9 and 10), the number of types of atomic nuclei of the chamber sensor desorbing axions also increases.

Figure 3. Photographs of the Sun by Simferopol on 08/06/2023 at 08:55 Moscow time. 30 fps.

Figure 4 shows a photograph of the star 24 hours later, when the magnetic storm ended. The absence of axion tracks is seen.

Figure 4. Photographs of the Sun by Simferopol on 08/07/2023 at 06:55 Moscow time. 30 fps.

On August 8, flashes of the magnetic storm on the Sun resumed and axion tracks were registered again, Figure 5.

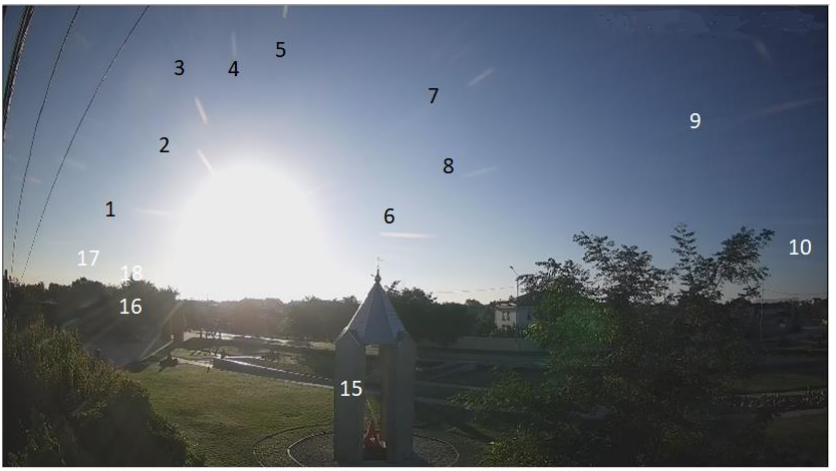

Figure 5. Photographs of the Sun by Simferopol on 08/08/2023 at 06:40 Moscow time. 30 fps.

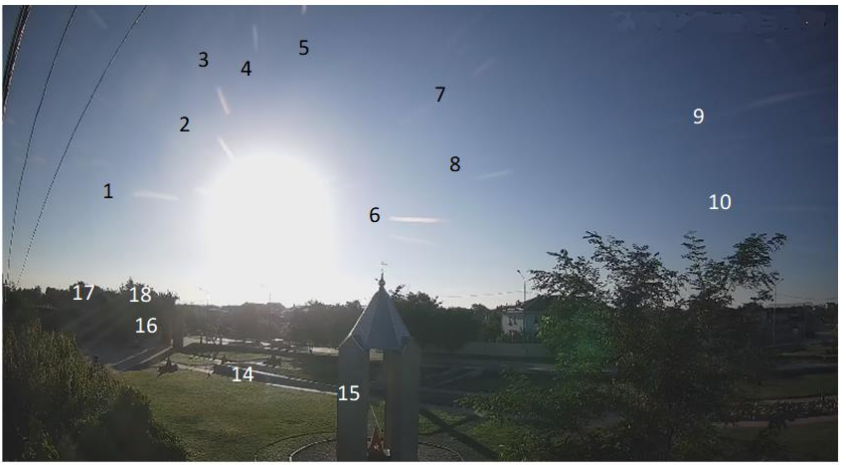

Figure 6. Photographs of the Sun by Simferopol on 08/08/2023 at 06:50 Moscow time. 30 fps.

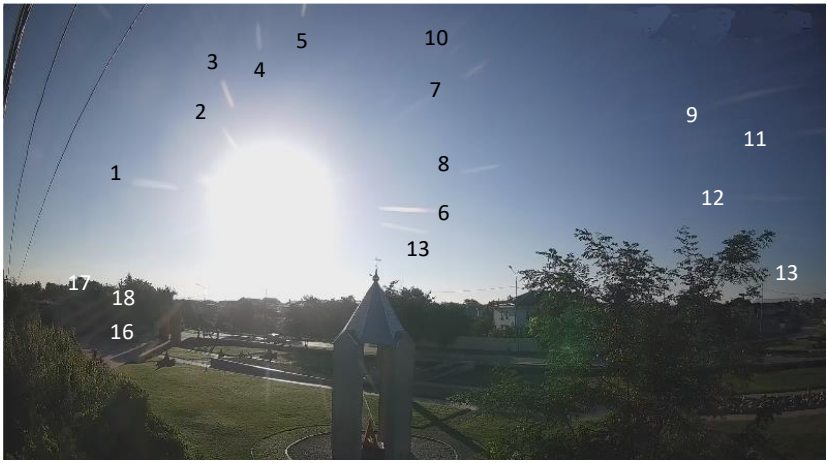

Figure 7. Photographs of the Sun by Simferopol on 08/08/2023 at 06:54 Moscow time. 30 fps.

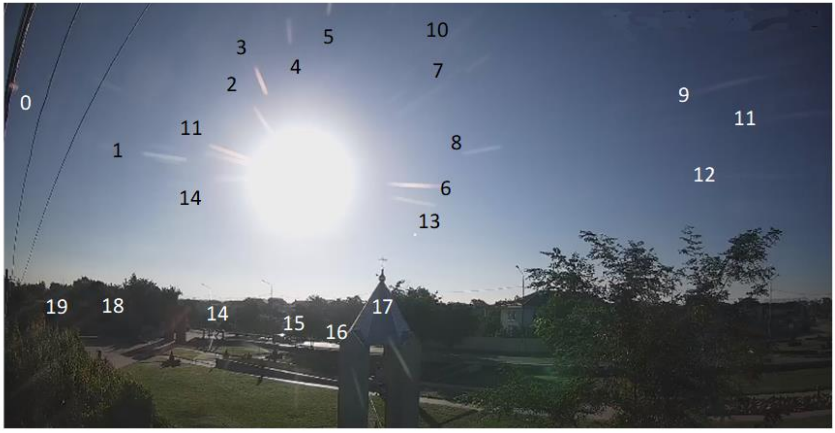

Figure 8. Photographs of the Sun by Simferopol on 08/08/2023 at 07:10 Moscow time. 30 fps.

Note that at this time, solar wind flows from magnetic storms on the star touched our planet (https://earth-chronicles.ru/news/2023-08-06-173248). We also note that axion tracks were seen from uranium ships, which we could not register in the visible range. This indicates their use of strong magnetic fields, which generate axions.

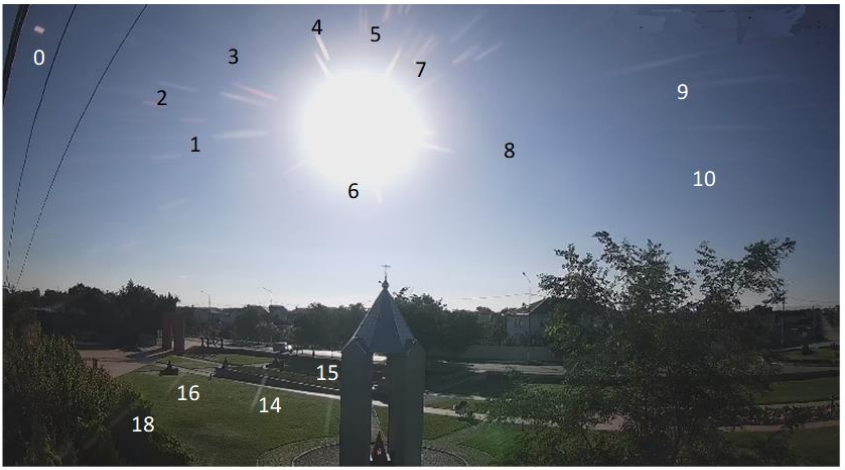

Figure 9. Photographs of the Sun by Simferopol on 08/08/2023 at 07:47 Moscow time. 30 fps. Kp = 4.

Figure 10. Photographs of the Sun by Simferopol on 08/08/2023 at 08:40 Moscow time. 30 fps. Kp = 4.

An analysis of the photographs showed that as the level of the star above the horizon increases, the axion tracks move away from the sensor in the direction of the Sun, a celestial body with a greater mass and temperature. The model of this phenomenon - the influence of the Earth's gravitational field on the position of the decay tracks of axions, which, like neutrinos, carry away

mass from the planet, is given in Figure 11. According to this model, the lower the star above the horizon, the stronger the influence of the planet's gravitational field (https://ru.wikipedia.org/wiki/Strength_of_gravitational_field) on the process of desorption of its masses in the form of axions. At the same time, the process, like any event, includes the time factor. Thus, the duration of the influence of the planet's gravitational field strength on the process of axion desorption plays an important role here. It can be seen from the Figures that the tracks from different protons of the nuclei of the sensor atoms are located directly in front of the camera at the earliest hours of sunrise. As the star's altitude increases, this influence decreases and the tracks move away from the sensor in the direction of high masses and temperatures, with a high FOP (Figure 1) content on the Sun.

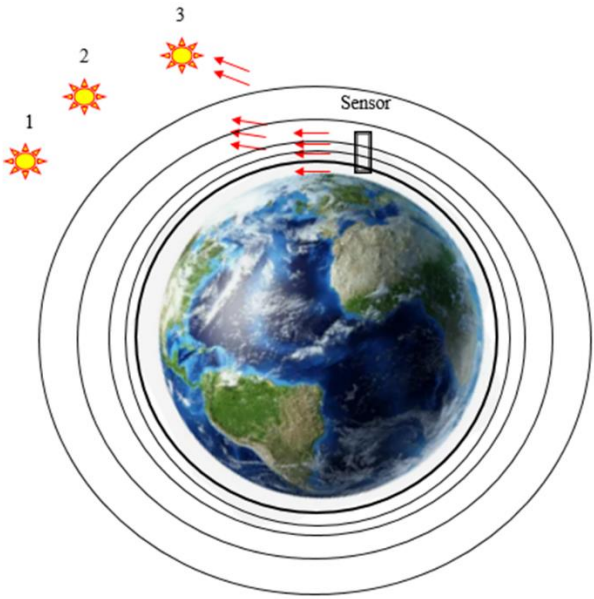

Figure 11. A model of the influence of the height of a star above the horizon on the position of the tracks of axions desorbed from the planet in the direction of the Sun. The density of lines of tension of the gravitational field of the Earth is given conditionally in the form of concentric circles.

Since axions are characterized by gravitational and electromagnetic properties (https://translated.turbopages.org/proxy_u/en-ru.ru.21af6ad5-64d31666-fe8f54fe-74722d776562/https/en.wikipedia.org/wiki/Axion), then the second factor should also be excluded.

The removal of axion tracks from the sensor, with an increase in the star's altitude, therefore, can be understood as an acceleration stage or the time of initiation of decay to photons. Then the decay of axions can be considered as a certain critical rate at which its kinetic energy (E_k) exceeds the potential (E_p) of a cluster built from photons [3].

$$E_к = mv^2/2 > E_p = mgh,$$

where g is not constant (https://en.wikipedia.org/wiki/Eotvos_(unit), https://dxdy.ru/topic1857.html) and depends on the nature of matter, v is velocity, *m* is mass, as vector quantity [3] and h interaction distance.

It can be seen from the photographs that the tracks have a certain thickness, length and brightness, which should be understood as the desorption of many axions by the sensor nuclei and their decay into many photons.

Conclusion

Registration of axion tracks is possible with simple digital cameras.

The tracks are the result of desorption of axions from the protons of the camera's sensor nuclei, that is, from the Earth's surface in the direction of freely oscillating protons (FOPs) in the high temperature regions of the massive Sun.

The appearance of axion tracks directly depends on the intensity of magnetic storms on the star.

With an increase in the intensity of magnetic storms on the star, the number of tracks increases as a result of the increasing involvement of the protons of the camera sensor nuclei in the process of desorption of axions.

The temperature distribution (content of FOP) in magnetic storms selectively activated the desorption of axions from the protons of the atom nuclei in camera sensor.

The duration of the tracks is approximately the same and equals 0.03 s on average.

The lower the Sun is above the horizon, the closer the tracks are to the camera sensor and vice versa, the higher the star is above the horizon, the further the tracks are from the camera surface.

Sponsoring

To continue working in this direction, we are looking for sponsors. Please write to us.

References

[1] Zubow K., Zubow A.V., Zubow V.A. The Way to the ETIs. Applied gravitational mass spectroscopy. Nova Sci. Publ. NY, 2014. https://www.novapublishers.com/catalog/product_info.php?products_id=42668&osCsid=5bd85d42dc273360fd48126de7be9daf.

[2] Malte Buschmann, Raymond T. Co, Christopher Dessert, and Benjamin R. Safdi. Axion Emission Can Explain a New Hard X-Ray Excess from Nearby Isolated Neutron Stars. Phys. Rev. Lett. 2021, v. 126, p. 021102. https://journals.aps.org/prl/abstract/10.1103/PhysRevLett.126.021102.

[3] Zubow A., Zubow K., Zubow V.A. Preon. Mass and force constant of oscillations in the series of its homologues - elementary particles. Horizons in World Physics. Ed. Albert Reimer. NY, 2023, vol. 311, pp.. in print.

[4] https://yandex.com/images/search?img_url=https%3A%2F%2Fsun9-50.userapi.com%2Fimpf%2Fc638924%2Fv638924384%2F25316%2F9nkLWBM-J8Y.jpg%3Fsize%3D604x313%26quality%3D96%26sign%3D7817fc00447a8747a8ac01853a9a453d%26c_uniq_tag%3D4b83HkQJhrltzXb4r6KkfCw0PE9L7jS90BsLtoZcUUY%26type%3Dalbum&lr=112251&pos=38&rpt=simage&source=serp&stype=image&text=какие%20частоты%20видит%20камера%20видеонаблюдения https://yandex.com/images/search?img_url=https%3A%2F%2Fsun9- 50.userapi.com%2Fimpf%2Fc638924%2Fv638924384%2F25316%2F9nkLWBM-J8Y.jpg%3Fsize%3D604x313%26quality%3D96%26sign%3D7817fc00447a8747a8ac01853a9a453d%26c_uniq_tag%3D4b83HkQJhrltzXb4r6KkfCw0PE9L7jS90BsLtoZcUUY%26type%3Dalbum&lr=112251&pos=38&rpt=simage&source=serp&stype=image&text= which%20frequencies%20%20camera%20ofsurveillance%20sees.

[5] Zubow K., Zubow A.V., Zubow V.A. The Phenomenon of Proton Dissolving in Vacuum and of Proton Condensation from Vacuum. Two Forms of Protons, Structure of Nuclei, Electrons and Atoms. *J. of modern physics*, vol.1, no.1, 2010 pp.175-184.
https://www.researchgate.net/publication/228928173_The_Phenomenon_of_Proton_Dissolving_in_Vacuum_and_of_Proton_Condensation_from_Vacuum_Two_Forms_of_Protons_Structure_of_Nuclei_Electrons_and_Atoms.

[6] Zubow A., Zubow K., Zubow V.A. Nature of Energy. Phenomenon of Electric Neutral Particles' Emission in Chemical and Mechano-Chemical Reactions. Horizons in World Physics. Nova Sci. Publish. NY, 2014, vol. 22, pp. 37-52. https://www.novapublishers.com/catalog/product_info.php?products_id=50340&osCsid=994455a7a

fd05deb707594aaf444ed06. - International Journal of Condensed Matter, Advanced Materials, and Superconductivity Research, 2014, volume 13 Issue 1. https://www.novapublishers.com/catalog/product_info.php?products_id=53555&osCsid=9dc3348f7b2274186a8949c752b7f142. https://search.proquest.com/openview/7c94c1b2dd200409780d7691af1dd5aa/1?pq-origsite=gscholar&cbl=2034855.

Chapter 10

Photos of Axion Tracks in the Double Planet Earth-Moon in a New Cloud of Preons

Kristina Zubow[1,*]
Viktor A. Zubow[1]
and Anatoly Zubow[2]
[1]Zubow Consulting, NPO. Germany
[2]Group of the Telecommunication Networks Division, TU, Berlin, Germany

Abstract

Photographs of the tracks of the Moon's axions are presented against the background of the tracks of the Earth's axions during the period of intense magnetic storms on the Sun (December 2023) as a result of falling into the preon cloud. Traces of lunar axions directed towards the center of the Earth and multidirectional tracks of Earth axions in the region of the preon cloud with different preon contents were discovered. A model of the preon cloud is given. A conclusion is made about the vector nature of the masses and the priorities in the routes of axions in the Moon-Earth-preon cloud system. It has been suggested that the cloud of preons is a "guest" from an accumulation of dark energy in the Universe (voids). A new model of the aging of the Universe as a process of mass agglomeration is being discussed.

Keywords: axions, photographs, tracks, preons, cloud, Moon, Earth,void, aging of the Universe

[*] Corresponding Author's Email: vzubow@googlemail.com.

In: Horizons in World Physics. Volume 312
Editor: Albert Reimer
ISBN: 979-8-89113-513-0

1. Introduction

Previously, we proposed an objective method for optical registration of flows of terrestrial axions (https://ru.wikipedia.org/wiki/Axion) in the direction of stars and star clusters [1, 2] with local appearances of very high temperatures. Then the cause of the occurrence of magnetic storms on stars was discovered as a consequence of the imbalance of baryonic protons with their dissolved form in the physical vacuum - preons [3, 4]. This equilibrium was disrupted when clouds of preons appeared in the visible part of the Universe [5, 6]. At the beginning of December 2023, the appearance of a new giant cloud of preons was discovered from the constellation Virgo. In this favor, it was of interest to trace the dynamics of the cloud and its influence on the double planet Earth-Moon.

The purpose of this message was the experimental detection of a new cloud of preons moving towards the solar system, its influence on the Moon and the double planet Earth-Moon (https://ru.wikipedia.org/wiki/Double_planet).

2. Analysis and Discussion

At the end of November 2023, using a digital camera, it was possible to register new flows of terrestrial axions, Figure 1. It became clear that a new cloud of preons was rapidly approaching us.

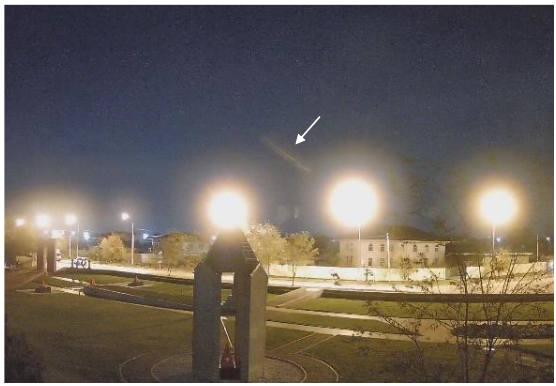

Figure 1. Photograph of a package of tracks (indicated by an arrow) of terrestrial axions (Simferopol, Russia) 11/26/2023 at 01:37 CET.

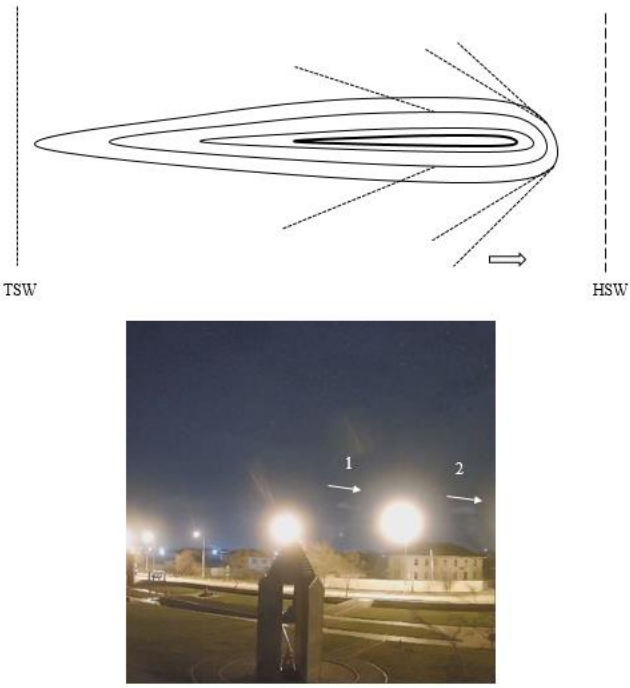

Figure 2. Photograph of terrestrial axions on 12/03/2023 at 01:03 CET. Simferopol, Russia. 1 – Flow of axions from the constellation Virgo and 2 this flow in the opposite direction (Neptune). A model of the preon cloud is given above the photograph. HSW – head shock wave, TSW – terminal shock wave [7]. Isobars inside the cloud are shown by lines of different thicknesses

Four days later, the tracks of the earth's axions (Figure 2, directions 1 and 2) made it clear that we had already into a cloud of preons, moving very quickly from the direction of the constellation Virgo in the direction of a giant clump of baryonic masses in the Universe.

The new preon cloud was distinguished by high heterogeneity of preon concentrations within it. It was expressed in the multi directionality of tracks and their shapes in different areas of the cloud, Figure 3. Streams 3, 5 and 6 are presented in the form of torches from a set of tracks, indicating the presence of shock fronts in the cloud within these heterogeneities in the direction of movement. The very direction of movement of the cloud and the presence of a shock front in the form of a shock wave indicates the presence in the Universe of a very strong preon attractor, which may be a region of space with a high concentration of very large masses of dark and baryonic matter. An alternative could be the cloud flying, like a “hole” in the

intergalactic vacuum, into the Universe visible to us and the cloud being absorbed by its dark and baryonic matter. This alternative seems to us the most likely.

Thus, the aging of the Universe proceeds along the route of transformation of dark energy (preons) into dark and then into baryonic matter, and the agglomeration of baryonic matter to a giant center with a giant mass and then its decay.

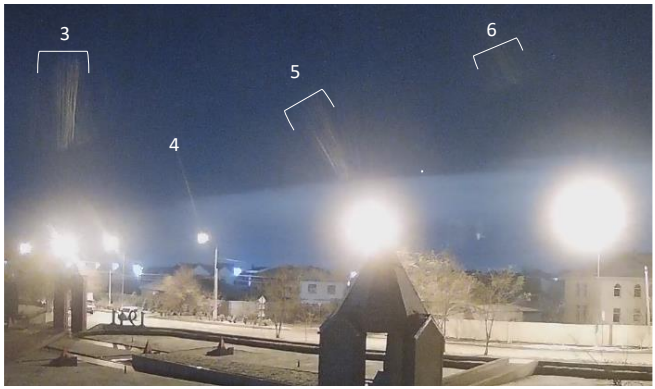

Figure 3. Photograph of tracks (indicated by an arrow) of terrestrial axions (Simferopol, Russia) 12/04/2023 at 21:21 CET. 3, 5 and 6 – track torches, 4 – a strong and narrow trace of the decay of axions into photons.

Figure 4 shows a photograph of axion tracks in the system of the double planet Earth-Moon, at the moment of the rise of our satellite. The flow of axions of the Moon (7) towards the center of our planet is visible. At the same time, the multi directionality of the tracks of the Earth's axions was preserved, which means that the double planet is located in a cloud of preons.

To understand the reproducibility of the results, multiple photographs were taken of the state of the axion tracks in the Moon-Earth system. Figure 5 shows a photograph of axion traces at the time of moonrise on December 5, 2023 at 01:36 Northeast time. As can be seen in this case, the satellite detects a flow of axions to the center of our planet. These facts confirm our earlier conclusions that in the hierarchy of masses there is a general flow from small masses towards larger ones [6]. That is, in the taxon of masses there is a dominance of large masses at the expense of small ones. Mass is a vector quantity, and the Universe, as it ages, becomes denser.

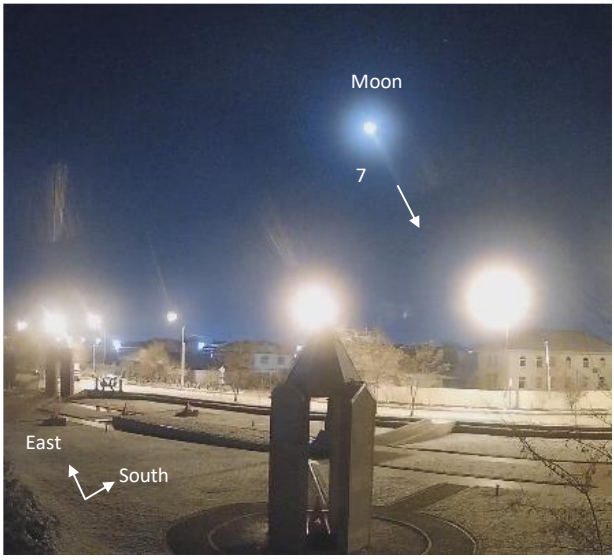

Figure 4. Photograph of axion tracks in the Earth-Moon double planet system, 12/04/2023 at 23:57 CET. Simferopol, Russia.

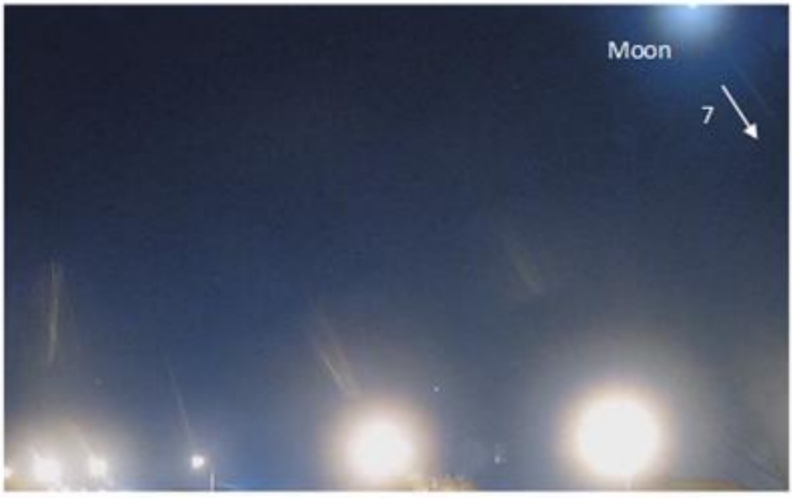

Figure 5. Photograph of axion tracks in the Earth-Moon double planet system, 12/05/2023 at 01:36 CET. Simferopol, Russia.

On December 7, 2023, the axion tracks disappeared.

Figure 6 shows a model of absorption of dark energy by the surrounding masses of dark and baryonic matter, for understanding.

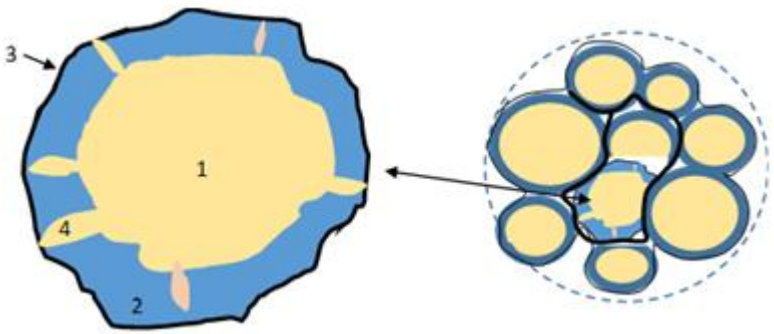

Figure 6. Model of dissolution of dark energy (1, 74%) in dark (2, 22%) and baryonic (3, 4%) matter through the ejection of preon clouds (4) into the latter. On the right is a model of the "emulsion" of the Universe (fragment, 2D projection).

So, the current state of the Universe can be understood as an emulsion of three types of matter, and aging as an agglomeration of masses.

From June 2023 to December 10, 2023, the preon cloud created gravitational noise with frequencies of 19.739, 20.147 and 20.417 kHz. These signals disappeared after the cloud went beyond the horizon of the Universe.

Conclusion

At the beginning of December 2023, the solar system was in a new, rapidly moving cloud of preons.

The preon cloud is heterogeneous.

The cloud has an extremely high temperature.

A preon cloud is a region of space with dark energy.

The movement of the preon cloud has a shock wave front.

The preon cloud is a "hole" in the vacuum of the Universe.

A preon cloud is a dissolved form of a proton in a physical vacuum.

A cloud of preons is a "guest" from an accumulation of dark energy in the Universe (voids).

Heterogeneities of preon concentrations in the cloud cause the generation of axion flows in the double planet Earth-Moon in the direction of heterogeneities of preon concentrations in the cloud.

In the Earth-Moon double planet, the flow of lunar axions is directed towards the Earth.

The cloud of preons moves in the direction of a strong attractor - a region in the Universe with a giant clot of baryonic matter.

Gravitational noise from the movement of a preon cloud can be used to detect its approach and forecast magnetic storms on the Sun.

Mass is a vector quantity.

The universe is an emulsion of masses of three forms of matter.

The aging of the universe follows the path of agglomeration of masses.

References

[1] Zubow, A., Zubow, K., Zubow, V. A. **(**2023). Photos of Earth's axion tracks. *Horizons in World Physics*. Ed. Albert Reimer. NY, vol. 312, pp.., in print.

[2] Zubow, A., Zubow, K., and Zubow, V. A. **(**2023). A giant cloud of preons (voids) in our Universe. Monitoring Earth's axions. *Horizons in World Physics*. Ed. Albert Reimer. NY, vol. 312, pp.., in print.

[3] Zubow, K., Zubow, A. V., and Zubow, V. A. (2014). The Way to the ETIs. *Applied gravitational mass spectroscopy*. Nova Sci. Publ. NY, https://www.novapublishers.com/catalog/product_info.php?products_id=42668&osCsid=5bd85d42dc273360fd48126de7be9daf.

[4] Zubow, K., Zubow, A. V., and Zubow, V. A. (2010). The Phenomenon of Proton Dissolving in Vacuum and of Proton Condensation from Vacuum. Two Forms of Protons, Structure of Nuclei, Electrons and Atoms. *J. of modern physics*, vol. 1, no. 1, pp. 175-184. https://www.researchgate.net/publication/228928173_The_Phenomenon_of_Proton_Dissolving_in_Vacuum_and_of_Proton_Condensation_from_Vacuum_Two_Forms_of_Protons_Structure_of_Nuclei_Electrons_and_Atoms.

[5] Zubow, A., Zubow, K., and Zubow, V. A. (2023). Preon. Mass and force constant of oscillations in the series of its homologues - elementary particles. *Horizons in World Physics*. Ed. Albert Reimer. NY, vol. 311, pp. 199…202. (Horizons in World Physics. Volume 311 – Nova Science Publishers (novapublishers.com).

[6] Zubow, K., Zubow, A., and Zubow, V. (2023). New constant Q = 8.97082E-10, $m^2/s^2 \cdot kg^3$, In E = $Q \cdot m^4$, Vector nature of masses. *Horizons in World Physics.* Ed. Albert Reimer. NY, vol. 311, pp. 189…198.(Horizons in World Physics. Volume 311 – Nova Science Publishers (novapublishers.com).

[7] Album of the flow of liquids and gases. Ed. M. Van Dycke. Moscow. Mir. 1986.

Chapter 11

New Cloud of Preons. Approaching the Solar System. Photos of Earth's Axion Tracks

Anatoly Zubow[2]
Kristina Zubow[1,*]
and Viktor A. Zubow[1]
[1]Zubow Consulting, NPO, Germany
[2]Group of the Telecommunication Networks Division, TU, Berlin, Germany

Abstract

Based on photographs of axion tracks, the appearance of a new cloud of preons in the constellation Virgo was recorded in November 2023. The cloud moved towards the solar system at high speed (~1.5E9***c***). Photographs of the Earth's axion tracks in the direction of the preon cloud are presented. Strong magnetic storms are predicted in star systems, including our Sun, through which the cloud passes.

Keywords: axions, photographs, tracks, cloud, preons, stars, magnetic storms, dark energy

1. Introduction

Previously, we proposed an objective method for optical registration of fluxes of terrestrial axions in the direction of stars and star clusters [1, 2] with local manifestations of very high temperatures. Axion flows arise when clouds of preons appear [3, 4].

* Corresponding Author's Email: vzubow@googlemail.com.

In: Horizons in World Physics. Volume 312
Editor: Albert Reimer
ISBN: 979-8-89113-513-0

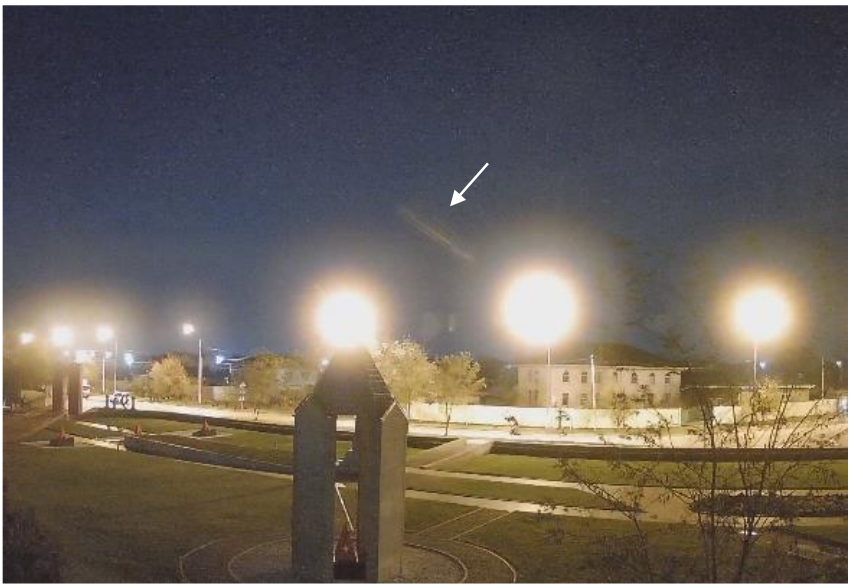

Figure 1. Photograph of a bundle of tracks (indicated by an arrow) of terrestrial axions (Simferopol, Russia) 11/26/2023 at 01:37 CET.

Figure 2. Photograph of a set of tracks (indicated by an arrow) of terrestrial axions (Simferopol, Russia) 11/26/2023 at 04:28 CET. Angle 43°.

The purpose of this report was the experimental detection of a new cloud of preons moving towards the solar system.

2. Analysis and Discussion

In November 2023, using a digital camera, it was possible to record the flows of terrestrial axions in the direction of the constellation Virgo, Figure 1.

Four hours later, photography was repeated, Figure 2.

As can be seen from Figures 1 and 2, the flow of terrestrial axions (https://ru.wikipedia.org/wiki/Axion) has a pronounced directionality and is represented by a set of thin lines (tracks), as a result of the decay of axions into photons.

Figure 3. Photograph of terrestrial axions on November 28, 2023 at 20:28 CET. Simferopol, Russia.

To ensure reproducibility of the results, photographs were taken a third time, Figure 3. In the enlarged image, the axion fluxes are indicated by two arrows, with the upper flux being the most pronounced and also represented by a narrow packet of thin lines, and the lower one by a wide scatter of tracks.

Let's observe the dynamics of axion tracks. Figures 4...6 show photographs of interchangeable axions taken from the same place as in Figures 1, 2 and 3.

Figure 4. Photograph of terrestrial axions on November 29, 2023 at 18:15 CET. Simferopol, Russia. Angle 55°.

Over the course of several days, the angle of the axion torch above the horizon sharply increased by more than 10°. The torch itself became wider. A torch appeared at the second source, on the left. The distance from the beginning of the tracks to their source has increased slightly.

The next photograph (Figure 5) shows the activation of four axion sources. The angle of the plume above the horizon has increased by 10° in just one day. This may indicate that the preon cloud is approaching the solar system at very high speed. The cloud of preons, according to [4], is an element of dark energy space; the form of protons dissolved to preons in the physical vacuum is concentrated in it [5, 6].

Figure 5. Photograph of terrestrial axions on November 30, 2023 at 00:46 CET. Simferopol, Russia. Angle 65°.

Figure 6 shows a photograph of the tracks of terrestrial axions at 01:03 CET on December 3, 2023. The appearance of new tracks (1 and 2) is visible, indicating that our planet is already inside the cloud of preons. In this case, track 1 is directed to the constellation Virgo (the appearance of a new cloud),

and track 2 is directed to Neptune, to clouds front. The splitting of signals 3 and 4 indicates the heterogeneity of the cloud, that is, within the cloud itself there is a gradient of preon concentrations. This bifurcation can also be seen in Figures 2...5. The speed of movement of the cloud can be estimated from all photographs as approximately ~50E13 km/s. This speed is 1.5E9 faster than the speed of light. The movement of the cloud and its heterogeneities should cause the appearance of a shock front (shock wave). Such a front was registered on December 1, 2023 in the form of strong magnetic storms on the Sun (https://meteoagent.com/de/vorhergesagt-warnungen-sonnensturme).

Figure 6. Photograph of terrestrial axions on December 03, 2023 at 01:03 CET. Simferopol, Russia. Angle 67°.

From June 2023 to December 10, 2023, the preon cloud created gravitational noise with frequencies of 19.739, 20.147 and 20.417 kHz. These signals disappeared after the cloud went beyond the horizon of the Universe.

Conclusion

The approach of the preon cloud will cause strong magnetic storms on stars, including the Sun.

The preon cloud is heterogeneous.

The cloud has an extremely high temperature.

A preon cloud is a region of space with dark energy.

The movement of the preon cloud must have a shock front. Shock fronts must also have heterogeneities inside the cloud.

Gravitational noise from the movement of a preon cloud can be used to detect its approach and forecast magnetic storms on the Sun.

References

[1] Zubow A., Zubow K., Zubow V. A. *Photos of Earth's axion tracks*. Horizons in World Physics. Ed. Albert Reimer. NY, 2023, vol. 312, pp.., in print.

[2] Zubow A., Zubow K., Zubow V. A. *A giant cloud of preons (voids) in our Universe.* Monitoring Earth's axions. Horizons in World Physics. Ed. Albert Reimer. NY, 2023, vol. 312, pp.., in print.

[3] Zubow A., Zubow K., Zubow V. A. *Preon. Mass and force constant of oscillations in the series of its homologues - elementary particles*. Horizons in World Physics. Ed. Albert Reimer. NY, 2023, vol. 311, pp. 199…202. (Horizons in World Physics. Volume 311 – Nova Science Publishers (novapublishers.com).

[4] Zubow K., Zubow A., Zubow V. *New constant Q=8.97082E-10, m2/s2·kg3, In E=Q·m4. Vector nature of masses*. Horizons in World Physics. Ed. Albert Reimer. NY, 2023, vol. 311, pp. 189…198. Horizons in World Physics. Volume 311 – Nova Science Publishers (novapublishers.com).

[5] Zubow K., Zubow A. V., Zubow V. A. *The Way to the ETIs*. Applied gravitational mass spectroscopy. Nova Sci. Publ. NY, 2014. https://www.novapublishers.com/catalog/product_info.php?products_id=42668&osCsid=5bd85d42dc273360fd48126de7be9daf .

[6] Zubow K., Zubow A. V., Zubow V. A. *The Phenomenon of Proton Dissolving in Vacuum and of Proton Condensation from Vacuum. Two Forms of Protons, Structure of Nuclei, Electrons and Atoms*. J. of modern physics, 2010, vol.1, no.1, pp.175-184. https://www.researchgate.net/

publication/228928173_The_Phenomenon_of_Proton_Dissolving_in_Vacuum_and_of_Proton_Condensation_from_Vacuum_Two_Forms_of_Protons_Structure_of_Nuclei_Electrons_and_Atoms.

Chapter 12

Theory of Molecular Optical Activity: Classical and Quantum Approaches

Alexei M. Frolov
Department of Applied Mathematics,
University of Western Ontario,
London, Ontario, Canada

Abstract

The basic principles of classical, semi-classical and quantum theories of molecular optical activity are discussed. These theories are valid and can be applied for dilute solutions of optically active organic molecules. It is shown that all phenomena known in the classical theory of molecular optical activity can be described with the use of one pseudo-scalar which is a uniform function of the incident light frequency ω. The relation between optical rotation and circular dichroism is derived from the basic Kramers-Kronig relations. In our discussion of the general theory of molecular optical activity we introduce the tensor of molecular optical activity, or optical activity tensor (OTA, for short). It is shown that to evaluate the optical rotation and circular dichroism at arbitrary frequencies one needs to know only nine (9 = 3 + 6) molecular tensors. The quantum (or semi-classical) theory of molecular optical activity is also briefly discussed. We also discuss a possibility to measure the optical rotation and circular dichroism at wavelengths which correspond to the vacuum ultraviolet region, e.g., for 100 nm $\geq \lambda \leq$ 170 nm.

PACS: 33.55.+b and 33.20.Ni

In: Horizons in World Physics. Volume 312
Editor: Albert Reimer
ISBN: 979-8-89113-513-0

1. Introduction

In this study we discuss the classical theory of molecular optical activity. This theory was originally developed for solutions of various optically active organic molecules. Our analysis begins with the classical theory of optical activity based on the Maxwell's equations for electromagnetic field(s). Any optical active substance is described in this theory with the use of a few phenomenological parameters. The main goal of the classical theory of optical activity is to derive some useful relations between these parameters in various cases. In general, these parameters also depend upon frequencies and relations between such parameters take different forms for different frequencies. We also consider semi-classical theory of optical activity of molecules which was originally developed by Rosenfeld in [1]. In this theory all molecules are considered as quantum systems, while radiation is considered classically. This old theory is still widely used, since it produces a very good agreement with many experimental results. In particular, the semi-classical theory of optical activity can be used at short and very short wavelengths, e.g., for wavelengths which correspond to vacuum ultraviolet. On the other hand, it is clear that the complete theory of optical activity can be based only on quantum mechanics of molecules and quantum theory of radiation.

This work has the following structure. Basics of the classical theory of molecular optical activity in dilute solutions of organic substances can be found in the next Sections. Here we introduce the optical rotatory parameter β. The four Stokes parameters are defined in Section III. These parameters are very convenient to describe quasi-monochromatic light. The phenomenon of circular dichroism is described in Section IV. It appears that the two fundamental $\omega-$dependent functions (optical rotation and circular dichroism) which can be defined for an arbitrary optically active solution can be written in the form of one complex function. The well known Kramers-Kronig relation between the real and imaginary parts of this functions must always be obeyed. For limited intervals of frequencies this produces a very useful relation which allows to determine, e.g., the circular dichroism by using the known expressions for optical activity. Tensor of molecular optical activity is explicitly defined in Section V. The formulas obtained in this Section are very useful in applications, since they allow to express the optical activity by using only the two basic molecular properties (the electric dipole and magnetic dipole momenta). Concluding remarks can be found in the last Section.

2. Classical Theory of Molecular Optical Activity

Let us briefly discuss the classical theory of optical activity. In classical theory the optical activity always denotes the ability of the material under study to rotate the plane of polarization of the left- and right-circularly polarized light. Currently, the study of optical activity also includes optical rotation at different wavelengths, circular dichroism, and differential scattering of left- and right-circularly polarized light [2]. All these phenomena are manifestations of natural optical activity which is a characteristic of chiral molecules (in contrast with achiral or non-active molecules). Note that there are also various phenomena which correspond to so-called induced optical activities. In such cases the achiral molecules can show some optical activity, if they are placed in a relatively strong electric and/or magnetic fields. In this study we restrict ourselves to the analysis of natural optical activity only.

In general, the optical activity is uniformly related to the spatial dispersion, i.e. to the non-local relation between the electric induction $\mathbf{D}$ and electric field $\mathbf{E}$. For the Cartesian components of these vectors we can write [3]

$$D_i(\mathbf{r},t) = E_i(\mathbf{r},t) + \int_0^\infty d\tau \int d^3\mathbf{r}_1 F_{ij}(\tau,\mathbf{r},\mathbf{r}_1) E_j(t-\tau,\mathbf{r}_1) \qquad (1)$$

where $F_{ik}(\tau,\mathbf{r},\mathbf{r}_1) = F_{ki}(\tau,\mathbf{r}_1,\mathbf{r})$ is the kernel of integral operator. For monochromatic field components $\mathbf{E}(\mathbf{r},t) = \mathbf{E}(\mathbf{r})\exp(-\imath\omega t)$ and Eq.(1) takes the form

$$D_i(\mathbf{r}) = E_i(\mathbf{r}) + \int d^3\mathbf{r}_1 f_{ij}(\omega;\mathbf{r},\mathbf{r}_1) E_j(\mathbf{r}_1) \qquad (2)$$

This equation with the kernel $f_{ij}(\omega;\mathbf{r},\mathbf{r}_1)$ expresses a non-local relation between $\mathbf{D}$ and $\mathbf{E}$ which is also called spatial dispersion. In general, the kernel $f_{ij}(\omega;\mathbf{r},\mathbf{r}_1)$ in Eq.(2) rapidly decreases with interatomic distances. In many cases such a kernel is very small already at distances $\approx 3\ a$, where a designates some average (or effective) atomic dimension. Briefly, the relation, Eq.(2), is written in the form

$$D_i(\mathbf{r}) = \int d^3\mathbf{r}_1 \cdot \epsilon_{ij}(\omega;\mathbf{r},\mathbf{r}_1) E_j(\mathbf{r}_1) \qquad (3)$$

where ϵ_{ij} is some non-local operator (tensor) which also depends upon the frequency ω (see below). The 3×3 tensor $\hat{\epsilon} = \epsilon_{ij}$ is the dielectric tensor (also called electric permittivity). From the transparency of the media it follows that

all nine matrix elements ϵ_{ij} are real and all three eigenvalues of this tensor are positive.

In all studies of optical activity in organic compounds only infinite, homogeneous media are considered, a convention adopted in this work. Unless otherwise specified, the absorption of radiation is assumed to be absent at all frequencies considered below. In such cases the kernel in Eq.(2) depends only on the difference $\mathbf{R} = \mathbf{r} - \mathbf{r}_1$. The functions $\mathbf{D}$ and $\mathbf{E}$ in infinite, homogeneous media can be expanded in a Fourier integral with the respect to Cartesian coordinates as well as time. Finally, this allows one to obtain the following relation between the corresponding Cartesian components of the vectors $\mathbf{D}$ and $\mathbf{E}$

$$D_i(\mathbf{k}) = \epsilon_{ij}(\omega;\mathbf{k})E_j(\mathbf{k}) = \\ = \left[\delta_{ij} + \int_0^{\infty} d\tau \int d^3\mathbf{R} f_{ij}(\tau,\mathbf{R}) \exp[\imath(\omega\tau - \mathbf{k}\cdot\mathbf{R})]\right] E_j(\mathbf{k}) \quad (4)$$

In other words, the dielectric tensor $\epsilon_{ik}(\omega;\mathbf{k})$ (also called electric permittivity) takes the form

$$\epsilon_{ij}(\omega,\mathbf{k}) = \delta_{ij} + \int_0^{\infty} d\tau \int d^3\mathbf{R} f_{ij}(\tau,\mathbf{R}) \exp[\imath(\omega\tau - \mathbf{k}\cdot\mathbf{R})] \quad (5)$$

As follows from this formula the dielectric tensor is a function of the field frequency ω and wave vector $\mathbf{k}$. In general, the dependence of the dielectric tensor ϵ_{ij} on ω is called dispersion, while the analogous dependence upon the wave vector $\mathbf{k}$ represents the spatial dispersion. The spatial dispersion of $\epsilon_{ij}(\mathbf{k})$ is responsible for optical activity (see below).

In solutions of organic substances the optical activity corresponds to the case of weak spatial dispersion, i.e. $k =\mid \mathbf{k} \mid$ is small. In such cases the tensor $\varepsilon_{ij}(\omega,\mathbf{k})$ can be expanded in powers of the wave vector $\mathbf{k}$, e.g.,

$$\epsilon_{ij}(\omega,\mathbf{k}) = \epsilon_{ij}^{(0)}(\omega) + \gamma_{ijl}(\omega)k_l + \beta_{ijlm}(\omega)k_lk_m + \alpha_{ijlmn}(\omega)k_lk_mk_n + \ldots \quad (6)$$

Such an expansion is valid, if the first term in Eq.(6), i.e. $\epsilon_{ij}^{(0)}(\omega)$, has no zeros in a given range of frequencies ω. Since in this study we restrict ourselves to the consideration of transparent (or slightly absorbing) solutions only, then we can neglect the imaginary part of dielectric tensor $\epsilon_{ij}^{(0)}(\omega)$.

If these two conditions are obeyed, then for small $\mathbf{k}$ only a very few first terms in such an expansion are important. Let us restrict to the two lowest order

terms (the second of which is responsible for optical activity), i.e. we can write

$$\epsilon_{ij}(\omega, \mathbf{k}) = \epsilon_{ij}^{(0)}(\omega) + \gamma_{ijl}(\omega)k_l = \epsilon_{ij}^{(0)}(\omega) + \imath\frac{\omega}{c}\gamma_{ijl}(\omega)n_l \tag{7}$$

where $\mathbf{n} = \frac{c}{\omega}\mathbf{k}$ and $\gamma_{ijl}n_l$ is an antisymmetric tensor of the second rank (upon indexes i and j). For tensor γ_{ikl} the antisymmetry means $\gamma_{ijl} = -\gamma_{jil}$. If absorption of radiation is absent, then the tensor γ_{ijl} is real, i.e., $\gamma_{ijl}^{*} = \gamma_{ijl}$. These two conditions mean that the $\gamma_{ijl}n_l$ tensor can be re-written into another form $\gamma_{ijl}n_l = \frac{c}{\omega}e_{ijl}g_l$, where e_{ijl} is the complete antisymmetric tensor, while g_l is the $l-$th component of the axial giration vector $\mathbf{g}$. In tensor algebra this relation is called the duality relation. In general, the giration vector $\mathbf{g}$ is a function of the unit wave vector $\mathbf{n}$, i.e. $(\mathbf{g})_i = g_{il}n_l$, where g_{il} is the pseudotensor of the second rank. In isotropic media $g_{il} = \delta_{il}f$ and such a pseudotensor is reduced to a singlepseudoscalar f, while the γ_{ijl} tensor is essentially reduced to the complete antisymmetric tensor e_{ijl}. In this case the tensor γ_{ijl} is represented in the form $\gamma_{ijl}(\omega) = \frac{c}{\omega}e_{ijl}f(\omega)$, and therefore,

$$\mathbf{D} = \epsilon^{(0)}\mathbf{E} + \imath f(\omega)(\mathbf{E} \times \mathbf{n}) \tag{8}$$

Note again that this equation can be applied only in those cases when the absolute value of $f(\omega)$ is much smaller than the minimal eigenvalue of the tensor $\epsilon^{(0)}(\omega)$.

As is well known (see, e.g., [3]) in an arbitrary dielectric media we always have $\mathbf{D} \cdot \mathbf{n} = 0$. In this case from Eq.(8) one also finds that $\mathbf{E} \cdot \mathbf{n} = 0$. For a monochromatic wave we can write the Maxwell equations

$$\frac{\omega}{c}\mathbf{H} = (\mathbf{k} \times \mathbf{E}) \quad and \quad \frac{\omega}{c}\mathbf{D} = (\mathbf{k} \times \mathbf{H}) \tag{9}$$

It follows from here that $\mathbf{k} \perp \mathbf{D} \perp \mathbf{H}$ and also that $\mathbf{E} \perp \mathbf{H}$. In three-dimensional space this means that the three vectors $\mathbf{E}, \mathbf{D}$ and $\mathbf{k}$ are co-planar. This simplifies drastically the following analysis of optical activity in isotropic media.

Consider now the energy transfer. In general, the direction of the energy flux is given by Poynting vector $\mathbf{S} = \frac{c}{4\pi}(\mathbf{E} \times \mathbf{H})$. Now by using the unit vector $\mathbf{n}$ defined above ($\mathbf{n} = \frac{c}{\omega}\mathbf{k}$) we can write for the Poynting vector

$$\mathbf{S} = \frac{c}{4\pi}(\mathbf{E} \times \mathbf{H}) = \frac{c}{4\pi}[\mathbf{n}E^2 - (\mathbf{E} \cdot \mathbf{n})\mathbf{E}] \tag{10}$$

The total energy flux through an element dS of surface orthogonal to $\mathbf{n}$ is

$$dW = \frac{c}{4\pi}[E^2 - (\mathbf{E}\cdot\mathbf{n})^2]d\Omega = \frac{c}{4\pi}E^2 sin^3\Theta d\Theta d\Phi \tag{11}$$

where Θ is the angle between the vector $\mathbf{E}$ and outer normal to this surface element dS, i.e. $\mathbf{n}$. Also, it follows from the two equations of Eq.(9) that $\mathbf{D} = n^2\mathbf{E} - \mathbf{n}(\mathbf{n}\cdot\mathbf{E})$. On the other hand the basic relation between vectors $\mathbf{D}$ and $\mathbf{E}$ is $\mathbf{D} = \hat{\epsilon}\mathbf{E}$, where $\hat{\epsilon}$ is the dielectric tensor. From here one finds the following equation written in Cartesian components

$$(n^2\delta_{ij} - n_i n_j - \epsilon_{ij})E_j = 0 \tag{12}$$

where ϵ_{ij} are the components of dielectric tensor.

Formally, this equation coincides with the corresponding eigenvalue equation for the dielectric tensor ϵ_{ik}. However, the eigenvalues of this tensor are the functions of three spatial directions. By using some unitary transformation, one can reduce Eq.(12) to the principal axes of the tensor ϵ_{ij} which are also called the principal dielectric axes. In fact, there are some advantages to writing Eq.(12) in the principal dielectric axes. In this case it exactly coincides with Fresnel's equation which is the main equation of crystal optics. In general, Eq.(12) determines the wave-vector surface in the n_x, n_y, n_z coordinates. Such surfaces depend upon three constant coefficients $\epsilon_x, \epsilon_y, \epsilon_z$ (eigenvalues of the dielectric tensor ϵ_{ij}).

For homogeneous solutions the Fresnel's equation simplifies significantly, since is these systems $\epsilon_x = \epsilon_y = \epsilon_z$. We want to consider such a transition in the two following steps. First, consider the case of two different eigenvalues $\epsilon_x = \epsilon_y = \epsilon_\perp$ and $\epsilon_z = \epsilon_\parallel$ (these values of parameters correspond to uniaxial crystals). In this case the Fresnel's equation can be factorized to the form

$$(n^2 - \epsilon_\perp)[\epsilon_\parallel n_z^2 + \epsilon_\perp(n_x^2 + n_y^2) - \epsilon_\perp\epsilon_\parallel] = 0 \tag{13}$$

where $\mathbf{n} = (n_x, n_y, n_z)$ is the direction of the light propagation. In other words, an equation of the fourth order (upon n) is reduced to the product of the two quadratic equations

$$n^2 = n_x^2 + n_y^2 + n_z^2 = \epsilon_\perp \tag{14}$$

$$\frac{n_z^2}{\epsilon_\perp} + \frac{n_x^2 + n_y^2}{\epsilon_\parallel} = 1 \tag{15}$$

where the first equation is the equation of a sphere, while the second equation determines an ellipsoid. The sphere represents the propagation of ordinary waves. Such waves have the same refractive index $n = \sqrt{\epsilon_\perp}$. The second equation represents the so-called extraordinary waves which are directly related with the optical activity. Let us consider the extraordinary waves in homogeneous solutions, or in crystals of a cubic system. These two cases can be obtained as the limit of Eq.(15) when $\epsilon_\parallel \to \epsilon_\perp$. In reality, it can be written in the two different forms $\epsilon_\parallel = \epsilon_\perp \pm \Delta$, where the positive parameter $\Delta \to 0$. In such cases, Eq.(14) does not change, while the second equation takes the form

$$\frac{n_z^2}{\epsilon_\perp} + \frac{n_x^2 + n_y^2}{\epsilon_\perp \pm \Delta} = 1 \quad or \quad \frac{n^2 cos^2\theta}{\epsilon_\perp} + \frac{n^2 sin^2\theta}{\epsilon_\perp \pm \Delta} = 1 \tag{16}$$

where $n_x = n \cdot \sin\theta\cos\phi, n_y = n \cdot \sin\theta\sin\phi, n_z = n \cdot \cos\theta$, where θ is the angle between the optical axis and vector $\mathbf{n}$.

In homogeneous solutions the orientation of chiral molecules is random, i.e. we have to replace the factors $cos^2\theta$ and $sin^2\theta$ in the last equation by their mean values $\frac{1}{2}$. This gives

$$\frac{1}{\epsilon_\perp} + \frac{1}{\epsilon_\perp \pm \Delta} = \frac{2}{n^2} \tag{17}$$

or

$$\frac{2}{n^2} = \frac{\epsilon_\perp + \epsilon_\perp \pm \Delta}{\epsilon_\perp(\epsilon_\perp \pm \Delta)} \approx \frac{2(\epsilon_\perp \pm \frac{1}{2}\Delta)}{(\epsilon_\perp \pm \frac{1}{2}\Delta)^2} = \frac{2}{(\epsilon_\perp \pm \frac{1}{2}\Delta)} \tag{18}$$

From here one finds that $n^2 = \epsilon_\perp \pm \frac{1}{2}\Delta$, or in other words, we have two different refractive indices $n_1^2 = \epsilon_\perp + \frac{1}{2}\Delta$ and $n_2^2 = \epsilon_\perp - \frac{1}{2}\Delta$. This means that two different refracted wave are formed and, formally, we have to consider the double refraction or birefringence. However, the parameter Δ is small (in fact, very small) in comparison with n^2. Therefore, the overall scale of such a birefringence is $\approx \Delta$.

Result can be obtained in a slightly different way with the use of some microscopic identities. Indeed, let us note that for homogeneous solutions of chiral molecules $\epsilon_{ij} = \epsilon \cdot \delta_{ik} + \imath\frac{c}{\omega} f(\omega) e_{ikl} n_l$, where e_{ikl} is the complete antisymmetric tensor. In this case we do not need to use the complete Fresnel's equation to produce the same answer as above. The chiral activity can be described with the use of only one numerical parameter $f(\omega)$ which is pseudoscalar. In fact, such a parameter can be introduced in a slightly different way. Indeed, the Maxwell

equations in the case of homogeneous solutions take the form

$$\mathbf{D} = \epsilon\mathbf{E} - g\frac{\partial \mathbf{H}}{\partial t} \quad , \quad \mathbf{B} = \mu\mathbf{H} + g\frac{\partial \mathbf{E}}{\partial t} \tag{19}$$

where g is a some constant, which depends upon ω. By taking into account polarization of media by the electric and magnetic field we can write, e.g., for the $\mathbf{D}$ vector

$$\mathbf{D} = (1 + 4\pi N\alpha)\mathbf{E} - 4\pi N\frac{\beta}{c}\frac{\partial \mathbf{H}}{\partial t} \tag{20}$$

where α is the static polarizability, while β is the so-called optical rotatory parameter, or optical rotation, for short. As follows from Eq.(20) the parameter β is also a pseudoscalar. The parameter β determines the optical rotation, i.e. the rotation of the plane of left- and right-circularly polarized light when it passes through an optically active medium. Also, in this equation N is the number of chiral molecules per unit volume. It follows from the last two equations that $\epsilon = 1 + 4\pi N\alpha$ and $g = 4\pi N\frac{\beta}{c}$. The relation between factor g and the indices of refraction for circularly polarized light can also be obtained from Eq.(20)

$$\chi_L = \sqrt{\epsilon} - 2\pi\omega g \quad \text{and} \quad \chi_R = \sqrt{\epsilon} + 2\pi\omega g \tag{21}$$

Now it is easy to find the overall rotation (δ) when the light propagates the distance z in some chiral media

$$\delta = \frac{\pi z}{\lambda}(\chi_R - \chi_L) = \frac{4\pi^2 z}{\lambda^2}g = 4\pi^2\nu^2 z \cdot g = \frac{16\pi^3\nu^2 N z}{c} \cdot \beta \tag{22}$$

Note that the optical rotatory parameter β (as well as α) which follows from Eq.(20) can rigorously be determined only with the use of the quantum mechanics of molecules. This will be our goal in the third Section.

3. Stokes Parameters

As follows from its definition any monochromatic wave has a certain polarization. However, in actual optical experiments it is almost impossible to create a beam of pure monochromatic waves, and usually we have to operate with real light which contains frequencies distributed in a small interval $\Delta\omega$ around the main frequency ω. The means that the real light is, in fact, a mixture of light

quanta with different polarizations. An arbitrary property of such a beam of light, e.g., the electric field $\mathbf{E}$, in the real light depends upon time. If the frequency distribution $\Delta\omega$ around ω is narrow, then the $\mathbf{E}(t)$ function can be represented in the form $\mathbf{E}(t) = \mathbf{E}_0(t)exp(-\imath\omega t)$, where $\mathbf{E}_0(t)$ is a slowly varying function of time t which determines the polarization of the actual light. From the last formula one can expect that such a polarization will be slowly changing in time, i.e. we are dealing with the partially polarized light [4].

In regular experiments we cannot observe the polarization properties of electromagnetic waves directly. Instead, one measures the intensity distribution of light when it passes through various physical bodies. This means we are dealing with quadratic functions of the field. In other words, in actual experiments we are measuring the components of the following tensor $J_{\alpha\beta} = \overline{E_{0\alpha}E^*_{0\beta}}$, where $E_{0\alpha}$ and $E^*_{0\beta}$ are the Cartesian components of the slow varying $\mathbf{E}_0(t)$ vector. The line over the product of the two complex vectors mean the value averaged in time. If all vectors are represented in the form $\mathbf{E}(t) = \mathbf{E}_0(t)exp(-\imath\omega t)$, then the $E_{0\alpha}E^*_{0\beta}$ product is the only value which has non-zero time-average. Other similar combinations, i.e., $E^*_{0\alpha}E^*_{0\beta}$ and $E_{0\alpha}E_{0\beta}$, contain rapidly oscillating factors $exp(-2\imath\omega t)$ which gives zero upon time averaging.

Since in any plane wave one finds $\mathbf{E} \perp \mathbf{n}$, where $\mathbf{n}$ is the direction of wave propagation, then the $J_{\alpha\beta}$ tensor has only four components. Moreover, the $J_{\alpha\beta}$ tensor also contains the total intensity of the wave $J = \sum_\alpha J_{\alpha\alpha} = \overline{\mathbf{E}\cdot\mathbf{E}^*}$. This value has nothing to do with with polarization of the wave and can be excluded by introducing the tensor $\rho_{\alpha\beta} = \frac{J_{\alpha\beta}}{J}$. The tensor $\rho_{\alpha\beta}$ has the unit trace and it is called the polarization tensor. It can be shown that the polarization tensor is hermitian, i.e. $\rho^*_{\alpha\beta} = \rho_{\beta\alpha}$. Now, we can introduce the degree of polarization P which is defined as

$$P = \sqrt{1 - 4det(\rho_{\alpha\beta})} = \sqrt{1 - 4\rho_{11}\rho_{22} + 4 \mid \rho_{12} \mid^2} \tag{23}$$

where $det(\rho_{\beta\alpha})$ is the determinant of the 2×2 matrix $\rho_{\beta\alpha}$.

An arbitrary hermitian 2×2 matrix can be represented in the following form

$$\rho_{\alpha\beta} = \frac{1}{2}(\rho_{\alpha\beta} + \rho_{\beta\alpha}) + \frac{1}{2}(\rho_{\alpha\beta} - \rho_{\beta\alpha}) = S_{\alpha\beta} - \frac{\imath}{2}e_{\alpha\beta}A \tag{24}$$

where $S_{\alpha\beta}$ is the real symmetric 2×2 tensor. The analogous non-symmetric 2×2 tensor in two-dimensional space is reduced to the unit antisymmetric tensor $e_{12} = -e_{21}$ and pseudoscalar A. The pseudoscalar A is called the degree of

circular polarization. It is bounded between -1 and +1. The case of a light wave with linear polarization corresponds to the $A = 0$ value. The waves with circular polarization correspond to the values $A = +1$ (right-circular) polarization and $A = -1$ (left-circular polarization).

An alternative expansion for an arbitrary hermitian 2×2 matrix is performed with the use of three Pauli matrices $\hat{\sigma}_i$ $(i = x, y, z)$ (see, e.g., [5]) and one unit matrix $\hat{I}$. It is written in the form

$$\rho_{\alpha\beta} = \frac{1}{2}\Big(\hat{I} + \xi_1\hat{\sigma}_x + \xi_2\hat{\sigma}_y + \xi_3\hat{\sigma}_z\Big) = \frac{1}{2}\left(\begin{array}{cc} 1+\xi_3 & \xi_1 - \imath\xi_2 \\ \xi_1 + \imath\xi_2 & 1-\xi_3 \end{array} \right)$$

The parameters ξ_1, ξ_2 and ξ_3 which appear in this formula are the so-called Stokes parameters. In general, any intensity measurement may be written as a linear combination of these three parameters and one additional Stokes parameter ξ_0 which is the total intensity of the scattered light. The determinant of the $\rho_{\beta\alpha}$ tensor is

$$det(\rho_{\alpha\beta}) = \frac{1}{4}(1 - \xi_1^2 - \xi_2^2 - \xi_3^2) \tag{25}$$

while the degree of polarization is $P = \sqrt{\xi_1^2 + \xi_2^2 + \xi_3^2}$. The Stokes parameters ξ_1 and ξ_3 determine the degree of the linear polarization, while the parameter ξ_2 shows the degree of circular polarization. Note that the parameter ξ_2 coincides with the pseudoscalar A introduced above. From three Stokes parameters one can construct the two scalars (ξ_2 and $\sqrt{\xi_1^2 + \xi_3^2}$) which are invariants under Lorentz transformations. The three Stokes parameters also have a number of other advantages in actual applications.

4. Circular Dichroism

In all formulas above we have neglected the absorption of light during its propagation in the dense media. In actual cases the absorption of light always occurs. At some frequencies, e.g., in the vacuum ultraviolet region, it plays a very important role and cannot be ignored even in the first approximation. In reality the situation is even more complicated, since light waves with different circular polarization are absorbed differently by the media. This is called circular dichroism (CD). Such a differential absorption of light with left- and right-circular polarizations can directly (and substantially) affect the observed optical

activity. It appears that optical rotation and differential absorption of light with different circular polarizations can be considered as the two manifestations of one phenomenon.

In general, a detailed study of circular dichroism at different frequencies allows one to develop a new approach for analysis of organic substances. In this Section we want to discuss the modification which is required in all formulas presented above. The absorption of light is described by introducing an imaginary part into the permittivity tensor $\epsilon_{ij}(\omega, \mathbf{r})$, or in other words, by considering static polarizability α as a complex value. However, we are not interested here in the total light absorption. Our interest is related to a very specific difference between absorption of light with left- and right-circular polarizations. It is clear that a complex static polarizability α, Eq.(20), cannot describe such differences. As follows from Eq.(20) this goal can be achieved by considering the optical rotatory parameter β as a complex value.

In these cases the parameter β is represented as the sum of its real and imaginary parts, i.e. $\beta = \beta_1 + \imath\beta_2$, where β_1 and β_2 are two functions of the frequency ω. These two functions, however, are not completely independent, since there are two additional connections between them which follow from the Kramers-Kronig relations. This follows from the fact that $\beta(\omega)$ is the response function [3], [7] which is an analytical function in the upper half ω plane (for now, we consider the frequency ω as a complex variable) (see, e.g., [7]). This allows us to use Cauchy's theorem for $\beta(\omega)$:

$$\beta(z) = \frac{1}{2\pi\imath} \oint_C \frac{\beta(\omega')d\omega'}{\omega' - z} \tag{26}$$

The contour C can be chosen to consist of the real frequency axis ω and a great semicircle at infinity in the upper half plane. The function $\beta(\omega)$ vanishes rapidly at infinity, i.e. there is no contribution to the integral from the great semicircle. Finally, Cauchy's integral is written in the form

$$\beta(z) = \frac{1}{2\pi\imath} \int_{-\infty}^{+\infty} \frac{\beta(\omega')d\omega'}{\omega' - z} \tag{27}$$

where z now is any point in the upper $\omega-$half plane and the integral is taken over the real axis. In fact, we want to place the point z at the real axis. This can be done by approaching the real axis from above, i.e. by representing the complex variable z in the form $z = \omega + \imath\varepsilon$. This gives

$$\beta(\omega) = \frac{1}{2\pi\imath} \int_{-\infty}^{+\infty} \frac{\beta(\omega')d\omega'}{\omega' - \omega - \imath\varepsilon} \tag{28}$$

The denominator in the last formula can be written in the form [7]

$$\frac{1}{\omega' - \omega - \imath\varepsilon} = P\Big(\frac{1}{\omega' - \omega}\Big) + \pi\imath\delta(\omega' - \omega) \tag{29}$$

where the symbol P means the principal part, while $\delta(x)$ designates the Dirac delta-function. Now Eq.(28) takes the form

$$\beta(\omega) = \frac{1}{\pi\imath} P \int_{-\infty}^{+\infty} \frac{\beta(\omega')d\omega'}{\omega' - \omega} \tag{30}$$

By separating here the real and imaginary parts one finds

$$\begin{aligned} Re\beta(\omega) &= \frac{1}{\pi} P \int_{-\infty}^{+\infty} \frac{Im\beta(\omega')d\omega'}{\omega' - \omega} \\ Im\beta(\omega) &= -\frac{1}{\pi} P \int_{-\infty}^{+\infty} \frac{Re\beta(\omega')d\omega'}{\omega' - \omega} \end{aligned} \tag{31}$$

This is the most general Kramers-Kronig relations written for the optical rotatory parameter β. In general, it can be shown that the $Re\beta(\omega)$ is an even function in ω, while $Im\beta(\omega)$ is odd. This allows one to transform the last two integrals in Eq.(31) to the integrals taken over positive frequencies only, i.e.

$$\begin{aligned} Re\beta(\omega) &= \frac{2}{\pi} P \int_{0}^{+\infty} \frac{\omega'[Im\beta(\omega')]d\omega'}{(\omega')^2 - \omega^2} \\ Im\beta(\omega) &= -\frac{2\omega}{\pi} P \int_{0}^{+\infty} \frac{[Re\beta(\omega')]d\omega'}{(\omega')^2 - \omega^2} \end{aligned} \tag{32}$$

These formulas can be used in actual applications which include the optical rotatory parameter β. By using Eq.(22) we can re-write these formulas for the corresponding angles $\delta = \theta + \imath\kappa$

$$\begin{aligned} \theta(\nu) &= \frac{2}{\pi} P \int_{0}^{+\infty} \frac{\nu'\kappa(\nu')d\nu'}{(\nu')^2 - \nu^2} \\ \kappa(\nu) &= -\frac{2\nu}{\pi} P \int_{0}^{+\infty} \frac{\theta(\nu')d\nu'}{(\nu')^2 - \nu^2} \end{aligned} \tag{33}$$

where we have also introduced the linear frequency $\nu = \frac{\omega}{2\pi}$ (ω is called the circular frequency). The importance of the linear frequencies ν follows from the fact that these values are usually used in actual experiments. In general,

Eq.(33) represents the explicit relation between the actual optical rotation (angle θ) and circular dichroism (angle κ). As follows from Eq.(33) the optical rotation known for all frequencies allows one to determine the circular dichroism at each frequency [6]. In reality, however, one finds a number of restrictions which exist in the solution of this problem. Most of such restrictions follow from the fact that optical rotations in the VUV region ($\lambda \leq 150\ nm$) are not known even approximately. On the other hand, it is clear that for each molecule the VUV area of wavelengths contains many resonance lines which are crucially important to describe the absorption of radiation. If we ignore the VUV region of wavelengths, then we can restore the circular dichroism at all frequencies only approximately (in reality, very approximately). For some limited areas of wavelengths, however, such a reconstruction can be quite accurate and complete. Usually, these areas of wavelengths are located far from the VUV region.

Note also, that the experimental knowledge of the $\theta(\nu)$ and $\kappa(\nu)$ values for large number of different frequencies $\nu_1, \nu_2, \ldots, \nu_n$ is used to detect uniformly the corresponding organic substance. Formally, such an identification allows one to solve many problems of quantative and qualitative analysis of the mixtures of chiral organic substances.

5. Tensor of Molecular Optical Activity. Rotation Power

In the middle of 1930's Placzek shown [8] that a significant number of effects related to the interaction between atom(s) and electromagnetic field can be described with the use of only one tensor, later known as the tensor of light scattering. In particular, the differential scattering cross-section of light by an atom (or any other electron containing system) can be written in the form

$$d\sigma = \frac{\omega(\omega + \omega_{12})^3}{\hbar^2 c^4} \mid (C_{ik})_{21} (\mathbf{e}_i')^* \mathbf{e}_k \mid^2 do' \tag{34}$$

where $(C_{ik})_{21}$ is the 3×3 tensor of light scattering, while $\mathbf{e}_i$ and $\mathbf{e}_k$ are the polarization vectors of the incident and final photons. The integration in Eq.(34) is performed over the angular variables of the final photon which is designated by the superscript $'$. Here and everywhere below we shall assume that the angular volume element do' has the form $do' = sin\theta' d\theta' d\phi$. The explicit expression for

the light scattering tensor $(C_{ik})_{21}$ is [9]

$$(C_{ik})_{21} = \sum_n \Big[\frac{(d_i)_{2n}(d_k)_{n1}}{\omega_{n1} - \omega - \imath 0} + \frac{(d_k)_{2n}(d_i)_{n1}}{\omega_{n1} + \omega' - \imath 0} \Big] \tag{35}$$

where $\omega' = \omega + \omega_{12}$, while d_i and d_k are the corresponding components of the vector of the dipole moment $\mathbf{d}$. Note that the differential cross-section $d\sigma$, Eq.(34), corresponds to the lowest order approximation upon the fine structure constant $\alpha \approx \frac{1}{137}$ and contains only the electric dipole-dipole interaction.

The Placzek approach for atoms suggests attempting to derive an analogous method for molecules which would describe their optical activity. In this Section this problem is considered in detail and it is shown that in the lowest order approximation can be described by the tensor $(C_{ik})_{21}$ of light scattering and by the four (or two in some cases) new tensors. These tensors are called the tensors of (molecular) optical activity. Note that in many actual cases the four/two tensors of optical activity are reduced to one tensor only. To produce the closed analytical expressions for these tensors below we shall assume that the electromagnetic field is represented as a combination of plane waves. Each of these plane waves has its own frequency ω and polarization which is represented by the vector $\mathbf{e}$. The wave functions of the incident and final photons can be taken in the form (see, e.g., [9])

$$\mathbf{A}_{\mathbf{e}\omega} = \sqrt{\frac{2\pi}{\omega}} exp(-\imath\omega t + \imath \mathbf{k}\cdot\mathbf{r})\mathbf{e} \quad ,$$

$$\mathbf{A}_{\mathbf{e}'\omega'} = \sqrt{\frac{2\pi}{\omega'}} exp(-\imath\omega' t + \imath \mathbf{k}'\cdot\mathbf{r}')\mathbf{e}' \quad , \tag{36}$$

where ω and ω' are the corresponding frequencies, while vectors $\mathbf{e}$ and $\mathbf{e}'$ represent the polarization of the incident and final photons, respectively. Below, we shall consider the plane waves in the transverse (or radiation) gauge, where $div\mathbf{A} = 0$. In this gauge one finds $\mathbf{k}\cdot\mathbf{e} = 0$ and $\mathbf{k}'\cdot\mathbf{e}' = 0$. Note that in calculations for the final photon we need to use the wave function which is conjugate to its wave function, i.e. $\mathbf{A}^*_{\mathbf{e}'\omega'}$. As follows from these equations the electric $\mathbf{E}$ and magnetic $\mathbf{H}$ fields are

$$\mathbf{E}_{\mathbf{e}\omega} = -\frac{\partial}{\partial t}\mathbf{A}_{\mathbf{e}\omega} = -\imath\sqrt{2\pi\omega}\mathbf{e} exp(-\imath\omega t + \imath\mathbf{k}\cdot\mathbf{r}) \tag{37}$$

$$\mathbf{H}_{\mathbf{e}\omega} = curl\mathbf{A}_{\mathbf{e}\omega} = \imath\sqrt{\frac{2\pi}{\omega}}(\mathbf{k}\times\mathbf{e}) exp(-\imath\omega t + \imath\mathbf{k}\cdot\mathbf{r})$$

By introducing the unit vector $\mathbf{n} = \frac{\mathbf{k}}{\omega}$ we can re-write the last equation in the form

$$\mathbf{H}_{\mathbf{e}\omega} = \imath\sqrt{2\pi\omega}(\mathbf{n} \times \mathbf{e})exp(-\imath\omega t + \imath\mathbf{k} \cdot \mathbf{r}) \tag{38}$$

Analogous expressions can be obtained for the $\mathbf{E}_{\mathbf{e}'\omega'}$ and $\mathbf{H}_{\mathbf{e}'\omega'}$ fields which are related with the $\mathbf{A}^*_{\mathbf{e}'\omega'}$ wave function.

From these equations one finds the following expressions for the electric dipole and magnetic dipole interactions. In fact, for each of the $(\mathbf{e}, \omega)$-components of the $\mathbf{E}$ and $\mathbf{H}$ vectors we have

$$V^e_{\mathbf{e}\omega} = -\mathbf{d} \cdot \mathbf{E}_{\mathbf{e}\omega} = \imath\sqrt{2\pi\omega}(\mathbf{d} \cdot \mathbf{e})exp(-\imath\omega t + \imath\mathbf{k} \cdot \mathbf{r}) \tag{39}$$

and

$$V^m_{\mathbf{e}\omega} = -\mathbf{m} \cdot \mathbf{H}_{\mathbf{e}\omega} = -\imath\sqrt{2\pi\omega}[\mathbf{m} \cdot (\mathbf{n} \times \mathbf{e})]exp(-\imath\omega t + \imath\mathbf{k} \cdot \mathbf{r}) \tag{40}$$

where $\mathbf{d}$ and $\mathbf{m}$ are the vectors of the electric and magnetic dipole moments, respectively. In the lowest order approximation the one-photon matrix elements of the V^e and V^m interactions equal zero identically. The first non-zero contribution can be found only in the second order of perturbation theory. In the second order approximation the matrix element V_{21} for the transition between states 1 and 2 is written in the following form [9]

$$V_{21} = \sum_n \Big(\frac{V'_{2n} V_{n1}}{\mathcal{E}_1 - \mathcal{E}^I_n} + \frac{V_{2n} V'_{n1}}{\mathcal{E}_1 - \mathcal{E}^{II}_n} \Big) \tag{41}$$

where the notation $\mathcal{E}$ designates the total energy of the system ('molecule + photons'), i.e. in the case considered here we have $\mathcal{E}^I_n = E_n$ and $\mathcal{E}^{II}_n = E_n + \omega + \omega'$. The matrix elements V_{ab} represent absorption of the photon with the wave vector $\mathbf{k}$. Analogously, the matrix elements V'_{ab} represent emission of the photon with the wave vector $\mathbf{k}'$. In the general case, in Eq.(41) the $V = V_{21}$ interaction is represented in the form $V = V^e + V^m + V^{qe} + V^{qm} + \ldots$ and $V' = (V^e)' + (V^m)' + (V^{qe})' + (V^{qm})' + \ldots$, where V^e, V^m, V^{qe} are the electric dipole, magnetic dipole and electric quadruple interactions, respectively. Keeping only lowest order terms in the expansion of V in terms of the fine-structure constant $\alpha \approx \frac{1}{137}$, we can write $V \approx V^e + V^m$ and $V' \approx (V^e)' + (V^m)'$. In this case

one finds from Eq.(41)

$$V_{21} = \sum_n \left[\frac{(V^e)'_{2n} V^e_{n1}}{\mathcal{E}_1 - \mathcal{E}^I_n} + \frac{(V^e)_{2n} (V^e)'_{n1}}{\mathcal{E}_1 - \mathcal{E}^{II}_n} \right] + \sum_n \left[\frac{(V^e)'_{2n} V^m_{n1}}{\mathcal{E}_1 - \mathcal{E}^I_n} + \frac{(V^e)_{2n} (V^m)'_{n1}}{\mathcal{E}_1 - \mathcal{E}^{II}_n} + \frac{(V^m)'_{2n} V^e_{n1}}{\mathcal{E}_1 - \mathcal{E}^I_n} + \frac{(V^m)_{2n} (V^e)'_{n1}}{\mathcal{E}_1 - \mathcal{E}^{II}_n} \right] + \sum_n \left[\frac{(V^m)'_{2n} V^m_{n1}}{\mathcal{E}_1 - \mathcal{E}^I_n} + \frac{(V^m)_{2n} (V^m)'_{n1}}{\mathcal{E}_1 - \mathcal{E}^{II}_n} \right] + \ldots \tag{42}$$

By neglecting here by all terms $\sim V^m V^m$ and other terms of higher orders in the fine structure constant α, we obtain the following formula for the differential cross-section of light scattering $d\sigma$

$$d\sigma = \mid V_{21} \mid^2 \frac{(\omega')^2 do'}{4\pi^2} = d\sigma_{ee} + d\sigma_{em} \tag{43}$$

where $d\sigma_{ee}$ is the part of the total cross-section which can be reduced to the expression given above (see Eq.(34)). This part of the cross-section is not related with the optical activity. The second term in the right-hand side of Eq.(43) is significantly smaller, in the general case, than the first term, i.e. $d\sigma_{em} \ll d\sigma_{ee}$. However, the second term in Eq.(43) is a great interest, since it represents all lowest order effects which are determined by the molecular optical activity.

As follows from Eq.(42) in order to determine the part of the total cross-section responsible for molecular optical activity in the lowest order approximation we need to obtain the explicit formulas for the matrix elements of the $V^e V^e$, $V^e V^m$, and $V^m V^e$ products. The arising expressions are extremely complicated, since each of the V^e and/or V^m interactions contains an infinite number of $V^e_{\mathbf{e}\omega}$ and $V^m_{\mathbf{e}\omega}$ components. In the $V^e V^m$ and/or $V^m V^e$ products one finds an infinite number of cross-terms which explicitly depend upon coordinates. These terms cannot be computed without a complete and accurate knowledge of the molecular electron density $\rho_e(\mathbf{r})$.

However, we can introduce an approximation that the wavelengths λ of the incident and final photons are significantly larger than typical linear sizes of molecule a (our light scatterer). In this case we have $\mathbf{k} \cdot \mathbf{r} \leq \mid \mathbf{k} \mid\mid \mathbf{r} \mid \ll \frac{a}{\lambda} \approx 0$. In this approximation one finds from Eqs.(39) and (40)

$$\mathbf{E}_{\mathbf{e}\omega} = -\imath\sqrt{2\pi\omega}\mathbf{e} exp(-\imath\omega t) \tag{44}$$

and

$$\mathbf{H}_{\mathbf{e}\omega} = \imath\sqrt{2\pi\omega}(\mathbf{n} \times \mathbf{e}) exp(-\imath\omega t) \quad . \tag{45}$$

Therefore, we can write

$$V^e_{\mathbf{e}\omega} = \imath\sqrt{2\pi\omega}(\mathbf{d}\cdot\mathbf{e})exp(-\imath\omega t) = \imath\sqrt{2\pi\omega}(\mathbf{d}_\omega\cdot\mathbf{e}) \tag{46}$$

and

$$V^m_{\mathbf{e}\omega} = -\imath\sqrt{2\pi\omega}[\mathbf{m}\cdot(\mathbf{n}\times\mathbf{e})]exp(-\imath\omega t) = -\imath\sqrt{2\pi\omega}[\mathbf{m}_\omega\cdot(\mathbf{n}\times\mathbf{e})] \tag{47}$$

where $\mathbf{d}_\omega$ and $\mathbf{m}_\omega$ are the corresponding Fourier-components of the dipole and magnetic moments of the molecule. Note that with the identity $\mathbf{m}\cdot(\mathbf{n}\times\mathbf{e}) = \mathbf{e}\cdot(\mathbf{m}\times\mathbf{n})$, the formula for magnetic interaction can also be written in another form

$$V^m_{\mathbf{e}\omega} = -\imath\sqrt{2\pi\omega}[(\mathbf{m}_\omega\times\mathbf{n})\cdot\mathbf{e}] \tag{48}$$

which is similar to the formula for $V^e_{\mathbf{e}\omega}$ in which the vector of the dipole momentum $\mathbf{d}$ is replaced by the vector-product $\mathbf{m}_\omega\times\mathbf{n}$.

Now, we can write the lowest order term upon the magnetic interaction in the differential cross-section $d\sigma$ of the light scattering

$$\begin{aligned} d\sigma = &\left|\sum_n \frac{(\mathbf{d}_{2n}\cdot\mathbf{e}')(\mathbf{d}_{n1}\cdot\mathbf{e})}{\omega_{n1}-\omega-\imath 0} + \frac{(\mathbf{d}_{2n}\cdot\mathbf{e})(\mathbf{d}_{n1}\cdot\mathbf{e}')}{\omega_{n1}+\omega'-\imath 0}\right| \\ &\left|\sum_n \frac{(\mathbf{d}_{2n}\cdot\mathbf{e}')[(\mathbf{m}_{n1}\times\mathbf{n})\cdot\mathbf{e}]}{\omega_{n1}-\omega-\imath 0} + \frac{[(\mathbf{m}^*_{2n}\times\mathbf{n})\cdot\mathbf{e}'](\mathbf{d}_{n1}\cdot\mathbf{e})}{\omega_{n1}-\omega-\imath 0} + \right. \\ &\left.\frac{(\mathbf{d}_{2n}\cdot\mathbf{e})[(\mathbf{m}^*_{n1}\times\mathbf{n})\cdot\mathbf{e}']}{\omega_{n1}+\omega'-\imath 0} + \frac{[(\mathbf{m}_{2n}\times\mathbf{n})\cdot\mathbf{e}](\mathbf{d}_{n1}\cdot\mathbf{e}')}{\omega_{n1}+\omega'-\imath 0}\right| \cdot \frac{\omega(\omega')^3}{\hbar^2c^4}do' \end{aligned} \tag{49}$$

where the notation $\mathbf{e}'$ designates the vector $(\mathbf{e}')^*$. This notation is also used in the two following equations. This equation can be re-written as

$$\begin{aligned} d\sigma = &\left|\sum_n \frac{(\mathbf{d}_{2n}\cdot\mathbf{e}')(\mathbf{d}_{n1}\cdot\mathbf{e})}{\omega_{n1}-\omega-\imath 0} + \frac{(\mathbf{d}_{2n}\cdot\mathbf{e})(\mathbf{d}_{n1}\cdot\mathbf{e}')}{\omega_{n1}+\omega'-\imath 0}\right| \\ &\left|\sum_n \frac{(\mathbf{d}_{2n}\cdot\mathbf{e}')[\mathbf{m}_{n1}\cdot(\mathbf{n}\times\mathbf{e})]}{\omega_{n1}-\omega-\imath 0} + \frac{[\mathbf{m}^*_{2n}\cdot(\mathbf{n}\times\mathbf{e}')](\mathbf{d}_{n1}\cdot\mathbf{e})}{\omega_{n1}-\omega-\imath 0} + \right. \\ &\left.\frac{(\mathbf{d}_{2n}\cdot\mathbf{e})[\mathbf{m}^*_{n1}\cdot(\mathbf{n}\times\mathbf{e}')]}{\omega_{n1}+\omega'-\imath 0} + \frac{[\mathbf{m}_{2n}\cdot(\mathbf{n}\times\mathbf{e})](\mathbf{d}_{n1}\cdot\mathbf{e}')}{\omega_{n1}+\omega'-\imath 0}\right| \cdot \frac{\omega(\omega')^3}{\hbar^2c^4}do' \end{aligned} \tag{50}$$

In these equations and below the notation $\mathbf{m}^*$ stands for the vector which is a complex conjugate vector to the vector of magnetic dipole moment $\mathbf{m}$. In quantum mechanics (in the coordinate representation) we always have $\mathbf{d}^* = \mathbf{d}$, but $\mathbf{m}^* \neq \mathbf{m}$. Note that the vector $\mathbf{n}$ in these equations corresponds to the direction of the scattered light. Formally, this vector can be oriented in an arbitrary

spatial direction, but in almost all modern experiments on optical activity in homogeneous solutions the direction of the scattered light always coincides with the direction of the incident light. This means that our differential cross-section must be multiplied by a delta-function $\delta(\mathbf{n}_{in} - \mathbf{n})$ and integrated over the angular variables $o' = (\theta', \phi')$ of the unit vector $\mathbf{n} = (cos\theta' cos\phi', cos\theta' sin\phi', sin\theta')$ which represents the direction of the final photon. The unit vector $\mathbf{n}_{in}$ describes the direction of the incident photon. This produces the following expression for the cross-section σ

$$\sigma = \frac{4\pi\omega(\omega+\omega_{12})^3}{\hbar^2 c^4} \cdot \left| \sum_n \frac{(\mathbf{d}_{2n}\cdot\mathbf{e}')(\mathbf{d}_{n1}\cdot\mathbf{e})}{\omega_{n1}-\omega-\imath 0} + \frac{(\mathbf{d}_{2n}\cdot\mathbf{e})(\mathbf{d}_{n1}\cdot\mathbf{e}')}{\omega_{n1}+\omega'-\imath 0} \right| \left| \sum_n \frac{(\mathbf{d}_{2n}\cdot\mathbf{e}')[\mathbf{m}_{n1}\cdot(\mathbf{n}_{in}\times\mathbf{e})]}{\omega_{n1}-\omega-\imath 0} + \frac{[\mathbf{m}^*_{2n}\cdot(\mathbf{n}_{in}\times\mathbf{e}')](\mathbf{d}_{n1}\cdot\mathbf{e})}{\omega_{n1}-\omega-\imath 0} + \frac{(\mathbf{d}_{2n}\cdot\mathbf{e})[\mathbf{m}^*_{n1}\cdot(\mathbf{n}_{in}\times\mathbf{e}')]}{\omega_{n1}+\omega'-\imath 0} + \frac{[\mathbf{m}_{2n}\cdot(\mathbf{n}_{in}\times\mathbf{e})](\mathbf{d}_{n1}\cdot\mathbf{e}')}{\omega_{n1}+\omega'-\imath 0} \right| \quad (51)$$

where $\omega' = \omega + \omega_{12}$ and unit-vector $\mathbf{n}_{in}$ designates the direction of propagation of the incident photon.

The expression, Eq.(51), can be cast in the following form

$$\sigma = \frac{4\pi\omega(\omega+\omega_{12})^3}{\hbar^2 c^4} \cdot \left|(C_{ik})_{21}(\mathbf{e}'_i)^*\mathbf{e}_k\right| \cdot \left|(\hat{S}_{ik})_{21}(\mathbf{e}')^*_i(\mathbf{n}_{in}\times\mathbf{e})_k + (\hat{T}_{ik})_{21}(\mathbf{n}_{in}\times(\mathbf{e}')^*)_i\mathbf{e}_k + (\hat{U}_{ik})_{21}(\mathbf{e})_i(\mathbf{n}_{in}\times(\mathbf{e}')^*_k) + (\hat{V}_{ik})_{21}(\mathbf{n}_{in}\times\mathbf{e}')_i(\mathbf{e}'_k)^*\right| \quad (52)$$

where $(S_{ik})_{21}, (T_{ik})_{21}, (U_{ik})_{21}$ and $(V_{ik})_{21}$ are 3×3 tensors, while the dipole-dipole tensor $(C_{ik})_{21}$ is defined above in Eq.(35). Here we assume that, in the general case, the vectors $\mathbf{e}'$ and $\mathbf{e}$ which represent the polarization of light are complex. Each of these tensors is represented as a sum of its irreducible components, e.g., $S_{ik} = S^0\delta_{ik} + S^s_{ik} + S^a_{ik}$, where

$$S^0 = \frac{1}{3}S_{ii} \quad , \quad S^s_{ik} = \frac{1}{2}(S_{ik}+S_{ki}) - S^0\delta_{ik} \quad , \quad S^a_{ik} = \frac{1}{2}(S_{ik}-S_{ki}) \quad (53)$$

Note also that S^0, T^0, U^0 and V^0 are called the scalar parts of the S, T, U and V tensors, respectively. The components with the superscripts s and/or a (e.g., T^s, T^a) are the symmetric and antisymmetric parts of the tensor. All components of the $S^0, T^0, U^0, V^0, S^s_{ik}, T^s_{ik}, U^s_{ik}, V^s_{ik}, S^a_{ik}, T^a_{ik}, U^a_{ik}$ and V^a_{ik} tensors contain the products of the corresponding components of the $\mathbf{d}$ and $\mathbf{m}$ vectors, which are the vectors of the electric dipole momentum and magnetic dipole

momentum, respectively. The vector-operators which represent the electric and magnetic dipole momenta are assumed to be self-conjugate. Furthermore, as mentioned above in the coordinate representation the vector $\mathbf{d}$ is a real vector (i.e. $\mathbf{d}^* = \mathbf{d}$), while the vector $\mathbf{m}$ is a complex vector (i.e. $\mathbf{m}^* \neq \mathbf{m}$). For instance, the explicit expressions for the S^0, T^0, U^0 and V^0 tensors (they are called the scalar-components) are

$$(S^0)_{21} = \frac{1}{3}\sum_n \frac{(d_i)_{2n}(m_i)_{n1}}{\omega_{n1} - \omega} \quad , \quad (T^0)_{21} = \frac{1}{3}\sum_n \frac{(m_i^*)_{2n}(d_i)_{n1}}{\omega_{n1} - \omega} \quad , \quad (54)$$

$$(U^0)_{21} = \frac{1}{3}\sum_n \frac{(d_i)_{2n}(m_i^*)_{n1}}{\omega_{n2} + \omega} \quad , \quad (V^0)_{21} = \frac{1}{3}\sum_n \frac{(m_i)_{2n}(d_i)_{n1}}{\omega_{n2} + \omega} \quad ,$$

respectively. Analogous formulas for the symmetric and antisymmetric parts of the S, T, U and V tensors are significantly more complicated. These formulas and the physical meaning of all irreducible components of these S, T, U and V tensors will be discussed elsewhere.

Thus, we have shown that all phenomena related to the optical activity can completely be described with the use of only four tensors: $\hat{S}_{21}, \hat{T}_{21}, \hat{U}_{21}$ and $\hat{V}_{21}$. The fifth tensor $\hat{C}_{21}$ (the tensor of electric-dipole light scattering) is included in the formula for the cross-section as an amplification factor. These five tensors have fifteen irreducible tensor-components $C^0, C^s_{ik}, C^a_{ik}, S^0, T^0, U^0, V^0, S^s_{ik}, T^s_{ik}, U^s_{ik}, V^s_{ik}, S^a_{ik}, T^a_{ik}, U^a_{ik}$ and V^a_{ik}. The first three tensors C^0, C^s_{ik}, C^a_{ik} here have nothing to do with the optical activity itself. Instead they determine the amplification factor which also appears to be $\omega-$dependent. The optical activity is described by the twelve tensors ($S^0, T^0, U^0, V^0, S^s_{ik}, T^s_{ik}, U^s_{ik}, V^s_{ik}, S^a_{ik}, T^a_{ik}, U^a_{ik}$ and V^a_{ik}). In many real applications, however, the total number of independent tensors can be reduced. For instance, if the 1- and 2-states are identical and $\omega_{21} = 0$ (Rayleigh scattering), then to describe optical activity one needs only two tensors (not four!) with six irreducible components. This case corresponds to the regular optical activity (optical rotation) measured in modern experiments with dilute solutions of organic molecules. Furthermore, if the polarization vectors are always chosen as real (not complex), then to describe the optical activity one needs only one 3×3 tensor with three irreducible components. However, the explicit $\omega-$dependence of such a tensor will be quite complicated. All such cases will be considered in our next study.

The intensity of the scattered light I' is uniformly related to the intensity of

the incident light I by the relation

$$I' = \left(\frac{\omega'}{\omega}\right)\sigma I \tag{55}$$

As follows from the formula for the cross-section σ, Eq.(51), in any optically active solution the intensity of the (scattered) light will always be rotated during its propagation along the direction $\mathbf{n}_{in}$. The factor $\left(\frac{\omega'}{\omega}\right)\sigma$ in the last formula can be considered as the rotation power. As follows from the last formula the uniform combination of the twelve tensors mentioned above multiplied by the amplification factor, Eq.(35), allows one to determine the so-called rotation power of the given optically active solution for the initially polarized light. Note that only our approach produces the correct and complete formula for the $\omega-$dependence of the rotation power.

6. Quantum Theory of Molecular Optical Activity

As can be seen above, the physical origin of the relations between different parameters used in classical theory of optical activity remains unknown. The corresponding analytical expressions, numerical values and all possible relations between some 'phenomenological' parameters can be found only with the use of modern quantum theory based on Quantum Electrodynamics. The first and very important step in the development of quantum origin of optical activity was made by Rosenfeld almost 80 years ago [1]. In the following papers [13], [14] and books [15] the quantum theory of molecular optical activity has been developed to its modern level. Below, we shall follow these studies. Our main goal in this Section is to obtain the relation between the optical rotatory parameter β from Eq.(22) and properties of an isolated molecule. For an isolated molecule the optical rotatory parameter β can only be a function of the molecular 2^{ℓ}-pole moments. In reality, however, only a few moments with small ℓ ($\ell = 1, 2$) contribute noticeably. As we mentioned above the parameter β is a pseudoscalar. Therefore, the first (largest) term in the expansion of β in terms of 2^{ℓ}-pole molecular momenta is proportional to the scalar product of the dipole vector and the pseudovector of the magnetic moment $\mathbf{d} \cdot \mathbf{m}$. The second term must be proportional to the product $\mathbf{d} \cdot \hat{Q} \cdot \mathbf{m}$, where $\hat{Q}$ is the second order tensor of the electric quadropole momentum.

Below, we shall assume that all molecular wave functions (for the ground and excited states) are known (or can be determined) to very good accuracy. In

this case, by using Rosenfeld's formula one can calculate the optical rotatory parameter β (in some studies it is also called the chiral response parameter)

$$\beta = \frac{c}{6\pi\hbar}\sum_b \frac{Im\Big[\langle a \mid \mathbf{d} \mid b\rangle\langle b \mid \mathbf{m} \mid a\rangle\Big]}{\nu_{ab}^2 - \nu^2} \tag{56}$$

where the summation is taken over all intermediate states. In this equation we use the linear frequencies ν instead of circular frequencies ω, where $\omega = 2\pi\nu$. The notation Im designates the imaginary part of the terms written in brackets. Symbols a and b stand for the quantum (molecular) states, while $\mid a\rangle$ and $\mid b\rangle$ mean the corresponding wave functions. Rosenfeld's formula is based on an assumption that all molecular states (ground and excited) have zero widths. In other words, these states are stable, i.e. the decay time is infinite. In general, this is not a very realistic assumption and we need to introduce finite line widths, e.g., $\gamma_{ab}(\nu) = \frac{4\pi^2 e^2 |\mathbf{D}_{ab}|^2 (\nu_a - \nu_b)^3}{3\epsilon_0 \hbar c^3}$ (in SI-units and in the lowest order dipole approximation [10]). The Rosenfeld formula for the optical rotation δ can now be written in the form

$$\delta = \frac{16\pi^2 N z}{3hc}\sum_b \frac{\nu^2 R_{ab}}{\nu_{ab}^2 - \nu^2 + \imath\nu\gamma_{ab}} \tag{57}$$

where $R_{ab} = Im\Big[\langle a \mid \mathbf{d} \mid b\rangle\langle b \mid \mathbf{m} \mid a\rangle\Big]$ is the so-called rotating power. By separating the real and imaginary parts of this expression one finds for the actual optical rotation

$$\theta = \frac{16\pi^2 N z}{3hc}\sum_b \frac{\nu^2(\nu_{ab}^2 - \nu^2) R_{ab}}{(\nu_{ab}^2 - \nu^2)^2 + \nu^2\gamma_{ab}^2} \tag{58}$$

and for the circular dichroism

$$\kappa = -\frac{16\pi^2 N z}{3hc}\sum_b \frac{\nu^3 \gamma_{ab} R_{ab}}{(\nu_{ab}^2 - \nu^2)^2 + \nu^2\gamma_{ab}^2} \tag{59}$$

where the notations from formula Eq.(33) are used. The definition of rotating power given above corresponds to the dipole-dipole approximation. In the higher order approximation the rotating power must be taken in the form $R_{ab} = Im\Big[\langle a \mid \mathbf{d} \mid b\rangle\langle b \mid \mathbf{m} \mid a\rangle + \sum_{cd}\langle a \mid \mathbf{d} \mid c\rangle\langle c \mid \hat{Q} \mid d\rangle\langle d \mid \mathbf{m} \mid a\rangle\Big]$.

In reality it is very difficult to calculate the matrix elements R_{ab} accurately. However, a number of useful approximate formulas have been derived from the expressions Eq.(58) and Eq.(59). For instance, if in some experiment we can see N peaks in the $\theta(\lambda)$ function and K peaks in the $\kappa(\lambda)$ function, then it is possible to approximate our experimental data by using the two following formulas

$$\theta(\lambda) = \sum_{i=1}^{N} \frac{A_i(\lambda^2 - \lambda_i^2)}{(\lambda^2 - \lambda_i^2)^2 + B_i} \quad \text{and} \quad \kappa(\lambda) = \sum_{j=1}^{K} \frac{C_j \lambda}{(\lambda^2 - \lambda_j^2)^2 + D_j} \tag{60}$$

where all numerical parameters A_i, B_i, C_i and D_i must be determined by using the experimental values of θ and κ at different wavelengths $\lambda = \frac{1}{\nu}$. Numerical examples can be found in the book by Djerassi [6].

Rosenfeld's theory of optical activity allows one to determine the relations between basic molecular properties and actual optical rotation and circular dichroism observed in experiments. Indeed, by applying the known molecular wave functions one can compute the values of $\langle a \mid \mathbf{d} \mid b \rangle$ and $\langle b \mid \mathbf{m} \mid a \rangle$ which are used in formulas for θ and κ above. By using these values we can evaluate the rotating powers R_{ab}. Then we can try to approximate the curves $\theta(\nu)$ and $\kappa(\nu)$ obtained in actual experiments. During this step all line widths γ_{ab} can be varied as numerical parameters. In practice, this approach works approximately only for some simple molecules. For many molecules of interest, e.g., for complex molecules used in cancer research, the current accuracy of the numerical determination of the $\langle b \mid \mathbf{m} \mid a \rangle$ values is not sufficient to make accurate comparisons with experiments. In particular, the signs of the $\langle b \mid \mathbf{m} \mid a \rangle$ values can be wrong in a number of cases. In addition to this, Rosenfeld's theory of optical activity is essentially a semi-classical theory, since all radiation fields in this theory are considered classically. The most rigorous analysis of molecular optical activity can be performed only on a basis of modern quantum electrodynamics (QED) [9]. This will be one of our goals in future studies.

7. Specific Rotation by Chiral Organic Molecules

In previous Sections we have briefly considered some theoretical aspects of the molecular optical activity at arbitrary wavelengths. In this Section we discuss a few basic features which are known for optically active organic molecules in solutions. In general, if some organic molecule has non-zero electric and magnetic

moments, then its optical rotation θ, Eq.(58), differs from zero. Such a molecule shows a number of phenomena which are usually designated as 'optical activity', or briefly, as an optical rotation of plane-polarized light. In principle, any molecule which does not coincide with its mirror image can be optically active. Moreover, for each optically active molecule one can always find another non-identical form of the same molecule which is related to the original molecule through reflection. These two forms of one molecule are called enantiomers, specifically $D-$ and $L-$ enantiomers, which naturally refer to the right- and left-handed forms, respectively. In many sources the D- and L-enantiomers of various molecules are discussed. However, it should be emphasized that currently there is no uniform relation between the absolute configuration of complex molecules and their ability to be left- and/or right-rotating. Here it is not our intention to summarize all basic rules found for numerous organic substances which are optically active. Instead, we restrict ourselves to an analysis relevant to observation of optical activity in the vacuum ultraviolet region.

The most interesting cases can be observed in various organic molecules, i.e. in molecules which include one or more carbon atoms. Formally, one carbon atom in a molecule which is bonded to four different atoms and/or groups of atoms is sufficient for manifestation of optical activity. In general, such a carbon atom is called an asymmetric atom, or a chiral center. In many cases the optical activity can be observed in molecules with two, three and more asymmetric carbon atoms (for more detail, see, e.g., [11], [12] and references therein). A very well known example is the tartaric acid which may exist in the form of D- and L-enantiomers and in its meso-form which has no optical activity. Note also that a number of organic molecules with no chiral centers show overall optical activity, e.g., allenes, spiranes and biphenyls. Such systems are considered as inherently dysymmetric. The active electrons in these molecules are delocalized over a chiral nuclear system.

In this work we restrict ourselves to the consideration of organic molecules with one asymmetric carbon atom (chiral center). In general, the observed optical rotation θ, Eq.(58), produced by one asymmetric carbon atom in a molecule will be small. However, if some additional conditions are combined with each other, then the actual optical rotation θ increases to moderate, large and very large values. It was shown more than sixty years ago that 'close' presence of some special groups of atoms can increase the actual optical rotation by a few orders of magnitude. Such special groups are called 'chromophors'. Typical examples of chromophors are the $-NH_2$, $>CO$, $-CN$, $-C_6H_5$ groups and some

others. It should be emphasized that none of these groups is optically active, but each amplifies significantly the optical activity of the neithbouring chiral center.

Currently, there are a few dozens of different atomic groups which are recognized as regular basic chromophors and a large number of special groups of atoms which become chromophors only at certain wavelengths. In general, any group of atoms which has excessive $\pi-$electron density can be considered as a potential chromophor and any experimental study of optical activity in organic molecules is reduced to the analysis of various chromophors and their influence on one of more asymmetric carbon atom(s). The problem contains many complications. For instance, if one of the hydrogen atoms in a benzene ring bonded with a chiral carbon center is replaced by the $-NH_2$ group, then one finds the new chromophor $-C_6H_4NH_2$ which has a different influence on this chiral center. In other words, the change in optical activity of the chiral center produced by the new chromophor ($-C_6H_4NH_2$) cannot be predicted accurately and uniformly from the analogous information known for the $-C_6H_5$ and $-NH_2$ groups. In general, the delocalization of $\pi-$electrons in various organic molecules can be used to create a huge number of 'new' chromophors. Moreover, if the same chiral center is bonded to both the $-C_6H_5$ and $-NH_2$ groups, the amplification of its chiral activity will be drastically different from the previous case. In addition to this one also finds that substitution of one hydrogen atom in the $-C_6H_5$ chromophor by, e.g., the $-CH_3$ group will also have a noticeable effect on overall optical activity. The following experimental analysis must detect (and investigate) a direct relation between the actual optical activity and position of the hydrogen atom (in the benzene ring) which was replaced by the $-CH_3$ group.

It is important for the general theory that each chromophore group can be represented by a number of poles located in the complex plane of frequencies ν (so-called ν-plane). In other words, any chromophore group has a number of poles in the complex ν-plane associated with it. If such a pole is close to the real axis, then in experiments one finds large and very large values of optical rotation δ and circular dichroism κ, respectively. In real organic molecules one finds not one, but a few different chromophore groups. The experimental curves for the $\delta(\nu)$ and $\kappa(\nu)$ values measured for $\nu > 0$ in actual organic molecules are the result of interaction between various poles located in a complex frequency plane (ν) at different frequencies. In general, the interaction between different chromophores produces very complicated spectra for the optical rotation $\delta(\nu)$ and circular dichroism $\kappa(\nu)$. The complexity of these spectra rapidly increases

as the number of poles per unit frequency interval increases. In particular, this is the case for vacuum ultraviolet wavelengths, since almost all known chromophors have many absorption lines located in VUV region.

Conclusion

We have considered the phenomena of optical activity in homogeneous solutions of various organic substances. The classical macroscopic theory based on Maxwell equations in dielectric (or nonconducting) media is discussed in detail. The Stokes parameters for almost monochromatic light are defined rigorously. The relations between the optical rotation and circular dichroism are derived from the basic Kramers-Kronig relations. These relations allow one to obtain/evaluate, e.g., the circular dichroism by using the known values of optical rotation at the same frequencies. The explicit expression for the tensors of molecular optical activity are derived. Our formulas derived for the tensor(s) of molecular optical activity can be used to explain a large number of phenomenon currently known in molecular optical activity. Note that our formulas can successfully be applied to the case of the Raileigh (or non-shifted) scattering when $\omega_{21} = 0$ and also to the cases when $\omega_{21} \neq 0$ (shifted or combined light scattering). It is shown that all known lowest order effects of optical activity must be described with the use of finite number of tensors, e.g., five, three and even one tensor(s).

We also briefly consider the quantum (or semi-classical) theory of molecular optical activity developed by Rosenfeld in [1]. In this theory all molecules are quantum systems, while all electromagnetic fields are described by classical Maxwell equations. A possibility to extend measurements of optical rotation and circular dichroism into the vacuum ultraviolet region is discussed. Currently, this task seems to be extremely difficult, since there are a large number of unsolved problems which must be considered before the whole procedure can be usefully implemented. Moreover, it is clear that even the requisite experimental technique will have many fundamental differences from the technique applied for traditional wavelengths. Nevertheless, we can expect that measurements of optical rotation and circular dichroism in the vacuum ultraviolet region will produce a large volume of very valuable experimental data. These measurements will open a new avenue for some important discoveries and improvements in our current understanding of optical activity of organic molecules.

References

[1] L. Rosenfeld, *Z. Phys.* **52**, 161 (1928).

[2] M. Born and E. Wolf, *Principles of Optics*. (4th edition, Pergamon Press, New York (1968)).

[3] L.D. Landau and E.M. Lifshitz, *Electrodynamics of Continuous Media*, (2nd Ed., Pergamon Press, New York, (1984)).

[4] L.D. Landau and E.M. Lifshitz, *The Classical Theory of Fields*, (4th Ed., Pergamon Press, New York, (1979)).

[5] P.A.M. Dirac, *Principles of Quantum Mechanics*, (Oxford: Clarendon Press, 4th Ed., 1958).

[6] C. Djerassi, *Optical Rotatory Dispersion*, (McGraw-Hill, New York, (1960)).

[7] J.D. Jackson, *Classical Electrodynamics*, (2nd Ed., John Wiley and Sons, New York, (1975)).

[8] G. Placzek, in: *Handbuch der radioologie* [*Handbook of radiology*] Ed. E. Marx, (Academishe, Leipzig, (1934)), **6**, 205.

[9] V.B. Beresteskii, E.M. Lifshitz and L.P. Pitaevskii, *Quantum Electrodynamics*, (2nd Ed., Pergamon Press, New York, (1984)).

[10] R. Loudon, *The Quantum Theory of Light*, (2nd Ed., Clarendon Press, Oxford, UK (1983)).

[11] S.F. Mason, *Molecular Optical Activity and Chiral Discrimination*, (Cambridge University Press, London, (1982)).

[12] J.D. Roberts and M.C. Caserio, *Basic principles of Organic Chemistry*, (2nd Ed., W.A. Benjamin, Inc., Menlo Park, (1977)).

[13] E.U. Condon, Optical Rotatory Power, *Rev. Mod. Phys.* **9**, 432 (1937).

[14] W. Kauzmann, J. Walter and H. Eyring, Optical Activity, *Chem. Rev.* **26**, 339 (1940).

[15] H. Eyring, J. Walter and G.E. Kimball, *Quantum Chemistry*, (John Wiley And Sons Inc. (1944)).

Chapter 13

Classical Solutions for N-Dimensional Schrödinger and Wave Equations

Svetlin G. Georgiev*
Sorbonne University, Paris, France

Abstract

In this chapter we investigate the IVPs for n-dimensional Schrödinger and wave equations. A new topological approach is applied to prove the existence of at least one classical solution and at least two nonnegative classical solutions for the considered IVPs. The arguments are based upon recent theoretical results.

MSC 37C25, 47H10, 58J20

Keywords: Schrödinger equation, wave equation, existence, classical solution.

* Corresponding Author's Email: svetlingeorgiev1@gmail.com.

In: Horizons in World Physics. Volume 312
Editor: Albert Reimer
ISBN: 979-8-89113-513-0

1. Introduction

In this paper we investigate for existence of classical solutions the IVPs for n-dimensional Schrödinger and wave equations

$$\begin{aligned} iu_t-\Delta u &= |u|^{p-1}u, \quad t>0, \quad x\in\mathbb{R}^n, \\ u(0,x) &= u_0(x), \quad x\in\mathbb{R}^n, \end{aligned} \tag{1}$$

and

$$\begin{aligned} u_{tt}-\Delta u &= |u|^{p-1}u, \quad t>0, \quad (x,y)\in\mathbb{R}^n, \\ u(0,x) &= v_0(x), \quad u_t(0,x)=v_1(x), \quad x\in\mathbb{R}^n, \end{aligned} \tag{2}$$

respectively, where

(H1) $u_0\in\mathcal{C}^2(\mathbb{R}^n)$, $0\leq u_0\leq B$ on $\mathbb{R}^n$, $p\geq 1$,

(G1) $v_0,v_1\in\mathcal{C}^2(\mathbb{R}^n)$, $0\leq v_0,v_1\leq B$ on $\mathbb{R}^n$,

where B is a positive constant. Here Δ is the Laplace operator.

The one-dimensional Schrödinger equation with certain type of analytic initial data in L^2 was investigated in [9] and the authors have proved existence of global analytic solutions. The Schrödinger equation was investigated extensively for initial data in the Sobolev spaces H^s. Recently, the theory of analytic solutions for partial differential equations of Schrödinger type was developed(see [2, 3, 4] and references therein).

The wave equation (2) was investigated for local well-posedness in the homogeneous Sobolev spaces $\dot{H}^s$ in [7] and the authors showed that the optimal regularity in dimension two is as follows

$$\begin{cases} \frac{3}{4}-\frac{1}{p-1}, & 3<p<5, \\ 1-\frac{2}{p-1}, & p>5. \end{cases} \tag{3}$$

In this paper we investigate the equations (1) and (2) for existence and non uniqueness of classical solutions.

The paper is organized as follows: in the next section, we give some auxiliary results. In Section 3 we prove existence of at least one classical solution and existence of at least two nonnegative classical solutions for the IVP (1). In Section 4 we prove existence of at least one classical solution and existence of at least two nonnegative classical solutions for the IVP (2).

2. Preliminary Results

In this paper, we will use some nonlinear alternatives, in one hand, to develop a new fixed point theorem and in another hand to study the existence of solutions for Problem (1). The following theorem will be used to prove Theorems 3.

Theorem 1. *Let E be a Banach space, Y a closed, convex subset of E,*

$$U = \{x \in Y \ : \ \|x\| < R\},$$

with $R > 0$. Consider two operators T and S, where

$$Tx = \varepsilon\, x, \ x \in \overline{U},$$

for $\varepsilon \in \mathbb{R}$, and $S : \overline{U} \to E$ be such that

(i) *$I - S : \overline{U} \to Y$ continuous, compact and*

(ii) *$\{x \in Y : x = sgn(\varepsilon)\lambda(I-S)x, \quad \|x\| = R\} = \emptyset$, for any $\lambda \in \left(0, \frac{1}{|\varepsilon|}\right)$, where $sgn(\varepsilon)$ is the signum of ε.*

Then there exists $x^* \in \overline{U}$ such that

$$Tx^* + Sx^* = x^*.$$

Proof. We have that the operator $\frac{1}{\varepsilon}(I-S) : \overline{U} \to Y$ is continuous and compact. Suppose that there exist $x_0 \in \partial U$ and $\mu_0 \in (0,1)$ such that

$$x_0 = \mu_0 \frac{1}{\varepsilon}(I - S)x_0,$$

that is

$$x_0 = sgn(\varepsilon)\, \frac{\mu_0}{|\varepsilon|}\, (I - S)x_0.$$

This contradicts the condition (ii). From Leray-Schauder nonlinear alternative, it follows that there exists $x^* \in \overline{U}$ so that

$$x^* = \frac{1}{\varepsilon}(I - S)x^*$$

or

$$\varepsilon\, x^* + Sx^* = x^*,$$

or

$$Tx^* + Sx^* = x^*.$$

□

Let X be a real Banach space.

Definition 1. *A mapping $K : X \to X$ is said to be completely continuous if it is continuous and maps bounded sets into relatively compact sets.*

The concept for l-set contraction is related to that of the Kuratowski measure of noncompactness which we recall for completeness.

Definition 2. *Let Ω_X be the class of all bounded sets of X. The Kuratowski measure of noncompactness $\alpha : \Omega_X \to [0, \infty)$ is defined by*

$$\alpha(Y) = \inf \left\{ \delta > 0 : Y \subset \bigcup_{j=1}^{m} Y_j \quad \text{and} \quad diam(Y_j) \leq \delta, \quad j \in \{1, \dots, m\} \right\},$$

where $diam(Y_j) = \sup\{\|x - y\|_X : x, y \in Y_j\}$ is the diameter of Y_j, $j \in \{1, \dots, m\}$.

For the main properties of measure of noncompactness we refer the reader to [1].

Definition 3. *A mapping $K : X \to X$ is said to be l-set contraction if it is continuous, bounded and there exists a constant $l \geq 0$ such that*

$$\alpha(K(Y)) \leq l\alpha(Y),$$

for any bounded set $Y \subset X$. The mapping K is said to be a strict set contraction if $l < 1$.

Obviously, if $K : X \to X$ is a completely continuous mapping, then K is 0-set contraction (see [6], pp. 264).

Definition 4. *Let X and Y be real Banach spaces. A mapping $K : X \to Y$ is said to be expansive if there exists a constant $h > 1$ such that*

$$\|Kx - Ky\|_Y \geq h\|x - y\|_X$$

for any $x, y \in X$.

Definition 5. *A closed, convex set $\mathcal{P}$ in X is said to be cone if*

1. *$\alpha x \in \mathcal{P}$ for any $\alpha \geq 0$ and for any $x \in \mathcal{P}$,*

2. $x, -x \in \mathcal{P}$ *implies* $x = 0$.

Denote $\mathcal{P}^* = \mathcal{P}\backslash\{0\}$.

Lemma 1. *Let X be a closed convex subset of a Banach space E and $U \subset X$ a bounded open subset with $0 \in U$. Assume that there exists $\varepsilon > 0$ small enough and $K : \overline{U} \to X$ is a strict k-set contraction that satisfies the boundary condition:*

$$Kx \notin \{x,\ \lambda x\} \text{ for all } x \in \partial U \text{ and } \lambda \geq 1 + \varepsilon.$$

Then the fixed point index $i\,(K, U, X) = 1$.

Proof. Consider the homotopic deformation $H : [0, 1] \times \overline{U} \to X$ defined by

$$H(t, x) = \frac{1}{\varepsilon + 1} tKx.$$

The operator H is continuous and uniformly continuous in t for each x, and the mapping $H(t, .)$ is a strict set contraction for each $t \in [0, 1]$. In addition, $H(t, .)$ has no fixed point on ∂U. On the contrary,
• If $t = 0$, there exists some $x_0 \in \partial U$ such that $x_0 = 0$, contradicting $x_0 \in U$.
• If $t \in (0, 1]$, there exists some $x_0 \in \mathcal{P} \cap \partial U$ such that $\frac{1}{\varepsilon+1} tKx_0 = x_0$; then $Kx_0 = \frac{1+\varepsilon}{t} x_0$ with $\frac{1+\varepsilon}{t} \geq 1 + \varepsilon$, contradicting the assumption. From the invariance under homotopy and the normalization properties of the index, we deduce

$$i\,(\frac{1}{\varepsilon + 1} K, U, X) = i\,(0, U, X) = 1.$$

Now, we show that

$$i\,(K, U, X) = i\,(\frac{1}{\varepsilon + 1} K, U, X).$$

We have

$$\frac{1}{\varepsilon + 1} Kx \neq x,\ \forall\, x \in \partial U. \tag{4}$$

Then there exists $\gamma > 0$ such that

$$\|x - \frac{1}{\varepsilon + 1} Kx\| \geq \gamma,\ \forall\, x \in \partial U.$$

On other hand, we have $\frac{1}{\epsilon+1} Kx \to Kx$ as $\epsilon \to 0$, for $x \in \overline{U}$. So, for ε small enough

$$\|Kx - \frac{1}{\varepsilon + 1} Kx\| < \frac{\gamma}{2},\ \forall\, x \in \partial U.$$

Define the convex deformation $G:[0,1]\times\overline{U}\to X$ by

$$G(t,x)=tKx+(1-t)\frac{1}{\varepsilon+1}Kx.$$

The operator G is continuous and uniformly continuous in t for each x, and the mapping $G(t,.)$ is a strict set contraction for each $t\in[0,1]$ (since $t+\frac{1}{\varepsilon+1}(1-t)<t+1-t=1$). In addition, $G(t,.)$ has no fixed point on ∂U. In fact, for all $x\in\partial U$, we have

$$\begin{aligned}\|x-G(t,x)\| &= \|x-tKx-(1-t)\tfrac{1}{\varepsilon+1}Kx\|\\ &\geq \|x-\tfrac{1}{\varepsilon+1}Kx\|-t\|Kx-\tfrac{1}{\varepsilon+1}Kx\|\\ &> \gamma-\tfrac{\gamma}{2}>\tfrac{\gamma}{2}.\end{aligned}$$

Then our claim follows from the invariance property by homotopy of the index. □

Proposition 1. *Let $\mathcal{P}$ be a cone in a Banach space E. Let also, U be a bounded open subset of $\mathcal{P}$ with $0\in U$. Assume that $T:\Omega\subset\mathcal{P}\to E$ is an expansive mapping with constant $h>1$, $S:\overline{U}\to E$ is a l-set contraction with $0\leq l<h-1$, and $S(\overline{U})\subset(I-T)(\Omega)$. If there exists $\varepsilon\geq 0$ such that*

$$Sx\notin\{(I-T)(x),\quad (I-T)(\lambda x)\}\ \text{for all}\ x\in\partial U\cap\Omega\ \text{and}\ \lambda\geq 1+\varepsilon,$$

then the fixed point index $i_*(T+S,U\cap\Omega,\mathcal{P})=1$.

Proof. The mapping $(I-T)^{-1}S:\overline{U}\to\mathcal{P}$ is a strict set contraction and it is readily seen that the following condition is satisfied

$$(I-T)^{-1}Sx\notin\{x,\lambda x\}\quad\text{for all}\quad x\in\partial U\quad\text{and}\quad\lambda\geq 1+\epsilon.$$

Our claim then follows from the definition of i_* and Lemma 1. □

The following result will be used to prove our main result.

Theorem 2. *Let $\mathcal{P}$ be a cone in a Banach space E; Ω a subset of $\mathcal{P}$ and U_1,U_2 and U_3 three open bounded subsets of $\mathcal{P}$ such that $\overline{U}_1\subset\overline{U}_2\subset U_3$ and $0\in U_1$. Assume that $T:\Omega\to\mathcal{P}$ is an expansive mapping with constant $h>1$, $S:\overline{U}_3\to E$ is a k-set contraction with $0\leq k<h-1$ and $S(\overline{U}_3)\subset(I-T)(\Omega)$. Suppose that $(U_2\setminus\overline{U}_1)\cap\Omega\neq\emptyset$, $(U_3\setminus\overline{U}_2)\cap\Omega\neq\emptyset$, and there exists $u_0\in\mathcal{P}^*$ such that the following conditions hold:*

(i) $Sx \neq (I-T)(x-\lambda u_0)$, *for all* $\lambda > 0$ *and* $x \in \partial U_1 \cap (\Omega + \lambda u_0)$,

(ii) *there exists* $\epsilon \geq 0$ *such that* $Sx \neq (I-T)(\lambda x)$, *for all* $\lambda \geq 1+\epsilon$, $x \in \partial U_2$ *and* $\lambda x \in \Omega$,

(iii) $Sx \neq (I-T)(x-\lambda u_0)$, *for all* $\lambda > 0$ *and* $x \in \partial U_3 \cap (\Omega + \lambda u_0)$.

Then $T+S$ *has at least two non-zero fixed points* $x_1, x_2 \in \mathcal{P}$ *such that*

$$x_1 \in \partial U_2 \cap \Omega \text{ and } x_2 \in (\overline{U}_3 \setminus \overline{U}_2) \cap \Omega$$

or

$$x_1 \in (U_2 \setminus U_1) \cap \Omega \text{ and } x_2 \in (\overline{U}_3 \setminus \overline{U}_2) \cap \Omega.$$

Proof. If $Sx = (I-T)x$ for $x \in \partial U_2 \cap \Omega$, then we get a fixed point $x_1 \in \partial U_2 \cap \Omega$ of the operator $T+S$. Suppose that $Sx \neq (I-T)x$ for any $x \in \partial U_2 \cap \Omega$. Without loss of generality, assume that $Tx+Sx \neq x$ on $\partial U_1 \cap \Omega$ and $Tx+Sx \neq x$ on $\partial U_3 \cap \Omega$, otherwise the conclusion holds. By [5, Proposition 2.16] and Proposition 1, we have

$$i_*(T+S, U_1 \cap \Omega, \mathcal{P}) = i_*(T+S, U_3 \cap \Omega, \mathcal{P}) = 0 \text{ and } i_*(T+S, U_2 \cap \Omega, \mathcal{P}) = 1.$$

The additivity property of the index yields

$$i_*(T+S, (U_2 \setminus \overline{U}_1) \cap \Omega, \mathcal{P}) = 1 \text{ and } i_*(T+S, (U_3 \setminus \overline{U}_2) \cap \Omega, \mathcal{P}) = -1.$$

Consequently, by the existence property of the index, $T+S$ has at least two fixed points $x_1 \in (U_2 \setminus U_1) \cap \Omega$ and $x_2 \in (\overline{U}_3 \setminus \overline{U}_2) \cap \Omega$. □

3. The Schrödinger Equation

In this section we will investigate the IVP (1).

3.1. Auxiliary Results

Let $X = \mathcal{C}^1([0,\infty), \mathcal{C}^2(\mathbb{R}^n))$ be endowed with the norm

$$\|u\| = \max\left\{ \sup_{(t,x)\in[0,\infty)\times\mathbb{R}^n} |u(t,x)|, \sup_{(t,x)\in[0,\infty)\times\mathbb{R}^n} |u_t(t,x)|, \right.$$

$$\left. \sup_{(t,x)\in[0,\infty)\times\mathbb{R}^n} |u_{x_j}(t,x)|, \sup_{(t,x)\in[0,\infty)\times\mathbb{R}^n} |u_{x_jx_j}(t,x)|, \quad j \in \{1,\dots,n\} \right\},$$

provided it exists. For $u \in X$, define the operator

$$\begin{aligned} S_1u(t,x) &= i(u(t,x)-u_0(x)) - \int_0^t \Delta u(t_1,x)dt_1 \\ &\quad - \int_0^t |u(t_1,x)|^{p-1}u(t_1,x)dt_1, \end{aligned}$$

$(t,x) \in [0,\infty)\times\mathbb{R}^n$.

Lemma 2. *Suppose* $(H1)$. *Let* $u \in X$ *satisfies the equation*

$$S_1u(t,x)=0, \quad (t,x)\in[0,\infty)\times\mathbb{R}^n. \tag{5}$$

Then u *is a solution to the IVP* (1).

Proof. We have

$$\begin{aligned} 0 &= i(u(t,x)-u_0(x)) - \textstyle\int_0^t \Delta u(t_1,x)dt_1 \\ &\quad - \textstyle\int_0^t |u(t_1,x)|^{p-1}u(t_1,x)dt_1, \end{aligned} \tag{6}$$

$(t,x)\in[0,\infty)\times\mathbb{R}^n$, which we differentiate with respect to t and we get

$$0 = iu_t(t,x) - \Delta u(t,x) - |u(t,x)|^{p-1}u(t,x), \tag{7}$$

$(t,x)\in[0,\infty)\times\mathbb{R}^n$. Now, we put $t=0$ into (6) and we arrive at

$$0 = u(0,x)-u_0(x), \quad x\in\mathbb{R}^n.$$

This completes the proof. □

Let $B_1=\max\{2B, nB+B^p\}$.

Lemma 3. *Suppose* $(H1)$. *If* $u\in X$, $\|u\|\leq B$, *then*

$$|S_1u(t,x)|\leq (1+t)B_1, \quad (t,x)\in[0,\infty)\times\mathbb{R}^n.$$

Proof. We have

$$\begin{aligned}
|S_1u(t,x)| &= \Big|i(u(t,x)-u_0(x)) - \int_0^t \Delta u(t_1,x)dt_1 \\
&\quad - \int_0^t |u(t_1,x)|^{p-1}u(t_1,x)dt_1\Big| \\
&\le |u(t,x)| + |u_0(x)| + \int_0^t \sum_{j=1}^n |u_{x_jx_j}(t_1,x)|dt_1 \\
&\quad + \int_0^t |u(t_1,x)|^p dt_1 \\
&\le 2B + nBt + B^p t \\
&= 2B + (nB+B^p)t \\
&\le B_1(1+t), \quad (t,x)\in[0,\infty)\times\mathbb{R}^n.
\end{aligned}$$

This completes the proof. □

Below, suppose that

(H2) there exist a function $g \in \mathcal{C}([0,\infty)\times\mathbb{R}^n)$ so that $g > 0$ on $(0,\infty)\times(\mathbb{R}^n\backslash\{0\})$,

$$g(0,x) = g(t,0,x_2,\ldots,x_n) = \cdots = g(t,x_1,x_2,\ldots,x_{n-1},0) = 0,$$

$(t,x)\in[0,\infty)\times\mathbb{R}^n$, and a positive constant A such that

$$\begin{aligned}
&2^{3n+1}(1+t+t^2)\prod_{j=1}^n(1+|x_j|+x_j^2) \\
&\quad\times\int_0^t\Big|\int_0^x g(t_1,s)ds\Big|dt_1 \le A,
\end{aligned}$$

where $\int_0^x = \int_0^{x_1}\ldots\int_0^{x_n}$, $ds = ds_n\ldots ds_1$. In the end of this section we will give an example for such function g and such constant A. For $u\in X$, define

the operator

$$S_2u(t,x)=\int_0^t\int_0^x(t-t_1)\prod_{j=1}^n(x_j-s_j)^2g(t_1,s)S_1u(t_1,s)dsdt_1,$$
$$(t,x)\in[0,\infty)\times\mathbb{R}^n.$$

Lemma 4. *Suppose* $(H1)$ *and* $(H2)$. *If* $u\in X$ *satisfies the equation*

$$S_2u(t,x)=0,\quad (t,x)\in[0,\infty)\times\mathbb{R}^n, \tag{8}$$

then u *is a solution to the IVP* (1).

Proof. We differentiate two times in t and three times in x_j, $j\in\{1,\dots,n\}$, and we find

$$g(t,x)S_1u(t,x)=0,\quad (t,x)\in[0,\infty)\times\mathbb{R}^n.$$

Hence,

$$S_1u(t,x)=0,\quad (t,x)\in(0,\infty)\times(\mathbb{R}^n\backslash\{0\}).$$

Since $S_1u(\cdot,\cdot)$ is a continuous function on $[0,\infty)\times\mathbb{R}^n$, we get

$$\begin{aligned}0&=\lim_{t\to0}S_1u(t,x)=S_1u(0,x)\\&=\lim_{x_1\to0}S_1u(t,x)=S_1u(t,0,x_2,\dots,x_n)\\&=\lim_{x_n\to0}S_1u(t,x)=S_1u(t,x_1,\dots,x_{n-1},0),\quad (t,x)\in[0,\infty)\times\mathbb{R}^n.\end{aligned}$$

Thus,

$$S_1u(t,x)=0,\quad (t,x)\in[0,\infty)\times\mathbb{R}^n.$$

Now, applying Lemma 2, we get the desired result. □

Lemma 5. *Suppose* $(H1)$ *and* $(H2)$. *If* $u\in X$, $\|u\|\leq B$, *then*

$$\|S_2u\|\leq AB_1.$$

Proof. We will use the inequality $(x+y)^p \leq 2^p(x^p+y^p)$, $p>0, x>0, y>0$. We have

$$\begin{aligned}
|S_2u(t,x)| &= \left|\int_0^t\int_0^x (t-t_1)\prod_{j=1}^n (x_j-s_j)^2 g(t_1,s)S_1u(t_1,s)dsdt_1\right| \\
&\leq \int_0^t\left|\int_0^x (t-t_1)\prod_{j=1}^n (x_j-s_j)^2 g(t_1,s)|S_1u(t_1,s)|ds\right|dt_1 \\
&\leq B_1\int_0^t\left|\int_0^x (t-t_1)(1+t_1)\prod_{j=1}^n (x_j-s_j)^2 g(t_1,s)ds\right|dt_1 \\
&\leq B_1 2^{3n+1}t(1+t)\prod_{j=1}^n (1+|x_j|+x_j^2)\int_0^t\left|\int_0^x g(t,s)ds\right|dt_1 \\
&\leq AB_1, \quad (t,x)\in[0,\infty)\times\mathbb{R},
\end{aligned}$$

and

$$\begin{aligned}
\left|\frac{\partial}{\partial t}S_2u(t,x)\right| &= \left|\int_0^t\int_0^x \prod_{j=1}^n (x_j-s_j)^2 g(t_1,s)S_1u(t_1,s)dsdt_1\right| \\
&\leq \int_0^t\left|\int_0^x \prod_{j=1}^n (x_j-s_j)^2 g(t_1,s)|S_1u(t_1,s)|ds\right|dt_1 \\
&\leq B_1\int_0^t\left|\int_0^x (1+t_1)\prod_{j=1}^n (x_j-s_j)^2 g(t_1,s)ds\right|dt_1 \\
&\leq B_1 2^{3n+1}(1+t)\prod_{j=1}^n (1+|x_j|+x_j^2)\int_0^t\left|\int_0^x g(t,s)ds\right|dt_1 \\
&\leq AB_1, \quad (t,x)\in[0,\infty)\times\mathbb{R},
\end{aligned}$$

and

$$\begin{aligned}\left|\frac{\partial}{\partial x_k}S_2u(t,x)\right| &= \left|\int_0^t\int_0^x (t-t_1)\prod_{j=1,j\neq k}^{n}(x_j-s_j)^2(x_k-s_k)g(t_1,s)S_1u(t_1,s)dsdt_1\right|\\ &\leq \int_0^t\left|\int_0^x (t-t_1)\prod_{j=1,j\neq k}^{n}(x_j-s_j)^2(x_k-s_k)g(t_1,s)|S_1u(t_1,s)|ds\right|dt_1\\ &\leq B_1\int_0^t\left|\int_0^x (t-t_1)(1+t_1)\prod_{j=1,j\neq k}^{n}(x_j-s_j)^2(x_k-s_k)g(t_1,s)ds\right|dt_1\\ &\leq B_1 2^{3n-2}t(1+t)\prod_{j=1,j\neq k}^{n}(1+|x_j|+x_j^2)|x_k|\int_0^t\left|\int_0^x g(t,s)ds\right|dt_1\\ &\leq AB_1,\quad (t,x)\in[0,\infty)\times\mathbb{R}^n,\end{aligned}$$

$k\in\{1,\ldots,n\}$, and

$$\begin{aligned}\left|\frac{\partial^2}{\partial x_k^2}S_2u(t,x)\right| &= \left|\int_0^t\int_0^x (t-t_1)\prod_{j=1,j\neq k}^{n}(x_j-s_j)^2g(t_1,s)S_1u(t_1,s)dsdt_1\right|\\ &\leq \int_0^t\left|\int_0^x (t-t_1)\prod_{j=1,j\neq k}^{n}(x_j-s_j)^2g(t_1,s)|S_1u(t_1,s)|ds\right|dt_1\\ &\leq B_1\int_0^t\left|\int_0^x (t-t_1)(1+t_1)\prod_{j=1,j\neq k}^{n}(x_j-s_j)^2g(t_1,s)ds\right|dt_1\\ &\leq B_1 2^{3n-3}t(1+t)\prod_{j=1,j\neq k}^{n}(1+|x_j|+x_j^2)\int_0^t\left|\int_0^x g(t,s)ds\right|dt_1\\ &\leq AB_1,\quad (t,x)\in[0,\infty)\times\mathbb{R}^n,\end{aligned}$$

$k\in\{1,\ldots,n\}$. Therefore

$$\|S_2u\|\leq AB_1.$$

This completes the proof. □

3.2. Main Results

Our first main result is as follows.

Theorem 3. *Suppose* $(H1)$ *and* $(H2)$. *Then the IVP* (1) *has at least one solution in* $\mathcal{C}^1([0,\infty),\mathcal{C}^2(\mathbb{R}^n))$.

Proof. Below, suppose

(H3) $\epsilon \in (0,1)$, A and B satisfy the inequalities $\epsilon B_1(1+A) < 1$ and $AB_1 < 1$.

Let $\widetilde{Y}$ denote the set of all equi-continuous families in X with respect to the norm $\|\cdot\|$. Let also, $Y = \overline{\widetilde{Y}}$ be the closure of $\widetilde{Y}$,

$$U = \{u \in Y : \|u\| < B\}.$$

For $u \in \overline{U}$ and $\epsilon > 0$, define the operators

$$T(u)(t,x) = \epsilon u(t,x),$$

$$S(u)(t,x) = u(t,x) - \epsilon u(t,x) - \epsilon S_2(u)(t,x), \quad (t,x) \in [0,\infty) \times \mathbb{R}^n.$$

For $u \in \overline{U}$, we have

$$\begin{aligned} \|(I-S)(u)\| &= \|\epsilon u + \epsilon S_2(u)\| \\ &\leq \epsilon\|u\| + \epsilon\|S_2(u)\| \\ &\leq \epsilon B + \epsilon A B_1. \end{aligned}$$

Thus, $S : \overline{U} \to X$ is continuous and $(I-S)(\overline{U})$ resides in a compact subset of Y. Now, suppose that there is a $u \in Y$ so that $\|u\| = B$ and

$$u = \lambda(I-S)(u)$$

or

$$u = \lambda\epsilon\,(I+S_2)(u), \tag{9}$$

for some $\lambda \in \left(0, \frac{1}{\epsilon}\right)$. Note that $(Y, \|\cdot\|)$ is a Banach space. Assume that the set

$$\mathcal{A} = \{u \in Y : u = \mu(I+S_2)(u), \quad 0 < \mu < 1\}$$

is bounded. By (9), it follows that the set $\mathcal{A}$ is not empty set. Then, by Schaefer's Theorem, it follows that there is a $u^* \in Y$ such that

$$u^* = (I+S_2)(u^*), \tag{10}$$

or

$$S_2(u^*) = 0,$$

i.e., u^* is a solution to the problem (1). Assume that the set $\mathcal{A}$ is unbounded. Then, by Schaefer's Theorem, it follows that the equation

$$u=\mu(I+S_2)(u),\quad u\in Y,$$

has at least one small solution $u^*\in Y$ for any $\mu\in[0,1]$. In particular, for $\mu=1$, there is a $u^*\in Y$ such that (10) holds and then it is a solution to the problem (1). Let now,

$$\{u\in Y : u=\lambda_1(I-S)(u),\ \|u\|=B\}=\emptyset$$

for any $\lambda_1\in\left(0,\frac{1}{\epsilon}\right)$. Then, from Theorem 1, it follows that the operator $T+S$ has a fixed point $u^*\in Y$. Therefore

$$\begin{aligned} u^*(t,x) &= T(u^*)(t,x)+S(u^*)(t,x)\\ &= \epsilon u^*(t,x)+u^*(t,x)\\ &\quad -\epsilon u^*(t,x)-\epsilon S_2(u^*)(t,x),\quad (t,x)\in[0,\infty)\times\mathbb{R}^n, \end{aligned}$$

whereupon

$$S_2(u^*)(t,x)=0,\quad (t,x)\in[0,\infty)\times\mathbb{R}^n.$$

From here, u^* is a solution to the problem (1). □

Our next result is as follows.

Theorem 4. *Suppose* $(H1)$ *and* $(H2)$. *Then the IVP* (1) *has at least two non-negative solutions in* $\mathcal{C}^1([0,\infty),\mathcal{C}^2(\mathbb{R}^n))$.

Proof. Suppose

(H4) Let $m>0$ be large enough and A, B, r, L, R_1 be positive constants that satisfy the following conditions

$$r<L<R_1,\quad \epsilon>0,\quad R_1>\left(\frac{2}{5m}+1\right)L,$$

$$AB_1<\frac{L}{5}.$$

Let

$$\widetilde{P} = \{u \in X : u \geq 0 \quad \text{on} \quad [0,\infty) \times \mathbb{R}^n\}.$$

With $\mathcal{P}$ we will denote the set of all equi-continuous families in $\widetilde{P}$. For $v \in X$, define the operators

$$\begin{aligned} T_1 v(t,x) &= (1+m\epsilon)v(t,x) - \epsilon\frac{L}{10}, \\ S_3 v(t,x) &= -\epsilon S_2 v(t,x) - m\epsilon v(t,x) - \epsilon\frac{L}{10}, \end{aligned}$$

$t \in [0,\infty)$, $x \in \mathbb{R}^n$. Note that any fixed point $v \in X$ of the operator $T_1 + S_3$ is a solution to the IVP (1). Define

$$\begin{aligned} U_1 &= \mathcal{P}_r = \{v \in \mathcal{P} : \|v\| < r\}, \\ U_2 &= \mathcal{P}_L = \{v \in \mathcal{P} : \|v\| < L\}, \\ U_3 &= \mathcal{P}_{R_1} = \{v \in \mathcal{P} : \|v\| < R_1\}, \\ R_2 &= R_1 + \frac{A}{m}B_1 + \frac{L}{5m}, \\ \Omega &= \overline{\mathcal{P}_{R_2}} = \{v \in \mathcal{P} : \|v\| \leq R_2\}. \end{aligned}$$

1. For $v_1, v_2 \in \Omega$, we have

$$\|T_1 v_1 - T_1 v_2\| = (1+m\varepsilon)\|v_1 - v_2\|,$$

whereupon $T_1 : \Omega \to X$ is an expansive operator with a constant $h = 1 + m\varepsilon > 1$.

2. For $v \in \overline{\mathcal{P}}_{R_1}$, we get

$$\begin{aligned} \|S_3 v\| &\leq \varepsilon\|S_2 v\| + m\varepsilon\|v\| + \varepsilon\frac{L}{10} \\ &\leq \varepsilon\left(AB_1 + mR_1 + \frac{L}{10}\right). \end{aligned}$$

Therefore $S_3(\overline{\mathcal{P}}_{R_1})$ is uniformly bounded. Since $S_3 : \overline{\mathcal{P}}_{R_1} \to X$ is continuous, we have that $S_3(\overline{\mathcal{P}}_{R_1})$ is equi-continuous. Consequently $S_3 : \overline{\mathcal{P}}_{R_1} \to X$ is a 0-set contraction.

3. Let $v_1 \in \overline{\mathcal{P}}_{R_1}$. Set

$$v_2 = v_1 + \frac{1}{m}S_2v_1 + \frac{L}{5m}.$$

Note that $S_2v_1 + \frac{L}{5} \geq 0$ on $[0,\infty)\times\mathbb{R}^n$. We have $v_2 \geq 0$ on $[0,\infty)\times\mathbb{R}^n$ and

$$\begin{aligned}\|v_2\| &\leq \|v_1\| + \frac{1}{m}\|S_2v_1\| + \frac{L}{5m}\\ &\leq R_1 + \frac{A}{m}B_1 + \frac{L}{5m}\\ &= R_2.\end{aligned}$$

Therefore $v_2 \in \Omega$ and

$$-\varepsilon m v_2 = -\varepsilon m v_1 - \varepsilon S_2 v_1 - \varepsilon\frac{L}{10} - \varepsilon\frac{L}{10}$$

or

$$\begin{aligned}(I-T_1)v_2 &= -\varepsilon m v_2 + \varepsilon\frac{L}{10}\\ &= S_3v_1.\end{aligned}$$

Consequently $S_3(\overline{\mathcal{P}}_{R_1}) \subset (I-T_1)(\Omega)$.

4. Assume that for any $v_0 \in \mathcal{P}^*$ there exist $\lambda > 0$ and $z \in \partial\mathcal{P}_r \cap (\Omega + \lambda v_0)$ or $z \in \partial\mathcal{P}_{R_1} \cap (\Omega + \lambda v_0)$ such that

$$S_3z = (I-T_1)(z-\lambda v_0).$$

Then

$$-\epsilon S_2 z - m\epsilon z - \epsilon\frac{L}{10} = -m\epsilon(z-\lambda v_0) + \epsilon\frac{L}{10}$$

or

$$-S_2 z = \lambda m v_0 + \frac{L}{5}.$$

Hence,

$$\|S_2 z\| = \left\| \lambda m v_0 + \frac{L}{5} \right\| > \frac{L}{5}.$$

This is a contradiction.

5. Suppose that for any $\epsilon_1 \geq 0$ small enough there exist a $x_1 \in \partial\mathcal{P}_L$ and $\lambda_1 \geq 1 + \epsilon_1$ such that $\lambda_1 x_1 \in \overline{\mathcal{P}}_{R_1}$ and

$$S_3 x_1 = (I - T_1)(\lambda_1 x_1). \tag{11}$$

In particular, for $\epsilon_1 > \frac{2}{5m}$, we have $x_1 \in \partial\mathcal{P}_L$, $\lambda_1 x_1 \in \overline{\mathcal{P}}_{R_1}$, $\lambda_1 \geq 1 + \epsilon_1$ and (11) holds. Since $x_1 \in \partial\mathcal{P}_L$ and $\lambda_1 x_1 \in \overline{\mathcal{P}}_{R_1}$, it follows that

$$\left(\frac{2}{5m} + 1\right) L < \lambda_1 L = \lambda_1 \|x_1\| \leq R_1.$$

Moreover,

$$-\epsilon S_2 x_1 - m\epsilon x_1 - \epsilon\frac{L}{10} = -\lambda_1 m\epsilon x_1 + \epsilon\frac{L}{10},$$

or

$$S_2 x_1 + \frac{L}{5} = (\lambda_1 - 1) m x_1.$$

From here,

$$2\frac{L}{5} \geq \left\| S_2 x_1 + \frac{L}{5} \right\| = (\lambda_1 - 1) m \|x_1\| = (\lambda_1 - 1) m L,$$

and

$$\frac{2}{5m} + 1 \geq \lambda_1,$$

which is a contradiction.

Therefore all conditions of Theorem 2 hold. Hence, the IVP (1) has at least two solutions u_1 and u_2 so that

$$\|u_1\| = L < \|u_2\| < R_1,$$

or

$$r < \|u_1\| < L < \|u_2\| < R_1.$$

□

Example 1. *Below, we will illustrate our main results in this section. Let B and*

$$R_1=10,\ L=5,\ p=4,\ r=4,\ m=10^{50},\ A=\frac{1}{10B_1},\ \epsilon=\frac{1}{5B_1(1+A)}.$$

Then $B_1=4$ and

$$AB_1=\frac{1}{10}<B,\quad \epsilon B_1(1+A)<1,$$

i.e., $(H3)$ holds. Next,

$$r<L<R_1,\quad \epsilon>0,\quad R_1>\left(\frac{2}{5m}+1\right)L,\quad AB_1<\frac{L}{5}.$$

i.e., $(H4)$ holds. Take

$$h(s)=\log\frac{1+s^4\sqrt{2}+s^8}{1-s^4\sqrt{2}+s^8},\quad l(s)=\arctan\frac{s^4\sqrt{2}}{1-s^8},\quad s\in\mathbb{R},\quad s\neq\pm1.$$

Then

$$\begin{aligned} h'(s) &= \frac{8\sqrt{2}s^3(1-s^8)}{(1-s^4\sqrt{2}+s^8)(1-s^4\sqrt{2}+s^8)},\\ l'(s) &= \frac{4\sqrt{2}s^3(1+s^8)}{1+s^{16}},\quad s\in\mathbb{R},\quad s\neq\pm1. \end{aligned}$$

Therefore

$$\begin{aligned} \lim_{s\to\pm\infty}\sum_{r=0}^{4}s^rh(s) &= \lim_{s\to\pm\infty}\frac{h(s)}{\frac{1}{\sum_{r=0}^{4}s^r}}\\ &= \lim_{s\to\pm\infty}\frac{h'(s)}{-\frac{\sum_{r=0}^{3}(r+1)s^r}{\left(\sum_{r=0}^{4}s^r\right)^2}}\\ &= -\lim_{s\to\pm\infty}\frac{8\sqrt{2}s^3(1-s^8)\left(\sum_{r=0}^{4}s^r\right)^2}{\left(\sum_{r=0}^{3}(r+1)s^r\right)(1-s^4\sqrt{2}+s^8)(1-s^4\sqrt{2}+s^8)}\\ &\neq \pm\infty \end{aligned}$$

and

$$\lim_{s\to\pm\infty}\sum_{r=0}^{4}s^r l(s)=\lim_{s\to\pm\infty}\frac{l(s)}{\frac{1}{\sum_{r=0}^{4}s^r}}$$

$$=\lim_{s\to\pm\infty}\frac{l'(s)}{-\frac{\sum_{r=0}^{3}(r+1)s^r}{\left(\sum_{r=0}^{4}s^r\right)^2}}$$

$$=-\lim_{s\to\pm\infty}\frac{4\sqrt{2}s^3(1+s^8)\left(\sum_{r=0}^{4}s^r\right)^2}{(1+s^{16})\left(\sum_{r=0}^{3}(r+1)s^r\right)}$$

$$\neq \pm\infty.$$

Consequently

$$-\infty<\lim_{s\to\pm\infty}\left(\sum_{r=0}^{4}s^r\right)h(s)<\infty,$$

$$-\infty<\lim_{s\to\pm\infty}\left(\sum_{r=0}^{4}s^r\right)l(s)<\infty.$$

Hence, there exists a positive constant C_1 *so that*

$$\sum_{r=0}^{4}|s|^r\left(\frac{1}{16\sqrt{2}}\log\frac{1+s^4\sqrt{2}+s^8}{1-s^4\sqrt{2}+s^8}+\frac{1}{8\sqrt{2}}\arctan\frac{s^4\sqrt{2}}{1-s^8}\right)\leq C_1,$$

$s\in\mathbb{R}^n$. *Note that* $\lim_{s\to\pm1}l(s)=\frac{\pi}{2}$ *and by [8] (pp. 707, Integral 79), we have*

$$\int\frac{dz}{1+z^4}=\frac{1}{4\sqrt{2}}\log\frac{1+z\sqrt{2}+z^2}{1-z\sqrt{2}+z^2}+\frac{1}{2\sqrt{2}}\arctan\frac{z\sqrt{2}}{1-z^2}.$$

Let

$$Q(s)=\frac{s^3}{(1+s^{16})},\quad s\in\mathbb{R}^n,$$

and

$$g_1(t,x)=Q(t)Q(x_1)\dots Q(x_n),\quad t\in[0,\infty),\quad x\in\mathbb{R}^n.$$

Then there exists a constant $C>0$ such that

$$2^{3n+1}(1+t+t^2)\prod_{j=1}^{n}(1+|x_j|+x_j^2)\int_0^t\left|\int_0^x g_1(t_1,z)dz\right|dt_1\leq C,$$
$$(t,x)\in[0,\infty)\times\mathbb{R}^n.$$

Let

$$g(t,x)=\frac{A}{C}g_1(t,x),\quad (t,x)\in[0,\infty)\times\mathbb{R}^n.$$

Then

$$2^{3n+1}(1+t+t^2)\prod_{j=1}^{n}(1+|x_j|+x_j^2)\int_0^t\left|\int_0^x g(t_1,z)dz\right|dt_1\leq A,$$
$$(t,x)\in[0,\infty)\times\mathbb{R}^n.$$

i.e., $(H2)$ holds. Therefore for the IVP

$$\begin{aligned} iu_t-\Delta u &= |u|^3u,\quad t>0,\quad x\in\mathbb{R}^n,\\ u(0,x) &= \tfrac{1}{(1+|x|^2)(1+|x|^4)},\quad x\in\mathbb{R}^n, \end{aligned}$$

are fulfilled all conditions of Theorem 3 and Theorem 4.

4. The Wave Equation

In this section, we will investigate the IVP (2). Let $X=\mathcal{C}^2([0,\infty),\mathcal{C}^2(\mathbb{R}^n))$ be endowed with the norm

$$\begin{aligned} \|u\| = \max\Big\{ &\sup_{(t,x)\in[0,\infty)\times\mathbb{R}^n}|u(t,x)|,\quad \sup_{(t,x)\in[0,\infty)\times\mathbb{R}^n}|u_t(t,x)|,\\ &\sup_{(t,x)\in[0,\infty)\times\mathbb{R}^n}|u_{tt}(t,x)|,\\ &\sup_{(t,x)\in[0,\infty)\times\mathbb{R}^n}|u_{x_j}(t,x)|,\quad \sup_{(t,x)\in[0,\infty)\times\mathbb{R}^n}|u_{x_jx_j}(t,x)|,\\ &j\in\{1,\dots,n\}\Big\}, \end{aligned}$$

provided it exists. For $u \in X$, define the operator For $u \in X$, define the operator

$$\begin{aligned} S_1u(t,x,y) &= u(t,x) - v_0(x) - tv_1(x) \\ &\quad - \int_0^t (t-t_1)(\Delta u(t_1,x) + |u(t_1,x)|^{p-1}u(t_1,x))dt_1, \end{aligned}$$

$(t,x) \in [0,\infty) \times \mathbb{R}^n$.

Lemma 6. *Suppose* $(G1)$. *Let* $u \in X$ *satisfies the equation*

$$S_1u(t,x) = 0, \quad (t,x) \in [0,\infty) \times \mathbb{R}^n. \tag{12}$$

Then u *is a solution to the IVP* (2).

Proof. We have

$$\begin{aligned} 0 &= u(t,x) - v_0(x) - tv_1(x) \\ &\quad - \textstyle\int_0^t (t-t_1)(\Delta u(t_1,x) + |u(t_1,x)|^{p-1}u(t_1,x))dt_1, \end{aligned} \tag{13}$$

$(t,x) \in [0,\infty) \times \mathbb{R}^n$, which we differentiate with respect to t and we get

$$\begin{aligned} 0 &= u_t(t,x) - v_1(x) \\ &\quad - \textstyle\int_0^t (\Delta u(t_1,x) + |u(t_1,x)|^{p-1}u(t_1,x))dt_1, \end{aligned} \tag{14}$$

$(t,x) \in [0,\infty) \times \mathbb{R}^n$. We differentiate (14) with respect to t and we find

$$0 = u_{tt}(t,x) - \Delta u(t,x) - |u(t,x)|^{p-1}u(t,x), \quad (t,x) \in [0,\infty) \times \mathbb{R}^n,$$

i.e., u satisfies the first equation of (2). Now, we put $t = 0$ into (13) and (14) and we arrive at

$$0 = u(0,x) - v_0(x), \quad 0 = u_t(0,x) - v_1(x), \quad x \in \mathbb{R}^n.$$

This completes the proof. □

Let $B_1 = \max\{2B, B, nB + B^p\}$.

Lemma 7. *Suppose* $(G1)$. *If* $u \in X$, $\|u\| \leq B$, *then*

$$|S_1u(t,x)| \leq (1+t+t^2)B_1, \quad (t,x) \in [0,\infty)\times\mathbb{R}^n.$$

Proof. We have

$$\begin{aligned}
|S_1u(t,x,y)| &= \Big|u(t,x)-v_0(x)-tv_1(x)\\
&\quad -\int_0^t (t-t_1)(\Delta u(t_1,x)+|u(t_1,x)|^{p-1}u(t_1,x))dt_1\Big|\\
&\leq |u(t,x)|+|v_0(x)|+t|v_1(x)|\\
&\quad +\int_0^t (t-t_1)(\sum_{j=1}^n |u_{x_jx_j}(t_1,x)|+|u(t_1,x)|^p)dt_1\\
&\leq 2B+tB+(nB+B^p)t^2\\
&\leq B_1(1+t+t^2), \quad (t,x,y)\in[0,\infty)\times\mathbb{R}^n.
\end{aligned}$$

This completes the proof. □

Below, suppose that

(G2) there exist a function $g \in \mathcal{C}([0,\infty)\times\mathbb{R}^n)$ so that $g>0$ on $(0,\infty)\times(\mathbb{R}^n\backslash\{0\})$,

$$g(0,x)=g(t,0,x_2,\dots,x_n)=\cdots=g(t,x_1,x_2,\dots,x_{n-1},0)=0,$$

$(t,x)\in[0,\infty)\times\mathbb{R}^n$, and a positive constant A such that

$$2^{3n+1}(1+t+t^2+t^3+t^4)\prod_{j=1}^n(1+|x_j|+x_j^2)$$
$$\times\int_0^t\Big|\int_0^x g(t_1,s)ds\Big|dt_1\leq A.$$

In the end of this section we will give an example for such function g and such constant A. For $u \in X$, define the operator

$$S_2u(t,x) = \int_0^t \int_0^x (t-t_1)^2 \prod_{j=1}^{n} (x_j - s_j)^2 g(t_1,s) S_1u(t_1,s) ds dt_1,$$
$$(t,x) \in [0,\infty) \times \mathbb{R}^n.$$

Lemma 8. *Suppose* $(G1)$ *and* $(G2)$. *If* $u \in X$ *satisfies the equation*

$$S_2u(t,x) = 0, \quad (t,x) \in [0,\infty) \times \mathbb{R}^n, \tag{15}$$

then u *is a solution to the IVP* (2).

Proof. We differentiate three times in t and three times in x_j, $j \in \{1,\dots,n\}$, and we find

$$g(t,x) S_1u(t,x) = 0, \quad (t,x) \in [0,\infty) \times \mathbb{R}^n.$$

Hence,

$$S_1u(t,x) = 0, \quad (t,x) \in (0,\infty) \times (\mathbb{R}^n \backslash \{0\}).$$

Since $S_1u(\cdot,\cdot)$ is a continuous function on $[0,\infty) \times \mathbb{R}^n$, we get

$$\begin{aligned} 0 &= \lim_{t \to 0} S_1u(t,x) = S_1u(0,x) \\ &= \lim_{x_1 \to 0} S_1u(t,x) = S_1u(t,0,x_2,\dots,x_n) \\ &= \lim_{x_n \to 0} S_1u(t,x) = S_1u(t,x_1,\dots,x_{n-1},0), \quad (t,x) \in [0,\infty) \times \mathbb{R}^n. \end{aligned}$$

Thus,

$$S_1u(t,x) = 0, \quad (t,x) \in [0,\infty) \times \mathbb{R}^n.$$

Now, applying Lemma 6, we get the desired result. □

As we have proved Lemma 5, one can obtain the following result

Lemma 9. *Suppose* $(G1)$ *and* $(G2)$. *If* $u \in X$, $\|u\| \le B$, *then*

$$\|S_2u\| \le AB_1.$$

As we have proved Theorem 3 and Theorem 4, one can obtain the following results.

Theorem 5. *Suppose* $(G1)$ *and* $(G2)$. *Then the IVP* (2) *has at least one solution in* $\mathcal{C}^2([0,\infty),\mathcal{C}^2(\mathbb{R}^n))$.

Theorem 6. *Suppose* $(G1)$ *and* $(G2)$. *Then the IVP* (2) *has at least two non-negative solutions in* $\mathcal{C}^2([0,\infty),\mathcal{C}^2(\mathbb{R}^n))$.

Example 2. *Let* A, B, R_1, L, r, m, p *and* ϵ *be as in Example 1. Then* $B_1=4$ *and* $(H3)$ *and* $(H4)$ *hold. Let also,* Q *be the same function as in Example 1. Take*

$$g_1(t,x)=Q(t)Q(x_1)\cdots Q(x_n),\quad t\in[0,\infty),\quad x\in\mathbb{R}^n.$$

Then there exists a constant $C>0$ *such that*

$$2^{3n+1}\left(\sum_{r=0}^{4}t^r\right)\prod_{j=1}^{n}\left(\sum_{r=0}^{2}|x_j|^r\right)\times\int_0^t\left|\int_0^x\int_0^y g_1(t_1,s)ds\right|dt_1\leq C,\quad (t,x)\in[0,\infty)\times\mathbb{R}^n.$$

Let

$$g(t,x)=\frac{A}{C}g_1(t,x),\quad (t,x)\in[0,\infty)\times\mathbb{R}^n.$$

Then

$$2^{3n+1}\left(\sum_{r=0}^{4}t^r\right)\prod_{j=1}^{n}\left(\sum_{r=0}^{2}|x_j|^r\right)\times\int_0^t\left|\int_0^x g(t_1,s)ds\right|dt_1\leq A,\quad (t,x)\in[0,\infty)\times\mathbb{R}^n.$$

i.e., $(G2)$ *holds. Therefore for the IVP*

$$\begin{aligned}u_{tt}-\Delta u &= |u|^3u,\quad t>0,\quad x\in\mathbb{R}^n,\\ u(0,x) &= \tfrac{1}{1+3|x|^2},\quad x\in\mathbb{R}^n,\\ u_t(0,x) &= \tfrac{1}{1+11|x|^6},\quad x\in\mathbb{R}^n,\end{aligned}$$

are fulfilled all conditions of Theorem 5 and Theorem 6.

Conclusion

In this chapter we consider IVPs for n-dimensional Schrödinger and wave equations. We investigate them for existence of at least one and existence of at least two classical solutions. For this aim, firstly we give suitable integral representations of the solutions of the considered problems. Then, we deduct some a-priori estimates for the solutions. Using the integral representations of the solutions, we define operators which fixed points are solutions of the investigated initial value problems. To ensure existence of fixed points of the defined operators we use some recent theoretical results. The approach proposed in this chapter can be used for other classes partial differential equations as well as for some classes ordinary differential equations.

References

[1] Banas, J.; Goebel, K. Measures of Noncompactness in Banach Spaces, *Lecture Notes in Pure and Applied Mathematics*, **60**. Marcel Dekker, Inc., New York, 1980.

[2] Bona, J; Grujic, Z; Kalisch, H. Algebraic Lower Bounds for the Uniform Radius of Spatial Analyticity for the Generalized KdV Equation, *Ann. Inst. H. Poincare Anal. Non Lineaire* 22 (2005), no. 6, 783797. MR 2172859.

[3] Bona, J; Grujic, Z; Kalisch, H. Global Solutions of the Derivative Schr´odinger Equation in a Class of Functions Analytic in a Strip, *J. Differential Equations* 229 (2006), no. 1, 186 203. MR 2265624.

[4] Bona, J; Grujic, Z; Kalisch, H. A KdV-type Boussinesq System: from the Energy Level to Analytic Spaces, *Discrete Contin. Dyn. Syst.* 26 (2010), no. 4, 11211139. MR 2600738.

[5] Djebali, S.; Mebarki, K. Fixed Point Index Theory for Perturbation of Expansive Mappings by k-set Contractions, *Top. Meth. Nonl. Anal.*, Vol 54, No 2 A(2019), 613–640.

[6] Drabek, P; Milota, J. *Methods in Nonlinear Analysis, Applications to Differential Equations*, Birkhäuser, 2007.

[7] Lindblad, H; Sogge, C. On Existence and Scattering with Minimal Regularity for Semilinear Wave Equations, *J. Funct. Anal.*, 130 (1995), pp. 357-426.

[8] Polyanin, A.; Manzhirov, A. *Handbook of Integral Equations,* CRC Press, 1998.

[9] Silva, D; Biyar, M. *Global Analytic Solutions for the Nonlinear Schrdinger Equation, Analysis*, 2020.

Chapter 14

Superstrongly Interacting Gravitons: Low-Energy Quantum Gravity and Vacuum Effects

Michael A. Ivanov*
Physics Department
Belarus State University of Informatics and Radioelectronics
Minsk, Belarus

Abstract

A brief review of the consequences of the hypothesis about the existence of a background of superstrong interacting gravitons is given. Gravity is seen as a shielding effect in a sea of low-energy gravitons, and Newton's constant can be calculated as a function of the background temperature. At very small distances, the phenomenon of asymptotic freedom arises. Restrictions on the geometric language and the ban on the existence of black holes are considered. Additional deceleration of massive bodies occurs due to forehead and backhead collisions with gravitons. Scattering of photons by background gravitons leads to a redshift of distant objects, their additional darkening and the appearance of a background of scattered photons. These effects could revolutionize cosmology because they don't need dark energy, the Big Bang, etc. to explain observations.

Keywords: Superstrongly interacting gravitons, low-energy quantum gravity, quantum mechanism of cosmological redshifts, cosmology

* Corresponding Author's Email: ivanovma@tut.by.

In: Horizons in World Physics. Volume 312
Editor: Albert Reimer
ISBN: 979-8-89113-513-0

1. Introduction

The equality of the inertial and gravitational masses of any body prompted Albert Einstein to come up with the idea of a geometric description of gravity. Supplemented by the postulate of local validity of special relativity, in which light propagates along null geodesics, it led to a theory describing forceless gravity, in which light is deflected near large bodies. General relativity takes into account the finite speed of gravity. The intensity of the interaction depends on the value of Newton's constant G, i.e. this theory is at a fundamental level no deeper than Newton's law of gravity. In both cases, the mechanism of gravity remains unknown. All the effects of the general theory of relativity are observed, which makes it a real diamond of theoretical physics.

The Friedmann-Lemaitre-Robertson-Walker metric is an exact solution of general relativity used in the modern standard cosmological model (LCDM) to describe cosmological expansion. Although its use is not possible during the early stages of expansion, it describes the redshift and the luminosity distance of remote galaxies, as well as the rate of expansion. To describe the observed dimming of distant objects, the discovery of dark energy was announced in 1998 [1, 2].

But there is a contradiction between general relativity and quantum mechanics, in which there is no trajectory for microparticles (the uncertainty principle of W. Heisenberg, 1927). This principle is essential to understanding electron diffraction on a crystal; at a distance scale of 10^{-10} m electrons behave like waves. In general relativity there are no restrictions on the masses of bodies, and it is expected that its use is possible up to the Planck distance scale, where some quantum effects should take place. One of the most promising candidates for the role of a theory of quantum gravity precisely on this scale and based directly on the geometric formulation of general relativity is considered to be loop quantum gravity [3]. This theory does not currently predict observable effects that would allow it to be tested, but it is under development.

I would like to describe here an alternative approach to gravity, based on the hypothesis of the existence of a background of superstrongly interacting gravitons. Gravity can then be viewed as a screening effect, which is a completely quantum phenomenon, without the need for quantization. Newton's constant can be calculated as a function of background temperature; this means that this approach is in some sense deeper than general relativity. Scattering of photons by background gravitons leads to a redshift of distant objects, their additional darkening and the appearance of a background of scattered photons. These effects can be very important for cosmology.

2. Gravity as the Screening Effect in the Sea of Gravitons

In author's papers [4, 5], a cross-section $\sigma(E, \epsilon)$ of interaction of a graviton with an energy ϵ with any body having an energy E was accepted to be equal to:

$$\sigma(E, \epsilon) = D \cdot E \cdot \epsilon, \tag{1}$$

where D is some new dimensional constant.

To ensure an attractive force which is not equal to a repulsive one, particle correlations should differ for *in* and *out* flux. For example, single gravitons of running flux may associate in pairs. If such pairs are destructed by collisions with a body, then quantities $< \epsilon >$ will distinguish for running and scattered particles ($< \epsilon >$ is an average energy of gravitons). Graviton pairing may be caused with graviton's own gravitational attraction or gravitonic spin-spin interaction. Then a force of attraction of two bodies due to pressure of graviton pairs F_2 will be equal to:

$$F_2 = \int_0^\infty \frac{\sigma(E_2, < \epsilon_2 >)}{4\pi r^2} \cdot 4\sigma(E_1, < \epsilon_2 >) \cdot \frac{1}{3} \cdot \frac{4 f_2(2\omega, T)}{c} d\omega = \tag{2}$$

$$\frac{8}{3} \cdot \frac{D^2 c (kT)^6 m_1 m_2}{\pi^3 \hbar^3 r^2} \cdot I_2,$$

where

$$I_2 \equiv \int_0^\infty \frac{x^5 (1 - \exp(-(\exp(2x) - 1)^{-1}))^2 (\exp(2x) - 1)^{-5}}{\exp(2(\exp(2x) - 1)^{-1}) \exp(2(\exp(x) - 1)^{-1})} dx = \tag{3}$$

$$2.3184 \cdot 10^{-6}.$$

The difference F between attractive and repulsive forces will be equal to:

$$F \equiv F_2 - F_2^{'} = \frac{1}{2} F_2 \equiv G_2 \frac{m_1 m_2}{r^2}, \tag{4}$$

where the constant G_2 is equal to:

$$G_2 \equiv \frac{4}{3} \cdot \frac{D^2 c (kT)^6}{\pi^3 \hbar^3} \cdot I_2. \tag{5}$$

If one assumes that G_2 coincides with the Newton's constant G, then it follows from the last expression that by $T = 2.7K$ the constant D should have the value:

$$D = 0.795 \cdot 10^{-27} m^2 / eV^2. \tag{6}$$

3. Asymptotic Freedom at Very Small Distances

Here, a portion of screened gravitons *for big distances between the bodies* is described by the factor $\sigma(E_2, <\epsilon_2>)/4\pi r^2$, which should be much smaller of unity. A net force is attractive, and it is equal to $F_2/2$. For small distances, the condition $\sigma(E_2, <\epsilon_2>) \ll 4\pi r^2$ will be broken. For example, $\sigma(E_2, <\epsilon_2>) \sim 4\pi r^2$ for two protons and $<\epsilon_2> \sim 10^{-3}\ eV$ at distances $r \sim 10^{-11}\ m$. This quantity is many orders larger than the Planck length.

When we compute a pressure force of graviton pairs in the limit case of super-short distances it turns out that this force almost vanishes. For this limit case, we should replace the factor $\sigma(E_2, <\epsilon_2>)/4\pi r^2$ by $1/2$ if a separation of interacting particles has a sense. If we accept this replacement, we get for the pressure force (acting on body 1):

$$F_2 = \int_0^\infty \frac{1}{2} \cdot 4\sigma(E_1, <\epsilon_2>) \cdot \frac{1}{3} \cdot \frac{4f_2(2\omega, T)}{c} d\omega = \tag{7}$$

$$\frac{8}{3} \cdot \frac{D(kT)^5 E_1}{\pi^2 \hbar^3 c^3} \cdot I_5,$$

where I_5 is the new constant:

$$I_5 \equiv \int_0^\infty \frac{x^4(1 - \exp(-(\exp(2x) - 1)^{-1}))(\exp(2x) - 1)^{-3}}{\exp((\exp(2x) - 1)^{-1}) \exp((\exp(x) - 1)^{-1})} dx = \tag{8}$$

$$4.24656 \cdot 10^{-4}.$$

Then the corresponding limit acceleration is equal to:

$$w_{lim} = G\frac{\pi}{D(kT)c^2} \cdot \frac{I_5}{I_2} = 3.691 \cdot 10^{-13}\, m/s^2. \tag{9}$$

This extremely small acceleration means that at very small distances (which are meantime many orders of magnitude larger than the Planck length) we have in this model the property which never has been recognized in any model of quantum gravity: almost full asymptotic freedom (for more details, see [6, 7]).

4. Restrictions on Geometric Language and the Ban on the Existence of Black Holes

In this model, the cross section $\sigma(E, \epsilon)$ of the interaction of a graviton with energy ϵ with any particle with energy E was taken equal to: $\sigma(E, \epsilon) = D \cdot E \cdot \epsilon$,, where D is a new dimensional constant (its estimate is: $D = 0.795 \cdot$

$10^{-27}m^2/eV^2$). We obtain the inverse square law for bodies if the condition of large distances r is satisfied: $\sigma(E, <\epsilon>) \ll 4\pi r^2$, where E is the bigger energy of a pair of bodies. This leads to an important consequence: some "atomic" structure of matter is needed [5, 8]. For microparticles, the property of asymptotic freedom arises at very small distances when this condition is violated.

But black holes have no structure, and this condition can only be satisfied at huge distances: for a solar-mass black hole, the condition would be satisfied at distances $r \gg 10^6\ AE$. On the other hand, in the model, screening of the background of superstrong interacting gravitons creates for any pair of bodies both an attractive force and a repulsive force due to the pressure of gravitons. This means that black holes that absorb any particles and do not re-emit them must have a much larger gravitational mass than the inertial one, i.e. for them, Einstein's equivalence principle will be violated. So, we have here a double ban on the existence of black holes. This could mean that the invisible supermassive objects at the centers of many galaxies, as well as other supposed black holes, are now misnamed.

5. Vacuum Effects

The interaction of any single massive body or photon with background gravitons leads to small effects, which to the observer will seem like vacuum effects. All of them are outside the scope of the special theory of relativity. Some of these effects may only manifest themselves at cosmological distances or on large time scales.

5.1. Deceleration of Massive Bodies Due to Collisions with Gravitons

The additional deceleration of massive bodies due to forehead and backhead collisions with gravitons was calculated in [9]. This deceleration w is equal to: $w = -H_0 c \cdot 4v^2/c^2 \cdot (1 - v^2/c^2)^{0.5}$, where H_0 is the Hubble constant, c is the velocity of light, v is the body's velocity relative to the background. For small velocities we have:

$$w \simeq -w_0 \cdot 4v^2/c^2. \tag{10}$$

In the Newtonian approach, if $\mathbf{u}$ is a more massive body's velocity relative to the background, M is its mass, and $\mathbf{V} = \mathbf{v} + \mathbf{u}$ is the velocity of the small body relative to the graviton background, we will have now the following equation of motion of the small body:

$$\ddot{\mathbf{r}} = -G\frac{M}{r^2} \cdot \frac{\mathbf{r}}{r} + \frac{4w_0}{c^2}(u \cdot \mathbf{u} - \mid \mathbf{v} + \mathbf{u} \mid \cdot (\mathbf{v} + \mathbf{u})), \tag{11}$$

where **r** is a radius-vector of the small body. Some results of numerical modeling of a motion of bodies in the central field by the influence of this additional deceleration are described in[10]. To evaluate a stability of planetary orbits in the solar system in a presence of the anomalous deceleration w, we can use the following trick: to increase w by hand to see a very small change of the orbit's radius, and to re-calculate a value of the resulting effect. In a case of the Earth-like circular orbit, i.e. by $M = M_{\odot}$, $r(0) = 1$ AU, given $u = 4 \cdot 10^5$ m/s and that three vectors **r**, **v**, **u** lie in one plane, we get by the replacement: $w \rightarrow 10^4 \cdot w$ for one classical period T: $\Delta r/r(0) = -1.08 \cdot 10^{-8}$ yr^{-1} by $\Delta t = 10^{-10} \cdot T$. It means that by the anomalous deceleration w we should have now: $\Delta r/r(0) = -1.08 \cdot 10^{-12}$ yr^{-1}. For the case when **u** is perpendicular to **r**, **v** we have: $\Delta r/r(0) = -7.2 \cdot 10^{-13}$ yr^{-1}. The Earth orbit will be stable enough to have not contradictions with the estimated age of it in the solar system. Results of modeling a star orbit in a galaxy in the similar way show that for $M = 10^{10} \cdot M_{\odot}$, $u = 5 \cdot 10^5$ m/s by $r(0) = 1$ kpc and $r(0) = 100$ kpc the ratio $\frac{w_0}{\ddot{r}(0)}$ is equal to 2.2 and 0.00022 respectively. By $r(0) = 1$ kpc the relative change of the distance to the center is $\Delta r/r(0) = -0.034$ during the time interval of $\simeq 30$ Gyr. By $r(0) = 1$ kpc the first unclosed external loop corresponds to 29.2 Gyr. At all scales closed orbits do not exist in the model: bodies inspiral to the center of attraction, but for the Earth-like orbits this effect is very small. When **u** is perpendicular to **r**, **v**, another effect takes place: the motion of the body in the central field is not planar.

5.2. Scattering of Photons on Gravitons of the Background

The Hubble constant is not connected here with any expansion of the universe, but only with energy losses of photons due to forehead collisions with gravitons of the background that causes redshifts of spectra of remote galaxies. The Hubble constant H in this model is described by the formula:

$$H = \frac{1}{2\pi} D \cdot \bar{\epsilon} \cdot (\sigma T^4), \tag{12}$$

where $\bar{\epsilon}$ is an average graviton energy, σ is the Stephan-Boltzmann constant, T is an effective temperature of the graviton background. Energy losses of photons due to forehead collisions with gravitons of the background leads to the geometrical distance/redshift relation of this model:

$$r(z) = ln(1 + z) \cdot c/H_0, \tag{13}$$

where H_0 is the Hubble constant, c is the velocity of light. We may introduce the Hubble parameter $H(z)$ in the following manner:

$$dz = H(z) \cdot \frac{dr}{c}, \tag{14}$$

to imitate the local Hubble law. Taking a derivative $\frac{dr}{dz}$, we get in this model without expansion for $H(z)$:

$$H(z) = H_0 \cdot (1+z). \tag{15}$$

The Hubble parameter $H(z)$ of this model is a linear function of z, that is in a big discrepancy with ΛCDM. As it was shown, this function fits available observations of $H(z)$ very well [12, 13].

The additional effect of decreasing a number of photons in a propagating beam due to non-forehead collisions with gravitons can explain the discovered in 1998 additional dimming of remote sources [1, 2]. These two effects give the luminosity distance/redshift relation of the model:

$$D_L(z) = c/H_0 \cdot \ln(1+z) \cdot (1+z)^{(1+b)/2}, \tag{16}$$

where the "constant" b belongs to the range 0 - 2.137 ($b = \frac{3}{2} + \frac{2}{\pi} \simeq 2.137$ for very soft radiation, and $b \to 0$ for very hard one). This relation fits cosmological observations of remote sources very well without dark energy [12]. To fit this model, observations should be corrected for no time dilation as: $\mu(z) \to \mu(z) + 2.5 \cdot \lg(1+z)$, where $\lg x \equiv \log_{10} x$, and the distance modulus: $\mu(z) \equiv 5lgD_L(z)(Mpc) + 25$. In [13], I have used 31 binned points of the JLA compilation from Tables F.1 and F.2 of [14] (diagonal elements of the correlation matrix in Table F.2 are dispersions of distance moduli). Varying the value of b, we find the best fitting value of this parameter: $b = 2.365$ with $\chi^2 = 30.71$. It means that the best fitting has 43.03% C.L. This value of b is 1.107 times greater than the theoretical one. For the Hubble constant we have in this case: $< H_0 > \pm\sigma_0 = (69.54 \pm 1.58)\frac{km}{s \cdot Mpc}$. Results of the best fitting are shown in Fig. 1.

After non-forehead collisions, scattered photons should create the light-from-nowhere effect which has not an analog in the standard cosmological model. The ratio $\delta(z)$ of the scattered flux to the remainder reaching the observer is equal to [15]:

$$\delta(z) = (1+z)^b - 1. \tag{17}$$

By $b = 2.137$ we have, for example: $\delta(0.4) = 1.05$, i.e. this effect is big enough to explain a tentative detection of a diffuse cosmic optical background [20].

In this model, the functions $r(z)$ and $D_L(z)$ are found for radiation consisting of photons with energies $\hbar\omega \gg < \epsilon >$, where $< \epsilon >$ is the average graviton energy. But for $\hbar\omega \ll < \epsilon >$, e.g. for the radio band, the situation is more complicated [18]. In this case, only a small part of the background gravitons will transfer their momentum to photons in head-on collisions, and this momentum will often be of the same order as the photons' own momentum. This should lead to a large broadening of the emission spectrum towards

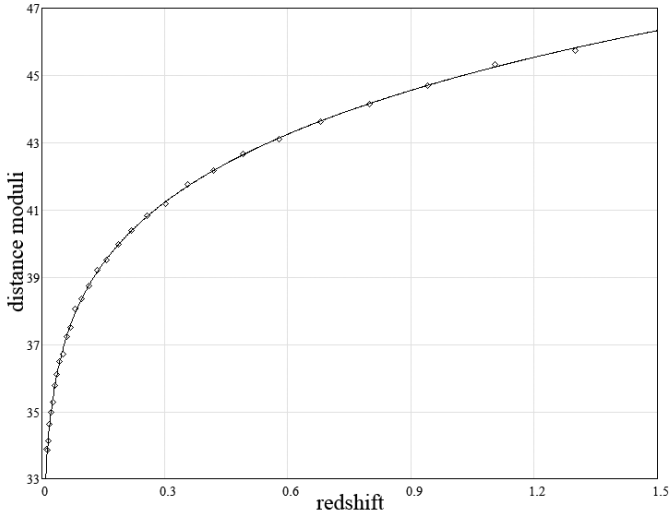

Figure 1. The theoretical Hubble diagram $\mu_0(z)$ of this model with $b = 2.365$ (solid); Supernovae 1a observational data (31 binned points of the JLA compilation) are taken from Tables F.1 and F.2 of [14] and corrected for no time dilation.

the red, and its redshift as a whole will be much smaller than expected for high-energy radiation. From another side, all gravitons with energies $\epsilon > \hbar\omega$ are able to get the photon momentum in such the collisions that should additionally attenuate the radiation flux. This means that the known redshift z and the constant parameter b are not enough to describe the situation; this issue remains open. This feature of the model may be important for measurements of the redshifted 21-cm radiation, which are now of great interest [19].

5.3. Lorentz Symmetry Violation Due to Interactions of Photons with the Graviton Background

The small average time delay of photons due to multiple interactions with gravitons of the background has place in this model. At enormous distances, this violates the basic postulate of the special theory of relativity about the constancy of the speed of light. The two variants of evaluation of the lifetime of a virtual photon are considered: 1) on a basis of the uncertainties relation (it is a common place in physics of particles) and 2) using a conjecture about constancy of the proper lifetime of a virtual photon. It is shown that in the first case the violation of Lorentz symmetry is insignificant: the ratio of the average delay time of photons to their propagation time is approximately 10^{-28}; in the second (with a new free model parameter), the delay is proportional to the

difference $\sqrt{E_{01}} - \sqrt{E_{02}}$, where $E_{01},\ E_{02}$ are the initial photon energies, and more energetic photons should come later, as in the first case [20].

To compute the average time delay of photons in the model [4, 5], it is necessary to find a number of collisions with gravitons of the graviton background on a small way dr and to evaluate a delay due to one act of interaction. Let us consider at first the background of single gravitons. Given the expression for H in the model, we can write for the number of collisions with gravitons having an energy $\epsilon = \hbar\omega$:

$$dN(\epsilon) = \frac{|dE(\epsilon)|}{\epsilon} = E(r) \cdot \frac{dr}{c} \frac{1}{2\pi} Df(\omega, T)d\omega, \tag{18}$$

where $f(\omega, T)$ is described by the Plank formula. In the forehead collision, a photon loses the momentum ϵ/c and obtains the energy ϵ; it means that for a virtual photon we will have:

$$\frac{v}{c} = \frac{E-\epsilon}{E+\epsilon};\ 1 - \frac{v}{c} = \frac{2\epsilon}{E+\epsilon};\ \ 1 - \frac{v^2}{c^2} = \frac{4\epsilon E}{(E+\epsilon)^2}. \tag{19}$$

5.3.1. Evaluation of the Lifetime of a Virtual Photon on a Basis of the Uncertainties Relation

The uncertainty of energy for a virtual photon is equal to $\Delta E = 2\epsilon$. If we evaluate the lifetime using the uncertainties relation: $\Delta E \cdot \Delta\tau \geq \hbar/2$, we get $\Delta\tau \geq \hbar/4\epsilon$. So as during the same time $\Delta\tau$ real photons overpass the way $c\Delta\tau$, and virtual ones overpass only the way $v\Delta\tau$, we have:

$$c\Delta t = c\Delta\tau - v\Delta\tau,$$

where Δt is the time delay, and the last one will be equal to:

$$\Delta t(\epsilon) = \Delta\tau(1 - \frac{v}{c}) \geq \hbar/2 \cdot \frac{1}{E+\epsilon}. \tag{20}$$

The full time delay due to gravitons with an energy ϵ is: $dt(\epsilon) = \Delta t(\epsilon)dN(\epsilon)$. Taking into account all frequencies, we find the full time delay on the way dr:

$$dt \geq \int_0^\infty \frac{\hbar}{2} \frac{E}{E+\epsilon} \cdot \frac{dr}{c} \frac{1}{2\pi} Df(\omega, T)d\omega. \tag{21}$$

The one will be maximal for $E \to \infty$, and it is easy to evaluate it:

$$dt_\infty \geq \frac{\hbar}{4\pi} \frac{dr}{c} \cdot D\sigma T^4. \tag{22}$$

On the way r the time delay is:

$$t_\infty(r) \geq \frac{\hbar}{4\pi}\frac{r}{c} \cdot D\sigma T^4. \tag{23}$$

In this model: $r(z) = c/H \cdot \ln(1+z)$; let us introduce a constant $\rho \equiv \hbar/4\pi \cdot D\sigma T^4/H = 37.2 \cdot 10^{-12} s$, then

$$t_\infty(z) \geq \rho \ln(1+z). \tag{24}$$

We see that for $z \simeq 2$ the maximal time delay is equal to $\sim 40\ ps$, i.e. the one is negligible.

In the rest frame of a virtual photon, a single parameter, which may be juxtaposed with an energy uncertainty, is mc^2. Accepting $\Delta E = mc^2$ in this frame, we'll get:

$$t(z) \geq \rho/2 \cdot \ln(1+z) \tag{25}$$

with the same ρ; now this estimate doesn't depend on E.

5.3.2. *The Case of Constancy of the Proper Lifetime of a Virtual Photon*

Taking into account that for a virtual photon after a collision $(E^{'}/c)^2 - p^{'2} > 0$, we may consider another possibility of lifetime estimation, for example, $\Delta\tau_0 = const$, where $\Delta\tau_0$ is the proper lifetime of a virtual photon (it should be considered as a new parameter of the model). Now it is necessary to transit to the reference frame of observer:

$$\Delta\tau = \Delta\tau_0/(1-\frac{v^2}{c^2})^{1/2} = \Delta\tau_0 \cdot \frac{E+\epsilon}{2\sqrt{\epsilon E}}, \tag{26}$$

accordingly:

$$\Delta t(\epsilon) = \Delta\tau(1-\frac{v}{c}) = \Delta\tau_0 \cdot \sqrt{\epsilon/E}. \tag{27}$$

Then the full time delay due to gravitons with an energy ϵ is:

$$dt(\epsilon) = \Delta t(\epsilon) dN(\epsilon) = \Delta\tau_0 \cdot \sqrt{\epsilon E} \cdot \frac{dr}{c}\frac{1}{2\pi} D f(\omega, T) d\omega, \tag{28}$$

and integrating it, we get:

$$dt = \Delta\tau_0 \cdot \sqrt{E(r)} \cdot \frac{dr}{c}\frac{1}{2\pi} D \int_0^\infty \sqrt{\epsilon} f(\omega, T) d\omega. \tag{29}$$

The integral in this expression is equal to:

$$\int_0^\infty \sqrt{\epsilon} f(\omega, T) d\omega \equiv \frac{1}{4\pi^2 c^2} \cdot \frac{(kT)^{9/2}}{\hbar^3} \cdot I_6, \tag{30}$$

where a new constant I_6 is the following integral:

$$I_6 \equiv \int_0^\infty \frac{x^{7/2} dx}{\exp x - 1} = 12.2681. \tag{31}$$

In this model, the energy of a photon decreases as: $E(r) = E_0 \exp(-Hr/c)$. The full delay on the way r now is:

$$t(r) = \Delta\tau_0 \cdot \frac{D}{8\pi^3 c^2} \cdot \frac{(kT)^{9/2}}{\hbar^3} \cdot I_6 \int_0^r \sqrt{E(r')} \cdot \frac{dr'}{c} = \tag{32}$$

$$= \Delta\tau_0 \cdot \frac{D}{8\pi^3 c^2} \cdot \frac{(kT)^{9/2}}{\hbar^3} \cdot I_6 \cdot \frac{2}{H} \cdot (\sqrt{E_0} - \sqrt{E(r)}).$$

Let us introduce a new constant ϵ_0 for which:

$$\frac{1}{\sqrt{\epsilon_0}} \equiv \frac{D}{8\pi^3 c^2} \cdot \frac{(kT)^{9/2}}{\hbar^3} \cdot I_6 \cdot \frac{2}{H},$$

so $\epsilon_0 = 2.391 \cdot 10^{-4}\ eV$, then

$$t(r) = \frac{\Delta\tau_0}{\sqrt{\epsilon_0}} \cdot (\sqrt{E_0} - \sqrt{E(r)}) = \Delta\tau_0 \sqrt{\frac{E_0}{\epsilon_0}} \cdot (1 - \exp(-Hr/2c)), \tag{33}$$

where E_0 is an initial photon energy. This delay as a function of redshift is:

$$t(z) = \Delta\tau_0 \sqrt{\frac{E_0}{\epsilon_0}} \cdot \frac{\sqrt{1+z} - 1}{\sqrt{1+z}}. \tag{34}$$

In this case, the time-lag between photons emitted in one moment from the same source with different initial energies E_{01} and E_{02} will be proportional to the difference $\sqrt{E_{01}} - \sqrt{E_{02}}$, and more energetic photons should arrive later, also as in the first case. To find $\Delta\tau_0$, we must compare the computed value of time-lag with future observations. An analysis of time-resolved emissions from the gamma-ray burst GRB 081126 [21] showed that the optical peak occurred (8.4 ± 3.9) *s later* than the second gamma peak; perhaps, it means that this delay is connected with the mechanism of burst.

5.3.3. An Influence of Graviton Pairing

Graviton pairing of existing gravitons of the background is a necessary stage to ensure the Newtonian attraction in this model. As it has been shown in [5], the spectrum of pairs is the Planckian one, too, but with the smaller temperature $T_2 \equiv 2^{-3/4}T$; this spectrum may be written as: $f(\omega_2, T_2)d\omega_2$, where $\omega_2 \equiv 2\omega$. Then residual single gravitons will have the new spectrum: $f(\omega, T)d\omega - f(\omega_2, T_2)d\omega_2$, and we should also take into account an additional contribution of pairs into the time delay.

We shall have now:

$$dN(\epsilon) = E(r) \cdot \frac{dr}{c}\frac{1}{2\pi}D(f(\omega, T)d\omega - f(\omega_2, T_2)d\omega_2), \tag{35}$$

and for pairs with energies 2ϵ :

$$dN(2\epsilon) = \frac{|dE(2\epsilon)|}{2\epsilon} = E(r) \cdot \frac{dr}{c}\frac{1}{2\pi}Df(\omega_2, T_2)d\omega_2. \tag{36}$$

After a collision of a photon with a pair, a virtual photon will have a velocity $v_2 : v_2/c = (E - 2\epsilon)/(E + 2\epsilon)$, and a mass m_2: $m_2c^2 = 2\sqrt{2\epsilon E}$.

For the case of subsection 5.3.1, after collisions with pairs: $\Delta E = 4\epsilon$, $\Delta\tau \geq \hbar/8\epsilon$, and we get:

$$\Delta t(2\epsilon) \geq \hbar/2 \cdot \frac{1}{E + 2\epsilon}. \tag{37}$$

Then due to single gravitons and pairs:

$$dt_2(\epsilon) = dt'(\epsilon) + dt(2\epsilon) \geq dt(\epsilon) - \hbar/2 \cdot \frac{\epsilon E}{(E + \epsilon)(E + 2\epsilon)} \cdot \frac{dr}{c}\frac{1}{2\pi}Df(\omega_2, T_2)d\omega_2, \tag{38}$$

where $dt'(\epsilon)$ is a reduced contribution of single gravitons, $dt(\epsilon)$ is its full contribution corresponding to formula (21). We see that if one takes into account graviton pairing, the estimate of delay became smaller. So as

$$\epsilon E/(E + \epsilon)(E + 2\epsilon) \to 0$$

by $\epsilon/E \to 0$, we have for the maximal delay in this case: $t_{2\infty}(r) \to t_\infty(r)$, i.e. the maximal delay is the same as in subsection 5.3.1.

Repeating the above procedure for the case of subsection 5.3.2, we shall get:

$$t_2(r) = [1 + (1 - 1/\sqrt{2}) \cdot (T_2/T)^{9/2}] \cdot t(r) \simeq 1.028 \cdot t(r), \tag{39}$$

where $t_2(r)$ takes into account graviton pairing, and $t(r)$ is described by formula (33). In this case, the full delay is bigger on about 2.8% than for single gravitons.

6. Virtual Massive Gravitons as Dark Matter Particles

Unlike models of expanding universe, in this model a problem of utilization of energy, lost by radiation of remote objects, exists (see [8]). A virtual graviton forms under collision of a photon with a graviton of the graviton background. It should be massive if an initial graviton transfers its total momentum to a photon; it follows from the energy conservation law that its energy $\epsilon^{'}$ must be equal to 2ϵ if ϵ is an initial graviton energy. By force of the uncertainty relation, one has for a virtual graviton lifetime τ : $\tau \leq \frac{\hbar}{\epsilon^{'}}$, i.e. for $\epsilon^{'} \sim 10^{-3}eV$ it is $\tau \leq 10^{-12}s$. By force of conservation laws for energy, momentum and angular momentum, the virtual graviton may decay into no less than three real gravitons. In a case of decay into three gravitons, their energies should be equal to $\epsilon, \epsilon^{''}, \epsilon^{'''}$, with $\epsilon^{''} + \epsilon^{'''} = \epsilon$. So, after this decay, two new gravitons with $\epsilon^{''}, \epsilon^{'''} < \epsilon$ inflow into the graviton background. It is a source of refilling the graviton background. Collisions of gravitons with massive bodies, leading to their deceleration [13], should provide the bulk of this replenishment.

From another side, a self-interaction of gravitons of the background should also lead to the formation of virtual massive gravitons with energies less than ϵ_{min} where ϵ_{min} is a minimal energy of gravitons of an interacting pare. If gravitons with energies $\epsilon^{''}, \epsilon^{'''}$ experience a series of collisions with gravitons of the background, their lifetime should increase. In every such a cycle collision-decay, an average energy of "redundant" gravitons will double decrease, and its lifetime will double or more increase. Only for ~ 93 cycles, a lifetime will have increased from $10^{-12}s$ to as minimum 1 Gyr. Such virtual massive gravitons, with the lifetime increasing from one collision to another, would be ideal dark matter particles. The ones will not interact with matter in any manner except usual gravitation. The ultracold gas of such gravitons will condense under the influence of gravitational attraction. In addition, even in the absence of the initial inhomogeneity in such the gas, it will easily arise. It is a way of cooling the graviton background.

The model of the composite fundamental fermions by the author [17] has all symmetries of the standard model of elementary particles on global level. Possibly virtual gravitons with very low masses are quite acceptable for the role of components of such the fermions.

7. How to Verify the Main Conjecture of This Approach

The main conjecture of this approach about the quantum nature of redshifts may be verified in a ground-based laser experiment. To do it, one should compare spectra of laser radiation before and after passing some distance l in a high-vacuum tube [12]. The temperature T of the graviton background coincides in the model with the one of CMB. Assuming $T = 2.7K$, we have for

the average graviton energy: $\bar{\epsilon} = 8.98 \cdot 10^{-4}$ eV. Because of the quantum nature of redshift, the satellite of main laser line of frequency ν would appear after passing the tube with a redshift of 10^{-3} eV/h, and its position should be fixed. It will be caused by the fact that on a very small way in the tube only a small part of photons may collide with gravitons of the background. The rest of them will have unchanged energies. The center-of-mass of laser radiation spectrum should be shifted proportionally to a photon path. Due to the quantum nature of shifting process, the ratio of satellite's intensity to main line's intensity should have the order: $\sim \frac{h\nu}{\bar{\epsilon}} \frac{H_0}{c} l$. Given a very low signal photon number frequency, one could use a single photon counter to measure the intensity of the satellite line after a narrow-band filter with filter's transmittance k. If q is a quantum output of a photomultiplier cathode, f_n is a frequency of its noise pulses, and n is a desired signal-to-noise ratio, then an evaluated time duration t of data acquisition would be equal to:

$$t = \frac{(\bar{\epsilon} c n)^2 f_n}{(H_0 q k P l)^2}, \tag{40}$$

where P is a laser power. Assuming for example: $n = 10$, $f_n = 10^3$ s^{-1}, $q = 0.3$, $k = 0.1$, $P = 200$ W, $l = 300$ km, we have the estimate: $t \approx 3 \cdot 10^3$ s. Such the value of l may be achieved if one forces a laser beam to whipsaw many times between mirrors in the vacuum tube with the length of a few kilometers.

Conclusion

In this approach, the main quantum effect of gravity is the inverse square law, postulated by Isaac Newton to explain the motion of bodies in the solar system. It is this effect that guarantees the irreversibility of time: when time is reversed, attraction should be replaced by repulsion thanks to the described mechanism of gravity. Here we can calculate the Newton and Hubble constants as functions of background temperature using the new dimensional constant D. A very large value of D makes gravity at the quantum level super strong. Of course, the question arises: where in high-energy physics could such a super-strong interaction be hidden? Perhaps the existence of three generations of fundamental fermions may be due to their complex nature; then their components can be connected by this interaction. On the other hand, background gravitons should create a region of very high perturbance near any microparticle, which gives us hope to explore in more detail using this approach the currently unknown nature of quantum uncertainty in the microworld, described by quantum mechanics.

The scattering of photons by background gravitons leads to three effects [15], two of which are observed, but currently have a different interpretation

based on the generally accepted cosmological paradigm. The cost of this interpretation is very high: cosmological expansion must be accepted to explain the redshift of distant objects, and their additional dimming requires the invention of dark energy to accelerate this expansion.When New Horizons observations [20] of the third effect (light from nowhere effect) will be confirmed, this triad can become a very important argument for changing the existing paradigm. If in the case of Big Bang cosmology we have to trust the main hypothesis without a chance to prove it, then the local quantum nature of the cosmological redshifts in this approach can be tested in the described laser experiment.

References

[1] Riess, A.G. et al. Observational Evidence from Supernovae for an Accelerating Universe and a Cosmological Constant. *AJ* (1998) 116:1009.

[2] Perlmutter, S. et al. Measurements of Ω and Λ from 42 High-Redshift Supernovae. *ApJ* (1999) 517: 565.

[3] Rovelli, C. Loop Quantum Gravity. *Living Reviews in Relativity* (2008) 11(1):5.

[4] Ivanov, M.A. Possible manifestations of the graviton background. *Gen. Rel. Grav.* (2001) 33:479; Erratum-ibid. (2003) 35:939; [astro-ph/0005084v2].

[5] Ivanov, M.A. *Screening the graviton background, graviton pairing, and Newtonian gravity.* [gr-qc/0207006].

[6] Ivanov, M.A. *Asymptotic freedom in low-energy quantum gravity.* [hep-th/0801.0291v3].

[7] Ivanov, M.A. A non-universal transition to asymptotic freedom in low-energy quantum gravity. *Journal of Gravitational Physics* (2008) 2(2):26.

[8] Ivanov, M.A. A fine quantum mechanism of classical gravity. *The Tenth Marcel Grossmann Meeting (MG10)*, 20-26 July 2003, Rio de Janeiro, Brazil; [gr-qc/0307093].

[9] Ivanov, M.A. *Deceleration of massive bodies due to forehead and backhead collisions with gravitons.* [https://vixra.org/pdf/1712.0097v1.pdf].

[10] Ivanov, M.A. *Modified dynamics of massive bodies in the graviton background.* [https://vixra.org/pdf/1907.0257v2.pdf].

[11] Ivanov, M.A. Gravitons as super-strong interacting particles, and low-energy quantum gravity. In the book *"Focus on Quantum Gravity Research"*, Ed. D.C. Moore, NY: Nova Science, 2006, 89-120; [hep-th/0506189].

[12] Ivanov, M.A. *Selected papers on low-energy quantum gravity.* [http://ivanovma.narod.ru/selected-papers-Ivanov2018.pdf].

[13] Ivanov, M.A. Low-energy quantum gravity and cosmology without dark energy. *Advances in Astrophysics* (2019) 4(1):1.

[14] Betoule, M. et al. *Improved cosmological constraints from a joint analysis of the SDSS-II and SNLS supernova samples.* [arXiv:1401.4064v2 [astro-ph.CO]].

[15] Ivanov, M.A. *Three Different Effects of the Same Quantum Nature.* PoS(EPS-HEP2021)114.

[16] Lauer, T.R., et al. New Horizons Observations of the Cosmic Optical Background. *ApJ* (2021) 906:77; [arXiv:2011.03052v2 [astro-ph.GA]].

[17] Ivanov, M.A. Primary Postulates of the Standard Model as Consequences of the Composite Nature of the Fundamental Fermions. *Nuovo Cimento* (1992) 105A:77; [hep-th/0207210].

[18] Ivanov, M.A. *Revealing the Quantum Origin of Gravity.* [https://vixra.org/pdf/2303.0023v1.pdf].

[19] Liu, A. et al. *Cosmology with the Highly Redshifted 21cm Line.* [arXiv:1903.06240v1 [astro-ph.CO]].

[20] Ivanov, M.A. *Lorentz symmetry violation due to interactions of photons with the graviton background.* [arXiv:0907.1032v2 [physics.gen-ph]].

[21] Klotz, A. et al. Correlated optical and gamma emissions from GRB 081126. *ApJ Lett.* (2009) 697:L18; [arXiv:0904.4786v1 [astro-ph.CO]].

Index

F

G

H

I

K

L

M

N

O

P

Q

R

S

T

U

V

W

Volume 312

HORIZONS IN WORLD PHYSICS

Albert Reimer
Editor

nova
science publishers
www.novapublishers.com

ISBN-13: 979-8-89113-522-2